Development of a One-Dimensional Electro-Thermophysical Model of the Snow Sea-Ice System: Arctic Climate Processes and Microwave Remote Sensing Applications

by

John Michael Hanesiak

A Thesis
Submitted to the Faculty of Graduate Studies
in partial fulfillment of the requirements
for the degree of

Doctor of Philosophy

Centre for Earth Observation Science
Department of Geography
University of Manitoba

Winnipeg, Manitoba, Canada, 2001

0-612-62637-7

Canada

THE UNIVERSITY OF MANITOBA

FACULTY OF GRADUATE STUDIES
*****
COPYRIGHT PERMISSION PAGE

Development of a One-Dimensional Electro-Thermophysical Model of
the Snow Sea-Ice System: Arctic Climate Processes and Microwave
Remote Sensing Applications

by

John Michael Hanesiak

A Thesis/Practicum submitted to the Faculty of Graduate Studies of The University

of Manitoba in partial fulfillment of the requirements of the degree

of

Doctor of Philosophy

John Michael Hanesiak © 2001

ABSTRACT

Snow covered sea ice plays a crucial role in the earth's climate. This includes polar biology, local, regional and world weather and ocean circulations as well as indigenous people's way of life. Recent research has indicated significant climate change in the polar regions, especially the Canadian arctic. Polar climate processes are also among the most poorly misrepresented within global circulation models (GCMs). The goal of this thesis is to improve our understanding and capability to simulate arctic climate processes in a predictive sense. An electro-thermophysical relationship exists between the thermophysical characteristics (climate variables and processes) and electrical properties (dielectrics) that control microwave remote sensing of snow-covered first-year sea ice (FYI). This work explicitly links microwave dielectrics and a thermodynamic model of snow and sea ice by addressing four key issues. These includes: 1) ensure the existing one-dimensional sea ice models treat the surface energy balance (SEB) and snow/ice thermodynamics in the appropriate time scales we see occurring in field experiments, 2) ensure the snow/ice thermodynamics are not compromised by differences in environmental and spatial representation within components of the SEB, 3) ensure the snow layer is properly handled in the modeling environment, and 4) how we can make use of satellite microwave remote sensing data within the model environment. Results suggest that diurnal processes are critical and need to be accounted for in modeling snow-covered FYI, similar to time scales acting in microwave remote sensing signatures. The parameterization of incident short-wave ($K\downarrow$) and long-wave ($L\downarrow$) radiation contain seasonal and environmental biases in some arctic locations (i.e. near polynyas) and have been adjusted to account for these biases. The representation of surface albedo needs to be improved in sea ice models. Surface and airborne measurements of albedo over FYI in the melt season suggest four distinct cover types that dominate albedo that need to be included in process models and GCMs. The $K\downarrow$, $L\downarrow$, and albedo are critical in the SEB and therefore indirectly impact snow and ice microwave dielectrics through the electro-thermophysical relationship. The snow layer representation in current sea ice models is not sufficient for linkages to snow and ice microwave dielectrics. A detailed mass and energy balance 1-D snow model is coupled to a FYI model, a type of model that has not

existed until now. Results suggest the coupled version of the model improves simulations of FYI over annual cycles. The addition of salinity in snow thermal conductivity and specific heat improves ice temperatures during the melt season but causes over estimations of ice temperatures in the cold season. Addition of salinity in the mass balance of the model (in future implementations) will improve ice temperature simulation during the cold season. Output from the coupled snow sea-ice model provides the required input to microwave dielectric models of snow and sea ice to predict microwave penetration depths within the snow and sea ice (an Electro-Thermophysical model of the Snow Sea Ice System (ETSSIS)). Results suggest ETSSIS can accurately simulate microwave penetration depths in the cold dry snow season and wet snow season (funicular snow regime). Simulated penetration depths become too large in the pendular snow regime since liquid water is not generated soon enough within the snow pack in the spring season. The inclusion of salinity in the mass balance of ETSSIS will improve the simulation of penetration depths in the pendular snow regime in future implementations of the model.

ACKNOWLEDGEMENTS

DEDICATION

This thesis is dedicated to my loving wife (Teresa) who has endured the challenges (mentally, financially and emotionally) of my academic endeavors as well as my Mom (Nadia) and Dad (John) for providing the initial opportunity to pursue post-secondary studies. My sincere love and gratitude goes to them as well as my Sister (Bonnie), who have all provided undaunted and endless support, understanding and belief in me ... and of course, Sadie too (our dog), who sat beside me on those long afternoons of computer work!

TABLE OF CONTENTS

LIST OF TABLES

LIST OF FIGURES

CHAPTER 1: Introduction and Statement of Objectives

1.1 Motivation

Sea ice plays an important role in the earth's climate. It supplies freshwater to the North Atlantic via ice export, it moderates ocean-atmosphere heat, moisture, and momentum exchanges, and it provides a biological habitat for primary production up to mammals. Ice that is expelled from the polar regions and carried into mid-latitudes by wind and ocean currents eventually melts, supplying a fresh water source in the upper ocean. This creates varying strata within the ocean system that drives oceanic circulation. The sea ice provides a layer of insulation between the relatively warm ocean water and the cold atmosphere in winter, severely limiting the amount of heat and moisture transfer from the ocean to the atmosphere during this season. The ice also acts to limit the atmospheric contribution to ocean currents by suppressing wind drag directly on the ocean surface. Primary production in the arctic strongly depends on the existence of ice, and without it, aquatic life and land mammals would be directly affected through food chain dynamics.

We expect to see the first and largest impact of CO_2 induced global climate change within the polar regions. Various feedbacks occur within the ocean-sea ice-atmosphere system which tend to amplify climate processes (Moritz and Perovich, 1998). We expect that sea ice plays a central role in these processes due to its control on the exchange of energy and mass between the ocean and atmosphere. Current global circulation models[1] (GCMs) suggest that warming in the arctic will be 2-3 times larger

---

[1] GCMs are computer models that simulate the earth's climate.

than the global mean warming (Kattenberg et al., 1996). A primary process that controls this enhanced polar warming is the sea ice-albedo[2] feedback (Curry et al., 1995). This feedback is driven by increased arctic air temperatures (associated with a global warming scenario) that ablates more ice, in turn decreasing the aerial extent of the ice pack. The ocean surface becomes more exposed releasing more heat into the atmosphere, and with a much lower surface albedo (0.1) compared to the snow/ice surface (0.8), the system absorbs more solar energy. The increased heat release and solar absorption acts to further enhance atmospheric warming, thereby, ablating more ice, and so on. However, critical feedbacks such as the cloud-sea ice feedback and any precipitation changes to the system act in complicated ways to enhance and counteract other feedbacks (see for example, Barry et al., 1984). The feedback processes occur over a continuum of spatial and temporal scales and the interaction of these processes makes long range climate modeling a difficult task.

Over the past decade there has been a detectable change in both the atmosphere and the ocean of the arctic (Serreze et al. 2000) as well as northern hemisphere snow cover characteristics (Brown, 2000). Sea level pressure over the arctic has decreased dramatically, signifying an anomalous circulation within the atmosphere (Walsh et al. 1996). At the same time the Arctic Atlantic Layer (200-500m) has warmed by about 1.5°C (Carmack et al. 1995), which may be related to an observed reduction in the thermodynamic equilibrium thickness[3] of sea ice within the Arctic Basin from 3.1 m to 1.8 m (Rothrock et al., 1999). This decrease in ice thickness may not be the result of thermodynamic forcing alone but by dynamic forcing, a fact that negates ice thickness decreases solely caused by global

_____

[2] albedo is defined as the ratio of energy reflected from a surface over energy incident upon the surface.

warming. Recent results show that sea ice concentrations are reducing at a rate of about 34,000 km^2 per year or 2.9% per decade (over the past 18 years) (Parkinson et al. 1999). Canadian GCMs are in agreement with these rates of decay and suggest a complete disappearance of the perennial ice pack (multi-year ice (MYI[4])) before 2100 (Boer et al. 2000). This implies that a greater amount of the arctic will become covered with seasonal sea ice (first-year ice (FYI) during the winter which has already been observed (Canadian Ice Service (CIS), pers comm). In fact, 1998 saw the least amount of MYI within the Canadian Arctic Archipelago since the CIS began records 20 years ago. Changes have been observed around the globe. Since 1945 the net mass of 80% of the glaciers in the arctic, Canadian and European mountains have significantly declined with an associated rise in sea level (8 cm between the years 1800 – 2000) (Greg Flato, pers. comm.). The North American snow pack has also seen a decline in its duration and southern extent over the past 20 years; Canadian GCMs are in agreement with these observations (Boer et al. 2000). However, it should be emphasized that it has yet to be proven that the changes being experienced have been caused by anthropogenic forcing and not due to natural climate variability. It is noteworthy however that the recent IPCC report concluded that the balance of evidence now suggests that there is a discernable influence of humans on the global climate system (IPCC, 1996).

With the importance of sea ice in the global climate and recent observations of significant changes in the polar regions, there is a need for improving our understanding of polar processes and further advancing our GCM capabilities. Polar processes are

---

[3] Thermodynamic equilibrium thickness is the mean pack ice thickness resulting from a balanced ocean-atmosphere climate system (i.e. atmospheric cooling is balanced by ocean warming).
[4] Formal definition of the sea ice types cited here can be found in MANICE (Manual of Standard Procedures for Observing and Reporting Ice Conditions; www.ec.gc.ca/manice/title_pg.htm)

among the most poorly understood and require greater attention (IPCC, 1996). Although the worlds GCMs generally agree that the arctic will warm as time goes on, they do not agree on the magnitude of these changes. Deficiencies arise from poorly understood processes and inadequate model physics/parameterizations[5]. Progress in climate modeling will depend on new data sets and their utility for improving and validating critical processes and parameterizations (IPCC, 1996). To illustrate a deficiency with current GCMs, the treatment of snow and sea ice is typically a single homogeneous slab with bulk physical properties. We know from field observations (Makshstas, 1991) and modeling (Maykut, 1978) that this treatment is not sufficient since the energy balance can be very different for various ice thicknesses and ice types (Papakyriakou, 1999). Snow has a very important role in the seasonal evolution of sea ice due to its high insulation and reflective properties, making its relationship with sea ice complex (Brown and Goodison, 1994; Barber et al., 1994; Papakyriakou, 1999). Snow warms the ice in winter because of its low thermal conductivity (high insulating properties) that inhibits ice growth. In the spring and early summer, the snow acts to enhance ice growth by reflecting most of the solar energy (inhibits internal heating) with its high albedo (Ebert and Curry, 1993). Thus, the timing of a heavy snowfall in a particular location will have different effects on the seasonal evolution of sea ice. The internal physical changes within the snow are also important for determining the net thermodynamic effect on sea ice through seasonal energy balance variations (Jordan et al., 1999).

---

[5] Parameterization is a technique to simulate a certain parameter through empirical formulations or combination of empirical and physical methods, as opposed to using a purely physical relationship.

One-dimensional[6] thermodynamic models of snow (Jordan et al., 1999) and sea ice (Flato and Brown, 1996; Ebert and Curry, 1993) are being used to investigate more detailed processes that control arctic climate processes. These models have much more detailed physical processes within the snow and sea ice than GCMs, and results from these investigations can provide better physical parameterizations for GCMs in the future. Most numerical simulations of multi-year and first-year sea ice using one-dimensional thermodynamic models have been conducted using daily average or monthly external forcing (see for example, Maykut and Untersteiner, 1971; Ebert and Curry, 1993; Flato and Brown, 1996). Studies such as those of Maykut and Untersteiner (1971) and Ebert and Curry (1993) focused on equilibrium simulations for multi-year sea ice using coarse monthly climatological forcing. Gabison (1987) used monthly averages of climatological data to compare a modeled annual first-year sea ice cycle to an observed climatological ice cycle for different Arctic locations. More recently, Flato and Brown (1996) used daily forcing simulations of land-fast first-year sea ice to illustrate the role of snowfall and air temperature in driving interannual variations in maximum ice thickness and the timing of snow/ice ablation. The importance of the snow layer on first-year sea ice has also been indicated by observations (Bown and Cote, 1992; Brown and Goodison, 1994; Barber et al., 1994). However, even current one-dimensional models have major deficiencies and work is ongoing to improve different components within them. Another limitation of these models is that they can not be directly applied to microwave remote sensing since the variables that control microwave dielectrics (defined in section 2.4) are either not

---

[6] One-dimensionality refers to thermodynamic processes operating in the vertical coordinate throughout the ocean-ice, snow-ice, snow-atmosphere interfaces and within the snow and ice layers.

simulated or not simulated in the proper time scales. Further discussion of this is provided throughout the thesis.

A particularly important time of year in the arctic is the spring and early summer (May and June) where the initiation of snow and ice melt toward complete melt can be fairly rapid (Ebert and Curry, 1993). In addition, the onset and progression of melt have large inter-annual and regional variations (Barry et al., 1989; Barber et al., 1998). The arctic spring and summer sees the largest solar irradiance which greatly enhances melt. The initiation, extent and rate of snow and ice melt are critical on the arctic sea ice balance and climate (Barry and Maslanik, 1989; Ebert and Curry, 1993). A controlling variable in the arctic energy balance is the short-wave[7] surface albedo. Central arctic albedo ranges from 0.8 (snow surface) in early spring before melt begins then declines to near 0.4 once melt ponds[8] and bare ice are present (see for example, Robinson et al., 1986; Lindsay and Rothrock, 1993, 1994). As the albedo declines, more short-wave energy is made available for melt, in turn decreasing the albedo further. Numerical models have major difficulty attempting to simulate the surface albedo with respect to its spatial and temporal variability, a characteristic that must be improved before we can adequately simulate seasonal changes in sea ice. More albedo observations are needed toward this goal.

The surface energy balance (SEB) (defined in Chapter 2), in which the albedo is a component, is crucial to sea ice (see for example, Zhang et al., 1996; Steffen and DeMaria, 1996) and its variations are critical for understanding the year to year differences in snow/ice decay. A key component of the surface energy balance is incident

---

[7] Short-wave refers to the portion of the electromagnetic spectrum between wavelengths 0.3 - 4 μm.
[8] Melt ponds (ponds of water) form on the ice surface from accumulated melted snow and surface ice melt.

atmospheric radiation (short-wave (K↓) and long-wave[9] (L↓)) upon the snow and ice surfaces that are major energy (heat) sources. The distinction between the wavelength ranges is that the short-wave has its origin from the Sun, and the long-wave is of terrestrial origin. Radiative fluxes are usually two orders of magnitude greater than the ocean heat flux at the ice underside and planetary boundary layer turbulent fluxes (see for example Ebert and Curry, 1993). These characteristics result in radiative fluxes dominating the overall sea ice thermodynamics. The diurnal SEB can affect snow grain growth, snow brine volume and snow wetness through thermodynamic processes which in turn all affect passive and active microwave remote sensing (see for example, Barber et al., 1994; Barber et al., 1995a). Changes in snow properties also strongly affect the surface albedo that feeds back into the SEB. In the absence of an adequate arctic radiation network, accurate model simulations of sea ice thermodynamics therefore require accurate incident radiation parameterizations.

Active[10] and passive[11] microwave remote sensing (in particular, active satellite Synthetic Aperture Radar (SAR) and passive satellite microwave radiometry) are proving to be valuable tools for investigating and monitoring arctic sea ice seasonal evolution. This portion of the spectrum provides information on the physical and electrical state of the surface with the added advantage of all-weather, day and night observations. The SAR scattering (or resulting returned signal) and SSM/I-measured emission is dominated by the combined geophysical and electrical conditions of the surface in the micro and macro scales. The evolution of the scattering and emission is related to the overall

---

[9] Long-wave refers to the portion of the electromagnetic spectrum between 3.5 – 50 μm.
[10] Active remote sensing is a device which sends out a signal to a target and then receives a returned signal from that target.
[11] Passive remote sensing is a device which measures an emitted signal from a target.

thermodynamics of the system and the control of temperature on both the physical and electrical properties of the volume (Barber et al., 1994). Recent work has shown that the temporal evolution of SAR scattering can be used to infer some physical (e.g., ice type, snow grain size, perhaps snow thickness, snow salinity, melt pond formation, and melt pond fraction) and SEB (e.g. short-wave flux, albedo, long-wave flux and thermal conductivity) attributes of the polar climate (see Barber et al., 1995a; Barber et al., 1998). Similarly, passive microwave sensors are valuable for monitoring sea ice extent and concentration throughout the polar regions (see for example, Weaver and Troisi, 1996; Weaver et al., 1987). The relationship between SAR and SSM/I signatures and the thermodynamic sea ice system brings about new ideas of how we can better understand the physical processes involved. Utilizing numerical techniques and remote observations in tandem can lead to improved ways in understanding and monitoring polar processes.

Considerable progress has been made in both the modeling and remote sensing communities dealing with sea ice processes, however, there are still major deficiencies with the models and research is still required to better understand the physical processes behind what we see in microwave satellite imagery.

The intent of my dissertation is to begin the process of linking thermodynamic models of snow and sea ice with satellite microwave remote sensing. A major impetus for combining remote sensing into sea ice numerical process models is to improve our understanding and monitoring of the arctic climate system where very few observations are available otherwise. Other research areas have also indicated the need for combining remote sensing with numerical models. Gower (1995) expressed that remote sensing products are essential to ocean research and "because of the major importance attached to

modeling (the earth's oceans), the WOCE (World Ocean Circulation Experiment) requires a major effort in assimilation of remote sensing data into the models". In the agricultural community, Brown (1995) has indicated that "remote sensing will be of great value for determining soil moisture over a wide area for initial soil moisture input to vegetation development models".

The integration of remote sensing and numerical sea ice models could lead to a new approach in looking at spatially and temporally complex, highly interrelated arctic cryospheric processes. The remote sensing data can also play a role in the initialization and validation of numerical sea ice models. Furthermore, remote sensing could become an integral component of the sea ice model creating a hybrid numerical model which explicitly considers spatial interrelationship of processes within the model environment. Remote sensing can also be used to replace some model parameterizations or constrain elements within the system. There are two main advantages of these approaches; 1) the combined use of remote sensing and modeling may be used to simulate as realistically as possible those variables that can not be derived from remote observations alone, such as the distribution of sea ice thickness, 2) using remote sensing in place of some model parameterizations, other processes in the model can be examined in more detail, such as, if surface albedo is well handled by remote observations, other variables/processes may be held accountable for "erroneous" model simulations. Another approach is through microwave forward and inverse scattering models that have advanced to a state that makes them valuable supplementary tools for understanding the remote observations (see reviews by Golden et al., 1998a,b) which in turn can be linked to thermodynamic models.

We are now in a position to begin the first steps of directly linking thermodynamic modeling with microwave remote sensing through the interactions of thermodynamics, dielectrics and the thermophysical properties of the snow/sea ice system. This is termed an 'electro-thermophysical' relationship and in what follows I explain how the thermodynamic and geophysical properties of the snow and sea ice control their microwave electrical and backscatter characteristics.

In the 'electro-thermophysical' framework, I strive to develop a model which couples knowledge of the scattering physics of the surface with a one-dimensional (1-D) thermodynamic model of the sea ice/snow system. The advantage of this approach is that the geophysical and electrical properties of the surface give rise to scattering and emission in the microwave portion of the spectrum; changes in the geophysical and or electrical state of the volume are driven by the thermodynamics across the interface. A model of these relationships would allow us to measure both the geophysical state of sea ice at any particular time and also evaluate the temporal evolution of this scattering over a period coinciding with the seasonal evolution of the surface. Since the SEB also evolves directly from the thermodynamic and physical state of the system, we also expect to be able to determine proxy measures of certain SEB state variables such as surface temperature, albedo, long-wave flux, surface atmospheric drag, etc. This information can also be useful in determining the timing of accretion and ablation and producing estimates of the mechanical strength of sea ice and/or timing of fast ice break-up.

My work includes a number of aspects dealing with snow covered FYI. This includes the critical processes that control the thermodynamics (growth and ablation) of snow covered smooth first-year sea ice (FYI) in a one-dimensional sense and how they

relate to microwave remote sensing. I limit my work to FYI not only to narrow my focus but to include a type of ice that is studied to a lesser degree than multi-year sea ice (MYI). In addition, at the current rate of arctic MYI depletion, there will be more FYI occupying the arctic oceans in the future. Numerical modeling and microwave remote sensing are also proving to be more useful tools for FYI. Smooth FYI (as opposed to rubbled and rafted FYI) is less complicated to study in terms of its flatter surface and more homogeneous physical structure, making it easier to simulate in numerical modeling and identifying relationships between ice thermodynamics and microwave remote sensing. Hence I also assume that the FYI is not a dynamic volume (i.e. the ice is not moving horizontally due to ocean currents or wind drag) which is typical of most FYI in the Canadian Arctic Archipelago (or fast-ice). This lends credence to the one-dimensionality assumption.

1.2 Thesis Objectives

The goal of my research is to conduct the initial steps necessary for combining a one-dimensional thermodynamic snow sea-ice model and microwave remote sensing that is related to arctic snow and sea ice processes. I eluded to several issues that need to be addressed and would advance the numerical model to a state where remote sensing could be better linked into the model environment. These include: 1) ensure the existing one-dimensional sea ice models treat the SEB and snow/ice thermodynamics in the appropriate time scales we see occurring in field experiments, 2) ensure the snow/ice thermodynamics are not compromised by differences in environmental and spatial representation within components of the SEB, 3) ensure that the snow layer is properly

11

handled in the modeling environment, and 4) how we can make use of satellite microwave remote sensing data with the model environment.

My specific research questions, which evolve directly from these issues are:

(1) Does the use of hourly and daily variable forcing result in a different simulation of the annual cycle of ice thermodynamics? If so, can the model parameterizations adequately represent specific processes over these shorter temporal scales, and is there a systematic bias in forcing the model with 'land based' versus 'on ice' measurements of input fluxes?

(2) How do selected parameterizations of $K\downarrow$ and $L\downarrow$ compare to *in situ* data and what are the characteristics of newer schemes that may be required?

(3) What are the broadband and spectral albedos over melting FYI as well as their local scale spatial variation (sub-km scale)? How do the surface albedos scale up to semi-regional (10's km) and regional (100's km) scales? What is the sensitivity of sea ice ablation to percent pond fraction and the associated spatial variability in surface albedo?

(4) Are there advantages of using a more sophisticated snow component within a coupled 1-D snow sea-ice model over a similar model that uses a single bulk property snow layer for annual cycles of snow-covered FYI?

(5) How can 1-D numerical models of snow-covered FYI be useful for microwave remote sensing applications?

In question (1) I examine whether hourly forcing (i.e. time step) results in a different simulation of ice thermodynamics than daily average forcing over an annual cycle using the sea ice model of Flato and Brown (1996). From field experiments, significant feedbacks operating between the atmosphere and the surface (e.g., albedo-snow grain growth; cloud cover-long-wave flux, etc.). The snow/ice properties do not scale linearly with radiative and turbulent fluxes in the SEB. I wish to examine this 'temporal scale' issue from both the perspective of parameterization of the model physics and integration of the thermodynamics over an annual cycle. In addition, I address the existing model parameterizations relative to *in situ* sea ice field observations made in the Canadian Archipelago between 1992 and 1993 during the Seasonal Ice Monitoring and Modeling Site (SIMMS) field programs (LeDrew and Barber, 1994). Specifically, I consider the model parameterizations of incident short-wave/long-wave radiation and albedo. This component will indicate how well the physics are handled within the existing parameterizations and help to ascertain where (if any) changes should be made when using shorter temporal scales. Finally, I am interested in differences in forcing which arise when using nearby land station versus *in situ* sea ice observations. Because regular annual observations do not exist over the ice, arctic meteorological observations from land stations are typically used to force sea ice models. However, local climate differences between on-ice and land are significant. This addresses the differences in ice simulations between using land-based forcing and on-ice forcing.

Question (2) deals with environmental and spatial differences in the incident radiative fluxes. That is, how accurate are the current incident radiation parameterizations for different arctic environments? For this analysis, I use unique *in situ* observations

13

taken in an arctic polynya[12] over terrestrial, fast-ice, marginal ice zone and open water environments during the 1998 International North Water (NOW) Polynya Project (Barber et al., 2001).

In question (3), I address the issue of albedo measurements (broadband and spectral) over a variety of FYI surfaces (including melt ponds) due to the dearth of information currently available. I then scale up the surface albedo measurements to regional scales (100's km) using aircraft aerial video and satellite data to show melt pond spatial variability and its albedo over FYI. Then I examine how the thermodynamic state (and mechanical strength) of the sea ice is affected by variations in fractional pond cover. In effect I am asking the question: "How important is it that the magnitude and spatial pattern of surface albedo (as examined above) is correctly parameterized within the annual cycle of sea ice ablation?" Measurements were made during C-ICE97 (Collaborative - Interdisciplinary Cryospheric Experiment 1997) conducted in Wellington Channel and Lancaster Sound, Nunavut.

Question (4) investigates model simulation differences in snow and ice physical and thermal evolution between a multiple layered coupled snow sea-ice model and a similar model that uses only a single bulk property snow layer. The one-dimensional mass and energy balance snow model (SNTHERM; Jordan et al., 1999) and sea ice model (Flato and Brown, 1996) are coupled at the snow-ice interface where fluxes of heat and radiation are transferred. Both models are coded in standard FORTRAN. The Simulation comparisons were conducted over a full annual cycle of FYI between 1992-93 as well as a specific shorter time period in 1992 to compare the models against measured

---

[12] A polynya is a body of water that remains primarily ice-free during the arctic winter months.

field data. This allowed a very detailed investigation into whether using a more sophisticated model is warranted for snow-covered FYI annual cycles.

The final question (5) illustrates the direct application of the coupled snow sea-ice model toward microwave remote sensing interpretation. The coupled model is linked to a microwave dielectric model; the amalgamation of the models produces a type of Electro-Thermophysical model of the Snow Sea-Ice System (ETSSIS). ETSSIS is directly compared to measured physical, thermodynamic and microwave dielectric variables to show how well and when the model reproduces them.

1.3 Thesis Structure

I begin by providing a discussion of the critical processes that control the thermodynamics within the FYI and snow surfaces over a range of temporal and spatial scales (Chapter 2 – section 2.1 and 2.2). Chapter 2 (section 2.3) also discusses how we can use numerical modeling to understand the critical processes, what processes are handled in these models, and what some of the deficiencies are. I limit the discussion primarily to one-dimensional thermodynamic models. Chapter 2 (section 2.4) outlines the utility of microwave remote sensing toward FYI thermodynamics. In particular, what processes we can observe in microwave imagery over the course of an annual cycle of FYI. Chapter 2 provides a thorough background to following chapters that address the five objectives in as many chapters. Research question 1 is discussed in Chapter 3 with the results being previously peer reviewed and published (see Hanesiak et al., 1999). Question 2 appears in Chapter 4 with the results being previously peer reviewed and

published (see Hanesiak et al., 2001a). Question 3 is addressed in Chapter 5 with the results being previously peer reviewed and published (see Hanesiak et al., 2001c). Chapter 6 contains results from question 4. Finally, question 5 results appear in Chapter 7 and in peer review for publication during the final version of this dissertation. The thesis concludes with a summary of results and research that should be conducted in the future (Chapter 8).

The usefulness of this work will be to advance our understanding and monitoring abilities of arctic snow covered sea ice processes. This will enable the climate modeling community to utilize new insights in future GCM implementation strategies. It can also be used toward operational sea ice applications when arctic ice decay becomes important for ocean navigation. Lastly, ETSSIS can be used to assist in the interpretation of satellite microwave remote sensing, a type of model that is unique for this purpose.

CHAPTER 2: Background

2.1 First-Year Sea Ice and its Snow Cover Characteristics

This section describes the critical thermodynamic processes within snow covered first-year sea ice over a variety of temporal and spatial scales. Sea ice has several stages of growth and development, classified by the World Meteorological Organization (WMO) and described in detail by the Manual of Standard Procedures for Observing and Reporting Ice Conditions (MANICE) (Figure 2.1). I pay particular attention to first-year sea ice (FYI) and begin with a brief description of the physical mechanisms of ice growth and snow evolution. An in depth discussion of snow and ice thermodynamics follows.
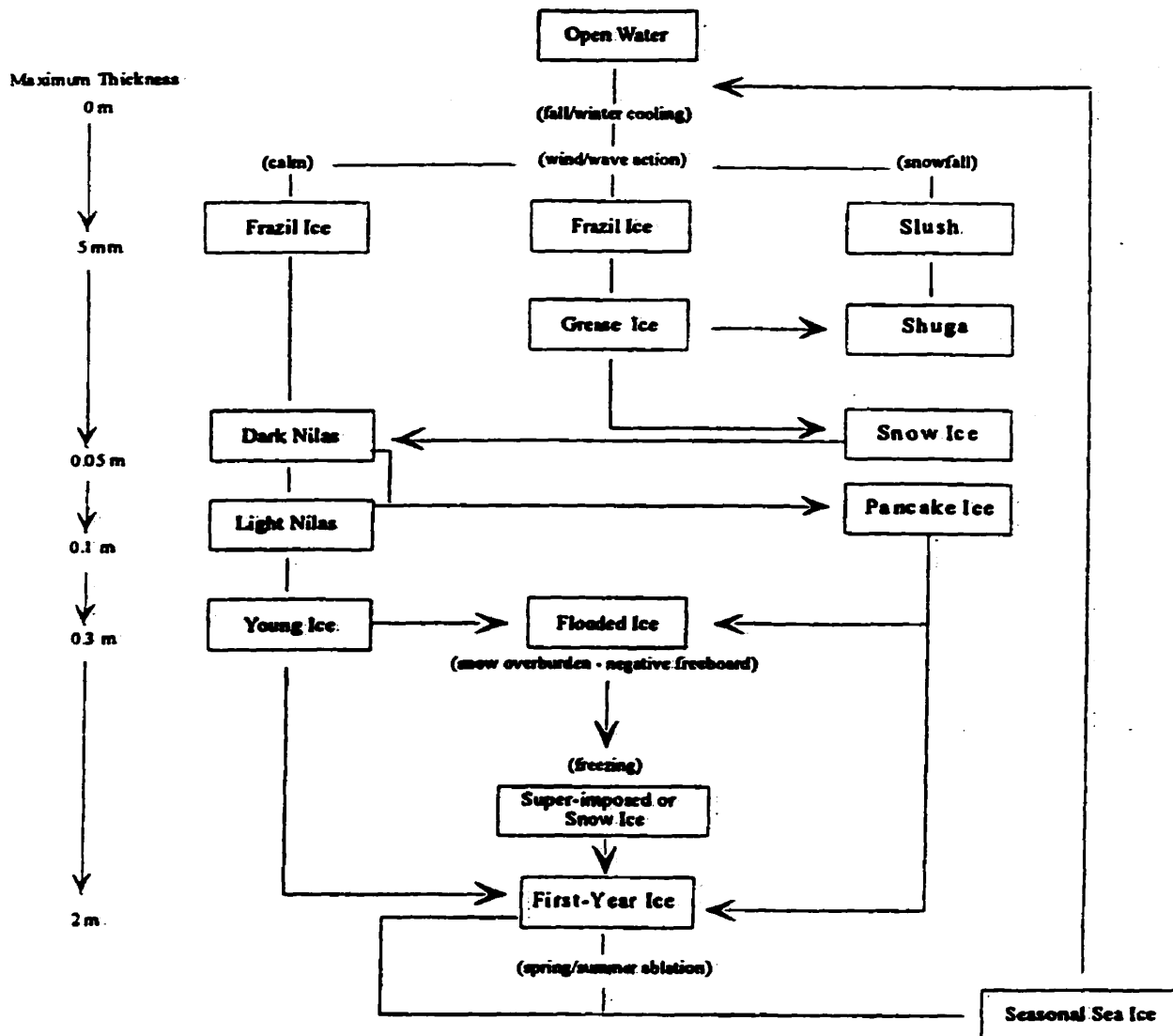
Figure 2.1: Stages of first-year ice growth, its thickness and external forcing (in brackets). Modified from Papakyriakou (1999).

New ice begins as frazil or slush (Figure 2.1) in the fall period during freeze-up (in temperatures ≤ -1.8°C) where heat is lost from the ocean to the atmosphere typically under windy conditions. Sea water has an average salinity of 32 ppt (parts per thousand), depressing its freezing temperature to below 0°C. As ice growth continues, grease ice and shuga (Figure 2.1) are formed (mixture of ice crystals and sea water), and continues to grow into more consolidated ice forms (nilas and pancake ice) over time. Conduction of

heat continues from the bottom to the top of the ice forming thicker young ice (0.3 m;

Figure 2.1). As young ice grows, vertical brine inclusions (mixture of salt and water)

form between ice columns that are near 1 mm in width but vary in size according to

growth rate (Figure 2.2) (Lofgren and Weeks, 1969). Salt that is trapped in the ice

structure is either in liquid brine form or solid depending on the ice temperature (Lock,

1990). Ice growth continues as a columnar structure to typical FYI thicknesses (30 – 200

cm). FYI is usually made up of 5-25% frazil ice (top layer) and 75-95% columnar ice

(Figure 2.2) (see for example, Weeks and Gow, 1980; Tucker et al., 1987). Typical FYI

densities are 880-910 kg m^{-3} with the variation primarily caused by air and salt content

(Fukusako, 1990). Density increases with increased salinity (if bubble content remains

constant) and decreases with increased porosity (Fukusako, 1990). This makes the

average bulk ice thermal conductivity near 2.1 W m^{-1} C^{-1}. All of the ice forms vary

widely over large spatial areas depending on proximity to land, other ice formations,

atmospheric wind and thermal conditions. This creates a myriad of ice conditions and ice

thickness once full consolidation takes place. Dynamic processes (ocean currents, wind

and ice contraction/expansion) also create various degrees of rough ice conditions

(ridged, rafted and rubbled ice) with pieces of ice extending upward from 0.5 – 3 m (not

including MYI floes). However, I am specifically interested in smooth FYI.
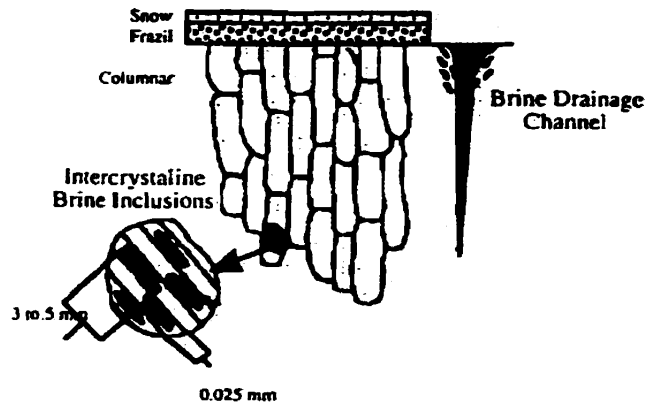
Figure 2.2: First-year sea ice physical characteristics showing the frazil and columnar positions relative to intercrystalline brine pockets and macroscale brine drainage channels. Adapted from Vant et al. (1978).

The brine inclusions are very important for heat conduction and latent heating within the sea ice (shown later). Brine is forced upward and downward within the ice layer as it grows. Brine and salt impurities that are forced upward out of the ice surface during initial ice growth form frost flowers (deformed tree-like structures that extend vertically on the ice surface between 2 – 6 cm). This results in the bottom snow layer (once snow has fallen) containing brine as well (see for example, Barber et al. 1995a) significantly affecting snow thermal properties (Papakyriakou, 1999). However, brine drainage is primarily of gravitational origin moving downward along the brine drainage channels (Bennington, 1963) and is ongoing over time as the ice grows. Brine pockets interconnect forming the tree-like brine channel within the ice from cm's to tens of cm's long (see Figure 2.2) (Lake and Lewis, 1970). The resulting FYI salinity profile over time appears as C-shaped (Figure 2.3). The rejection of brine out of the bottom of the sea ice has global ocean circulation ramifications. The more dense sea water at the ice underside creates an unstable ocean layer that generates the thermohaline ocean circulation and is a

fundamental process by forcing and maintaining global and regional ocean circulations (Aagaard et al., 1981).
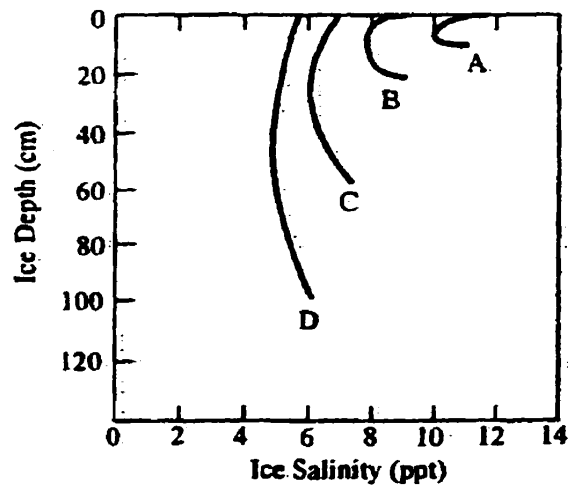
Figure 2.3: Typical salinity profiles for growing first-year sea ice. Curves A-D represent ice thickness between 10 to 100 cm. Adapted from Maykut (1985).

During the melt season (April – August), the available liquid water from the snow pack and melted top layer of ice forms melt ponds on the ice surface (Figure 2.4). Aerial melt pond fractions vary dramatically with time and location over the course of the melt season. Melt ponds reduce the surface albedo significantly with maximum pond aerial fractions near 75% on smooth FYI (see for example, Barber and Yackel, 1999). Pond fractions tend to decline to values between 35-50% once drainage takes place due to seal holes and cracks in the ice (Barber and Yackel, 1999). FYI typically breaks-up in summer due to dynamic effects and rarely completely ablates in the same location where it originally formed.

Ice Patches	0.45
Light Melt Pond	0.17
Dark Melt Pond	0.38
Albedo	0.49

Ice Patches	0.12
Light Melt Pond	0.56
Dark Melt Pond	0.33
Albedo	0.28
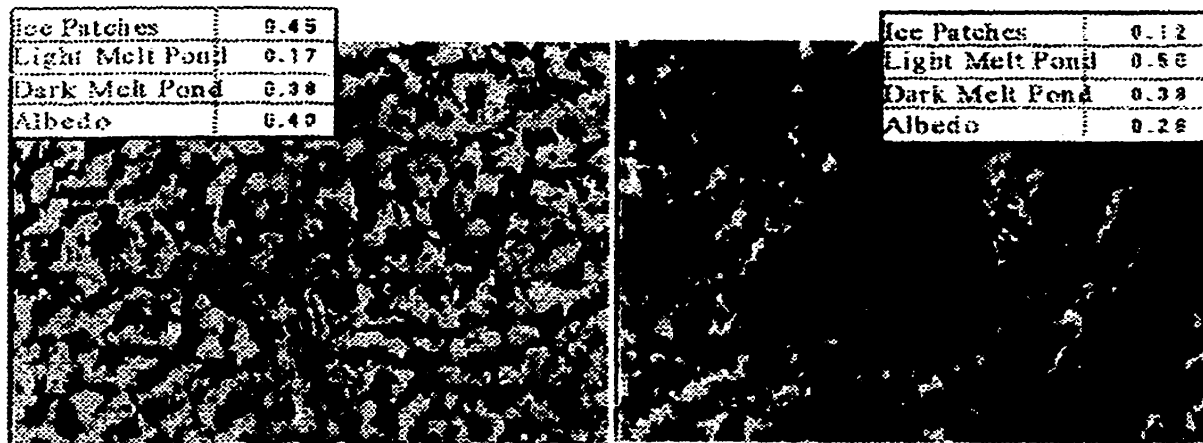
Figure 2.4: Examples of two melt pond first-year sea ice surfaces measured with aerial video (adapted from Barber and Yackel, 1999). Values in the tables suggest the average fractional areas of ice/snow patches, light colored ponds, dark colored ponds and aerial averaged albedo for both surfaces.

Snow becomes an important physical presence on sea ice once ice has formed. Snow is a porous mixture of ice grains of either single crystals or clusters of crystals (Alford, 1974) and has average bulk densities between $50 - 400$ kg m^{-3}. This makes the average bulk snow thermal conductivity considerably lower than FYI (0.4 W m^{-1} C^{-1}). The pores between ice crystals are filled with air, water vapor and liquid water if the snow is wet and/or melting (Colbeck, 1982). The snow layer and its physical properties are highly variable in space and time, controlled by various factors. Immediately after deposition, the snow transforms into a discrete layered medium through metamorphic[13] processes, overlying snow weight (overburden), freeze-thaw cycles, and wind transport (see for example Jordan et al., 1999). Density typically increases with depth provided there are no appreciable temperature gradients in the snow (Colbeck, 1982; Sturm, 1991). Most of what we know about snow and its internal physical changes is largely based on terrestrial surfaces (e.g. Alford, 1974; Anderson, 1976; Colbeck, 1982). Snow on sea ice

is different than terrestrial snow due to salinity and oceanic heating conducted upward within the ice (see for example, Drinkwater and Crocker, 1988; Barber et al., 1994). From field observations, we typically see a vertical salinity gradient in the snow between 10-17 ppt at the bottom-most snow layer and tapers off non-linearly to 0 ppt by 10-25 cm from the snow-ice interface. This reduces the snow thermal conductivity in the brine-laden regions by at least 100% in most cases (Papakyriakou, 1999). With such a low thermal conductivity, snow significantly suppresses (enhances) ice growth in the Fall/Winter (Spring) by insulating the heat transfer between the ocean-ice (atmosphere) and the atmosphere (ice) (see for example, Flato and Brown, 1996).

Metamorphism is a critical process that snow undergoes as it ages and evolves. There are two types of snow metamorphism, dry and wet, depending on temperature, density and liquid water profiles in the considered snow layer (Colbeck, 1973, 1980, 1983). Snow metamorphism drives snow cover evolution and affects snow density, porosity, strength, albedo, and thermal conductivity (Brun et al., 1992). Once a fresh snowfall occurs over sea ice, it rapidly undergoes metamorphic changes under a dry snow scenario, unless rain or warm air temperatures complicate the process.

Dry snow metamorphism implies that no liquid water is present in the snow pack, temperatures are sub-freezing, and the snow is in solid state in equilibrium with vapor. The equilibrium crystal shape (that is highly dependent on the environmental conditions) dominates the grain shape in the absence of strong temperature gradients. The growth rate of snow grains is limited by vapor diffusion that is driven by the vapor pressure gradient (Alford, 1974). The vapor pressure gradient is controlled by temperature, radius of

---

[13] Metamorphic processes are changes in snow morphology that take place as functions of temperature and pressure.

curvature and size of each snow grain. For example, warmer snow pack areas near the ice surface in winter can hold more vapor than colder areas at the snow surface. This produces a vertical vapor pressure gradient in which vapor travels upward through the snow pack. In addition, smaller and more curved snow grains contain higher vapor pressures than larger and less rounded grains (Colbeck, 1987). This implies the larger snow grains tend to grow at the expense of smaller grains (Colbeck, 1973).

There are two main types of dry snow metamorphism, equitemperature (ET) and temperature gradient (TG) processes. ET is defined by a small or no temperature gradient in the snow (0 to ~7°C m^{-1}) usually seen in spring, whereas TG has very high temperature gradients (15 – 70°C m^{-1}) typical of a winter snow pack (see for example, Colbeck, 1982). In dry snow ET metamorphism, snow grains reduce their surface free energy tending toward their stable state that is controlled by their radius of curvature and the surface to volume ratio. Snow grains naturally reduce their surface to volume ratio by expelling excess vapor. Both processes (curvature and surface to volume reduction) act to produce more rounded grains and increase snow density (Alford, 1974). Rounded crystals are typically small between less than 0.1 mm to 1.0 mm.

In dry snow TG metamorphism, the rate of vapor transport is very fast (kinetic growth) that builds angular, highly faceted grains that bond very poorly (Colbeck, 1982) (Figure 2.5). This process increases the crystal size but decreases the crystal number density (Colbeck, 1987, 1991) resulting in weak snow strengths and decreases in density. It should be mentioned that convective processes (air movement) within the snow pack also complicates the grain growth process and is largely unexplored, however, it is believed to be a non-negligible factor (Colbeck, 1989). Convective processes are difficult

to measure and are therefore ignored in detailed snow models. A wide range of faceted crystal types are found in the snow cover, including complex scrolls, cup-shaped crystals, plates, sheaths, and needles (Bradley et al., 1977). Faceted crystals can grow up to 3-4 cm in length (see Figure 2.5) and are commonly found in the hoar snow layer. The hoar layer is defined by larger faceted snow grains near the base of the snow pack where warmer temperatures and high temperature gradients exist, or within the snow volume where two discontinuous density layers exist. The bottom layer of the snow is typically termed the basal layer. Another type of faceted crystal known as surface hoar can develop at the snow-atmosphere interface. These crystals form by condensation from the atmosphere that is supersaturated compared to the snow surface. This can occur on cold clear arctic nights.
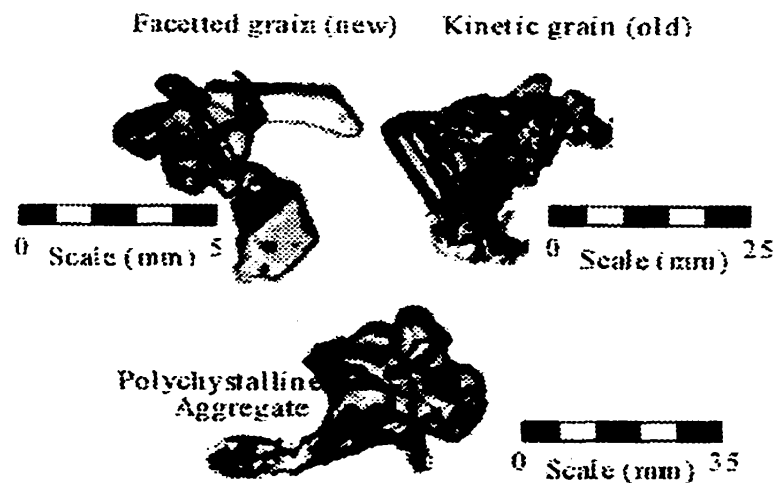
Figure 2.5: *Typical new (faceted) and old (kinetic) snow grains and aggregates of partially melted grains (polycrystalline) that result from the metamorphic processes described in the text (Adapted from Barber et al., 1999).*

Wet snow metamorphism is distinguished by low and high liquid water contents, typically termed the pendular and funicular regimes, respectively. In the pendular regime (1-8% liquid by volume), air makes continuous channels through the snow while liquid water travels between the crystals and air (Colbeck, 1982). Grain growth rates are accelerated due to liquid water with the small grains preferentially destroyed and larger grains become more rounded and well bonded (polycrystalline aggregate in Figure 2.5) (Colbeck, 1982). Snow strength is relatively high in the pendular regime since no melting occurs at the grain contacts and is further increased if the snow pack undergoes re-freezing (firmification). Conduction of heat within snow is increased if re-freezing takes place. In the funicular regime (8-15% liquid by volume), water occupies the pore spaces with little air and drains freely toward the ice surface (Colbeck et al., 1990). Grains are surrounded by water and have difficulty adhering, unlike the pendular regime. The snow pack shrinks in depth due to snow mass loss and also loses its overall mechanical strength as liquid water creates vertical channels within the snow. The smaller particles rapidly disappear once reaching a critical size (Colbeck, 1973). Increases in mean grain size in "wet" conditions can occur from about 0.3 to 0.8 mm in six days, and from 0.21 to 1.78 mm in nearly 40 days (Colbeck, 1982, 1986). In the funicular regime, since the snow is saline, brine is flushed toward the ice surface reducing the snow's layered salinity profile, forming slush at the base of the snow pack (called basal ice if refrozen).

2.2 Thermodynamics of Snow and Sea Ice

The atmosphere is the primary force behind the growth and decay of FYI with the surface energy balance (SEB) dominating. Ocean heat fluxes also contribute to ice

evolution while ice is present to counteract and balance atmospheric forcing (to produce

an equilibrium ice thickness in MYI). However, the ocean heat flux is assumed to be

somewhat constant and relatively small (2-30 W m^{-2}) compared to atmospheric forcing

for the type of ice under study here (Shirasawa and Ingram, 1997; Flato and Brown,

1996). A graphical depiction of the SEB and the thermodynamic variables involved in the

snow and ice layers outlines the major components (Figure 2.6).

$K\downarrow$ = incident SW flux
$K\uparrow$ = upwelling SW flux
Fa = absorbed SW flux
$L\downarrow$ = incident LW flux
$L\uparrow$ = upwelling LW flux
Fs = sensible heat flux
Fl = latent heat flux
Ft = transmitted SW flux
Fo = ocean heat flux

Q_{net} = net surface flux
Qm = internal latent heating
Qw = water movement heat
Qs = atmos-snow conductive flux
Qi= snow-ice conductive flux
Qo=ice-ocean conductive flux
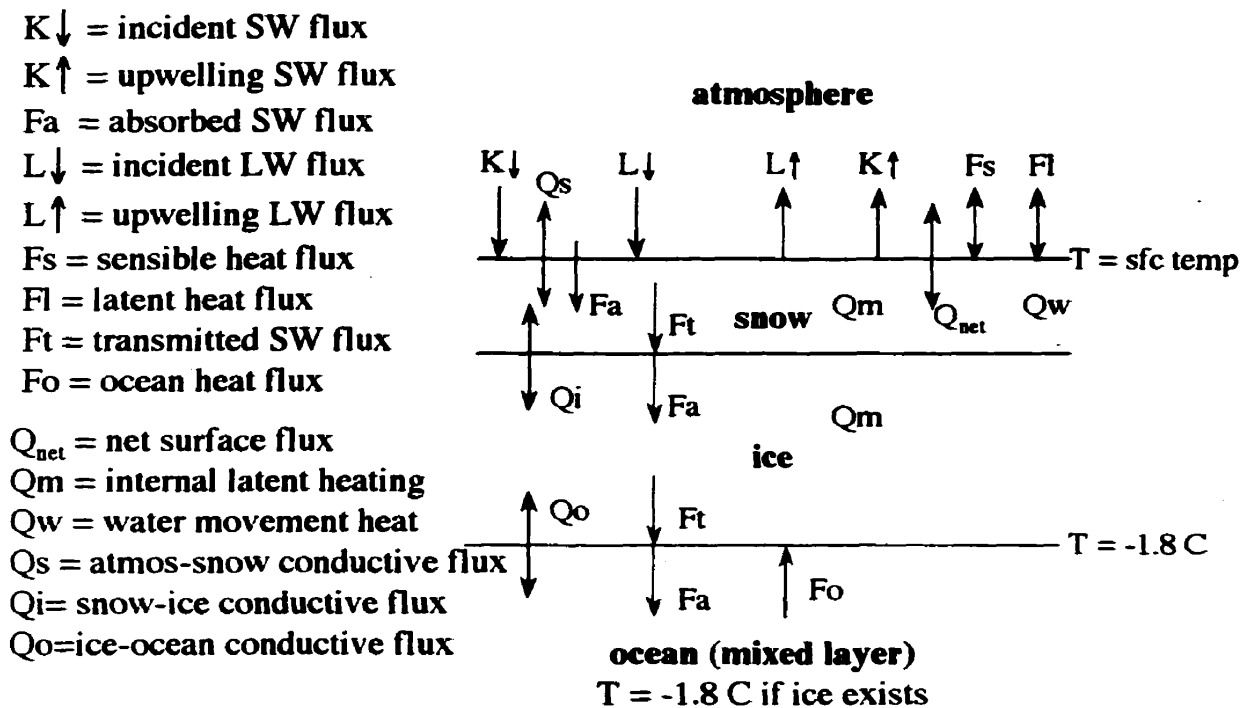
Figure 2.6: Depiction of the critical physical thermodynamic processes within snow covered first-year sea ice including the surface energy balance (SEB), internal snow/ice processes and conductive fluxes across each interface.

The corresponding SEB equation appropriate for modeling snow over sea ice

(Jordan et al., 1999) is (positive from the atmosphere toward the surface),

$$Q_{net} = K\downarrow - K\uparrow + L\downarrow - L\uparrow + F_s + F_l + F_{prec} \tag{2.1}$$

where, Q_{net} is the net atmospheric heating of the snow or ice surface, $K\downarrow$, $K\uparrow$, $L\downarrow$, $L\uparrow$ are the incident and reflected short-wave radiation, incident and up-welling long-wave radiation, respectively. F_s, F_l and F_{prec} are the sensible and latent heat fluxes and heat conducted by precipitation, respectively. The surface short-wave albedo is defined as the ratio of reflected solar radiation over the incident solar radiation,

$$\alpha = K\uparrow / K\downarrow \tag{2.2}$$

The energy within the snow volume can be estimated by (Papakyriakou, 1999),

$$dQ_s + Q_i - Q_s + Fa + Q_{ms} + Q_w = 0 \tag{2.3}$$

where, dQ_s is the net atmospheric heating ($Q_{net} + F_s + F_l$), Q_i is the conductive heat flux at the ice surface, Q_s is the conductive heat flux at the snow surface, Fa is the absorbed solar radiation, Q_{ms} is the phase transition energy, and Q_w is heat energy associated with water flow. Similarly, the energy contained within the ice volume is,

$$Q_o - Q_i + F_{ai} + Q_{mi} + F_o = 0 \tag{2.4}$$

where, Q_o is the conductive heat flux at the ice-ocean surface, F_{ai} and Q_{mi} are the absorbed solar radiation (in ice) and internal latent heating of the sea ice layer, respectively, and F_o is the heat flux from the ocean mixed layer toward the ice underside. I now continue with individual critical physical processes that control snow and sea ice thermodynamics, beginning with atmospheric forcing down to the ice underside.

2.2.1 Atmospheric Radiation Interaction with Snow and Ice

The solar short-wave (SW) portion of the spectrum occupies wavelengths between $0.15 - 3.0$ μm. This is subdivided into visible wavelengths ($0.36 - 0.75$ μm), near-infrared ($0.7 - 1.3$ μm), and mid-infrared (1.3 to 3.0 μm). The solar component of the arctic energy balance is seasonal due to the Earth's obliquity. The maximum solar zenith angle[14] in the arctic during the summer solstice is limited to about 47 degrees because of the earth's obliquity. High latitude locations (>66.5 degrees) are therefore in a state of darkness for up to six months of the year. Only when the sun rises above the horizon for longer periods of time through the spring does the short-wave radiation become increasingly dominant. This dominance continues through the spring and summer months when, at high latitudes, the sun does not drop below the horizon at all.

Long-wave radiation ($3.0 - 100$ μm; thermal infrared) is of terrestrial origin, with incident long-wave (L↓) emitted from the atmosphere all of the time. Up-welling long-wave radiation (L↑) is emitted from the surface and is also a continual annual process.

2.2.1.1 Incident Short-Wave Radiation

Incident SW (K↓) responds to seasonal, latitudinal, diurnal and atmospheric variations that significantly alter the arctic environment. The K↓ variations are highly variable due to rapid changes in cloud cover, water vapor, aerosols, and the relatively slower changes in surface features. The K↓ parameter is most sensitive to aerosol optical

depth and surface albedo under clear skies and cloud optical depth, cloud liquid water content and surface albedo under cloudy skies (Key et al., 1996; Leontyeva and Stamnes, 1993). K↓ is a key component in the SEB and accurate measurements and/or model parameterizations are required to numerically simulate seasonal snow and ice evolution. More will be said about K↓ in following sections.

2.2.1.2 Surface Reflection (Albedo)

Surface albedo is defined in equation (2.2). Several factors affect albedo, including wavelength, solar zenith angle, surface characteristics, and clouds (Ebert and Curry, 1993). In sea ice climatology, the albedo of the surface (with snow and/or melt ponds on it) is typically measured in the optical region of the spectrum over wavelengths between $0.3 - 3$ μm. However, the most responsive region within this spectrum to changes in the sea ice surface is the visible (VIS) and part of the near infra red (NIR) region ($0.3 - 1.1$ μm). Surface features such as a new snow cover, old snow, wet snow, saturated snow, and melt ponds, determine the overall albedo magnitude over first-year sea ice. Fresh snow acts as a highly reflective surface in the VIS and NIR whereas, older snow absorbs more of the VIS and NIR energy. The direct albedo of snow can show considerable daily variation (Petzold, 1977). This is due to several factors. For instance, a snow pack will slowly settle under its own weight, changing the size, shape, and spacing of crystals at the surface. Dust particles from the atmosphere will also accumulate on the snow pack darkening the surface and lowering the albedo (Warren and Wiscombe, 1981).

[14] Solar zenith angle is the angle between the local normal to the Earth's surface, and a line between a point

Wind is a significant factor since it can redistribute and compact snow. A 1 cm layer of freshly accumulated snow will result in a new albedo that is completely independent of that for the previous surface (Petzold, 1977). Finally, a change from powdery to granular snow occurs at the surface of a melting snow pack. This means that the albedo of a melting snow pack is going to change more rapidly than an accumulating snow pack (Petzold, 1977). When the snow melts in spring, melt ponds develop on the sea ice surface and significantly decreases the overall surface albedo. The formation of ponds and the associated drop in albedo causes further rapid sea ice ablation through the ice-albedo-feedback process (Curry et al., 1995). The extra SW radiation absorbed by the melt ponds is used to increase their depth and the volume of brine within the ice (Maykut, 1982).

Clouds and solar zenith angle also affect the surface albedo. Maximum total cloud cover occurs in the summer (up to 90%), minimum coverage occurs in the winter (40-50%), and the transitions between maximum and minimum values occur over short time periods in the spring and fall (Curry and Ebert, 1992). Clouds influence $K\downarrow$ and hence surface albedo in three ways: 1) clouds reflect a portion of the radiation that they intercept back into space, that is, they have their own albedo, 2) clouds selectively absord SW radiation at wavelengths greater than 0.7 microns, and 3) cloud cover controls the relative proportions of direct and diffuse radiation. Since the albedo of snow is greater for visible light than for near infrared radiation, albedo generally increases as cloud cover and cloud opacity increase (Petzold, 1977). Furthermore, the albedo of surfaces that do not scatter radiation equally in all directions (non-Lambertian reflectors) will increase as

on the Earth's surface and the sun.

the diffuse component increases (Curry and Ebert, 1992). Solar zenith angle effects show an 8-20% decrease in clear sky albedo as the zenith angle decreases from 80 - 45 degrees (Petzold, 1977).

Sea ice albedo is a critical climatological parameter controlling short-wave responses in the SEB, and has been a major focus in several modeling and observational studies (see for example, Shine and Henderson-Sellers, 1985; Ebert and Curry, 1993; Robinson et al., 1986; Ross and Walsh, 1987; De Abreu et al., 1994; Grenfell and Maykut, 1977; Grenfell and Perovich, 1984). Perovich (1996) summarized many of the scarce bulk (broadband[15]) and spectral[16] albedo measurements collected *in situ* for various surfaces over different kinds of sea ice. Broadband albedos range from 0.21 for melt ponds to 0.87 for dry new snow over first year ice (Table 2.1).

Table 2.1: Previous measurements of integrated albedo over various surfaces (data adapted from Perovich, 1996).

Surface Type	Integrated Albedo
Open Water	0.05
Old Pond	0.15
Ponds (1st Year)	0.21
Mature Pond	0.29
Melting Ice (blue)	0.33
Refrozen Pond	0.40
Bare First-Year Ice	0.52
Melting White Ice	0.56-0.68
Frozen White Ice	0.70
Melting Snow	0.77
Wind Packed Snow	0.81
New Snow	0.87

[15] Broadband albedo refers to the integrated spectral albedo across the optical wavelengths.
[16] Spectral albedo refers to the reflectance of energy at a particular wavelength in the optical spectrum.

Spectral snow albedos are typically highest in the VIS and drop off in the NIR (Figure 2.7). The magnitude and shape of the spectral albedo curves are strongly dictated by the snow grain size and amount of liquid water in the snow (Wiscombe and Warren, 1981). Few albedo measurements exist from the Canadian Archipelago compared to the Arctic Basin and Antarctic. De Abreu et al. (1995) measured first-year sea ice (FYI) spectral albedo in the Canadian Archipelago during the melt season showing the gradual decline in albedo is attributed to the evolving geophysical structure of the snow/ice volumes, increasing the contrast between the VIS and NIR spectral albedo.
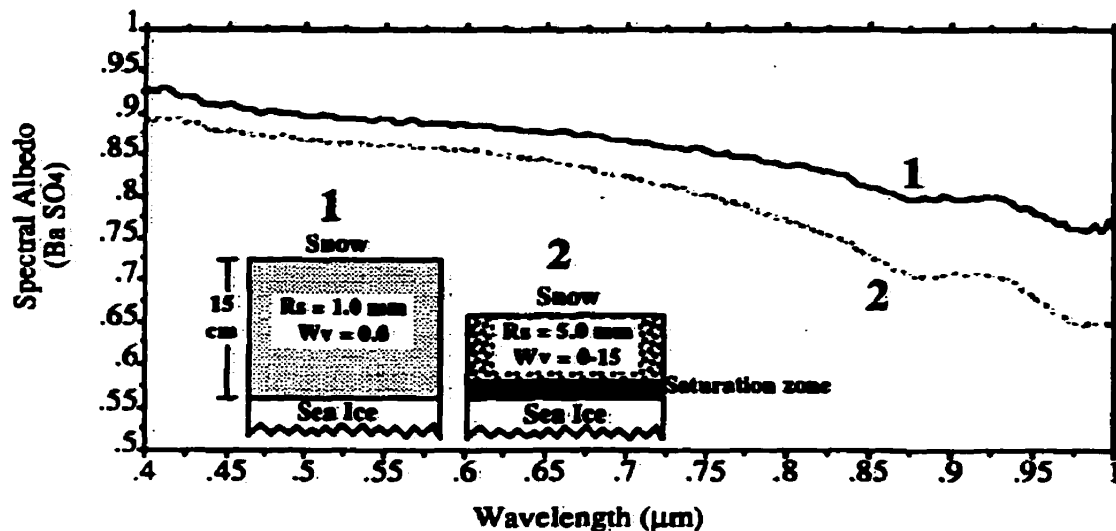
Figure 2.7: Two spectral albedo curves over snow covered sea ice. One (1) over dry snow, and the other (2) over freely draining snow. The curves are representative with respect to a barium sulphate reference panel. Site (2) ranges from 0 - 15% water by volume from the top of the snow pack to the bottom. (Adapted from Barber, 1993).

Very little work has been done to assess the spatial variability of albedo, mostly devoted to broad satellite-scale variations. Langleben (1971) suggested a linear decrease in albedo as a function of the degree of puddling in the Beaufort Sea, ranging between 0.6 (0% pond cover) to 0.3 (70% pond cover). More recently, Barber and Yackel (1999) used

33

video-derived albedo estimates near Resolute, Nunavut to show its spatial variability over linear transects during spring melt. Albedos ranged between 0.3 and 0.5 depending on its proximity to land, ice type and ice roughness (Barber and Yackel, 1999). Sea ice surface albedo derived from satellite sensors in the VIS/NIR wavelengths can obtain regional pixel-scale (~1 km) albedo estimates. Robinson et al. (1986) and Robinson et al. (1992) used DMSP (Defense Meteorological Satellite Program) data to produce realistic albedo maps of the Arctic Basin that was a good indicator of inter-annual variations in the mass and energy budget of the arctic. Robinson et al. (1986) calculated a net areal albedo of 0.53 for the central arctic, corroborating earlier estimates. More recently, De Abreu et al. (1994, 1996) compared *in situ* albedo to AVHRR (Advanced Very High Resolution Radiometer) albedo over FYI showing that the two agreed favorably (within ±5%) when accounting for atmospheric attenuation, viewing geometry, and sensor spectral response. Lindsay and Rothrock (1993, 1994) found mean monthly Arctic Basin albedos to range from 0.76 in April to 0.47 in August, 1989. More observations of surface albedo are needed over FYI, in particular, local albedos of specific surface features (different snow types, melt ponds, etc.) and how these scale up to regional aerial albedo. In addition, little is known about the sensitivity of FYI ablation and break-up potential to the seasonal progression of fractional melt pond cover and their associated albedo changes from year to year. This is important for understanding the partitioning of energy and how we can temporally and spatially represent albedo in numerical modeling studies.

2.2.1.3 Surface Absorption

Absorbed energy is used to heat the medium and create internal phase changes, if the melting temperature is reached or can be re-emitted as long-wave radiation (see below). The absorbed SW radiation for a given level (z) in the snow (or ice) is given by (adapted from Papakyriakou, 1999),

$$K_z^* = \int_{\lambda_1}^{\lambda_2} (K\downarrow_{z,\lambda} - K\uparrow_{z,\lambda}) d\lambda \tag{2.5}$$

where

$$K\uparrow_{(z,\lambda)} = \alpha_{(s,\lambda)} K\downarrow_{(o,\lambda)} \exp(-\kappa_\lambda z) \tag{2.6}$$

and $K\downarrow_{(o,\lambda)}$ is the incident snow surface short-wave radiation, κ_λ and $\alpha_{(s,\lambda)}$ are the spectral extinction coefficient (m^{-1}) and spectral albedo, respectively, and z is the vertical distance.

2.2.1.4 Surface Transmission

The remaining SW energy that is not reflected or absorbed by the snow layer is transmitted into the ice. This available ice energy acts as internal heating of the ice of which a certain portion is also transmitted into the top ocean (mixed) layer. Beer's law dictates the amount of energy that is transmitted through the ice, as in snow above,

$$K\downarrow_{(z,\lambda)} = K\downarrow_{(o,\lambda)} \exp(-\kappa_\lambda z) \tag{2.7}$$

where, κ_λ is the spectral extinction coefficient (m^{-1}). Maximum transmission of SW energy through the snow and ice occurs between the 0.45 to 0.55 μm region of the spectrum (Maykut and Grenfell, 1975) with most absorption in the infrared. Typical bulk extinction coefficients for dry snow range between 37 to 97 m^{-1} and 23 to 58 m^{-1} for wet snow (Fukami et al., 1985), depending on the snow density.

2.2.1.5 Long-Wave Radiation

All matter above absolute zero (-273.15°C or 0 K) emits energy as a function of its temperature, governed by the Stefan-Boltzman law,

$$L = \varepsilon\sigma T^4$$ (2.8)

where, L is the emitted long-wave radiation (W m^{-2}), ε is the long-wave emissivity, σ is the Stefan-Boltzman constant, and T is the medium's radiative temperature (K). The snow emissivity is near 0.99, whereas sea ice and water are typically 0.97 (Maykut, 1986). During the months of little or no short-wave input from the sun, the incident long-wave (LW) flux (L↓) is dominant in the arctic, although the LW flux remains important even in the spring. There are essentially three sources of LW radiation: 1) the atmosphere, 2) clouds, and 3) the surface. The L↑ is primarily controlled by the snow or ice surface temperature and its associated emissivity. As with the SW flux, clouds play an important role in the LW flux because they are able to absorb and re-emit a portion of the LW radiation they receive from the surface and surrounding atmosphere. Overall, they serve to reduce the amount of radiation lost to space by 28-55 W m^{-2}, although a large

portion of L↑ radiation is transmitted through clouds less than 320 m thick (Herman, 1986). The L↓ is most sensitive to precipitable water and aerosol optical depth under clear skies and cloud base height and cloud optical depth for cloudy skies (Key et al., 1996). The clear-sky L↓ flux is important during the polar winter. This is because temperatures in the troposphere dictate that condensates be in a predominantly crystaline state even under clear skies (ice crystals). The ice crystals are presumed to emit long-wave energy between 10-40 W m^{-2} greater than modeled winter clear-sky values (Curry and Ebert, 1992). L↓ is a key component in the SEB throughout the annual cycle and accurate measurements and/or model parameterizations are required to numerically simulate seasonal snow and ice evolution.

2.2.2 Heat Flow Through Snow and Ice

The temperature field in snow and ice is described by equations of heat and mass transfer with terms corresponding to internal melting, absorption of short-wave solar radiation, and evaporation/condensation. Water flow within the snow is also usually considered. Thermal processes in the snow and ice are different since snow has a much different physical make-up where compaction and internal evaporation/condensation affect the snow only. In addition, salt (brine) impurities in the snow and ice play a crucial role in their thermal behavior (Maykut and Untersteiner, 1971).

Wind transport of snow (blowing snow) is also a key factor for determining the overall snow depth over a particular point (Pomeroy et al., 1997) which affects the thermal and metamorphic processes in the snow layer over time (Jordan et al., 1999). In

37

fact, blowing and drifting snow create a spatial pattern of "snow dunes" on FYI that may be related to the spring melt pond spatial distribution. Snow distribution and depth on FYI is also critical for seasonal ice thermodynamics (see for example, Flato and Brown, 1996). The snow model (SNTHERM) by Jordan et al. (1999) allows one to tune the fractional stress gradient ($\tau_s^{-1} \, \partial \tau_s / \partial x$; where τ_s is the snow surface stress) to recreate actual snow depths (positive gradients remove snow, negative gradients accumulate snow). This parameter can be held constant or be allowed to vary in time.

The one-dimensional equation for the conservation of energy (of snow or ice) for the various constituents (i = ice, l = liquid, v = water vapor) is (from Jordan et al., 1999)

$$\frac{\partial}{\partial t} \int \rho_t h_t dz = - \sum_{k=i,l,v} \sum_s h_k J_k \bullet n + \sum_s k_t \nabla T \bullet n + \sum_s R_s \bullet n \qquad (2.9)$$

where t is time, ρ_t is the overall snow density (= $\rho_l + \rho_i$; bulk density of liquid and ice, respectively, discounting the gas), z is the vertical position relative to the interface between the snow and the sea ice, J_k is the flux of water constituent k (positive upward), the subscript t refers to the total medium (snow or sea ice), T is temperature (in kelvins), k_t is the thermal conductivity, and R_s is the net solar radiation (positive downward). The integral is taken over a control volume of thickness Δz; and the summation Σ_s is over the top and bottom surfaces, where n is the unit vector normal to the surface. The specific enthalpy h_k of a water constituent is (from Jordan et al., 1999)

$$h_k = \int_{273.15}^{T} c_k(T)dT + L_k \qquad (2.10)$$

where c_k is the specific heat of the constituent at constant pressure, L_t and L_v are the latent heats of freezing and sublimation, and $h_t = \Sigma_{k=i,l,v}\ h_k$. The first term on the right hand side of (2.9) is the heat flux due to water flow and vapor diffusion (disallowed in sea ice), the second term on the right side is the conduction, the last term is the subsurface absorption of solar radiation. The term on the left hand side represents the change in stored heat.

The parameters c_k, L_t, L_v, k_t, brine content/volume (v_b), and phase transition temperature for snow and sea ice depend strongly on its salinity and temperature. Due to the wide variety of empirical formulae for these parameters in snow and sea ice, they will not be described in detail. The main point is that brine tends to retard any heating or cooling forcing in the snow or sea ice.

Snow metamorphic and deposition-removal processes also need to be included as indirect thermodynamics factors since these processes affect snow thermodynamics. I only briefly discuss the relevant processes here. Metamorphism and deposition-removal of the snow pack directly affects snow density (at various degrees and levels in the snow), making the snow medium a layered structure. Hence the thermodynamics are affected, and in turn feed back into the metamorphic processes. Grain size and crystal shape also affect the snow density where smaller crystals and simpler shapes pack most efficiently, leading to denser snow (Jordan et al., 1999). Four primary processes act in the deformation rate of the snow pack, namely (after Jordan et al., 1999),

$$\frac{\partial}{\partial z}\left(\frac{\partial z}{\partial t}\right) = \left[\frac{\partial}{\partial z}\frac{\partial z}{\partial t}\right]_{metamorphism} + \left[\frac{\partial}{\partial z}\frac{\partial z}{\partial t}\right]_{overburden} + \left[\frac{\partial}{\partial z}\frac{\partial z}{\partial t}\right]_{melt} + \left[\frac{\partial}{\partial z}\frac{\partial z}{\partial t}\right]_{wind} \tag{2.11}$$

where, the term on the left side is the resulting deformation rate, the next term describes the metamorphic processes (wind packing, density changes, erosion and accumulation), followed by the overburden (weight of snow causing lower layers to compress), the melting term (when melt (freezing) causes the snow pack to shrink (remain the same) in depth), and finally an extra wind term (snow deposition-removal by the wind; i.e. blowing/drifting snow).

The surface temperature gradient is determined by turbulent sensible heat exchange between the snow and air, long-wave and short-wave radiation from the atmosphere and re-radiation from the snow surface, and by latent heat of snow evaporation (or condensation of water from the air) upon the snow surface. The melting of sea ice at its surface produces low-salinity brine and causes a drop in sea ice salinity (Ono and Krass, 1993). Water from snow melt leads to brine dilution and raises the freezing temperature, possibly causing further ice formation depending on the temperature. This process is important for ice generation during the Spring season (Ono and Krass, 1993).

The growth or decrease of the ice thickness at the ice-ocean interface is determined by heat-mass balance on the ice bottom (i.e. conductive flux in the ice close to the ice-ocean boundary and the turbulent heat flux from the ocean) and penetrating short-wave to the ice-ocean interface. This process is represented by (as in Flato and Brown, 1996),

$$\frac{\partial h_i}{\partial t}\Big|_{z=h} = \left(k_i \frac{\partial T}{\partial z}\Big|_{z=h} - \int_h^\infty K \downarrow I_o(1-\alpha)\kappa e^{-\kappa z} dz \right)\frac{1}{L_{fi}} \tag{2.12}$$

where, h_i is the ice thickness, k_i is the ice thermal conductivity, I_o is the fraction of short-wave radiation that penetrates the surface, α is the surface albedo, κ is the bulk extinction coefficient for short-wave radiation (i.e. asymptotic decay of short-wave energy into the ocean), and L_{fi} is the heat of fusion of sea ice. The integral represents the short-wave energy available to the ocean mixed layer that is assumed to be absorbed there to keep the mixed layer temperature at the freezing point.

Figure 2.8 shows the simplified resulting seasonal progression of temperature profiles within the snow and sea ice layers. Note the SW component with maximum daily average radiation (~ 400 W m^{-2}) at melt onset, where a significant amount of energy is available to the surface at this period. A snow layer may or may not be present during Freeze-Up, depending on the timing of snowfall. A snow layer during Freeze-Up significantly retards the ice growth rate (see for example, Flato and Brown, 1996). The snow temperature gradient in winter is greater than the ice due to thermal conductivity (and thermal diffusivity[17]) differences between the two mediums. During Early Melt, the temperature gradient in the snow reflects the diurnal nature of atmospheric heating and cooling, producing temperature waves in the snow over the course of a day. It also signals the beginning of snow metamorphism (Livingstone et al., 1987). The ice volume begins to show signals of warming. At Melt Onset, the snow volume contains liquid water at all times with the pedular and funicular regimes active at this stage; snow grain growth is accelerated (Colbeck, 1982) and albedo decreases significantly; conductive fluxes become larger within the snow; diurnal temperature variations are still present; and the ice continues to warm considerably. By Advanced Melt, the snow pack shrinks (if

present at all) with a near-isothermal temperature profile, liquid water is always present thereby decreasing the albedo further; bulk salinity in the snow and top ice layer decreases (Tucker et al., 1987); melt ponds develop on the ice surface and brine drainage in the ice is fully active; the ice volume becomes near-isothermal which creates ideal break-up conditions (due to a marked decrease in ice strength (Barber et al., 1998)).
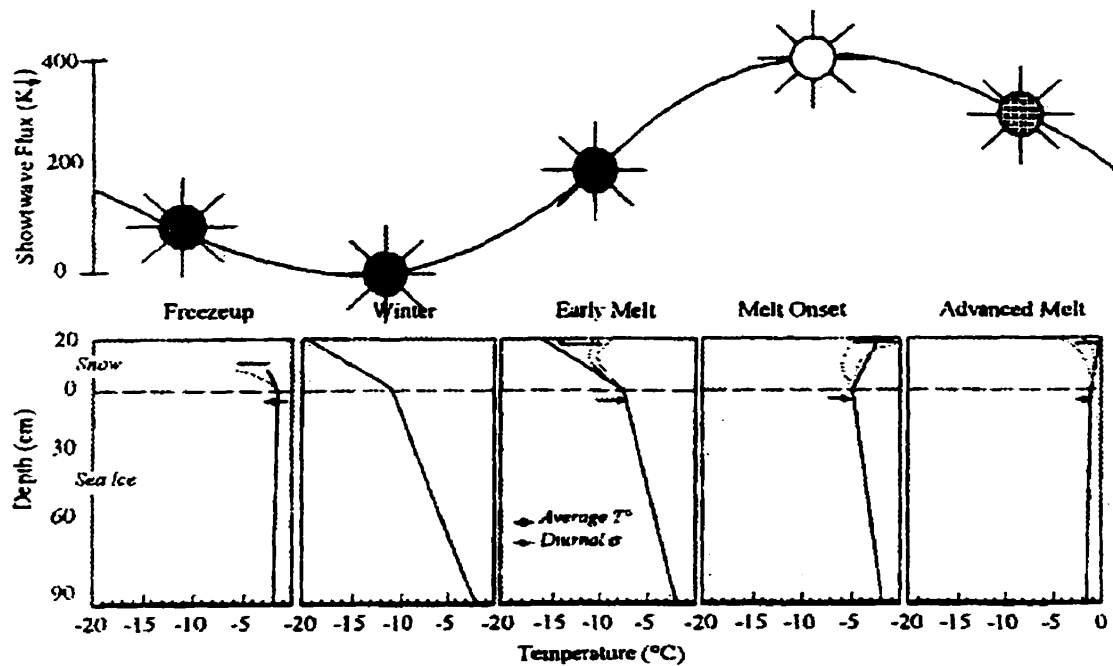
Figure 2.8: Categories of snow covered first-year sea ice thermodynamic regimes between freeze-up to advanced melt periods. Profiles are typical from 8 years of in situ data. Daily average solar energy (W m⁻²) available for each regime is also shown. (Adapted from Barber, 1997).

---

[17] Thermal diffusivity (khs) is the rate at which the surface induced temperature wave can travel within the medium (snow or ice); and related to thermal conductivity (ks) and heat capacity (C) by khs = ks / C.

2.3 Utility of Numerical Modeling for Snow Covered Sea Ice

This section is devoted to illustrating the utility of numerical modeling for advancing our understanding of snow covered sea ice climate processes. I begin with a brief historical perspective of sea ice modeling and continue with research results pertinent to this work that demonstrate the use of models to study snow and sea ice in a one-dimensional sense.

2.3.1 Historical Perspective

Before the advent of higher-speed computers (prior to the late 1960's), empirical relationships for ice growth and snow/ice thermodynamics were developed but offered little physical insight into the problems. Budyko (1966) developed one of the first physically representative thermodynamic models of ice through numerical techniques, however a major problem was the specification of surface temperature that ignored heat conduction effects on surface ablation and surface temperature. Maykut and Untersteiner (1971) (MU) offered a more complex thermodynamic model that considered atmospheric and oceanic fluxes to dictate the thermal regime of sea ice and snow in discrete layers. A general approach to estimating internal ice temperatures and thickness was to use heat conduction equations similar to section 2.2 that are still used in modern snow and sea ice models. The MU model included the effects of internal heating from solar radiation penetration, internal heat storage in brine pockets, and variation of specific heat and thermal conductivity of the ice/snow with temperature and salinity. However, the model

was limited by numerical techniques (required larger time steps and layer spacing), course albedo parameterization, poor turbulent flux parameterizations and could not grow ice from open water. More recently, Ebert and Curry (1993) (EC) developed a thermodynamic model as an offshoot of MU but with much more detail in many physical processes. These included a revised turbulent flux parameterization, improved albedo parameterization, greater flexibility in numerical technique that improved the overall thermodynamics, and improved atmospheric radiative forcing parameterizations. Flato and Brown (1996) (FB) considered a thermodynamic model for FYI (land-fast ice) that is similar to EC, with a different albedo parameterization and slightly different atmospheric forcing parameterizations, mainly for the purpose of inter-annual simulations. Recently, a model for snow layer thermodynamics and mass balance over sea ice has been developed by Jordan et al. (1999). The Jordan model is state of the art in that it treats most critical processes in a physical way with more detail paid to heat conduction specific to snow (layered mixture of dry air, ice, liquid water, and water vapor), phase changes, water flow, snow densification, grain growth, and effects from blowing/drifting snow.

2.3.2 Utility of Modeling

Results to date from numerical modeling studies of snow and sea ice have proven to be useful for a number of reasons. A key advantage of models is futuristic insight, i.e. so we can determine what the conditions may be like in the future. A second advantage is the output they produce. Models can generate a time series of information from any particular variable that is simulated by the model, for example surface albedo or snow/ice

surface temperature. A third advantage is conducting sensitivity studies. Sensitivity studies are an attractive component of models where we can perturb a single variable (or multiple variables) to investigate any changes in the simulation. For example, a control run simulation (initial simulation with known input and forcing) would be generated, then a second simulation would be produced by altering a variable (e.g. albedo). A comparison can be made between the control simulation and the altered albedo simulation to observe any major differences in the output parameters (such as snow/ice thickness over time). Sensitivity studies are useful for identifying: 1) variables and processes that control snow/ice evolution, 2) feedback mechanisms, and 3) which variables may be more "active" than others. This also allows us to investigate processes that would not otherwise be determined by field observations since we can not (in most cases) alter the physical characteristics of the forcing variables[18].

Current sea ice models simulate inter-annual and climatological (inter-yearly) sea ice conditions reasonably well (Figure 2.9) (Flato and Brown, 1996; Ebert and Curry, 1993), although major deficiencies are still present.

---

[18] Forcing variables are contained in the SEB (i.e. meteorological) and ocean mixed layer beneath the ice (ocean heat flux). They are the primary parameters that drive any processes acting on the snow and ice.
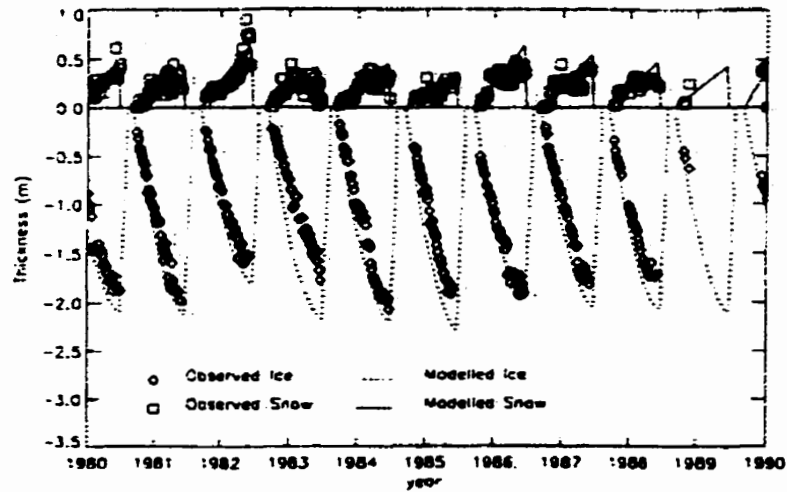
Figure 2.9: Time series of observed and modeled ice and snow thickness at Alert, Nunavut between 1980-1990. Ice thickness appears as negative values. (Adapted from Flato and Brown, 1996).

Data presented in Figure 2.9 stems from the FB model where they simulated the inter-annual variability of land-fast FYI between 1955 – 1990 in two different arctic locations (only Alert, Nunavut between 1980-90 is shown). The model simulation was generated using *daily-averaged* meteorological forcing (air temperature, relative humidity, wind, total cloud amount, and snowfall) from Alert spanning the years of simulation. Figure 2.9 shows what model output can generate and illustrate its utility for studying sea ice processes. The complexity of the EC model physics and processes is illustrated in Figure 2.10 (adapted from the sea ice model of Ebert and Curry, 1993).
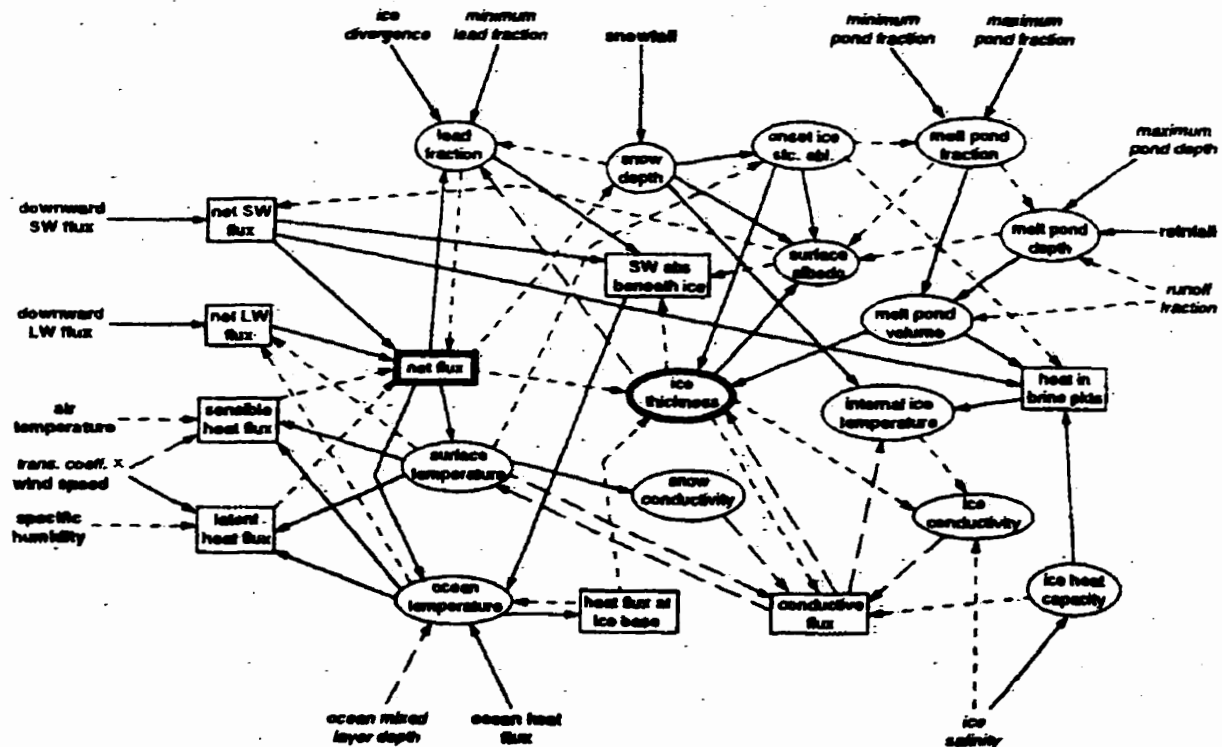
Figure 2.10: Modeled interactions (see text) between external forcing (bold) and parameter values (italic), and internal variables (ovals) and fluxes (boxes) for the Ebert and Curry (1993) one-dimensional thermodynamic sea ice model. (Adapted from Ebert and Curry, 1993).

Figure 2.10 shows the interactions and feedbacks relating the model variables and fluxes (ovals and boxes, respectively) to each other and to the specified values of the parameters and external forcing (italics and bold, respectively around the outside of the figure). A solid arrow indicates that a positive change in the first variable has a direct positive impact on the second variable (positive interaction), a short dashed arrow indicates that a positive change in the first variable impacts negatively on the second variable (negative interaction). Long dashed arrows represent positive or negative interactions, depending on the season. These interactions can be amplified or dampened by positive or negative feedback loops (Ebert and Curry, 1993). An even number of negative interactions between a series of interactions results in a positive feedback loop

where the initial variable becomes more positive because of the feedback, and so on. An odd number of negative interactions results in a net decline of the original variable (negative feedback loop). As an example, the surface albedo feedback indicates an increase in the SW or LW flux (or air temperature) acts to increase the net flux on the ice, warming the ice surface (Ebert and Curry, 1993). A warmer surface accelerates melt onset and melt rate, lowering the surface albedo and increasing the short-wave flux. Ice ablation is directly increased as a result of greater input energy (Ebert and Curry, 1993). This example clearly illustrates the utility of numerical models in identifying primary sea ice processes through sensitivity studies.

The degree of ice thickness changes to air temperature changes can be examined through similar sensitivity studies. Flato and Brown (1996) showed a 5°C increase (decrease) in air temperature would result in a decrease (increase) in land-fast ice thickness of 30 cm. Other studies (Parkinson and Kellogg, 1979; Semtner, 1987; Ebert and Curry, 1993) indicate temperature perturbations between 2-4°C would have great impacts on ice characteristics and cause the ice pack to disappear by the late melt season. It is very difficult to determine why the results are so different between the models, however, subtle differences between the formulations of ice thermodynamics, numerical methods and atmospheric fields may be enough to account for the discrepancies (Holland et al., 1993).

Mentioned earlier, the surface albedo is of primary interest for sea ice processes and modeling its seasonal evolution (parameterizing it) is very important for accurate sea ice simulations. Numerical models must parameterize the albedo since a complete physical model is not yet available, and a purely physical albedo model would be

computationally expensive. Modeling studies have shown that multiple albedos must be parameterized to properly account for dry snow as opposed to wet snow as well as bare, melting ice (Shine and Henderson-Sellers, 1985). The observed albedo for bare, melting ice ranges between 0.5 and 0.58 and this range can affect ice thickness by a factor of 2. This range in albedo also determined whether the ice was seasonal or multiyear ice (Shine and Henderson-Sellers, 1985). Flato and Brown (1996) also stressed that fixing the melting ice albedo to 0.55 and not accounting for intermediate melting ice albedos produced unrealistic multiyear ice scenarios in some land-fast arctic ice regions. Shine and Henderson-Sellers (1985) altered the dry snow albedo between 0.8 and 0.75 in which the difference in equilibrium ice thickness were 1 m and the date of total snow melt occurred one week earlier for the lower albedo. The wet snow albedo was altered between 0.7 and 0.65 where the difference in ice thickness at equilibrium was 1 m and total snow melt occurred 4 days earlier with the lower albedo.

Ebert and Curry (1993) included a more complex treatment for melting snow and ice where they explicitly considered melt pond effects on surface albedo. They found that the melt water runoff fraction (Fr) significantly altered the ice thickness. If no melt ponds were not allowed to exist (Fr=1), the equilibrium ice thickness was much too large (5.0 m compared to an average observed thickness of 3.0 m). If Fr < 0.5, the ice would completely disappear for a few weeks in the summer and have a mean annual thickness of 0.8 m. It is evident that the parameterization of albedo can be very complex and important for the short-wave and long-wave radiative processes. It is also evident that slight variations in albedo parameterizations between the different models can lead to differences in model output in many situations.

Another important part of the SEB are the incident radiative fluxes ($K\downarrow$ and $L\downarrow$), mentioned earlier. Incident radiation is primarily controlled by the atmosphere (discussed earlier) and snow and sea ice models parameterize these fluxes since more sophisticated methods are computationally inefficient (Key et al., 1996). Parameterizing these fluxes is tricky due to their relatively quick response to variables that control their variation (minutes to hours). With current radiation schemes, the equilibrium ice thickness of a one-dimensional thermodynamic sea ice model varies by 4 m for a ± 5% change in $K\downarrow$ and 12 m for a similar change in $L\downarrow$ (Ebert and Curry, 1993). The ice pack could completely disappear in summer for an increase in $L\downarrow$ greater than 2% (Ebert and Curry, 1993). Equilibrium ice thickness variations are greater for $L\downarrow$ since it acts all of the time compared to $K\downarrow$ that acts only during solar illumination. Recent examinations of arctic incident radiative flux sea ice model parameterizations have shown that the best existing parameterizations (Shine, 1984) can estimate *daily average* $K\downarrow$ to within 2% of the mean with an RMSE (root-mean-squared error) of 4% for clear skies and 21% for cloudy skies. The $L\downarrow$ parameterizations performed better, with an accuracy of about 1% of the mean and RMSE of 6% for both clear and cloudy skies (Efimova, 1961 for clear skies; Jacobs, 1978 for cloudy skies) (Key et al., 1996). The $L\downarrow$ parameterizations (clear and cloudy skies) of Maykut and Church (1973) were very close in accuracy to Efimova (1961) and Jacobs (1978).

The snow cover has a profound effect on ice growth and ablation, shown by modeling studies (and observations; see section 2.2). During the winter season, Ebert and Curry (1993) found that the snow layer decreased the ice thickness due to its insolating effects and allowing ablation at the ice underside to dominate the ice growth process. The

inter-annual variability in land-fast ice thickness is dominated by snowfall variations (Flato and Brown, 1996). An increase in snowfall rate caused the maximum ice thickness to decline until about double the present day value (1.7 mm day^{-1}) where the ice thickness would increase thereafter. This is due to a sufficient snow cover that submerges the ice into the water forming "slush ice" at the surface, increasing the ice thickness. The timing of a snowfall dictates the seasonal progression of FYI thickness where a large snowfall during initial ice growth (in the Fall) will retard ice growth, whereas as a large snowfall in Spring will enhance ice growth (Figure 2.11; G. Flato and R. Brown, pers. comm). The insulating snow in the Fall dominates (decreases) ice growth with little or no solar component at this time of year, and the high albedo snow surface in spring dominates (increases) ice growth by delaying ice melt.
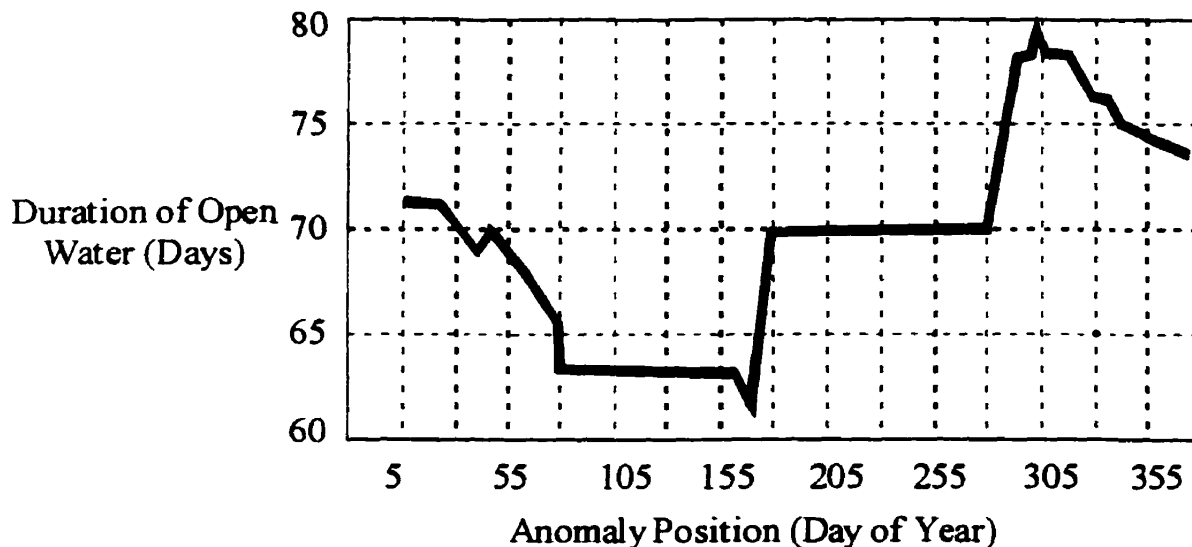
Figure 2.11: Effect of a 5-day period of snowfall (20 cm) on the open water duration of modeled first-year sea ice. The 5-day period was moved along, throughout the annual cycle (anomaly position) to show the impact of the timing of new snowfall on open water duration. (G. Flato and R. Brown, pers. com.).

Maykut and Untersteiner (1971) and Semtner (1976) both showed that a snowfall rate of 120 cm yr^{-1} increased the ice thickness without bound for two 1-D thermodynamic sea ice models. For land-fast ice scenarios, this unbounded ice thickness problem from large snowfall rates (extended high surface albedo) did not occur since the warm spring and summer air temperatures melted the snow which alleviated the strong snow albedo influence (Flato and Brown, 1996). Holland et al. (1993) found that increasing the snow fall rate to 200 cm yr^{-1} increased the average ice thickness by about 0.5 m in which case did not produce unstable ice characteristics for their dynamic-thermodynamic[19] sea ice model. It was concluded that the dynamic-thermodynamic model was less sensitive to snow parameter changes than a thermodynamic model (Holland et al., 1993). The reason for this was that there is a negative feedback between the dynamics and thermodynamics of the sea ice model (see Owens and Lemke, 1990) where a thermodynamic model would not capture these feedbacks. The dynamic-thermodynamic model example was included into the discussion since it further illustrates how different models (and their sophistication) can produce a variety of results.

Several models have been developed that contain detailed physics/parameterizations of physical processes and energy and mass exchange in the snow layer [e.g. Brun et al., 1989; Bader and Weilenmann, 1992; Loth et al., 1993; Gruell and Konzelmann, 1994; Lynch-Steiglitz, 1994; Jordan et al., (1999)]. These models simulate snow cover properties like density, grain size, liquid water (and others mentioned earlier) over time. However, most have applications to terrestrial surfaces and not over sea ice, except that of Jordan et al. (1999). Figure 2.12 illustrates the

performance of SNTHERM (snow model of Jordan et al., 1999) over a 6 month period. The model simulates the top snow layer temperature ($z = +50$ in Figure 2.12) reasonably well, but has greater difficulty in the spring period. This may be the result of snow depth not being accurate (too deep in model) during a storm passage in late February (Jordan et al., 1999). In Spring and Summer, the short-wave radiation is the main term in the SEB. Short-wave energy that was absorbed by the snow created a sub-surface temperature maximum similar to observations (Jordan et al., 1999). In Winter, the net long-wave balance is the main term in the SEB. The snow and ice cool in response to long-wave losses, however the sensible heat from the air to the surface mitigates the losses and nearly mirrors the emitted long-wave flux (Jordan et al., 1999).

[19] A dynamic-thermodynamic sea ice model includes two or three dimensional components taking into consideration ocean currents, wind and other dynamical effects.
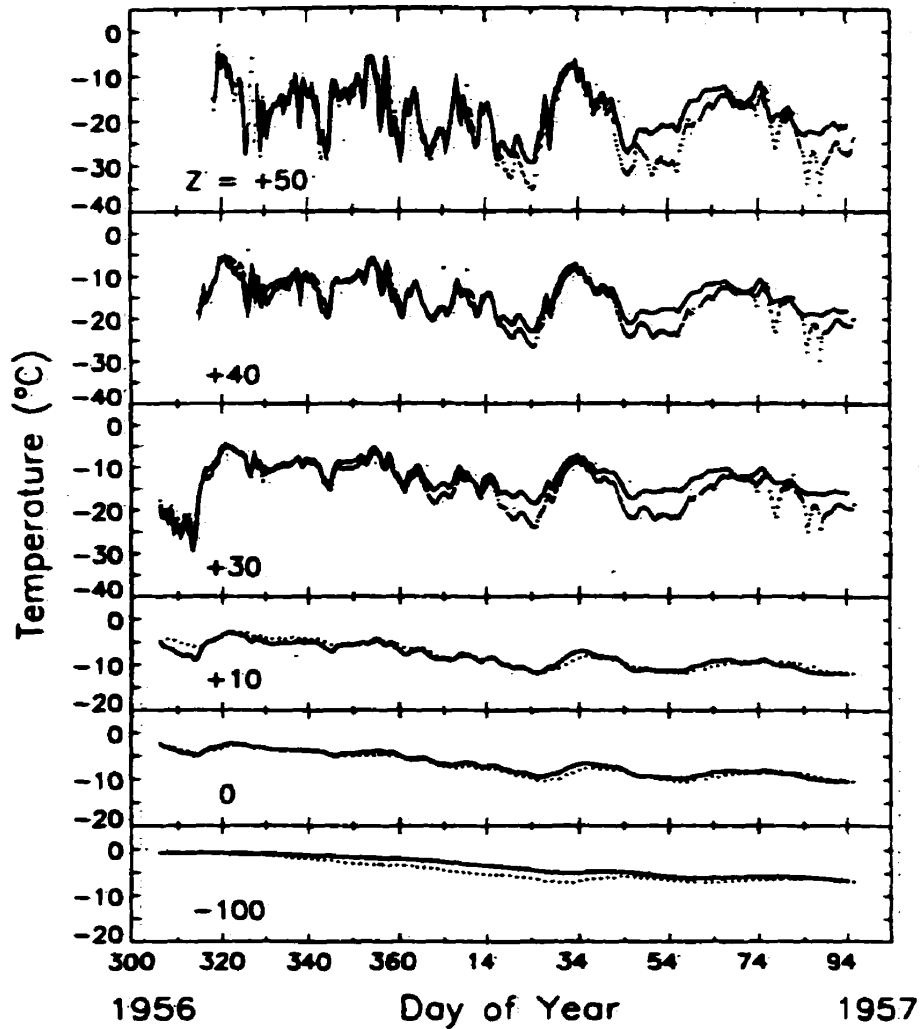
Figure 2.12: Modeled (line) and observed (dots) temperature traces at various depths in the snow and sea ice between November 1, 1956 to April 4, 1957. The snow-ice interface is at 0 cm. (Adapted from Jordan et al., 1999).

Jordan et al. (1999) suggests that SNTHERM has the third-generation snow parameterization for sea ice models. SNTHERM models more in-snow processes than EC and FB who treat the snow layer as a single slab with bulk homogeneous properties. SNTHERM has an order of magnitude greater vertical resolution and runs with an hourly time step[20], instead of a daily time step in EC and FB. This is important since we know (through field observations) that the snow layer and its processes act over smaller spatial

54

and temporal scales than the current sea ice models allow. This ultimately affects the sea ice that responds to snow layer thermodynamics. We also know that the SEB acts over diurnal (hourly and shorter) time scales that fits into the proper scaling of the snow model. An attractive approach is to have a detailed snow model and sea ice model coupled together that both operate over diurnal time scales.

2.3.3 Model Deficiencies

Current snow and ice models simulate many of the critical processes, however there are deficiencies that require further investigation, primarily in the SEB but also involving the thermal properties. Deficiencies outlined here are not exhaustive but are considered of primary interest.

An assumption that has been made by the modeling community is that the SEB can be simulated sufficiently over daily time scales for sea ice (daily time steps). From field work we see processes acting over much shorter time scales (and various spatial scales) ranging from hourly or less. These include surface radiative fluxes, micro and macro-scale processes in snow, sub-daily or daily melt pond evolution, and weekly and monthly ice thickness variations. All of these are tied together through feedback loops (see Figure 2.10) and illustrates the problem of scaling, temporally and spatially.

A technique that is used to force sea ice models is to use land-based meteorological data since measurements on the ice are typically not available (such as the study by FB). Conditions (either atmospheric or surface properties) spatially vary quite

[20] Time step refers to the spacing of time between consecutive iterations of the model (i.e. if the time step is

widely over the arctic and the assumption being made here may not be valid in some cases. For example, incident radiation varies over relatively short time scales and locations. The application of current incident radiation parameterizations may not be valid for all arctic regions due to factors above and is the reason why there are many types of parameterizations (see for example, Shine (1984); Bennett (1982); Efimova (1961); Maykut and Church (1973). In particular, the meteorological conditions, as we see in field observations, over arctic terrestrial, sea ice and open water regions may be quite different.

The surface albedo is another parameter not handled well in current snow and sea ice models. It also changes dramatically in time and space. Changes in micro and macro-scale snow properties (grain size and water content) alters the snow albedo over short periods and the spatial distribution (and thickness) of snow dictates the spatial representation of albedo. Currently, there are no physically-based snow albedo parameterizations under all conditions. Once melt ponds form, their spatial pattern and evolution significantly alter the local and aerial averaged albedo. Capturing these characteristics in an albedo parameterization (and being able to simplify them) is important and more work is required to do this.

A major deficiency with the sea ice models is the lack of detail in the snow layer. Accurate representation of snow over sea ice has been emphasized here as well as other studies (see for example, Brown and Goodison, 1994; Brown and Cote, 1992). A first step toward this is a coupled snow sea-ice model that contains enough detail in both mediums for future investigations of snow and sea ice processes.

---

1 h, the external forcing parameters must be provided at hourly intervals)

Other model deficiencies include:

1) Snow grain evolution is only parameterized and current schemes require validation during the melt season. More physically-based schemes are required.

2) Salinity effects on snow thermal conductivity and specific heat are not modeled (Jordan et al., 1999; Papakyriakou, 1999) nor is it accounted for in snow mass balance (i.e. brine generation in sub-freezing conditions).

3) Turbulent transfer parameterizations in the SEB with regards to vapor transport over cold snow surfaces need more attention (Papakyriakou, 1999).

4) Ice models may over-predict ice growth in Fall since they assume a constant (and too large) snow density during this period (Jordan et al., 1999).

5) Snow models do not account for ponding of water *within* the snow (Jordan et al., 1999).

6) Snow models create excessive basal ice due to the lack of water filtration across the snow-ice interface (Jordan et al., 1999).

7) More work is needed for drifting-blowing snow on erosion-accumulation of the snow pack (Pomeroy et al., 1997; Jordan et al., 1999).

A drawback to SNTHERM and ice models such as FB is they are too detailed for use in large-scale climate modeling (long integrations into the future). This is due to limited computing power and length of time to produce GCM-type simulations, even now with simplified physics in today's GCMs. However, detailed models are useful for the purpose of investigating small scale processes (temporally and their spatial

57

representations) and used to derive relationships that can be scaled-up to climatic time and spatial scales. We can then incorporate these scaled-up relationships into current GCMs.

2.4 Utility of Microwave Remote Sensing for Snow Covered Sea Ice

2.4.1 Background

This section is devoted to illustrating the utility of microwave remote sensing for advancing our understanding of snow covered sea ice climate processes. In particular, I outline research results that demonstrate the use of microwave remote sensing to study snow and sea ice.

Remote sensing of snow covered sea ice has created a diversification of how we use electromagnetic radiation (EMR) interactions to study sea ice processes and its spatial and temporal evolution. Much attention is being paid to linking reflectance, scattering and emission of EMR to physical variables which in turn are coupled through ocean-surface and surface-atmosphere processes to the linkages which control sea ice evolution. Remote sensing technologies are particularly appropriate for studies that focus on the temporal and spatial aspects of processes. Remote sensing measurements can also provide us with a broad area of fine spatial resolution data that can otherwise not be obtained with sparse surface instrumentation.

In the microwave region, both active and passive techniques are widely used for remote sensing of sea ice due to dampened cloud and precipitation effects. Scattering, thermal emission and to a lesser extent, rotational processes (polarization) are all important in the microwave interaction mechanisms with the surface (for example,

Barber et al., 1994; Drinkwater, 1989; Winebrenner et al., 1994). Scattering plays the most important role in microwave remote sensing which is a complex function of the dielectric properties[21], surface roughness and volume inhomogeneities. The relative scattering cross section[22] (σ^o) can change over time and space. The spatial variability is mostly a function of the geophysical properties that contribute to the volume dielectrics or the surface roughness of the snow/ice (Barber et al., 1995b; Onstott, 1992). The temporal changes are controlled by the dielectric mismatch across the air-snow and snow-ice interfaces. The key variables involved are the relative phases of water (ice, liquid and vapor), snow grain size, brine volume and surface roughness. In addition, scattering can be broken down into two key components; surface scattering and volume scattering. If there is a strong dielectric mismatch at a particular interface then the surface scattering will dominate.

Snow cover plays an important role in the microwave backscatter characteristics. Snow is essentially transparent in the Winter season but as the water content in the snow pack increases (due to increased Spring-time air temperatures), the penetration depth of the microwaves into the snow decreases (Drinkwater, 1989). As the penetration depth decreases, the average scattering from a snow covered ice surface contains an increasing contribution from the snow volume and snow surface geometry. The relative contribution of snow surface roughness to the backscatter of microwave energy increases as the free water content of the snow increases (Barber et al., 1991).

---

[21] Dielectric properties define the electrical conductivity of a material (such as snow or ice) relative to the wavelength and polarization of the electromagnetic energy (see Vant et al, 1974; Ulaby et al, 1986).
[22] The relative scattering cross section is an average of the scattering contributions (surface and volume) made by a medium (or mediums including their interfaces) (see for example Barber, 1993).

2.4.2 Microwave Remote Sensing of Sea Ice Through the Annual Cycle

Microwave remote sensing of sea ice has been available since the late seventies in which significant progress has been made since then in the amount of information that is obtainable. However, not all techniques that are used to extract geophysical variables from remote sensing are applicable throughout an annual cycle of sea ice due to many factors (see for example Drinkwater, 1989; Barber et al., 1995b). The spatial and temporal dynamic and physical changes in which sea ice undergoes throughout an annual cycle can be compartmentalized into 5 different stages, similar to Figure 2.8 in section 2.2. These include fall freeze up, winter, early melt, melt onset and advanced melt periods (after Livingstone et al., 1987). The following section will follow these 5 sea ice stages. This section includes a description of the current geophysical variables that are extractable from remote sensing technology during the different stages of sea ice growth and decay.

Table 2.2 summarizes the types of geophysical variables obtainable from microwave remote sensing of sea ice along with the types of sensors, frequencies/wavelengths, spatial resolution and temporal coverage of the remote measurements. Sample references of each technique are also included in the table. Each subsection will provide a discussion of the remote sensing techniques used to infer the variables in Table 2.2 as they are related to the different stages of sea ice growth/decay.

Table 2.2: Variables obtainable from microwave remote sensing for sea ice processes.
* Passive microwave satellite processing is done at the National Snow and Ice Data Center.
** Ice typing is done operationally at the Canadian Ice Service.

Variable	Satellite/Sensor/ Band	Wavelength/ Frequency	Resolution	Coverage	Sample Reference
Ice Mass Balance:					
Extent	ESMR (p. µwave) SMMR (p. µwave) SMM/I (p. µwave)	19 GHz 8,21,22,31,37 GHz 8,21,22,31,37, GHz	25 km 55 km 12 - 25 km	2 per day daily	Weaver & Troisi, 1996
Surface melt; Thickness	SMMR (p. µwave) SMM/I (p. µwave) ERS-1/2 (a. µwave) Radarsat (a. µwave)	8,21,22,31,37 GHz 8,21,22,31,37, GHz 5 cm (C-band), 23 cm (L-band)	55 km 12 - 25 km 30 - 100 m	2 per day daily 1-2 per day	Weaver et al., 1987 Johannessen et al., 1996 Weaver & Troisi, 1996 Fily & Rothrock, 1986 Barber et al., 1991 Markus & Cavalieri, 1996 Shuchman et al., 1996 Winebrenner, 1996 Malinas & Shuchman, 1994
Type; Concentration	SMM/I (p. µwave) SMMR (p. µwave) Radarsat (a. µwave)	8,21,22,31,37, GHz 8,21,22,31,37 GHz 5 cm (C-band)	25 km 25 km 30 - 100 m	daily 2 per day 1-2 per day	Weaver & Troisi, 1996 NSIDC * Can. Ice Service **
Motion/Velocity	ERS-1/2 (a. µwave) Radarsat (a. µwave)	5 cm (C-band)	30 - 100 m	1-2 per day	Fowler et al., 1994 Wilson et al., 2001
Surface SW Flux:					
Surface albedo; Melt ponds	ERS-1/2 (a. µwave) Radarsat (a. µwave)	3, 5 cm (C-band)	30, 100 m	1 - 2 per day	Barber & LeDrew, 1994 Weaver & Troisi, 1996 Yackel and Barber, 2000
Snow Thickness	ERS-1/2 (a. µwave)	3, 5 cm (C-band)	30, 100 m	1 – 2 per day	Barber and Nghiem, 1999
Net SW flux	ERS-1/2 (a. µwave)	3, 5 cm (C-band)	30, 100 m	1 - 2 per day	Barber et al., 1994
Transmitted PAR	ERS-1/2 (a. µwave)	3, 5 cm (C-band)	30, 100 m	1 - 2 per day	Barber & LeDrew, 1994
Surface LW Flux:					
Surface temperature	SMM/I (p. µwave) ERS-1/2 (a. µwave)	8,21,22,31,37, GHz 3, 5 cm (C-band)	25 km 30, 100 m	Daily 1 – 2 per day	Weaver & Troisi, 1996 Comiso, 1986 St. Germain & Cavalieri, 1996 Barber et al., 1994
LW flux	ERS-1/2 (a. µwave)	3, 5 cm (C-band)	30, 100 m	1 - 2 per day	Barber et al., 1995a
Net All Wave Flux:	ERS-1/2 (a. µwave)	5 cm (C-band)	30, 100 m	1 - 2 per day	Barber et al., 1995a
Sensible Heat Flux:					
Floe size stats	Radarsat (a. µwave)	5 cm (C-band)	100 km	Weekly	Weaver & Troisi, 1996
Atmos. drag	ERS-1/2 (a. µwave)	23 cm (L-band)	10 -100 m	1 - 2 per day	Burns, 1990

2.4.2.1 Fall Freeze Up
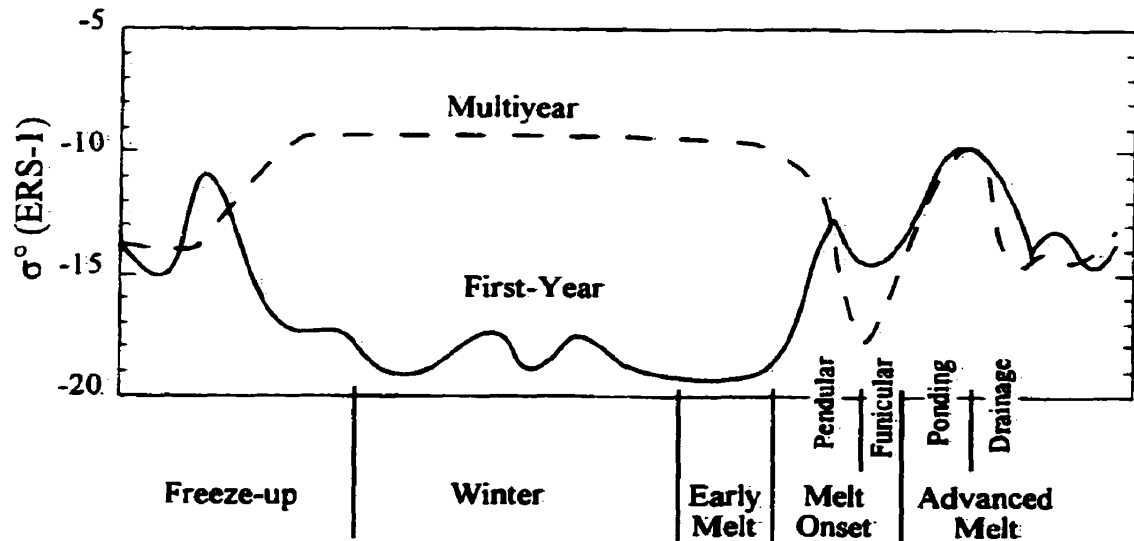
Figure 2.13: Typical ERS and RadarSat backscatter (σ^o) at 5.3 GHz for thick First-Year and Multi-Year sea ice over the seasonal cycle. (adapted from Barber et al., 1999).

Active microwave remote sensing of sea ice varies according to ice type (Figure 2.13). Note the difference between MYI and FYI. This is due to differences in surface and volume physical characteristics of the two types of ice. I limit the discussion to FYI only. The scattering is variable over the ocean surface as a function of wind speed and its high dielectric constant. As ice thickens, there is a decrease in scattering (Figure 2.13). Snow deposition further reduces scattering. The detection of first Fall freeze-up and tracking of its evolution using active microwave remote sensing has not been extensively exploited. However, some studies using SAR technology (satellite and space shuttle) in relation to leads have indicated that a distinction between thin ice regions and open water may be detected (Shuchman et al., 1996) as well as its thickness (Winebrenner, 1996). Shuchman et al. (1996) used ERS-1 SAR data to show that σ^o decreases (< -15 dB) within thin ice regions compared to higher σ^o values (> -7 dB) in open water along arctic leads. This trend may be applicable to the Fall freeze-up period in general since similar

physical processes occur. Shuchman et al. (1996) pointed out that the higher radar returns may also be caused by frost flowers on a thin ice surface as opposed to open water. Winebrenner (1996) indicated that thin ice (< 70 cm) thickness may be extracted from L-band (23 cm) SAR imagery using co-polar ratios and phases in backscatter, however, extensive testing and validation of the technique is required due to the limited number of ground observations in the study.

Burns (1990) showed SAR (23 cm wavelengths) may be useful in the marginal ice zone for inferring the atmospheric drag coefficient. SAR data in the 23 cm wavelength bands can reveal large scale topography (ridges, floes edges) in which high backscatter returns occur from small, broken and heavily deformed floes and rubble areas (Burns, 1990). In addition, the atmospheric drag coefficient increases with increased ice concentration and ice floe deformation in neutrally stratified atmospheric conditions. Atmospheric drag decreases in more atmospherically stable regimes in which surface roughness has a smaller influence. With the help of SAR data to determine the ice characteristics and a simple atmospheric boundary layer model, estimates of the atmospheric drag coefficient could be obtained in the marginal ice zone under neutral atmospheric stability (Burns, 1990).

Passive microwave sensors have been shown to decipher between open water, thin ice (0 - 9 cm) and thicker first year ice. Microwave surface observations indicated that a sharp rise in surface temperature during the first 1-2 cm of growth coincided to a decrease in brightness temperature at higher frequencies (≥ 37 GHz) (Wensnahan et al., 1993a). They attributed this increase in surface temperature to the upward transport of warm brine from the interior of the ice and resulted in the formation of a salinity

enhanced surface layer. Wensnahan et al. (1993b) later applied a principle component analysis technique to decipher between very thin (0 - 4 cm) and thin ice (4 - 9 cm) on microwave surface observations of sea ice. They pointed out that these thin ice ranges would be very difficult to detect by satellites due to spatial resolution and periodic enhanced speeds at which the ice can grow at these thicknesses. However, satellite-based microwave sensors have been shown to be good proxy indicators to thin ice regions outlined below.

Satellite passive microwave techniques at 85 GHz and 37 GHz using the SMM/I sensor have been shown to be able to distinguish between open water, thin ice and first year ice regions (Markus and Cavalieri, 1996; Grenfell, 1996). Two techniques [NASA team ice concentration algorithm (Cavalieri, 1994) and the Polynya Signature Simulation Method (PSSM) (Markus and Burns, 1995)] to distinguish thin ice from open water were tested against aircraft measurements in which good agreement was found (Markus and Cavalieri, 1996). Both techniques provided accurate open water/thin ice discrimination, however, the NASA team algorithm was better suited for larger scale analysis (25 km or greater) whereas, the PSSM was appropriate for spatial scales near 6 km. It was also pointed out that both techniques are only valid for seasonal ice zones and not as of yet applicable to the entire arctic.

A recent study by St. Germain and Cavalieri (1996) have linked SSM/I passive microwave radiances with surface temperatures in the arctic seasonal ice zone. Comparisons with other satellite brightness temperatures were good for several case studies in the seasonal ice zone, however, further research is required to refine the technique (St. Germain and Cavalieri, 1996).

Markus and Cavalieri (1996) also correlated SMM/I ice type/thickness (open water, thin ice and first year) recognition (using the PSSM and NASA algorithms) with other satellite brightness temperatures. They showed that as ice thickness increased, the brightness temperatures decreased with maximum temperature differences between the two techniques (PSSM and NASA) near 2 K. They also pointed out that the large temperature difference between the open water (275 K) and thin ice (268 K) in their case magnifies the importance of the first few centimeters of ice growth on the latent and sensible heat fluxes in that region.

2.4.2.2 Winter

Within first year ice, microwave scattering appears to oscillate according to changes in the oceanic and atmospheric heat fluxes but still provides a stable surface in which remote sensing can be useful (Barber et al., 1994). It has been shown (Barber and Nghiem, 1999) that this oscillation is driven by atmospheric forcing of the snow-ice interface temperature. An increase in the brine volume of the basal snow layer is induced by temperature waves that travel to the base of the snow pack. This increase in brine volume together with large kinetic snow grains create a sufficiently large volume scattering term to increase the total scattering above that of the ice surface (i.e. these oscillations are only found over smooth thick FYI). These thermodynamically driven oscillations can be found for surfaces below about −19 dB (Barber and Thomas, 1998).

Because of the stable nature of microwave scattering in winter over first year ice, several geophysical variables can be extracted from active and passive remote sensing

during this period (see Table 2.2). The separation between the scattering of different ice types during Winter (see Figure 2.13) also allows one to decipher smooth from rougher ice (Figure 2.14). In the active regime, the short-wave (0.3 - 3.0 μm) surface albedo and transmitted Photosynthetically Active Radiation (PAR) (0.4 - 0.7 μm) for a snow cover can be derived from ERS-1 SAR imagery at 5.3 GHz and 9.25 GHz (Barber and LeDrew, 1994). However, measurement of snow thickness may be required to make remote PAR observations a useful quantity. Although recently, a relationship between σ^o and the thermodynamics of the snow cover have shown that snow thickness may be extractable from SAR, but breaks down once water becomes present in the snow pack (Barber and Nghiem, 1999). Snow thickness determination over smooth FYI is in its infancy but results are promising. Barber and LeDrew (1994) developed a statistical relationship (quadratic) between σ^o and albedo and σ^o and transmitted PAR where as σ^o increased, albedo decreased and transmitted PAR increased. The primary physical variables causing the relationship between σ^o and albedo were the increased water volume of the snow pack and a larger contribution to snow volume scattering from the increase in the snow crystal radius (Barber and LeDrew, 1994). At very low water volumes (< 1% water by volume) in the snow pack, transmitted PAR to the snow/ice surface was almost non-existent. Once the water volume increased above 5%, transmitted PAR increased logarithmically with σ^o due to the increase in snow grain size and increased number density of the water inclusions (Barber and LeDrew, 1994).
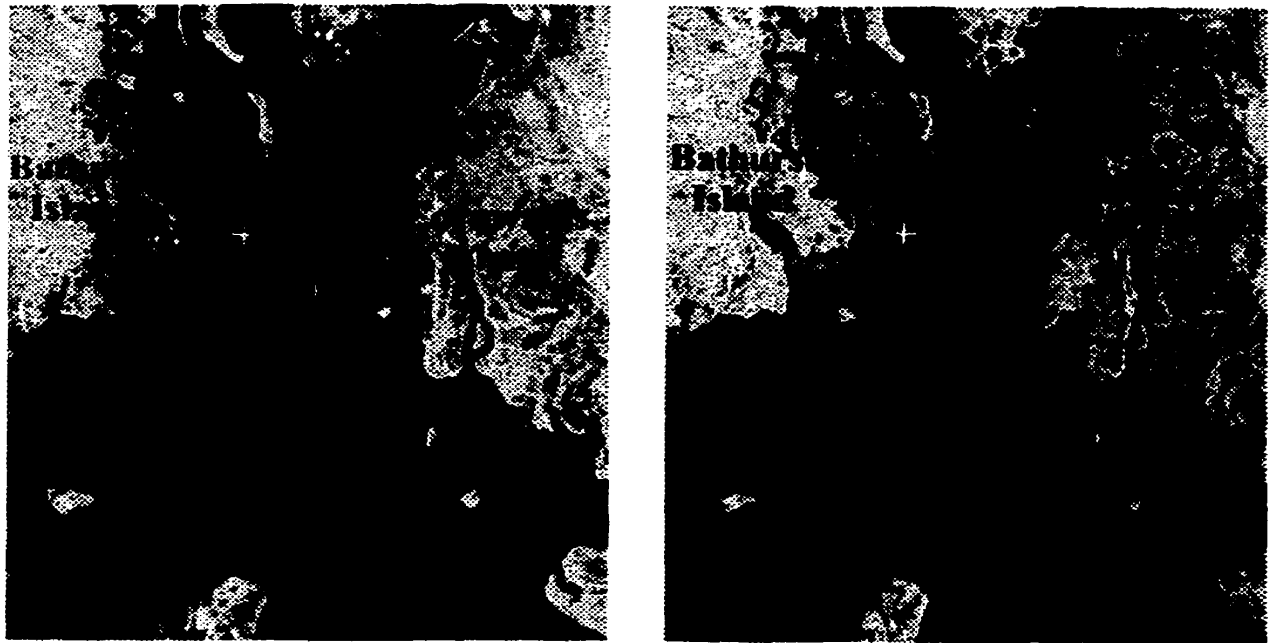
Figure 2.14: RadarSat imagery on January 31, 1999 (Winter; left) and June 27, 1999 (Advanced Melt; right) in McDougall Sound, Nunavut. Dark shades in Winter are smooth first-year ice, whiter shades are rougher (ridged and rubbled) first-year ice. During Advanced Melt, detail is lost due to water in liquid phase dominating the scene (see text). The "+" signifies smooth first-year sea ice. Due north is toward the top of the images.

Barber et al. (1994) showed there is a statistical relationship between the seasonal evolution of σ^o with surface temperature (T_{sfc}) and the net short-wave flux (K^*) over first year snow covered sea ice. This is due to both variables (T_{sfc} and K^*) either causing or covarying with the change in the dielectric properties responsible for the change in σ^o. An inverse relationship existed between both T_{sfc} and K^* relative to σ^o, and the influence of the surface temperature was about twice that of the net short-wave flux in explaining the variation in σ^o. Furthermore, Barber et al. (1995a) determined that T_{sfc} and the long-wave flux (L^*) could be considered statistically indistinguishable between first-year and multiyear sea ice, for conditions experienced during SIMMS'93 (Seasonal Sea Ice Monitoring and Modeling Site, 1993). The K^* and net all-wave flux (Q^*) were however

statistically distinguishable between the MYI and FYI sites. They attributed this result to the fact that T_{sfc} and L^* were, to a large degree, determined by characteristics of the atmospheric boundary layer and that K^* and Q^* were largely prescribed by the snow metamorphic state. Because the snow is distributed differently over multiyear versus first-year ice types, differences occurred in the seasonal evolution of these fluxes.

Maslanik and Maybee (1994) and Fowler et al. (1994) derived ice motions from interpolated ice displacements from ERS-1 data. The observed ice motion vectors were then used to initialize and validate a two-dimensional sea ice model. More recently, Wilson et al. (2001) is applying RadarSat imagery and operational software (TRACKER – used at the Canadian Ice Service) to derive ice motion vectors over time. The technique is has been validated using ice buoys from the 1998 International North Water (NOW) Polynya Project with good success.

Malinas and Shuchman (1994) developed a transfer function to convert SAR σ^o values to ice thicknesses using aircraft SAR and upward looking sonar data. The general observation was that an increase in ice thickness corresponded to an increase in σ^o for multi-year and first year ice types. However, the technique requires further verification and testing.

Satellite passive microwave remote sensing sensors provide another valuable source for winter sea ice monitoring and have been widely used for many studies (see for example Preller et al., 1992; Maslanik and Maybee, 1994). Algorithms for multi-channel microwave data can extract sea ice concentration for any given pixel, from which ice extent, ice area, water area and overall ice concentration can be derived for broader regions (see for example, Johannessen et al., 1996). Individual pixel concentrations can

be derived from SSM/I radiances in the frequencies at 19, 22, 37 and 85 GHz in conjunction with an algorithm such as NORSEX (Norwegian Remote Sensing Experiment; Svendsen et al., 1983) or the PSSM or NASA team algorithms (see Fall Freeze-Up section). Time series of ice extent, ice area and overall ice concentration can then be derived from individual-pixel ice concentrations of consecutive SMM/I imagery.

2.4.2.3 Early Melt

Within first-year sea ice, microwave scattering appears to be dominated by a combination of basal layer volume scattering and ice surface scattering (see Figure 2.13). During this period we would expect to find a significant difference in solar noon versus solar midnight observations as small amounts of water in liquid phase would contribute both to grain growth and the elevated temperatures would significantly increase the brine volume of the snow basal layer. The overall magnitude of σ° will be dependent on the ice surface micro-scale roughness and its surface brine volume. All of the geophysical variables extracted from microwave remote sensing (active and passive) in Table 2.2 are transferable to the Early Melt season.

2.4.2.4 Melt Onset

In first-year sea ice, melt onset is denoted by a rapid increase in σ° (see Figure 2.13). There are 2 mechanisms which are likely candidates for the observed increase. At relatively low water volumes (1 to 3 percent) the large wet snow grains in the basal

layer may contribute a significant volume scattering term to σ°. As the water in liquid phase continues to increase (but is maintained within the pendular regime) it is likely that the snow surface may also contribute a surface scattering term to σ° (Drinkwater, 1989; Livingstone and Drinkwater, 1991; Barber and LeDrew, 1994). In a case study done by Barber et al. (1995a) it was found that the snow volume scattering term was the dominant mechanism. A distinct dip in σ° at the FYI site corresponded with the transition from the pendular and funicular regimes. This transition marks the reduction of brine within the basal layer to near zero, an increase in the water in liquid phase at the base of the snow cover and a reduction of water in liquid phase in the top parts of the snow volume (as the surface begins to drain). These processes could lead to a reduction of both the volume scattering and snow surface scattering hypothesized to dominate the pendular regime conditions.

All of the geophysical variables extracted from microwave remote sensing (active and passive) in Table 2.2 may be transferable to the Melt Onset season. However, the high variability in the spatial patterns of most geophysical parameters within the icescape may produce large differences between pixels within the satellite imagery depending on the spatial resolution of the remote sensor.

2.4.2.5 Advanced Melt

In first-year sea ice, advanced melt is denoted by a rapid increase in σ° (see Figure 2.13). As surface water forms in the melt ponds there is an increase in the discontinuity at the air/water interface. We can expect a penetration depth on the order of

1 cm at 5.3 GHz (Ulaby et al. 1986). An increase in scattering occurs if the melt pond surfaces are wind roughened. The separation in scattering between ice types is also decreased (Figure 2.13) making detail in satellite SAR imagery "washed-out" due to water in liquid phase dominating during this period (see Figure 2.14). Once the ice surface begins to drain there is a pronounced decrease in the $\sigma°$. This period coincides with a reduction in the aerial extent of the melt ponds. The exact mechanisms for first-year ice scattering during the advanced melt period are also largely unknown.

Due to the high variability in the icescape during the Advanced Melt period, it is not known whether most of the geophysical variables that are extracted from remote sensing (appearing in Table 2.2) are valid. Most studies do not include this stage of sea ice evolution within the temporal scales of the techniques. This is mostly due to the limited number of surface observations for validation during this period in which dangerous ice conditions exist. However, Barber and Yackel (1999) and Yackel and Barber (2000) showed that SAR imagery may be able to infer surface albedo and melt pond fractions using ERS-1 or RADARSAT during advanced melt but only applied to first year land-fast sea ice in windy (2-3 m s^{-1}) conditions. They also indicated that the microwave scattering could be used to obtain an unambiguous measure of the onset of melt, by an increase in scattering over first year ice. Furthermore, the transition between pendular and funicular regimes may be detectable in first year scattering (Barber and Yackel, 1999).

2.5 Summary

In summary, the critical characteristics of snow-covered FYI including its physical and thermal attributes have been discussed in sections 2.1 and 2.2. These attributes occur over a wide range of spatial scales (microscale to synoptic) and temporal scales (seconds to years). I have also included a discussion of the current types of one-dimensional numerical models that are available to simulate the physical and thermal attributes of snow-covered FYI over various spatial and temporal scales (section 2.3). The discussion illustrated the utility of one-dimensional models for improving our understanding of arctic snow and sea ice processes, their advantages and deficiencies. The following section (2.4) illustrated the utility of satellite microwave remote sensing for monitoring and understanding physical processes within FYI over the various seasons. Chapter 2 has thus provided background material to issues that are addressed in my dissertation that primarily deal with using *in situ* data for advancing one-dimensional sea ice models to a state where they can be useful for application to microwave remote sensing. The first chapter (Chapter 3) deals with the issue of ensuring the one-dimensional sea ice models properly handle the temporal scales we see acting in field observations. Previous field work and microwave remote sensing observations suggest that diurnal time scales are important over seasonal snow-covered sea ice. In Chapter 3, I investigate the ability of a one-dimensional thermodynamic sea ice model to simulate annual cycles of FYI and its various physical and thermal processes over diurnal time scales, an investigation that has previously never been conducted.

CHAPTER 3: Role of Diurnal Processes in the Seasonal Evolution of Sea Ice and its Snow Cover

3.1 Introduction

In this chapter, I examine whether there is a need to consider diurnal time scale processes in a snow-covered FYI 1-D numerical modeling environment (using Flato and Brown, 1996) and whether the existing model appropriately handles these time scales in several critical parameterizations. Stated in Chapters 1 and 2, it is important that snow and sea ice models operate at surface energy balance time scales we see in field observations (typically hourly). It is also important to ensure the model parameterizations are able to work in these time scales and they are not compromised by spatial differences. An investigation of this type has previously never been done since it has been assumed that diurnal processes would produce similar modeling results as longer time scales. The results from this chapter have been published in the peer reviewed literature in Hanesiak et al. (1999). The primary objectives of this chapter are to examine the following research questions:

1) Does the use of hourly and daily varying forcing data result in a different simulation of the annual cycle of ice thermodynamics?

2) Do the parameterizations used in the model adequately represent specific processes over shorter temporal scales and are they valid when compared with 'on ice' measurements?

3) Is there a systematic bias in forcing the model with 'land based' versus 'on ice' measurements of input fluxes when using shorter temporal scales?

3.2 Data and Methods

3.2.1 Sea Ice Model

A thorough description of the one-dimensional thermodynamic sea ice model used in this work can be found in Flato and Brown (1996) where many of the physical processes discussed in chapter 2 are implemented. The model was designed to run with daily average forcing but was adapted to use hourly forcing and time step. This required modifications to the down-welling short-wave parameterization to account for diurnal variations in solar heating. Since a more detailed investigation involving the parameterized and observed down-welling short-wave ($K\downarrow$) and long-wave ($L\downarrow$) and surface albedo are conducted (sections 3.3.2 and 3.3.3), brief descriptions of how the model parameterizes these variables is given here. Chapter 4 looks at these parameterizations and tests their capabilities in greater detail.

$L\downarrow$ is computed using the parameterization of Maykut and Church (1973) for both clear-sky and all-sky fluxes and the $K\downarrow$ parameterization of Shine (1984) is used for both clear-sky and all-sky fluxes. Both parameterizations were found to be among the best for Arctic climates (Key et al., 1996) and will be further tested in chapter 4. Both the $L\downarrow$ and $K\downarrow$ parameterizations use a single total cloud fraction for computing all-sky fluxes. The $K\downarrow$ parameterization explicitly considers changes in albedo, relative humidity and cloud fraction however I employ a constant cloud optical depth (0.7 after Curry and Ebert, 1992 and used also in Flato and Brown, 1996) that may cause negative biases in this work under overcast conditions (see section 3.3.2). Due to the non-linearity of cloud fraction and relative humidity in the $K\downarrow$ parameterization, the daily average $K\downarrow$ computed over hourly intervals may be different than the single daily value $K\downarrow$ computed using a

daily-average cloud fraction and relative humidity. This holds even under clear skies with a constant surface albedo due to relative humidity changes. The impact of this in combination with other processes is shown in section 3.3.1.

The surface albedo parameterization is dictated by surface type (ice, snow, open water), surface temperature (melting or subfreezing), and ice thickness. The latter acts as a proxy for time during the melt season that attempts to capture melt pond evolution (Flato and Brown, 1996). The parameterization does not explicitly treat melt ponds nor does it partition the albedo into discrete wavelengths as in Ebert and Curry (1993). The dry snow albedo is set to 0.75 if the snow depth is ≥ 0.1 m and decreases according to snow depth less than 0.1 m and the cold ice albedo of Maykut (1982). When snow is melting, its albedo decreases to 0.65. The melting ice albedo parameterization is adapted from Heron and Woo (1994). The full formulation of the model's albedo parameterization can be found in Flato and Brown (1996).

The snow layer in the model is treated as a single layer with bulk homogeneous physical properties (ie: density $= 330$ kg m^{-3} when dry). When new snow is deposited on the surface, the albedo and density do not change, however, if the mean snow layer temperature is at or above freezing, its density increases to 450 kg m^{-3}. This serves as a proxy for the presence of liquid water and snow densification due to increased liquid water. The model does not physically consider variations in density over time, snow grain processes, liquid water content or brine inclusions.

The number of layers within the ice is arbitrary, however, fifty vertical layers are used here (one for snow and 49 for ice) to resolve diurnal thermodynamic fluctuations in the ice. A time step of 1 h is used for the diurnal cycle simulations and one day for the daily-average forcing simulations. The model is initialized with *in situ* data discussed in Section 3.2.2.

3.2.2 Data

The field observations were collected in the spring/summer periods during the SIMMS (Seasonal Ice Monitoring and Modeling Site) experiments between 1992-1993 near Resolute, Nunavut. The 1992 field season extended from Year Day (YD) 107 (April 18) to YD 177 (June 27) and the 1993 field season ran between YD 117 (April 27) and YD 170 (June 19). Figure 3.1 shows the geographic locations of Resolute and the first-year ice (FYI) field observations for both SIMMS experiments. The 1992-93 sea ice cycle was selected to perform the numerical model simulations since 1992 was atypically cool and 1993 was atypically warm. In 1992, a prolonged cool period extended into the late spring delaying the onset of melt. The 1993 spring field season was significantly warmer with much earlier melt than in 1992.
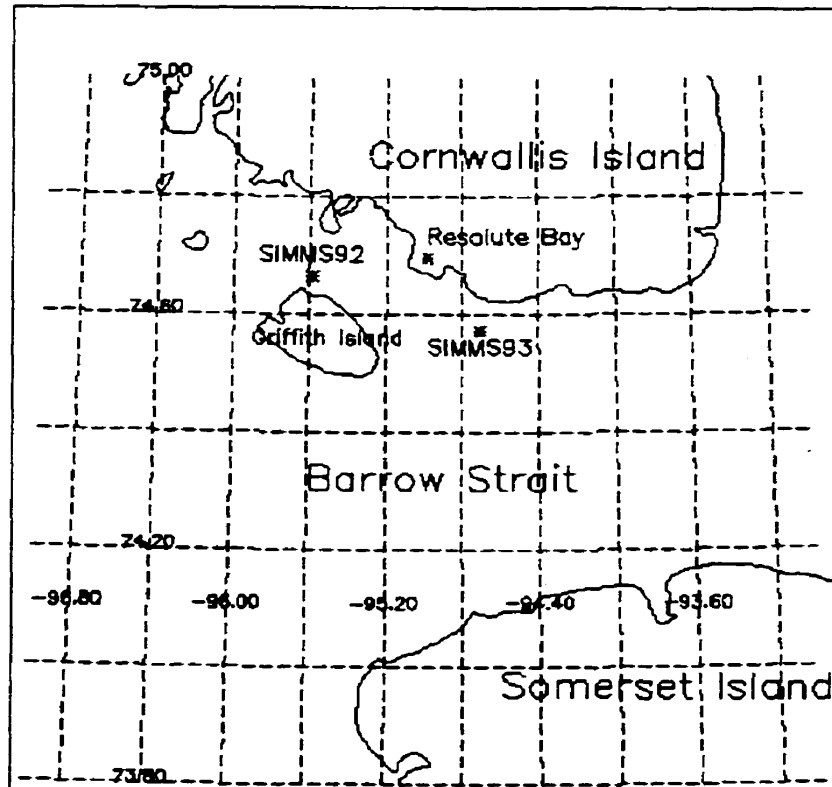
Figure 3.1: Geographical region of Resolute Bay, Nunavut and the first-year sea ice (FYI) field camps from SIMMS'92 and '93.

The field observations pertinent to this work include surface energy balance parameters such as incident and reflected short-wave radiation ($K\downarrow$, $K\uparrow$), net short-wave ($K^* = K\downarrow - K\uparrow$) down-welling and up-welling long-wave radiation ($L\downarrow$, $L\uparrow$), net long-wave ($L^* = L\downarrow - L\uparrow$) and net radiation ($Q^* = K^* + L^*$). The observations also include vertical temperature profiles within the snow/ice volumes and snow and ice thickness. A description of the instrumentation and measurement methods can be found in Barber et al. (1994; 1995a). The surface energy balance parameters and snow/ice temperature profiles were logged at 15 or 30 minute intervals depending on the field season. Instantaneous on-the-hour data were used for this work since this corresponds to the shortest time step/forcing used in the numerical model simulations. Snow and ice thickness was measured periodically throughout each field season.

Other surface observations include hourly standard meteorological observations taken at Resolute by the Meteorological Service of Canada (MSC). The pertinent data include air temperature (T_a), relative humidity (RH), wind speed (u), precipitation (sfall), and total cloud fraction (amount) (c).

3.3 Results and Discussion

3.3.1 Temporal Scaling Considerations

3.3.1.1 Hourly vs. Daily Forcing Comparisons

The sea ice model (Flato and Brown, 1996) was forced using hourly data and daily average data consisting of land-based MSC Resolute meteorological observations: T_a, RH, u, sfall, and c between YD 107, 1992 and YD 170, 1993. For simplicity, the hourly-forced simulation and daily average-forced simulation will be referred to as hourly simulation and daily simulation, respectively. The ice thickness obtained from both models agrees quite well with observations over the 1992 spring period except toward the end of the season (Figure 3.2). More discussion of this is given in section 3.3.3. Ice thickness measurement variability was about ± 0.1 m during the SIMMS field experiment. The 1992 break-up (BU) and freeze-up (FU) dates for the hourly (BU=YD189, FU=YD297) and daily (BU=YD202, FU=YD289) simulations indicates a 21 day longer open water duration for the hourly simulation. Care should be taken when interpreting the BU dates in particular since the model does not account for dynamic sea ice processes (i.e., wind and ocean currents). The modeled BU is defined by the complete disappearance of the sea ice whereas in reality, wind and oceanic forcing may induce BU prior to complete ablation in most Arctic regions. The Canadian Ice Service (CIS) charts

indicated the 1992 BU may have occurred between YD190 and YD197 and FU occurred between YD288 and YD295 within the surrounding Resolute Bay region. This suggests that the model-predicted BU and FU dates above are within the uncertainty of the observed dates. It again should be mentioned that it is not the intent to compare the predictive capabilities (explicitly using BU and FU) between the two forcing simulations, but to examine in a diagnostic sense, the differences between using hourly as opposed to daily average forcing.

Overall, the obvious differences between the hourly and daily simulations in Figure 3.2 are: 1) the open water duration is much longer (by 21 days) in the hourly run with break-up (freeze-up) occurring sooner (later); and 2) the snow ablates earlier but more gradually in the hourly simulation. The snow thickness differences between the field site measurements and model (using Resolute snowfall amounts) will be discussed later.

The 1993 maximum ice thickness was reached on an earlier date in the hourly simulation (2.19 m on YD149) compared to the daily simulation (2.13 m on YD155) (see Figure 3.2). This rather modest difference is related to the differences in freeze-up and break-up. Delayed melt in the daily run during the 1993 spring allowed the maximum ice thickness to be reached later in the year. In addition, the daily simulation ice growth rate is less than the hourly simulation due to a quicker FU date allowing an overall greater accumulation of snow thereby stunting ice growth.

A closer look at the modeled snow thickness during the 1992 spring period (YD120-YD175 in Figure 3.3) reveals that Year Days 133, 134, 139, 142, 149, and 154 onward were days with snow ablation in the hourly simulation, with complete snow ablation by YD165. In contrast, the daily run did not produce snow ablation until YD169 onward, with an abrupt disappearance of the snow pack (over 5 days). The observed snow thickness is much different than the modeled snow thickness due to: 1)

redistribution effects (blowing/drifting snow); 2) differences in precipitation amounts between the field site and Resolute; 3) sfall measurement error at Resolute; and 4) the assumption of a constant dry snow density in the model (330 kg m^{-3}).
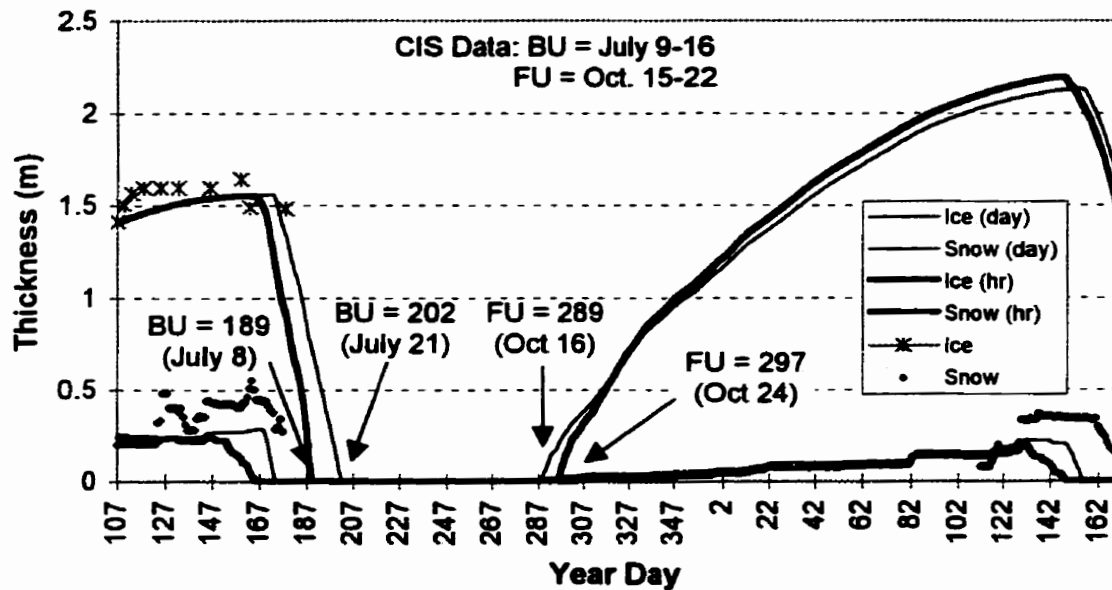
Figure 3.2: Time series of observed snow (dots) and ice (*) thickness, hourly forcing modeled snow/ice thickness (thick solid lines), and daily forcing modeled snow-ice thickness (thin solid line) from YD107 (April 18), 1992 to YD170 (June 19), 1993. Units are in m. Canadian Ice Service (CIS) estimated freeze-up and break-up dates are also indicated near the top of the figure.
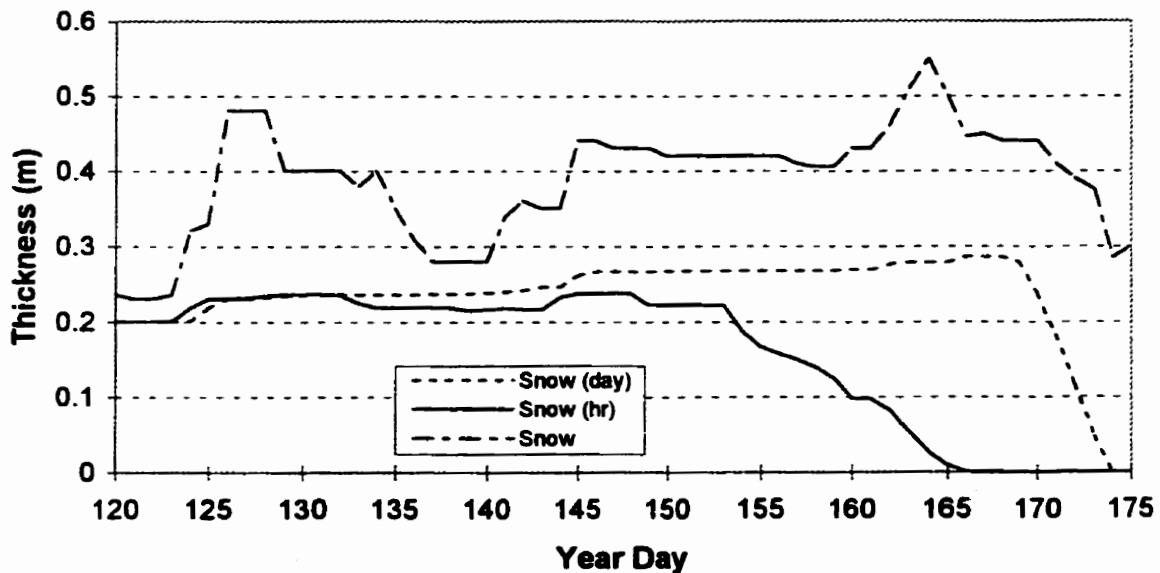
Figure 3.3: Time series of observed snow thickness (upper-most line), hourly forcing modeled snow thickness (solid line), and daily forcing modeled snow thickness (dashed line) from YD120 (May 1), 1992 to YD175 (June 25), 1992.

81

Sporadic diurnal snow ablation (some days with snow melt and some with no melt) and gradual decrease in snow thickness were associated with melting surface temperatures during certain hours, even though air temperatures were well below freezing (Figure 3.4a). However, the air temperature and surface temperature differences in Figure 3.4a are exaggerated in some cases indicated by the observed surface temperatures (see Figure 3.14c). More discussion of this is provided in section 3.3.3. The intent of Figure 3.4a is to show the associated changes in snow characteristics with surface temperature for the hourly simulation and compare them with the daily simulation that did not reach melting snow conditions until YD169 (Figure 3.4b). The gradual decline in snow thickness over the spring period (hourly run) is attributable to the freeze-thaw diurnal cycles of surface temperature as well as the addition of new snow during that period. These diurnal processes are typical of our SIMMS observations.

The diurnal freeze-thaw cycle is more obvious when looking at the modeled surface albedo over the 1992 spring period (Figure 3.5a). The surface albedo drops to the wet snow value (0.65 in the hourly simulation) when surface temperatures reach the melting point and returns to the dry snow value (0.75 in the model) once re-frozen. The albedo does not drop below the dry snow value in the daily run until YD169 (Figure 3.5b). It should also be noted that the diurnal albedo decreases take place during peak to medium solar exposure hours on days associated with diurnal melt. The impact of the diurnal albedo cycle is to increase the short-wave absorption and hence the amount of energy available for snow melt. More discussion of this is provided in the following section.
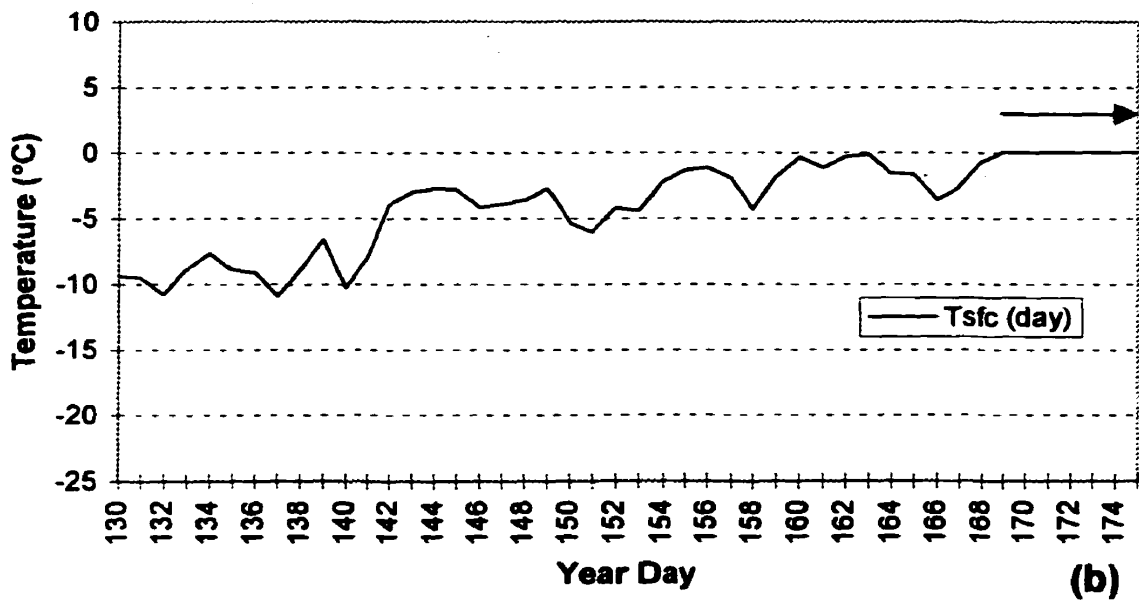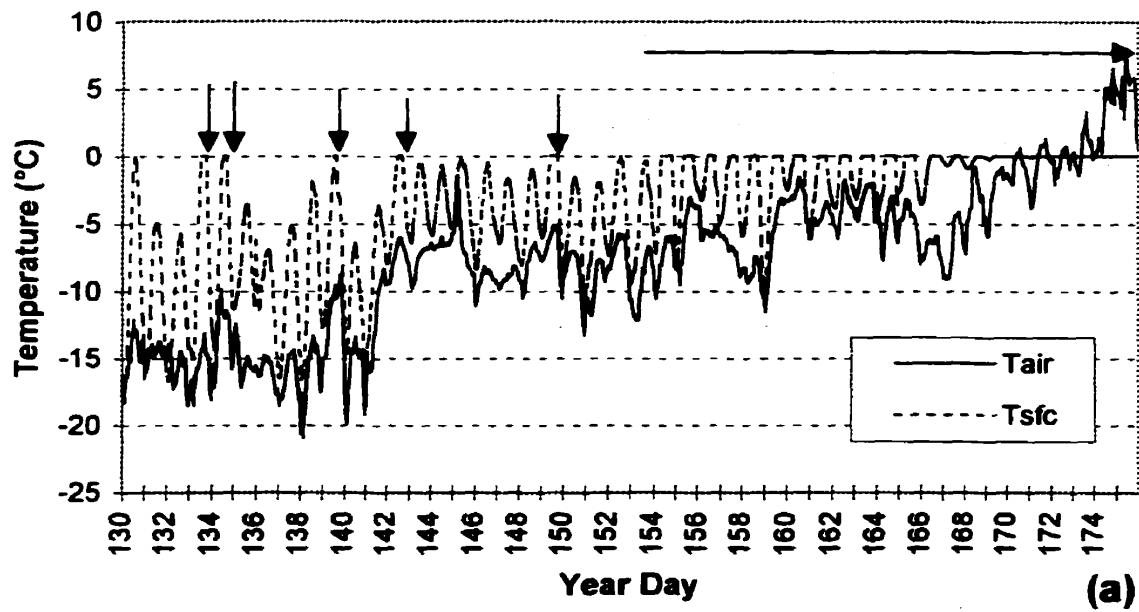
Figure 3.4: Time series of a) hourly forcing modeled surface temperature and ambient air temperature (°C) and b) daily forcing modeled surface temperature (°C) from YD130 (May 11), 1992 to YD175 (June 25), 1992. Arrows indicate days with surface melt.
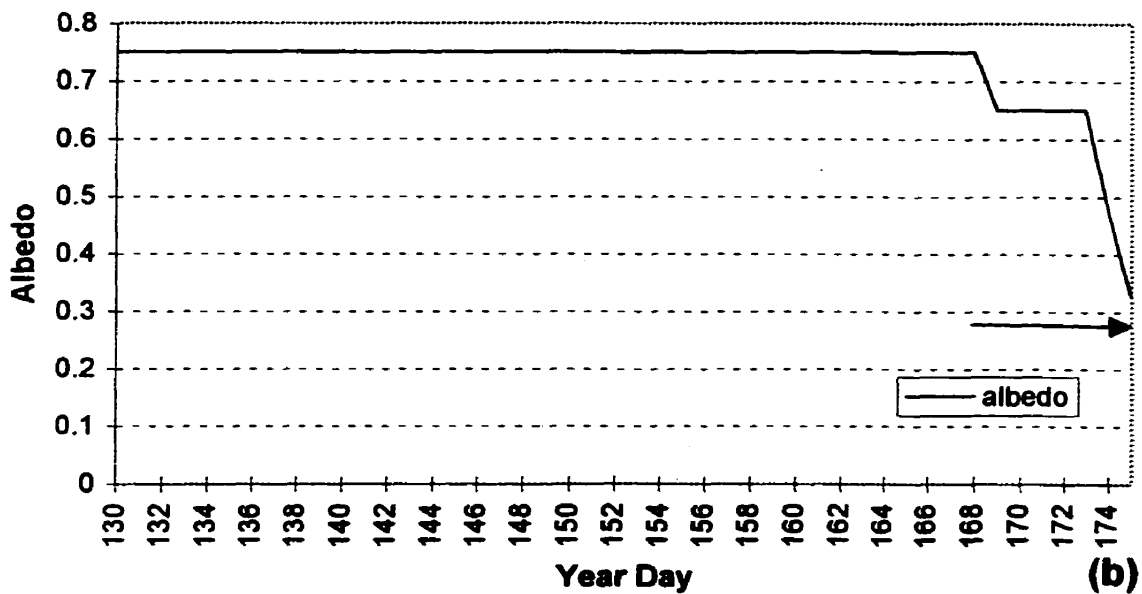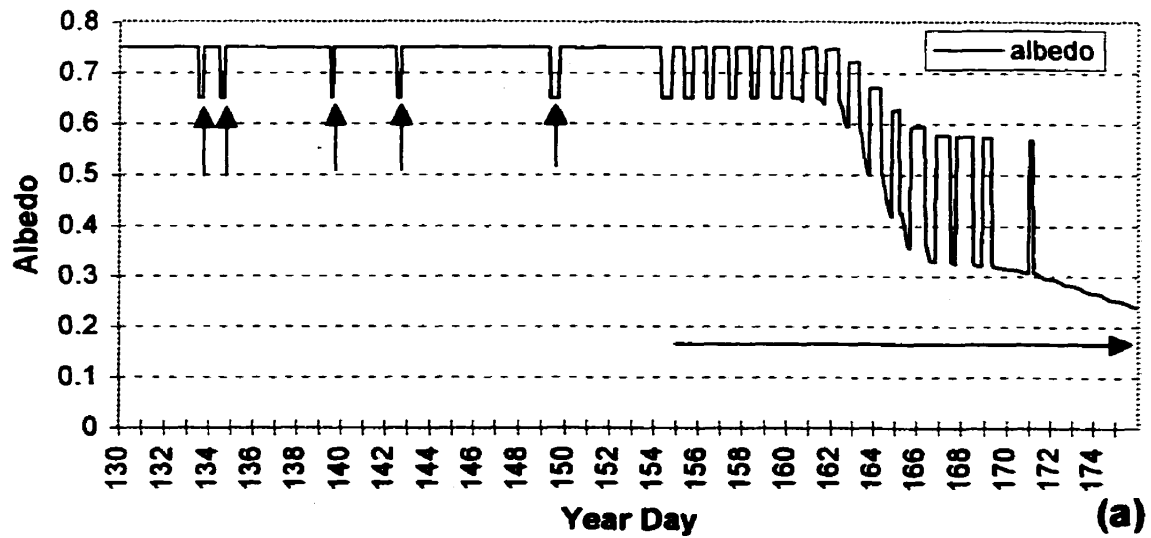
Figure 3.5: Time series of a) hourly forcing modeled surface albedo and, b) daily forcing modeled surface albedo from YD130 (May 11), 1992 to YD175 (June 25), 1992. Arrows indicate days with surface melt.

Other diurnal features that are typically observed are vertical temperature waves that propagate through the snow and ice layers due to the cyclic heating/cooling of the snow surface (Figure 3.6). These temperature changes alter the overall dielectric properties of the snow/ice making this phenomenon important for active and passive microwave satellite signatures of sea ice. The modeled vertical ice temperature profile (Figure 3.6) does exhibit these temperature waves in the early to mid spring season [however it is very difficult to see in Figure 3.6 since the amplitudes of these waves (<0.1°C) are significantly less than those observed in the field (0.4-0.5°C maximum)]. The diurnal temperature waves appear only when the snow cover is very thin (< 2 cm) late in the spring season (Figure 3.6). The dampened temperature waves in the early to mid spring season may be the result of the sea ice model's single slab representation of the snow layer and possibly deviations between actual and modeled snow/ice thermal diffusivities and heat capacities. The single-slab snow representation may hinder important thermodynamic processes by not accounting for density changes, snow grain processes, liquid water content and brine inclusions that affect the thermal conductivity of the snow. Formal testing of these speculations are beyond the scope of this work but are addressed again in later chapters.
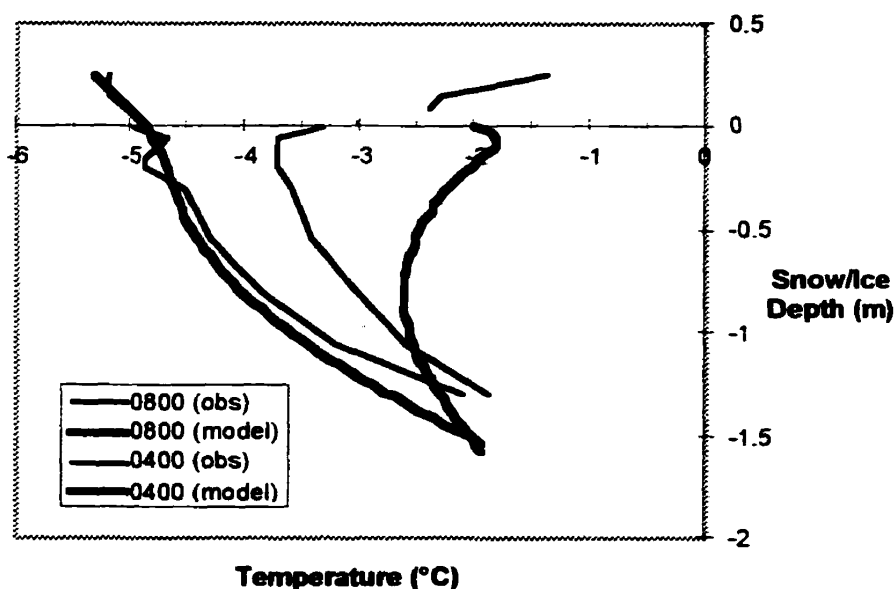
Figure 3.6: Examples of modeled (thick solid line) and observed (thin solid line) vertical snow/ice temperature profiles during the mid spring season at 0800 solar time on YD148 (colder profiles) and late spring season at 0400 solar time on YD165, 1992 (warmer profiles). Note that the snow array temperature measurements were only available to the +25 cm snow depth (with respect to the snow/ice interface), where actual snow depths were ~ 45 cm on YD148 and YD165. Modeled snow depths were near 25 cm on YD148 and 0 cm on YD165. The large discrepancies on YD165 are due to differences in modeled snow/ice conditions compared to observations (see text).

3.3.1.2 Causes for Hourly vs. Daily Forcing Differences

In this section I conduct sensitivity tests with the hourly and daily simulations to investigate the processes responsible for the differences in the previous section. From the results above, it is difficult to conclude immediately whether the open water duration difference is due mostly to the difference in snow ablation rates or other processes linked to the forcing differences. In other words, what processes (in the snow or ice) respond differently to shorter temporal scales in the forcing?

In order to investigate the snow ablation effects on the simulation differences, hourly and daily runs were conducted with no snow cover. In this case, the hourly

simulation open water duration is only 3 days longer (with BU occurring 1 day sooner) than the daily model run compared to 21 open water days (BU occurring 13 days sooner) when snow is included. It is clear then that processes involving the snow cover are responsible for the bulk of the break-up date and open water duration differences between the daily and hourly simulations. The question then becomes - what are the controlling processes?

A noticeable difference between the daily and hourly simulation time series of K^* (net short-wave flux) is that the hourly run produces a greater daily average K^* of 20.1 W m^{-2} (or 1400 W m^{-2} accumulated) over the 1992 spring period (Figure 3.7). The hourly run produces an even greater daily average K^* of 30 W m^{-2} (>1400 W m^{-2} accumulated) when considering only the time period from melt onset and beyond. The daily average K^* from the hourly simulation was computed by summing the hourly K^* values and dividing by the total numbers of hours in the day. The single K^* value computed from the daily simulation was then subtracted from the hourly simulation average to plot Figure 3.7. Once again, although the optical depth is held constant (0.7) and the albedo may be the same over the entire day, the daily average K^* for the hourly simulation may still be different than the daily simulation K^*, as discussed in section 3.2.1. The combination of incident short-wave and absorbed short-wave radiation are therefore quite different between the daily and hourly simulations.

A major difference between the hourly and daily runs is the distribution of down-welling short-wave radiation ($K\downarrow$) throughout the day. The hourly simulation $K\downarrow$ is distributed about solar noon, whereas the daily run $K\downarrow$ distribution is a constant equal to the daily average $K\downarrow$. This can have significant effects on snow melt initiation and duration. To illustrate this, a sensitivity run (TEST 1) was conducted on the hourly simulation with its hourly $K\downarrow$ set to its daily average value for each day. In this case, the

BU date was delayed to YD193 and the open water duration shortened by 5 days compared to the original hourly simulation (Table 3.1). This occurred due to a reduced number of days having snow melt as well as a shortening of snow melt duration for each day. This suggests that the diurnal cycle of $K\downarrow$ has an influence on snow melt initiation, but its neglect accounts for only about a quarter of the hourly/daily simulation difference.

Table 3.1: *The break-up dates and open water duration (days) for the daily model, hourly model, and sensitivity simulations TEST 1, TEST 2, TEST 3, TEST 4 and TEST 5 (see text).*

	Daily	Hourly	TEST 1	TEST 2	TEST 3	TEST 4
BU Date	JD202	JD189	JD193	JD195	JD200	JD191
OW Duration	87 days	108 days	103 days	98 days	91 days	105 days

As mentioned previously, the diurnal decreases in albedo (when melt occurred) took place during peak to medium solar exposure hours in the hourly simulation. This implies that an even greater amount of short-wave energy is absorbed by the snow during these hours due to the positive albedo feedback. To investigate the impact of this effect, the albedo was not allowed to decrease to its wet snow value (0.65) during melt events in the hourly simulation (TEST 2). In this case, the BU date was delayed to YD195 and the open water duration shortened to 98 days compared to the original hourly simulation (Table 3.1). This occurred due to a reduction of days having snow melt and therefore a shortening of snow melt duration. TEST 2 indicates that about half of the difference between the hourly/daily simulations can be attributed to the addition of short-wave energy during melt events due to the positive snowmelt albedo feedback.

To investigate the diurnal $K\downarrow$ distribution and albedo feedback impacts simultaneously, a sensitivity run (TEST 3) was conducted on the hourly simulation combining TEST 1 and TEST 2 (ie: daily-average $K\downarrow$ and no effect of melt on albedo). In

this scenario, the BU date was delayed to YD200 and the open water duration shortened by 17 days compared to the original hourly simulation (Table 3.1). The combined effects of increased short-wave absorption via albedo feedback and the $K\downarrow$ diurnal distribution therefore explains 10 out of the 12 BU days and 17 out of the 21 open water days difference between the daily/hourly simulations. The remaining difference must be attributable to some other component of the surface energy balance.

Analysis of the surface energy balance reveals that days associated with diurnal surface melt corresponded to days with very low latent and sensible heat fluxes (mostly due to calm winds) at peak daylight hours (Figure 3.8). The premise here is that the timing of very low latent/sensible heat loss in the hourly model was capable of increasing the likelihood of melt during peak to medium solar exposure. In contrast, the daily run uses a daily average wind speed that would in most cases never be zero, thus reducing the likelihood of melt for that day. To investigate this further, an hourly run (TEST 4) was conducted with wind speeds increased to 1.0 m s^{-1} when wind speeds were actually zero for any particular hour. The 1 m s^{-1} was approximately the daily average wind speed for only those days with melt occurring. In TEST 4, the BU date was delayed to YD191 and the open water duration shortened by 3 days compared to the original hourly simulation (Table 3.1). Increasing the wind (latent/sensible heat loss) in this fashion reduced the duration of melt events and also completely eliminated some melt days compared to the original hourly simulation, in turn prolonging BU.
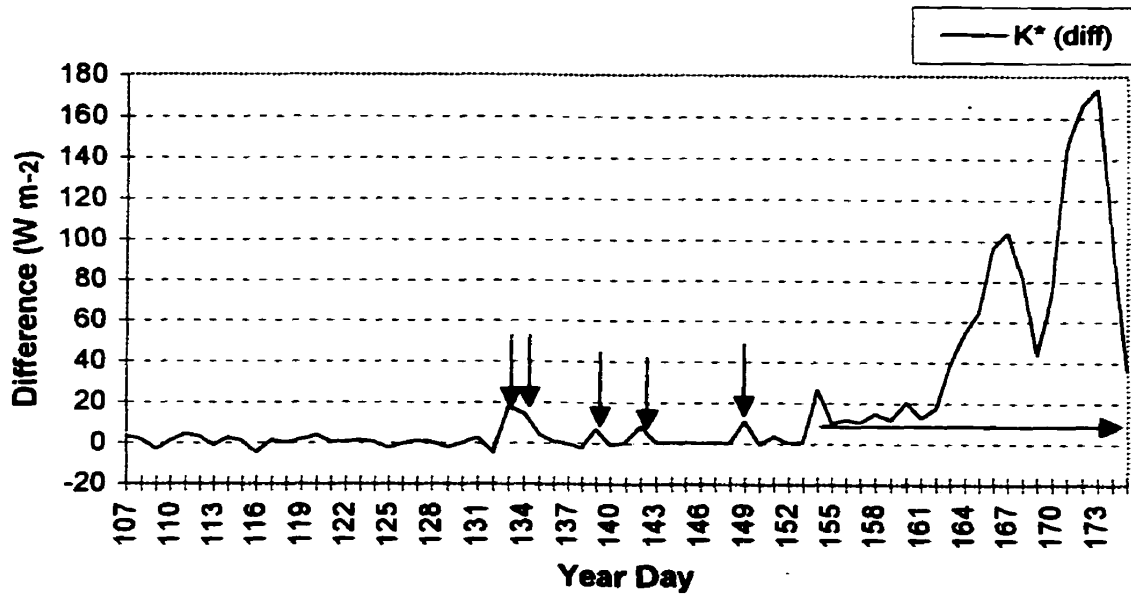
Figure 3.7: Time series of daily average K* difference (hourly model derived minus daily model) between YD107 (April 17) and YD175 (June 25), 1992. Positive difference: imply greater daily average K* in the hourly model. Arrows signify days with diurnal melt in the hourly model simulation.
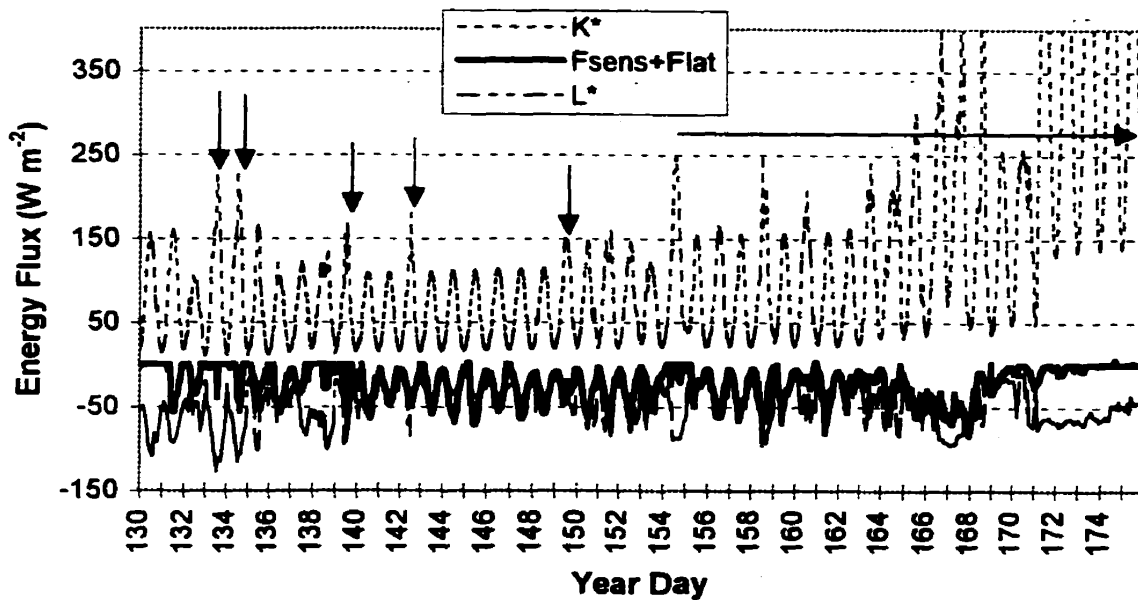
Figure 3.8: Time series of hourly forcing modeled surface energy balance between YD130 (May 11), 1992 to YD175 (June 25), 1992. Shown are the net short-wave flux (K*), net long-wave flux (L*) and the sum total of latent and sensible heat fluxes (Fsens + Flat). Units are in W m $^{-2}$. Positive values represent surface energy gain. Arrows indicate days with diurnal surface melt.

It is useful to quantify the combined effects of all processes above on the daily/hourly simulation differences (ie: TEST 3 and TEST 4 simultaneously). In producing an hourly simulation when combining TEST 3 and 4 (TEST 5), the BU date and open water duration become very similar to the original daily simulation (Table 3.1). TEST 5 therefore shows that the bulk of the daily/hourly simulation differences can be attributed to: 1) the diurnal distribution of $K\downarrow$ which acts to enhance snow melt events at peak to medium solar exposure hours; 2) the timing of very low latent/sensible heat loss that occurs during peak to medium solar exposure hours, further increasing the likelihood of a melt event; and most importantly 3) the timing of a melt event (during peak to medium solar exposure) which enhances the absorption of short-wave energy into the snow pack by reducing the surface albedo.

In further interest of model forcing, another model run was generated using forcing data by linearly interpolating the daily average values to hourly intervals which were then used to force the hourly simulations. This is typically done in modeling studies over larger time scales where monthly data may be interpolated to daily values for daily forcing or even shorter time steps (see for example, Maykut and Untersteiner (1971); Ebert and Curry (1993). The daily average incident short-wave radiation was also interpolated to hourly intervals, similar to the other meteorological forcing. In this case, the BU and open water duration dates were exactly midway (BU = YD196; open water duration = 99 days) between the standard hourly simulation and daily simulation. This is primarily due to the enhanced short-wave responses of the model that act on the snow layer over hourly time scales (as shown by TEST 3). This is illustrated further when the normal diurnal $K\downarrow$ distribution is used instead of the hourly interpolated daily average $K\downarrow$ forcing, where the simulated BU and open water duration becomes closer to the original hourly simulation (BU = YD192; open water duration = 103 days).

3.3.2 Parameterized vs. In Situ Radiative Fluxes and Albedo

In this section I compare parameterizations such as incident short-wave ($K\downarrow$) and long-wave ($L\downarrow$) radiation and surface albedo (α) used in the Flato and Brown (1996) model with *in situ* SIMMS'92/93 field data. The purpose is to assess whether the parameterizations used in the model adequately represent specific processes over shorter temporal scales and whether they accurately reflect 'on ice' measurements. This would then estimate the potential error in modeled ice and snow thermodynamics due to errors in forcing. It should be emphasized that differences between modeled and *in situ* data should be expected since the SIMMS'92/93 field sites were roughly 30 km from Resolute leading to differences in atmospheric forcing. In addition, some model parameterizations are intended to reflect area-averaged conditions and so may not represent the point conditions measured at the SIMMS field sites (eg. albedo). Unfortunately, no cloud observations were available during the SIMMS experiments, thus cloud variation comparisons (and the associated changes in $K\downarrow$ and $L\downarrow$) with Resolute were not possible. These factors create a rather crude comparison but can nevertheless illustrate the spatial and temporal scale characteristics between parameterized and *in situ* albedo/radiative fluxes.

As an example of atmospheric forcing differences between Resolute and the field sites, Figure 3.9 shows the time series of air temperature differences between Resolute and SIMMS'92 observations (Resolute - SIMMS). A mean bias of +0.5°C in Figure 3.9 indicates that land-based temperatures (Resolute) can be somewhat larger compared to on-ice conditions (SIMMS). Major differences occur during the morning hours (overnight lows) where land-based temperatures can be significantly warmer (~ 6-8°C) than over the ice.
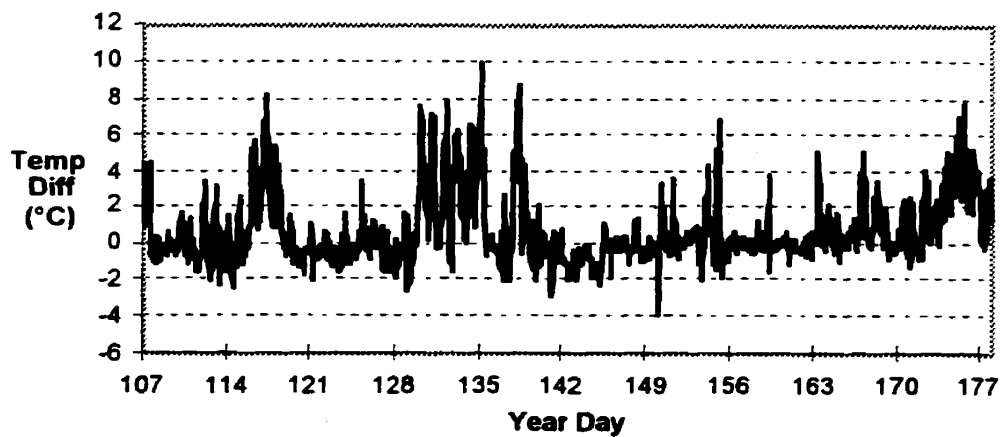
Figure 3.9: Time series of air temperature discrepancy (Resolute minus SIMMS) between Resolute and the SIMMS'92 field site between YD107 and YD177, 1992.

The hourly time series of K↓ and L↓ error (modeled - observed) over the spring period of 1992 are shown in Figures 3.10a-c. The K↓ error time series (in Figure 3.10a) only includes the first 9 days of the simulation/field experiment (for illustrative purposes) since it is difficult to visualize the entire time series. Low sun angle (< 25°) data were excluded from the analysis due to instrument limitations. The coefficient of determination between the modeled and observed K↓ was $R^2 = 0.91$ with the error varying between nearly zero and ± 250 W m^{-2} over the entire SIMMS'92 field period. The K↓ mean error was -23 W m^{-2} with a standard deviation of 89 W m^{-2}. The K↓ all sky mean error found here is larger than the mean error found by Key et al. (1996) (-3.2 W m^{-2} for the Shine (1984) scheme) who compared daily average observed and parameterized fluxes for two Arctic locations. Differences in local cloud conditions between the SIMMS field sites and Resolute may be a significant factor.
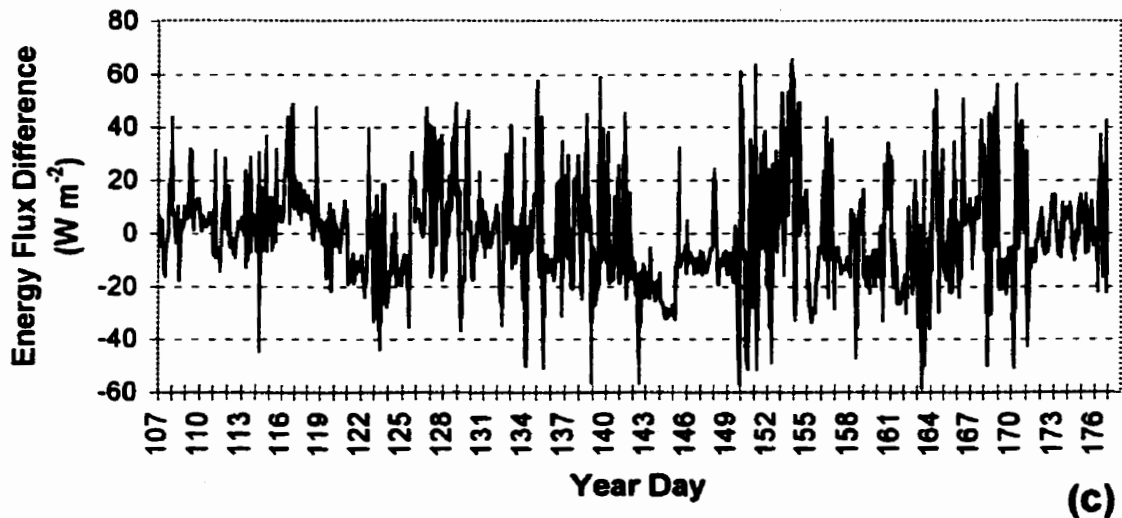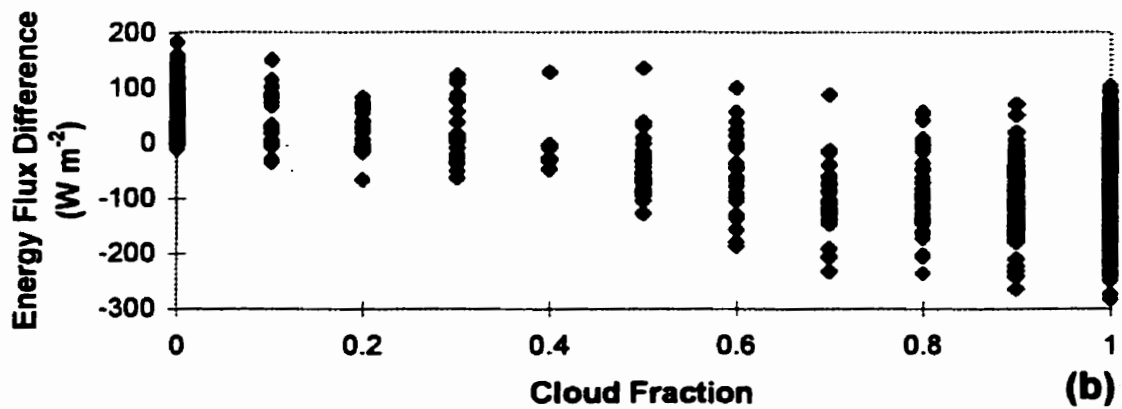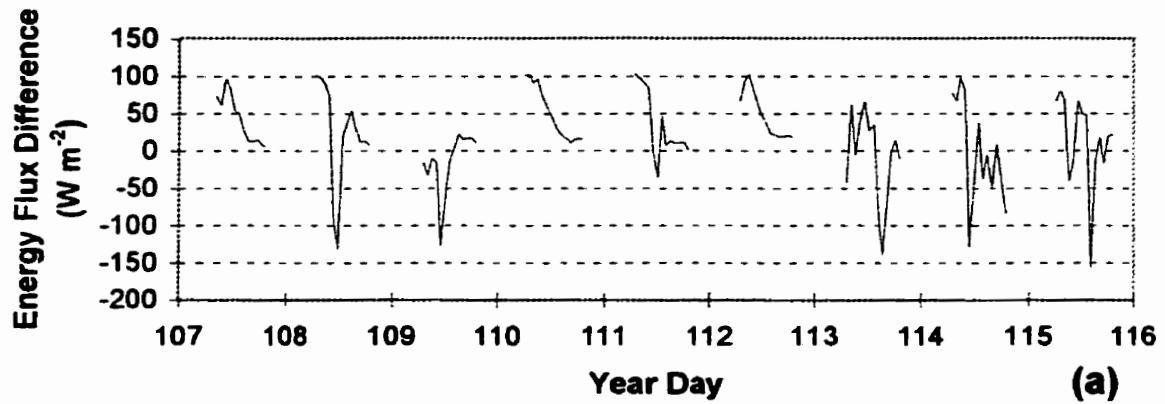
Figure 3.10: Modeled minus observed (a) incident short-wave error between YD107-116, 1992, (b) incident short-wave error versus total cloud fraction, and (c) incident long-wave error between YD107-177, 1992. Low sun angle (< 25°) data were excluded from the short-wave analysis due to measurement limitations.

The K↓ parameterization tended to overestimate clear sky K↓ by roughly 40-50 W m^{-2} on average and K↓ differences varied widely during complete overcast conditions (+125 W m^{-2} to -275 W m^{-2}). This can be visualized in Figure 3.10b where cloud-free conditions produced more positive biases (mean of +40 W m^{-2}) in K↓, and when complete overcast conditions occurred the discrepancy between modeled and observed values grew much larger with a more negative bias (-50 W m^{-2}). The main differences between modeled and observed K↓ is due to location/cloud differences between the SIMMS field sites and Resolute as well as cloud optical depth (held constant at 0.7) and tropospheric aerosol inhomogeneities pointed out by Key et al. (1996). Key et al. (1996) showed that the Shine (1984) clear sky and all sky K↓ parameterizations did not have sun angle biases but the all sky parameterizations had greater errors as the solar zenith angle (SZA) decreased. The 55-70° SZA errors for K↓ all sky point estimates were shown to range between ± 150 W m^{-2} (Key et al., 1996) which may be a significant contributor to the errors observed here. Larger discrepancies between modeled and observed K↓ values are expected to occur during total overcast situations due to the factors above, indicated in Figure 3.10b.

The time series of modeled-observed differences for L↓ (Figure 3.10c) are not as extreme as K↓ and no biases were found when comparing cloud-free conditions and total overcast conditions (not shown). However, the discrepancies in L↓ (modeled-observed) grew larger (+60 W m^{-2} to -40 W m^{-2}) during complete overcast events compared to clear skies (+20 W m^{-2} to -40 W m^{-2}) as expected due to similar factors as those for K↓. The mean L↓ error was -1 W m^{-2} with a standard deviation of 18.8 W m^{-2} and an R^2 = 0.91. The mean error found here is smaller than the all sky L↓ value (-9.7 W m^{-2}) reported by Key et al. (1996) for the same L↓ parameterization of Maykut and Church (1973).

The time series of surface albedo shows that the dry/new snow values used in the

model (0.75) are lower than observed (0.8-0.9) (Figure 3.11). The modeled albedo is intended to represent an area average that may differ from local conditions. Typical Arctic basin dry/new snow albedo observations have been shown to range between 0.8-0.98 (Radionov et al., 1997). The mean dry/new snow albedo for SIMMS'92 was 0.83 and 0.82 for SIMMS'93 (excluding the low sun angle data). The larger observed albedo compared to the modeled albedo may be significant since less short-wave radiation would be absorbed by the snow layer and may lead to less days with surface melt (see section 3.3.3).

In addition, there were several days when diurnal changes in albedo were observed during SIMMS'92/93 similar to what is portrayed in the model simulation. However, the model simulated more frequent diurnal melt events. Definite diurnal albedo patterns associated with snow surface freeze-thaw cycles were observed after YD168, 1992 where a mean albedo decrease of 0.07 ± 0.03 took place during snow melt events (Figure 3.12). Other Arctic observations indicate maximum diurnal albedo changes on the order of 0.11 (Radionov et al., 1997). The model assumes a 10% decline in albedo during snow surface melt over an area average. Observations suggest the associated drop in modeled albedo due to diurnal snow melt may be slightly excessive in most cases. This could also lead to enhanced snow melt and more frequent melt events in the model simulation. Further discussion will be provided in section 3.3.3.
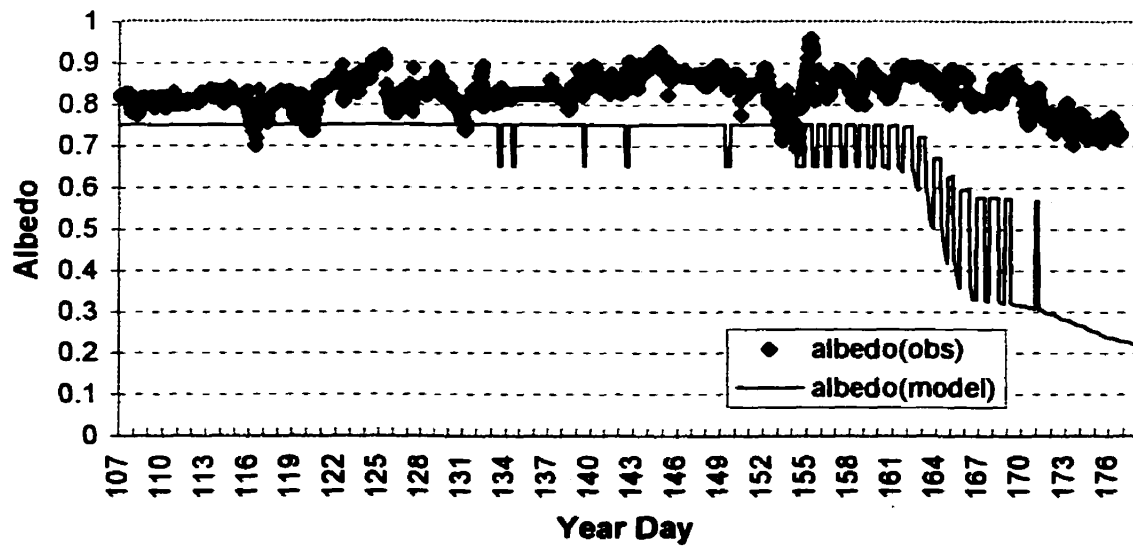
Figure 3.11: Time series of parameterized (solid line) and observed (*) surface albedo between YD107 and YD177, 1992.
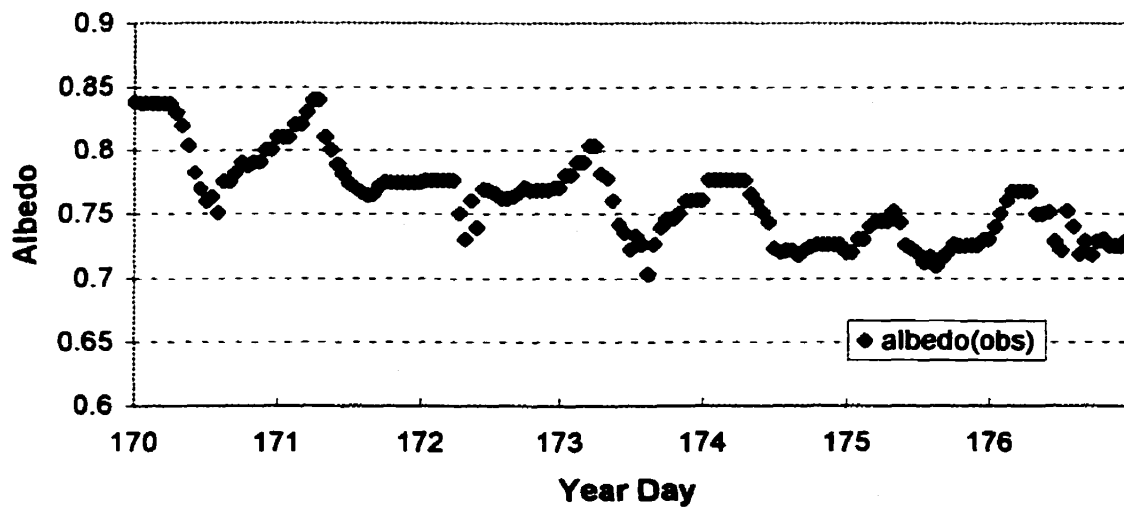
Figure 3.12: Diurnal time series of SIMMS'92 observed surface albedo between YD170-177.

3.3.3 Model Simulations Using Field Observation Forcing

The sea ice model was run with SIMMS'92 field data ($K\downarrow$, $L\downarrow$, T_a, wind speed and surface albedo) to investigate differences between using on-ice forcing as opposed to land-based forcing during the spring of 1992. The simulation was conducted for days 107-176, 1992 since full day field data did not exist beyond YD176. Direct comparisons of modeled surface temperatures (T_{sfc}), Q_{net} and snow/ice ablation rates were made between the standard hourly simulation (CONT) (section 3.3.1) and the SIMMS field data forcing simulation (SFS) over the 1992 spring period. Since relative humidity was not recorded at the SIMMS'92 field site, Resolute observations were used in the SFS simulation. The SIMMS'92 snow thickness measurements were not used to estimate actual snowfall amounts since it was impossible to exclude redistribution effects (blowing/drifting snow) from the data. Cloud fractions were not necessary since $K\downarrow$ and $L\downarrow$ field data were used instead of the $K\downarrow$ and $L\downarrow$ parameterizations. Resolute wind data was used between YD107-117 since usable SIMMS'92 wind speed data were only available beginning on YD118.
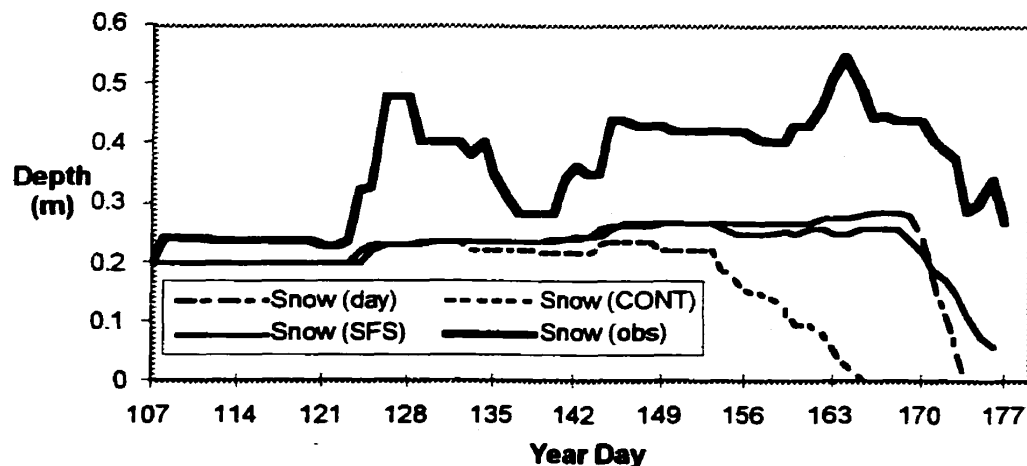
Figure 3.13: Comparison between observed (thick solid line), CONT (lower line), SFS (solid line), and daily forcing (dash-dot line) snow depth between YD107-177, 1992.

Using the SIMMS field data as forcing and replacement of the $K\downarrow$, $L\downarrow$ and albedo parameterizations produces very different spring period simulations compared to the control simulation (Figures 3.13 and 3.14). The snow layer does not disappear in the SFS run (minimum of 0.07 m on YD176) compared to complete ablation in CONT by YD165 (Figure 3.13). The SFS snow ablation is similar to the daily forcing model simulation but SFS has a much more realistic ablation curve compared to observations beyond YD165 (Figure 3.13). SIMMS researchers did not observe complete snow ablation and advanced melt (ponding) conditions in 1992 (p. comm, T. Papakyriakou). This suggests that the SFS simulation more accurately reproduced the regional conditions since complete snow ablation and advanced melt were not generated in the SFS run, whereas, CONT produced complete snow ablation and advanced ice melt stages.

The SFS run produced diurnal melt events similar to CONT, however, the onset of melt was much later (YD154 in SFS, YD133 in CONT) causing the number of melt events to be significantly reduced in the SFS simulation between YD107-177 (see Figure

3.13). Surface melt took place in the SFS simulation on YD154, 155, 160, 162, 163, and 168 onward. The later melt onset is most likely due to the overall increase in surface albedo (SFS mean $\alpha = 0.828 \pm 0.5$, CONT mean $\alpha = 0.63 \pm 0.1$) and wind speeds (SFS mean $u = 4.1 \pm 2.4$ m s^{-1}, CONT mean $u = 1.4 \pm 1.0$ m s^{-1}; the means were calculated between YD107-176, 1992). This suggests that the stronger winds in SFS compared to CONT play a significant role in the melt onset dates. It is interesting to note that the mean K$\downarrow$ and L$\downarrow$ for SFS (272.6 W m^{-2}, 232.4 W m^{-2}) and CONT (272.3 W m^{-2}, 231.4 W m^{-2}) were very similar but the SFS standard deviations (σ(K$\downarrow$) = 195.2 W m^{-2}, σ(L$\downarrow$) = 45.3 W m^{-2}) were slightly larger than CONT (σ(K$\downarrow$) = 176.4 W m^{-2}, σ(L$\downarrow$) = 38.3 W m^{-2}). This may indicate that although the mean radiative forcing was similar for both simulations, the different variations in radiative forcing may account for some of the differences between the simulations. Differences in air temperature between SFS and CONT is expected to have a minor influence on the snow layer simulation since T_a was quite similar in both simulations (SFS T_a mean = -11.7 $\pm$ 8.3°C, CONT T_a mean = -12.0 $\pm$ 8.4°C).
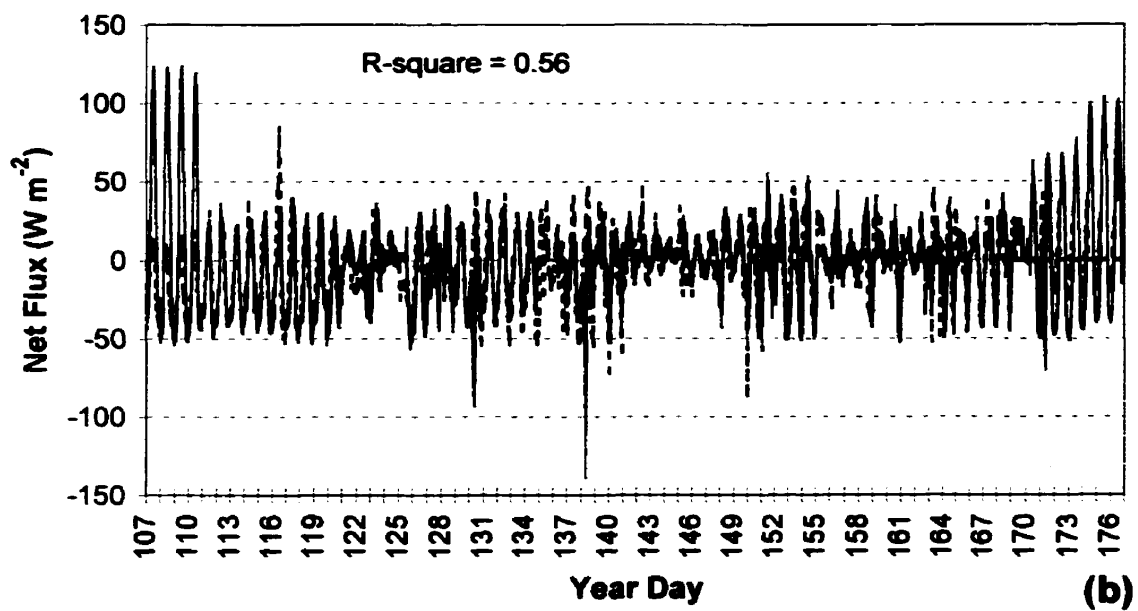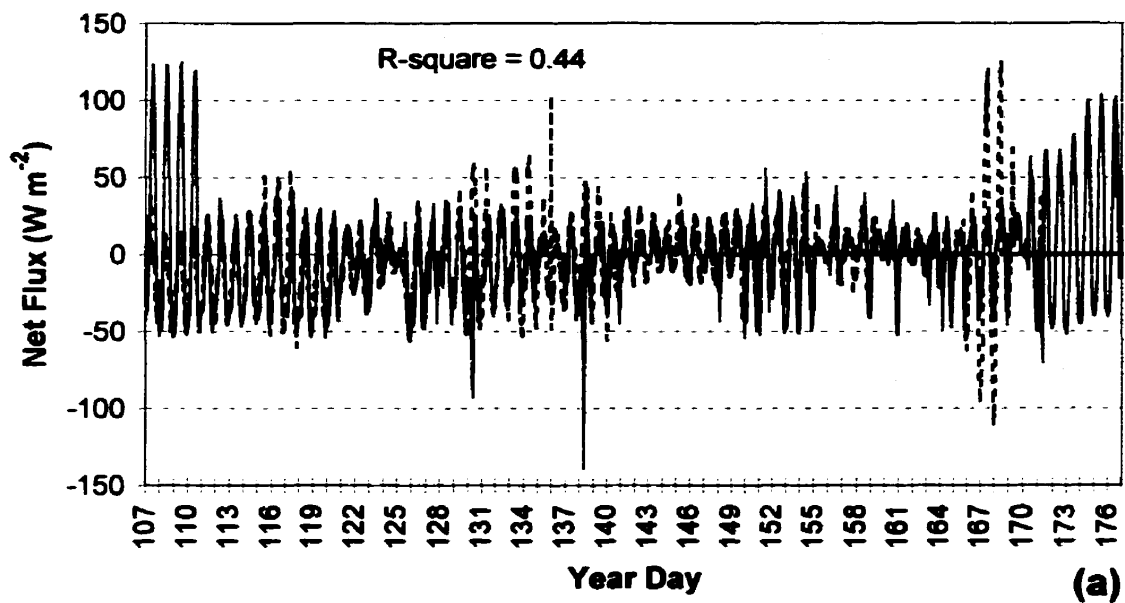
Figure 3.14a,b: Comparisons of Qnet between (a) CONT (black line) and SIMMS'92 observations (red line), (b) SFS (black line) and SIMMS'92 observations (red line).
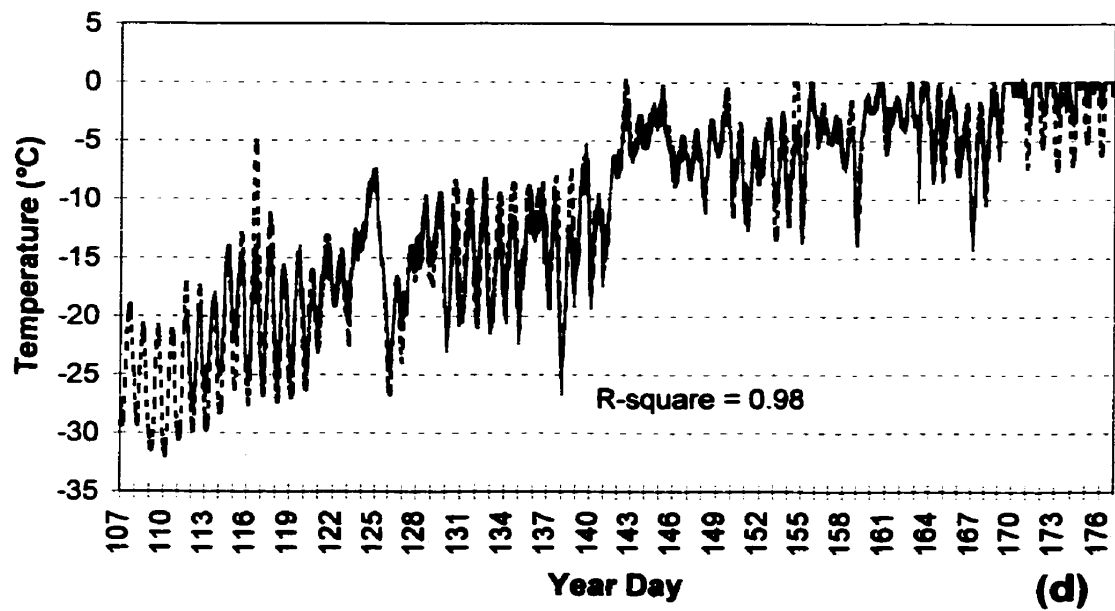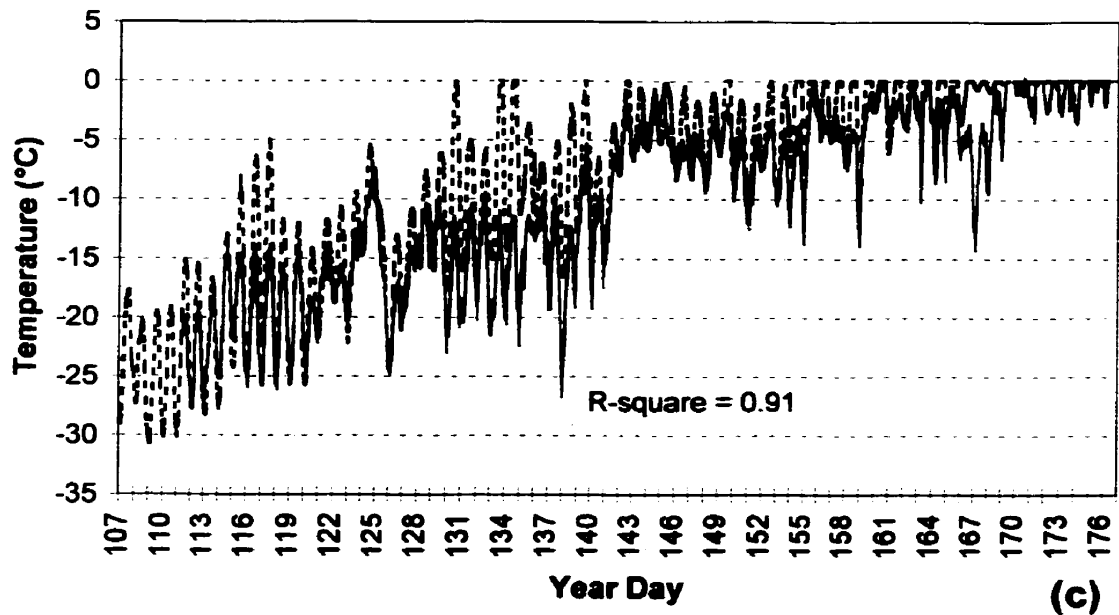
Figure 3.14c,d: Comparisons of Tsfc between (c) CONT (black line) and SIMMS'92 observations (red line), (d) SFS (black line) and SIMMS'92 observations (red line).

The SFS simulation produced improved estimates of Q_{net} and T_{sfc} compared to CONT, determined by direct comparison with SIMMS'92 measured values (Figure 3.14a-d). The Q_{net} R^2 for SFS is larger than the CONT simulation and the Q_{net} mean error (modeled-observed) and standard deviation (error) for SFS was slightly smaller than the CONT simulation (Table 3.2). YD107-110 were excluded from the statistics due to Q_{net} measurement errors on those days.

Table 3.2: Statistical comparisons (R^2, mean error (modeled - observed) and standard deviations) between the modeled (CONT and SFS) and observed net surface flux (Q_{net}) and surface temperatures (T_{sfc}). CONT is the standard hourly model simulation using 'land-based' forcing (from Section 3.3.1) and SFS is the 'on-ice' forcing simulation using SIMMS'92 field data.

	Qnet CONT/obs	Qnet SFS/obs	Tsfc CONT/obs	Tsfc SFS/obs
R-Square	0.44	0.56	0.91	0.98
Mean Error	-2.5	-2	2.5	-0.08
St. Dev.	30	25	3.1	1.7

The improvement in simulation using the field observations compared to using Resolute forcing and model $K\downarrow$, $L\downarrow$ and albedo parameterizations is also manifested when comparing the SFS and CONT T_{sfc} time series (Figure 3.14c,d). T_{sfc} was estimated using the measured $L\uparrow$ with an emissivity of 0.99 (similar to the model prescribed value) since direct measurements of surface temperatures were not available. The T_{sfc} R^2 for SFS is noticeably larger than the CONT simulation and the T_{sfc} mean error (modeled-observed) and standard deviation (error) for SFS was significantly smaller than the CONT simulation (Table 3.2). YD107-110 were excluded from the statistics due to unavailable $L\uparrow$ measurements on those days. The SFS simulation reproduced all of the days that had diurnal melting in the observations (Figure 3.14d). Observed $L\uparrow$ fluxes indicated that surface melt may have occurred on YD155, 160, 162, 163 and 169 onward. The SFS

simulation produced diurnal melt on all of these days as well as YD154 and 168. It is not known why there is discrepancy on these days. The statistics and Figures 3.14c,d suggest that the SFS simulation provides a better representation of the measured T_{sfc} than CONT over the spring of 1992.

3.4 Conclusions

The purpose of this chapter is to illustrate whether diurnal time scales are important to consider in modeling seasonal snow-covered FYI and whether the model parameterizations appropriately handle these time scales. This is important not only for resolving these time scales and processes in the models for arctic climate studies, but for advancing the model to a state that will be useful for microwave remote sensing applications. This chapter was also concerned with spatial differences inherent in the model environment through its forcing data. Typically, sea ice models use "land-based" forcing data to drive the simulations, however, difficulties may arise due to differences between "on-ice" meteorological conditions and "land-based" conditions. Three research questions were designed to address the above issues.

3.4.1 Question 1

Direct comparisons between a one-dimensional thermodynamic sea ice model using hourly forcing data and daily average forcing data showed significantly different results in terms of break-up dates, open water duration and snow ablation. Break-up occurred 13 days sooner, open water duration was lengthened by 21 days and snow ablation was initiated sooner but progressed gradually and more realistically (compared to

field observations) using hourly forcing. However, the hourly simulation produced much earlier melt onset and created advanced melt stages in 1992 which were not observed by SIMMS'92 researchers. Sensitivity tests showed that 12 of the 13 break-up day and 18 of the 20 open water day differences between the daily/hourly simulations is due to snow cover evolution differences within the simulations. Analysis has showed that short-wave exchange dominates these snow processes, as observed in the field. The diurnal distribution of down-welling short-wave energy is responsible for about 33% of the snow cover evolution (and hence the daily/hourly simulation) differences by acting to enhance snow melt events at peak to medium solar exposure hours. The diurnal variations in latent/sensible heat fluxes (mostly due to wind speeds) can explain about 17% of the daily/hourly model differences where some days have very low latent/sensible heat loss during peak to medium solar loading hours. The timing of these low latent/sensible heat loss events create a greater likelihood of a melt event to take place. In contrast, the daily average wind speed is rarely zero, thus reducing the likelihood of melt for that day. The dominant process, which leads to 50% of the snow cover evolution differences, is enhanced diurnal short-wave absorption due to albedo decreases during diurnal melt events occurring at peak to medium solar exposure hours (ie: a positive albedo feedback). It can therefore be concluded that non-linearities in the surface energy balance play a critical role in the melting of the snow layer which in turn affect the seasonal evolution (especially the spring melt period) of first-year sea ice.

3.4.2 Question 2

Comparisons between observed and model-parameterized $K\downarrow$, $L\downarrow$ and albedo showed the model parameterizations represented observations fairly well in some cases

and not so well in others. The Shine (1984) parameterization for $K\downarrow$ had a positive error of roughly 40 W m^{-2} on average during clear conditions and a slight negative bias of -50 W m^{-2} under complete overcast conditions. The mean $K\downarrow$ error (modeled-observed) was -23 W m^{-2} with a standard deviation of 89 W m^{-2} over the SIMMS'92/93 field seasons. The mean error here is larger than that reported by Key et al. (1996) (-3.2 W m^{-2}). Larger $K\downarrow$ discrepancies occurred under cloudy conditions compared to clear skies due to differences between SIMMS field sites and Resolute, NWT, (spatial/location limitations) as well as cloud optical depth (held constant in the model) and tropospheric aerosol inhomogeneities (Key et al., 1996). Errors can also be largely attributable to solar zenith angle variations as suggested by Key et al., 1996.

The $L\downarrow$ parameterization of Maykut and Church (1973) had smaller errors and no trends were found when comparing cloud-free conditions to clear skies. The mean $L\downarrow$ error was -1 W m^{-2} with a standard deviation of 18.8 W m^{-2}. The mean error is smaller than that of Key et al. (1996) (-9.7 W m^{-2}) and shows this $L\downarrow$ parameterization performs well even at hourly intervals. However, the low $L\downarrow$ mean error and standard deviation may be the result of a cancellation of errors due to cloud amount bias between Resolute and the SIMMS field site (spatial limitations).

The time series of modeled and observed surface albedo showed that the model may underestimate the dry/new snow albedo by roughly 0.05 to 0.15. The sea ice model assumes a dry/new snow albedo of 0.75 but regionally representative SIMMS'92/93 albedos were between 0.8-0.9 in the early spring periods. The modeled albedo decrease for wet snow (0.1) was slightly higher than observed (0.07 $\pm$ 0.03) and so the model's snow melt albedo feedback may be slightly too strong.

3.4.3 Question 3

When the sea ice model was forced directly with SIMMS'92 field data ($K\downarrow$, $L\downarrow$, air temperature, wind speed and albedo) it produced better representations of the modeled snow/ice ablation evolution as well as Q_{net} and surface temperature over the 1992 spring period. This case reproduced observed diurnal melt periods faithfully whereas the control run produced many more and earlier melt events. Also, complete snow ablation and advanced melt were not generated in this case, in agreement with observations. The overall improvement when forced with SIMMS observations was primarily due to greater turbulent fluxes (larger wind speeds), higher surface albedo and different radiative forcing compared to using land-based forcing (Resolute) and modeled $K\downarrow$, $L\downarrow$ and albedo parameterizations. I also note, based on eight (1990- 1997) consecutive years of the SIMMS and follow on C-ICE (Collaborative-Interdisciplinary Cryospheric Experiment) experiments that the differences between surface energy fluxes observed on-ice and those estimated from nearby land stations do not appear to be systematic. This means that it may be difficult to establish a correction term to account for various flux terms required in thermodynamic modeling of sea ice.

3.5 Summary

In summary, results suggest diurnal processes are important to consider and the parameterizations handle these time scales well in some cases and not so well in others.

This is an important step toward understanding the necessary model forcing time scales required for linking these types of models to microwave remote sensing in later chapters. The results also illustrate the time scales necessary to resolve when attempting to simulate annual cycles of snow-covered FYI. It is also important to consider the environmental conditions on the ice surface as opposed to land for monitoring sea ice evolution. That is, if *in situ* data are not available on the ice, remote observations from satellites may provide insight to environmental conditions there. The following chapter (Chapter 4) further investigates and supplements the analysis in this chapter in terms of the incident short-wave and long-wave model parameterizations. Incident radiation is a critical process within the SEB of FYI and a more thorough analysis of their parameterization schemes is warranted given the results thus far.

CHAPTER 4: Parameterization Schemes of Incident Radiation

4.1 Introduction

Thermodynamic sea ice models require precise parameterization of incident short-wave and long-wave fluxes over a variety of time and space scales as illustrated in Chapter 3. Chapters 1 and 2 outlined previous investigations of these fluxes, difficulties while trying to parameterize them and their importance to the snow/sea ice SEB. This chapter builds on results in chapter 3 by investigating in more detail sea ice model parameterization schemes of incident radiation. Coincident *in situ* radiation data comparing different arctic environments and spatial variations have previously never been available. Data presented here were collected in a marine polynya environment including terrestrial, shore fast-ice, marginal ice zone and open water regions during the International North Water Polynya (NOW) Project conducted between March – July 1998 (Barber et al., 2001). The two research question of this chapter are:

1) Are there any seasonal or environmental/spatial biases within selected $K\downarrow$ and $L\downarrow$ parameterizations compared against *in situ* field measurements?

2) Can we improve the parameterization representations for the different environments where possible?

Results from this investigation have previously appeared in the peer reviewed literature (Hanesiak et al., 2001a).

4.2 Data and Methods

4.2.1 Observational Data

Data collected were from the International North Water Polynya (NOW) Project during an intensive field campaign between March to the end of July 1998 (Barber et al., 2001). Three primary data collection platforms included a terrestrial camp (Cape Herschel) and fast-ice site (Rosse Bay) on the east coast of Ellesmere Island, Nunavut and the Canadian Coast Guard ice breaker Pierre Radisson in the NOW region (Figure 4.1).
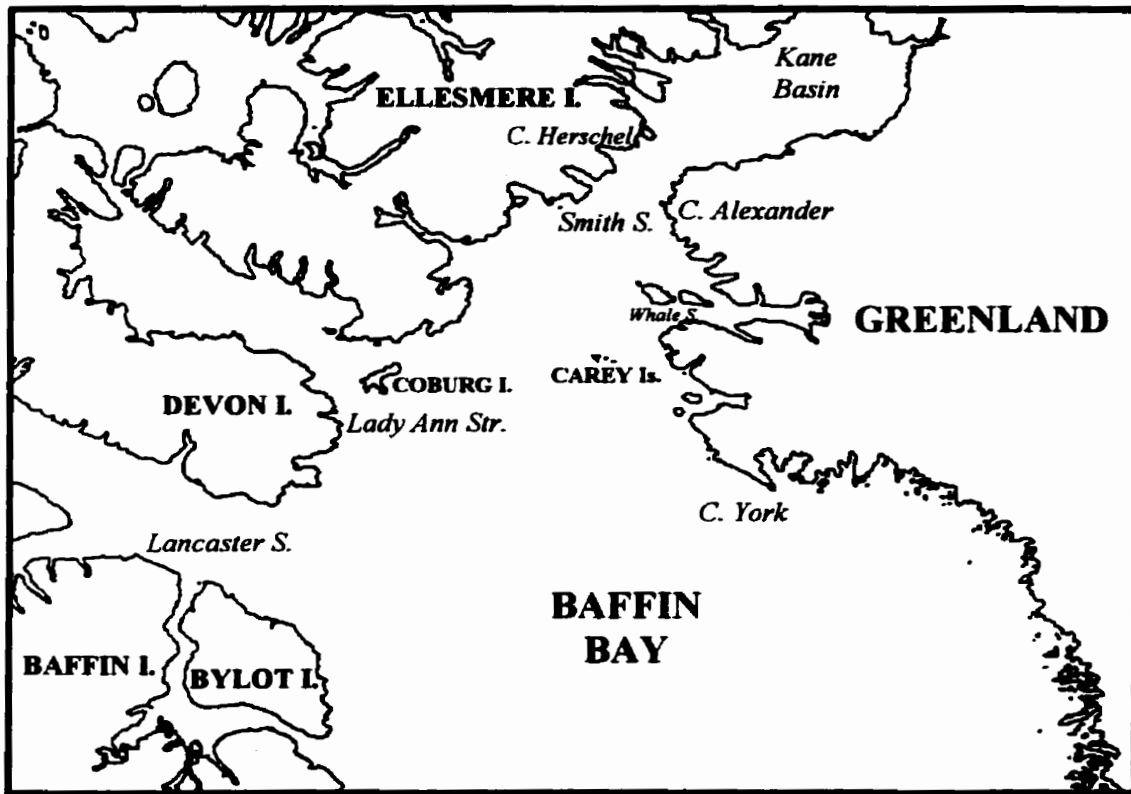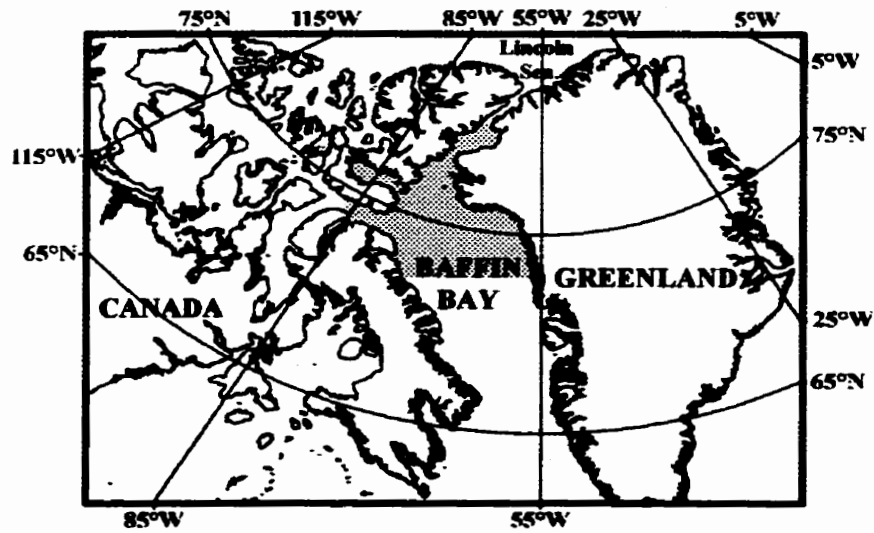
Figure 4.1a: Geographical region of the NOW '98 project (shaded region in top image). Smith Sound, Kane Basin and Cape Herschel appear at the north end of NOW (bottom image).
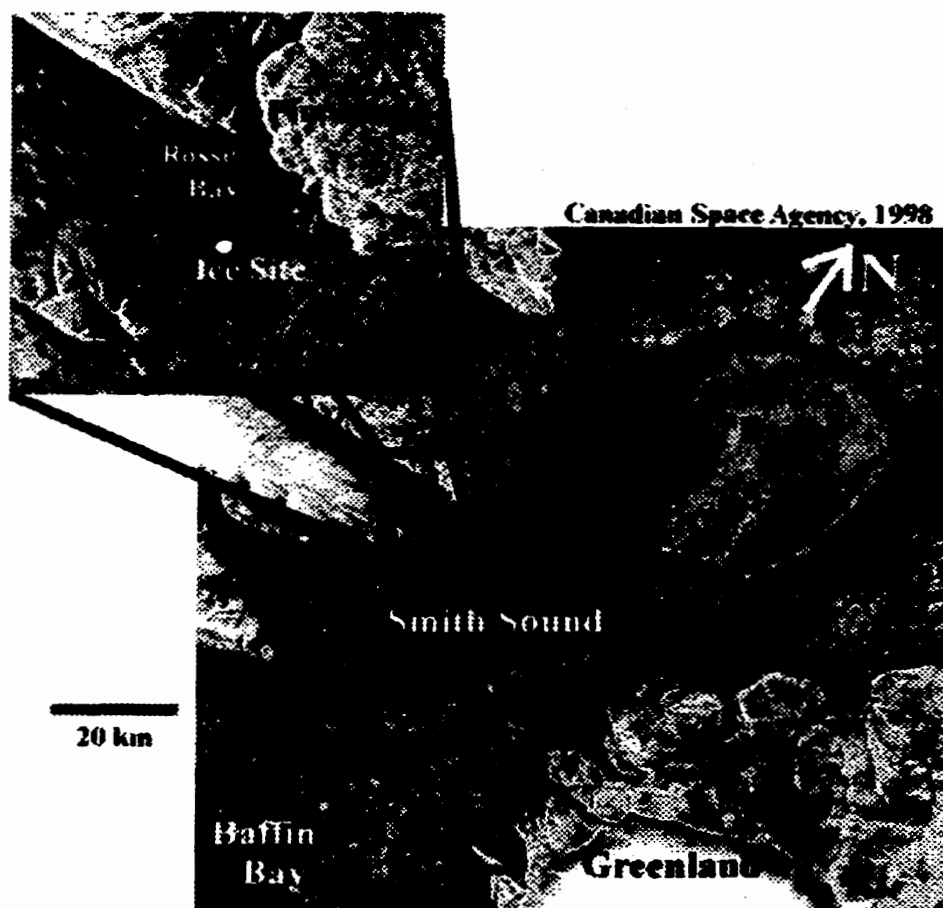
Figure 4.1b: Locations of the terrestrial camp (Cape Herschel) and ice site in Rosse Bay during the NOW'98 project. The image is a synthetic aperture radar (SAR) image from Radarsat-1. Dark shades represent smooth first-year ice in Rosse Bay and open water mixed with ice in Smith Sound and Kane Basin.

Cape Herschel is located 74.67° W, 78.65° N and the fast-ice site was 3.5 km due north of the terrestrial camp. The fast-ice regime was typified by smooth first year sea ice (Figure 4.1b; dark shades in Rosse Bay) with a snow cover ranging between 5 and 15 cm up to complete snow melt by early June. The terrestrial site was 100 m AMSL, with a full snow cover and gradual sloping terrain toward Rosse Bay. The fast-ice edge at Cape Herschel was initially 3-4 km off shore and decreased to less than 1 km by early June. Measurements of $K\downarrow$ and $L\downarrow$ were available from instruments that were mounted on the foredeck of the Canadian Coast Guard ice-breaker, *Pierre Radisson* from transects within NOW (Figure 4.2). Radiation flux densities were measured over several ice types and under a variety of atmospheric conditions. Data were measured every second and stored as one-minute averages. The terrestrial and ice camps were operational between Year-Day (YD) 89 (March 30) and YD155 (June 4) and the ice-breaker between approximately YD99 (April 9) to YD203 (July 22). This resulted in 601 h and 822 h of useful terrestrial site $K\downarrow$ and $L\downarrow$ data, respectively, 635 h and 915 h at the fast-ice site and 659 h and 988 h on the ice-breaker. There were less short-wave hours due to night-time darkness in the early spring and data quality control (see below).
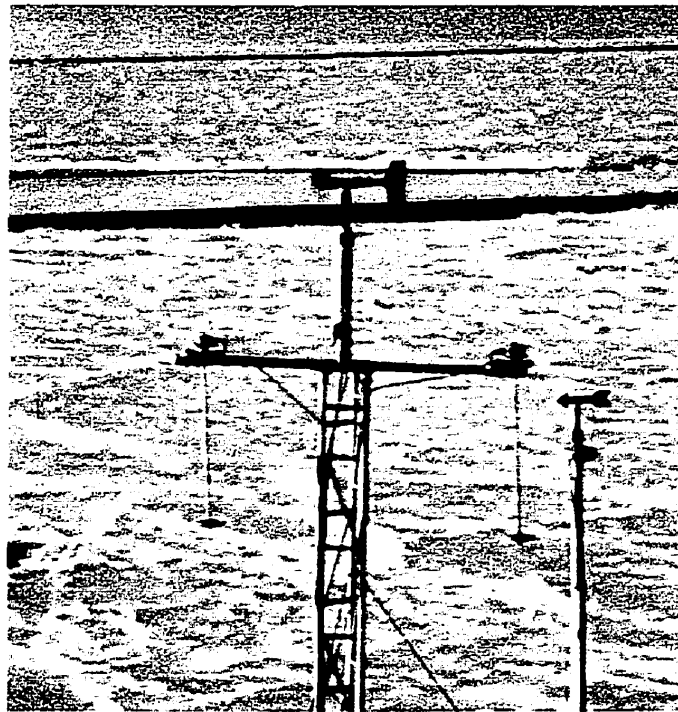
Figure 4.2: Incident radiation instrumentation on the ice breaker Pierre Radisson (top picture) and the fast-ice site near Cape Herschel (centre right in the bottom picture). Both photos were taken looking in a northerly direction.

114

Incident short-wave and long-wave radiation were sampled every 5 s by an Eppley pyranometer (model PSP) and pyrgeometer (model PIR) which was installed at both the Cape Herschell and Rosse Bay sites (Figure 4.2). The radiometers were mounted 1.2 m above the surface and recorded 15-minute radiation averages. Incident short-wave and long-wave radiation were measured using Eppley 8-48 "Black and White" Pyranometers on the ice-breaker, and pyrgeometers (model PIR) mounted on gimbles 6 m above the ship deck to ensure proper leveling in the mean. Measurement accuracy is estimated at ± 10 W m^{-2} and $\pm 2.5\%$ for the pyrgeometers (Philipona et al., 1995) and pyranometers (Latimer, 1978), respectively. The spectral response of the PSP and 8-48 pyranometers are determined by the glass dome over the sensors, which has uniform transmission for radiation in the wavelength range 0.285 to 2.8 μm. The spectral response of the PIR, determined by an interference filter inside a silicon dome, is from 3.5 to 50μm. A down-facing pyranometer (Eppley, model PSP) was installed off of a scaffold-type tower 2.55 m above the fast ice surface along with a down-facing pyranometer (Eppley 8-48) extending 3 m out from the bow of the *Pierre Radisson* to sample K↑. These radiation instruments are designed to measure the critical wavelengths of the solar and infra-red spectrums that control radiative fluxes. Supplementary hourly data included air temperature (T_a) (error approximately $\pm 0.1°$C), relative humidity (RH) (error $\pm$ 5%), total cloud fraction (c) (error $\pm$ 10%), and surface albedo ($\pm$ 0.03 albedo units) used as input for the radiative flux parameterizations (discussed below). The T_a and RH were measured 2 m above the surface at Cape Herschel using a relative humidity probe (CSI

207F) and 15 m above the water line of the ship. Surface albedo was estimated as the ratio of $K\uparrow$ to $K\downarrow$ at the Rosse Bay site and from the *Pierre Radisson*. Short-wave albedo estimates were continuous and stable at Rosse Bay, but intermittent on the ice-breaker due to rime build-up on the sensor. Total cloud fractions were determined from human hourly observations at the terrestrial/fast-ice sites and an all-sky time lapse video camera on the ship. The all-sky camera instrument is an all-weather camera looking downward on a hemispheric mirror that produced a 180° view of the celestial dome. Hourly averages of total cloud fraction were determined from analyses of the video images sub-sampled at 10-minute intervals. A discussion of the cloud conditions is provided by Hanafin and Minnett (2001). Incident radiation was measured over a temperature range between –30°C and +3°C from late winter to early summer at the terrestrial and fast-ice sites and –8°C to +12°C on the ice-breaker. As a result, there was little overlap of temperature and vapor pressure between the fast-ice and ice breaker measurements (i.e. the two environmental regimes were quite different).

Data were stratified into clear-sky (0 to 1 tenth coverage) and all-sky (2-10 tenths coverage) conditions, solar zenith angle (Z), and location (terrestrial, fast-ice, ice breaker). Seasonal variations according to air temperature were also investigated for parameterization seasonal biases. Clear-sky data were combined into 0 to 1 tenth sky cover since there was no difference between the mean short-wave and long-wave radiative fluxes associated with them. This resulted from hourly averaging and the short time the solar disk was obscured by cumulus clouds. The Z is used as an independent variable since some parameterizations have shown to contain Z biases (Key et al. 1996). In

116

addition, all $K\downarrow$ data with a $Z > 75°$ were omitted due to measurement error at these angles, especially albedo ($K\uparrow$ fluxes). Location stratification was performed for parameterization performance between the terrestrial, fast-ice and full marine environments. The fast-ice and terrestrial data sets are more accurate due to their stable measurement platforms and less prone to the harsh marine environment; they show smaller errors between the observed and estimated fluxes (see below).

4.2.2 Radiative Flux Parameterizations

Key et. al. (1996) discussed several simple $K\downarrow$ and $L\downarrow$ schemes that performed well in the Arctic that are still used in one-dimensional thermodynamic sea ice models and two-dimensional dynamic-thermodynamic models (see for example, Flato and Brown, 1996; Maslanik et al., 1995; Ebert and Curry, 1993). Only those parameterizations that were selected to outperform others (by Key et al.) were used in this work. The $K\downarrow$ parameterizations used include Bennett (1982) and Shine (1984) for clear skies and Jacobs (1978) and Shine (1984) for cloudy skies. The $L\downarrow$ parameterizations include Ohmura (1981), Efimova (1961) and Maykut and Church (1973) for clear skies and Jacobs (1978) and Maykut and Church (1973) for cloudy skies. The schemes are attractive for sea ice modeling due to their simplicity and computational ease and perform fairly well over daily and hourly averages in most cases (Key et al., 1996; Hanesiak et al., 1999). However, their performance can be affected by observational errors in input parameters

and unknown total column atmospheric conditions. I refrain from detailed discussions of the various parameterizations in light of Key et al.'s comprehensive review, and simply outline their empirical formulations.

The parameterizations have been categorized into clear sky and all-sky fluxes with similar conventions as Key et al. (1996), for consistency. The down-welling short-wave flux ($K\downarrow$), down-welling long-wave flux ($L\downarrow$) and solar constant ($S = 1356$) are in W m^{-2}; solar zenith angle (termed Z above) in degrees, near surface air temperature (T_a) in Kelvin, near surface vapor pressure (ea) in hPa, cloud fraction (c in tenths), cloud optical depth (τ), and surface albedo (α). A more detailed discussion of each parameterization can be found in Key et al., (1996). A brief description of each parameterization is outlined.

4.2.2.1 Short-Wave Clear Sky Flux

Key et al. (1996) indicated that the best clear sky $K\downarrow$ ($K\downarrow_{clr}$) parameterization in their study was that of Shine (1984) with Bennett (1982) performing reasonably well over daily averages. The Shine (1984) parameterization attempts to account for the near surface vapor pressure explicitly and was tested with a radiative transfer model. In comparison the scheme of Bennett (1982) is less comprehensive and is primarily intended for the estimation of mean monthly values.

The form of Bennett (1982) for $K\downarrow_{clr}$ is

$$K\downarrow_{clr} = 0.72 \, S \, \cos(Z) \qquad (4.1)$$

118

The form of Shine (1984) for $K\downarrow_{clr}$ is

$$K\downarrow_{clr} = (S\ cos^2(Z)) / [1.2\ cos(Z) + (1.0 + cos(Z))x10^{-3}\ ea + 0.0455] \quad (4.2)$$

4.2.2.2 Short-Wave All-Sky Flux

To parameterize cloud effects on the all-sky $K\downarrow$ flux, two approaches were found to perform reasonably well. One is to simply multiply the clear sky flux by a function of cloud fraction as in Jacobs (1978). Another more sophisticated approach is to account for surface changes (or albedo changes) affecting multiple reflections between the surface and cloud as well as cloud properties (or optical depth/thickness) as in Shine (1984) that performs well over shorter time periods (Key et al., 1996). I assume a constant cloud optical thickness (7.0) according to Ebert and Curry (1993) and input the computed hourly surface albedo from the Rosse Bay and ice-breaker platforms.

The form of Jacobs (1978) under all-sky conditions is

$$K\downarrow_{all} = K\downarrow_{clr}\ (1 - 0.33\ c) \quad (4.3)$$

The form of Shine (1984) under all-sky conditions is

$$K\downarrow_{cld} = (53.5 + 1274.5\ cos(Z))\ cos^{0.5}(Z) / [1 + 0.139\ (1 - 0.9345\ \alpha)\tau \quad (4.4a)$$

$$K\downarrow_{all} = (1 - c)\ K\downarrow_{clr} + c\ K\downarrow_{cld} \quad (4.4b)$$

119

4.2.2.3 Long-Wave Clear Sky Flux

Down-welling clear-sky long-wave radiation $(L\downarrow_{clr})$ is typically a function of near surface temperature and vapor pressure. Three commonly used parameterizations differ in their treatment of the atmospheric emittance. Ohmura (1981) considers the atmospheric emittance as a function of near surface air temperature. Maykut and Church (1973), on the other hand, assign a constant value to the atmosphere emittance, and Efimova (1961) make the term a function of near surface vapor pressure.

The form of Ohmura (1981) for $L\downarrow_{clr}$ is

$$L\downarrow_{clr} = \sigma\, (8.733\text{x}10^{-3}\, T_a^{0.788})\, T_a^4 \qquad (4.5)$$

The form of Maykut and Church (1973) for $L\downarrow_{clr}$ is

$$L\downarrow_{clr} = 0.7855\, \sigma\, T_a^4 \qquad (4.6)$$

The form of Efimova (1961) for $L\downarrow_{clr}$ is

$$L\downarrow_{clr} = \sigma\, (0.746 + 0.0066\, ea)\, T_a^4 \qquad (4.7)$$

4.2.2.4 Long-Wave All Sky Flux

An increase in $L\downarrow$ associated with clouds is a function of cloud fraction in expressions by Jacobs (1978) and Maykut and Church (1973). Jacobs (1978) developed a simple linear relationship between cloud emittance, cloud fraction and the clear-sky flux,

while the relationship of Maykut and Church (1973) is in power form. Cloud emissivity also differs between the two formulations.

The form of Jacobs (1978) $L\downarrow_{all}$ is

$$L\downarrow_{all} = L\downarrow_{clr} (1 + 0.26\ c) \tag{4.8}$$

The form of Maykut and Church (1973) $L\downarrow_{all}$ is

$$L\downarrow_{all} = L\downarrow_{clr} (1 + 0.22\ c^{2.75}) \tag{4.9}$$

4.2.3 Analysis Methods

The $K\downarrow_{clr}$ and $L\downarrow_{clr}$ schemes were individually tested. The all-sky $K\downarrow$ and $L\downarrow$ parameterizations require a clear-sky component, hence different combinations of the various schemes were performed. The $K\downarrow$ all-sky combinations included using: 1) the clear-sky of Shine with the cloudy sky correction of Shine, 2) the clear-sky of Bennett with the cloudy sky correction of Jacobs, 3) the clear-sky of Shine with the cloudy sky correction of Jacobs, and 4) the clear-sky of Bennett with the cloudy sky correction of Shine. The $L\downarrow$ all-sky combinations included using: 1) the clear-sky of MC with the cloudy sky correction of MC, 2) the clear-sky of Ohmura with the cloudy sky correction of Jacobs, 3) the clear-sky of Efimova with the cloudy sky correction of Jacobs, 4) the clear-sky of MC with the cloudy sky correction of Jacobs, and 5) the clear-sky of Efimova with the cloudy sky correction of MC.

The radiation and meteorological data were converted to hourly averages (centred on the hour). The meteorological data from each observing platform was used as input for

the parameterizations. The difference between the modeled and observed flux (difference parameter) was used to measure the performance of each scheme. Performance was quantified using statistical indices on the difference parameter such as simple linear regression tests for biases, mean bias error (MBE) and the root-mean-square error RMSE. The linear slope of regression lines fit along the difference parameter were statistically tested with an associated confidence interval to infer significant biases (slope significantly different from the mean) as functions of solar zenith angle (Z), season and the type of environment. Residual plots revealed that a linear model is appropriate for each regression line along the difference parameter.

For the seasonal bias analysis, the observed and estimated radiation were stratified into temperature regimes. The measured and estimated fluxes were binned according to the following temperature categories: (1) $T_a \leq -20°C$, (2) $-20°C < T_a \leq -14°C$, (3) $-14°C < T_a \leq -9°C$, (4) $-9°C < T_a \leq -2°C$, and (5) $T_a > -2°C$. The categories correspond to the main "seasonal" transitory atmospheric and sea ice conditions for the NOW region (Hanesiak, 1999) and allowing enough statistically viable data points for the comparisons in each temperature regime. The results of this analysis illustrates the seasonal bias inherent in the parameterizations and does not necessarily suggest that one scheme is superior since the simulated fluxes were within measurement errors in some cases.

4.3. Results

4.3.1 Parameterizations vs. Observations

4.3.1.1 Terrestrial and Fast-Ice Sites

The results from the analysis using data from the terrestrial and fast ice site were similar (generally within 2%). Consequently the following sections describes the performance of the models from the fast-ice site.

4.3.1.1.1 Incident Short-wave Fluxes

The results are in agreement with Key et al., (1996) showing that the Shine scheme is preferable to Bennett's equation (Figure 4.3 and Table 4.1). The Bennett scheme contains a negative Z bias with decreasing Z (Figure 4.3) within a 99% confidence interval. The Shine scheme performs well for the fast-ice data set with only 1.1 W m^{-2} mean error (5.0 W m^{-2} at the terrestrial site). The parameterization statistics in Table 4.1 are slightly better than Key et al. (1996). The cancellation of errors between negative and positive values may contribute to the low mean errors.

Table 4.1: Parameterized clear-sky short-wave flux error (estimated flux minus the measured fast-ice flux). Bracketed values are the corresponding ice-breaker results. The mean, mean error and RMSE are in W m^{-2}. The number of observations is also shown.

No. obs = 145(104)	Mean	R^2	Mean Error	RMSE
Observed	391.9(419.1)			
Shine	393.1(442.9)	0.99(0.91)	1.1(23.9)	15.9(48.8)
Bennett	373.1(426.3)	0.98(0.91)	-18.8(7.3)	21.6(47.8)

Shine Clear Sky

Error (W m^{-2})

300
200
100
0
-100
-200
-300

80 75 70 65 60 55 50
Solar Zenith Angle

Bennett Clear Sky

Error (W m^{-2})

300
200
100
0
-100
-200
-300

80 75 70 65 60 55 50
Solar Zenith Angle
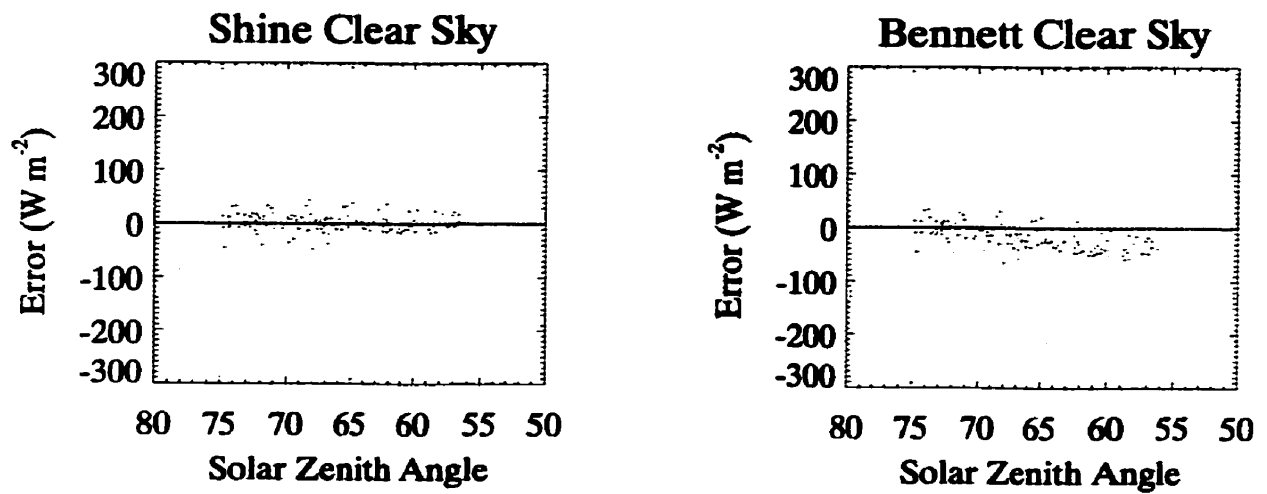
Figure 4.3: The clear-sky short-wave flux error for two parameterizations (modeled flux minus the observed flux at Rosse Bay).

For the K↓ all-sky combinations the results again support Key et al. (1996). The error statistics (Table 4.2) and error plots (Figure 4.4) show the best parameterization combination is Shine/Shine with a mean error of -2.1 W m^{-2} (3.1 W m^{-2} at the terrestrial site). The Jacobs cloudy-sky scheme depletes too much radiation when combined with the Shine and Bennett clear sky routines, shown by the highly negative mean errors.

Table 4.2: Parameterized all-sky short-wave flux error (estimated flux minus the measured fast-ice flux). Bracketed values are the corresponding ice-breaker results. The mean, mean error and RMSE are in W m^{-2}. The number of observations is also shown.

No. obs = 456(555)	Mean	R^2	Mean Error	RMSE
Observed	322.4(250.7)			
Shine/Shine	320.3(332.4)	0.83(0.76)	-2.1(81.7)	59.6(90.1)
Bennett/Jacobs	289.9(351.0)	0.85(0.71)	-32.4(100.3)	60.6(95.9)
Shine/Jacobs	304.0(370.1)	0.85(0.71)	-18.4(119.4)	57.9(96.5)
Bennett/Shine	315.1(322.5)	0.82(0.75)	-7.4(71.8)	61.3(90.8)
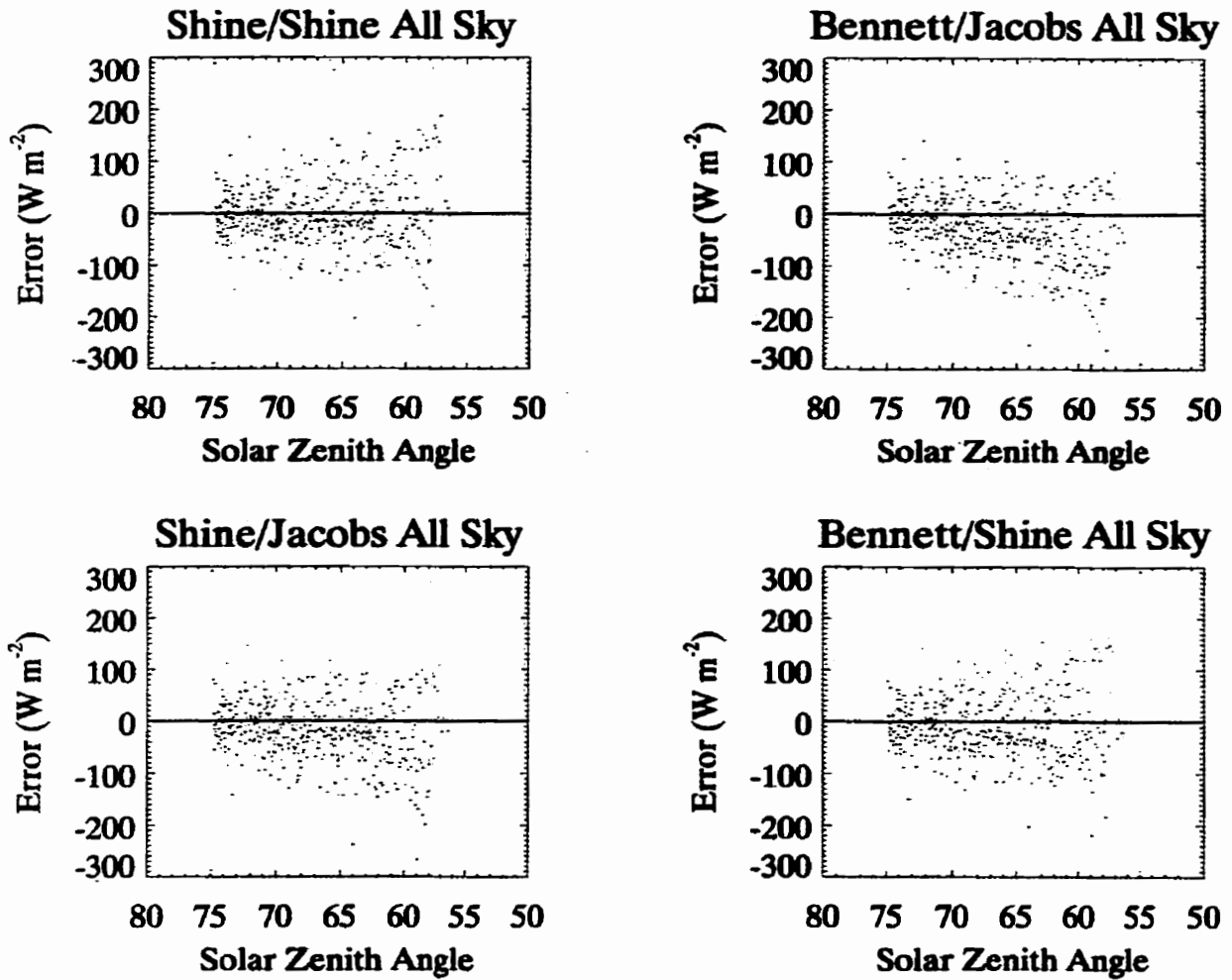
Figure 4.4: The all-sky short-wave flux error for four combinations of parameterizations (modeled flux minus the observed flux at Rosse Bay). The first name refers to the clear-sky parameterization used for that combination from Figure 4.3.

4.3.1.1.2 Incident Long-wave Fluxes

The parameterization of Ohmura performs better than both the Maykut-Church (MC) and Efimova's schemes (Table 4.3). Key et al., (1996) found the Efimova routine to perform best. The emittance of long-wave radiation is too high in both Maykut and Church's and Efimova's schemes for incident fluxes less than about 240 W m^{-2}. A similar trend is shown by Key for the MC model. If the clear-sky atmospheric emissivity is adjusted by roughly the same amount in MC (from 0.7855 to 0.729) and Efimova (0.746 to 0.7; the first coefficient independent of vapor pressure) during periods of low emittance (L↓< 240 W m^{-2}) the results from both parameterizations improves (Table 4.4 and Figure 4.5). The emissivities for each scheme was optimized to fit this data by minimizing the mean bias error (MBE) for each scheme.

Table 4.3: Parameterized clear-sky long-wave flux error (estimated flux minus the measured fast-ice flux). Bracketed values are the corresponding ice-breaker results. The mean, mean error and RMSE are in W m^{-2}. The number of observations is also shown.

No. obs = 200(131)	Mean	R^2	Mean Error	RMSE
Observed	197.5(235.4)			
MC	209.8(243.9)	0.97(0.80)	12.2(8.5)	7.3(17.8)
Ohmura	192.5(230.6)	0.97(0.80)	-4.9(-4.8)	6.6(17.3)
Efimova	207.9(247.9)	0.98(0.80)	10.4(12.5)	6.1(17.0)

Table 4.4: Parameterized clear-sky long-wave flux error (estimated minus measured fast-ice flux) when altering the emissivity in MC (from 0.7855 to 0.729) and Efimova (from 0.746 to 0.70). Bracketed values are corresponding ice-breaker results. The mean, mean error and RMSE are in W m^{-2}. The number of observations is also shown.

No. obs = 200(131)	Mean	R^2	Mean Error	RMSE
Observed	197.5(235.4)			
MC	197.6(238.0)	0.98(0.81)	0.1(2.7)	5.2(16.7)
Efimova	197.6(242.9)	0.98(0.80)	0.1(7.5)	5.2(17.8)

MC Clear Sky

Error (W m^{-2})

150
100
50
0
-50
-100
-150

100 150 200 250 300

Observed Flux (W m^{-2})

Ohmura Clear Sky

Error (W m^{-2})

150
100
50
0
-50
-100
-150

100 150 200 250 300

Observed Flux (W m^{-2})

Efimova Clear Sky

Error (W m^{-2})

150
100
50
0
-50
-100
-150

100 150 200 250 300
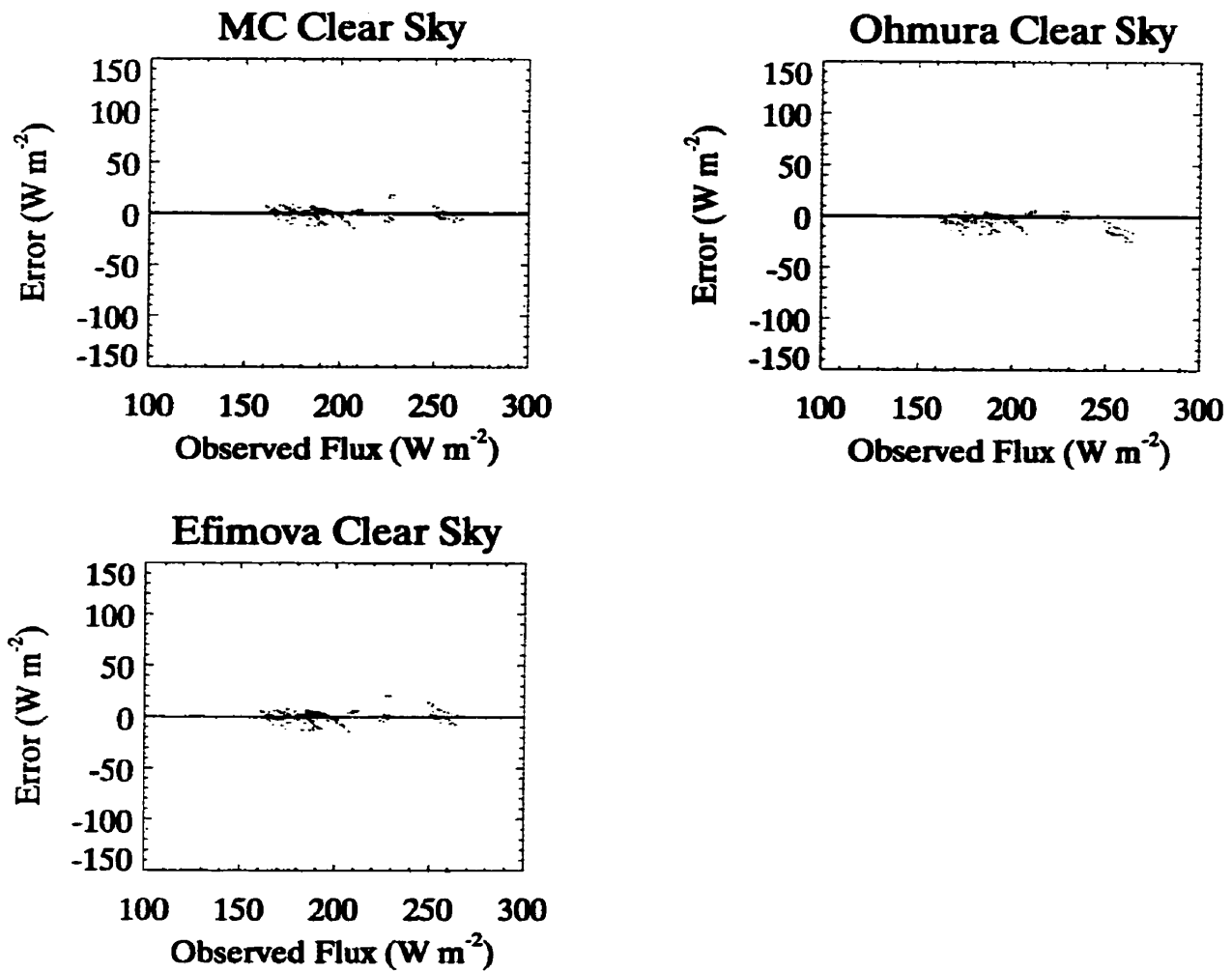
Observed Flux (W m^{-2})

Figure 4.5: The clear-sky long-wave flux error (modeled flux minus the observed flux) for the optimized emissivities in MC and Efimova to fit the Rosse Bay data (see text).

128

For the L↓ all-sky combinations, Efimova/MC had both the smallest MBE and RMSE of the combinations examined (Table 4.5). Key suggested the Efimova/Jacobs schemes perform best. If we consider the modifications to the clear-sky emission characteristics (above), the Efimova/Jacobs and the MC/Jacobs combination perform better than the Efimova/MC model (Table 4.6), with Efimova/Jacobs performing the best. The MC cloudy-sky correction for long-wave radiation consistently underestimates fluxes in cloudy skies.

Table 4.5: Parameterized all-sky long-wave flux error (estimated flux minus the measured fast-ice flux). Bracketed values are the corresponding ice-breaker results. The mean, mean error and RMSE are in $W\,m^{-2}$. The number of observations is also shown.

No. obs = 622(857)	Mean	R^2	Mean Error	RMSE
Observed	231.6(277.8)			
MC/MC	238.0(262.8)	0.92(0.73)	6.4(-15.1)	14.9(19.3)
Ohmura/Jacobs	226.1(260.5)	0.89(0.78)	-5.5(-17.3)	16.9(17.6)
Efimova/Jacobs	243.7(280.1)	0.90(0.79)	12.1(2.2)	16.3(17.4)
MC/Jacobs	251.8(282.6)	0.90(0.77)	20.1(4.8)	16.2(18.1)
Efimova/MC	230.4(260.4)	0.92(0.75)	-1.2(-17.4)	14.9(18.4)

Table 4.6: Parameterized all-sky long-wave flux error (estimated flux minus the measured fast-ice flux) when applying the new clear-sky formulations of Maykut-Church and Efimova from Table 4. The mean, mean error and RMSE are in $W\,m^{-2}$. The number of observations is also shown.

No. obs = 622	Mean	R^2	Mean Error	RMSE
Observed	231.6			
MC/MC	221.8	0.92	-9.8	15.4
Ohmura/Jacobs	226.1	0.89	-5.5	16.9
Efimova/Jacobs	229.6	0.89	-2.0	16.8
MC/Jacobs	234.6	0.89	2.9	16.9
Efimova/MC	217.1	0.92	-14.5	15.2
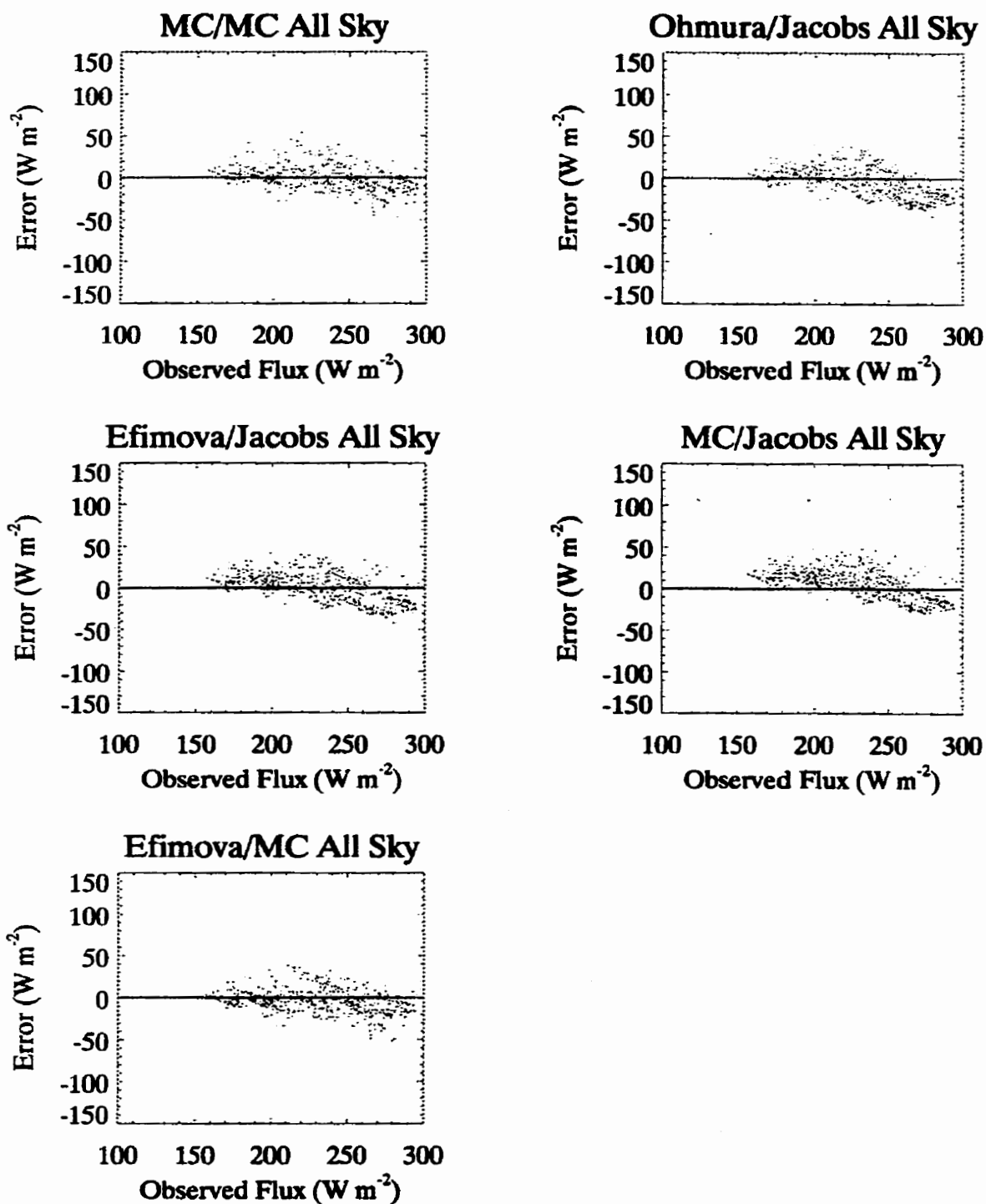
Figure 4.6: All-sky long-wave flux error for five combinations of parameterizations (modeled flux minus the observed flux at Rosse Bay). The first name refers to the clear-sky parameterization used for that combination using the optimized clear-sky emissivities in Figure 4.5 and optimized cloudy-sky emissivities of MC and Jacobs to fit the Rosse Bay data (see text).

A noticeable trait in the data and the results of Key et al. (1996) is a consistent negative slope (within a 99% confidence interval) in the $L\downarrow_{cld}$ error as the observed flux in Figure 4.5 increases (ie: the estimated flux underestimates real fluxes as the magnitudes of the fluxes increase). This suggests the cloudy sky emissivity is too small and needs to be increased. If the cloudy sky emissivity is increased in MC (from 0.2232 to 0.32) and Jacobs (from 0.26 to 0.275) the results are again different (Table 4.7 and Figure 4.6). The cloudy-sky emissivity of MC and Jacobs were optimized as before by minimizing the MBE for each scheme. After optimizing the cloud-sky emissivities, all of the parameterizations perform well based on the error indices (Table 4.7), however, the modified MC cloudy-sky formulation relaxes the negative slope (with 95% confidence) in the $L\downarrow_{cld}$ error (Figure 4.6) with increasing flux. This is due to the MC cloudy-sky exponential dependence in equation (4.9). The Jacobs cloudy-sky formulation neglects this exponential factor. Very similar results (within a few percent) were obtained using the terrestrial data.

Table 4.7: Parameterized all-sky long-wave flux error (estimated flux minus the measured fast-ice flux) when applying the new clear-sky formulations of Maykut-Church and Efimova from Table 4.4 and the new cloudy-sky formulation of Maykut-Church and Jacobs (see text). Bracketed values are the corresponding ice-breaker results. The mean, mean error and RMSE are in $W\,m^{-2}$. The number of observations is also shown.

No. obs = 622(857)	Mean	R^2	Mean Error	RMSE
Observed	231.6(277.8)			
MC/MC	231.9(265.1)	0.92(0.76)	0.3(-12.7)	13.9(20.3)
Ohmura/Jacobs	228.1(262.6)	0.89(0.78)	-3.5(-15.3)	16.6(17.7)
Efimova/Jacobs	231.7(276.5)	0.90(0.79)	0.1(-1.3)	16.4(18.3)
MC/Jacobs	236.7(278.8)	0.90(0.80)	5.0(0.9)	16.5(17.5)
Efimova/MC	227.1(262.9)	0.93(0.75)	-4.6(-14.9)	13.8(21.0)

4.3.1.1.3 Seasonal Trends

The superior parameterizations above and those modified to fit the NOW region were evaluated for seasonal bias using methods described in section 4.2.3. The Shine $K\downarrow_{clr}$ scheme has a positive seasonal bias (confidence interval of 99%) by slightly underestimating fluxes in the early part of the season and overestimating fluxes in the latter part of the season (Figure 4.7).

	T<-20°C	-20°<T<-14°C	-14°<T<-9°C	-9°<T<-2°C	T>-2°C
obs	287.5	350.7	402.2	473.7	411.7
Shine	282.4	339.1	402.4	471.8	432.1
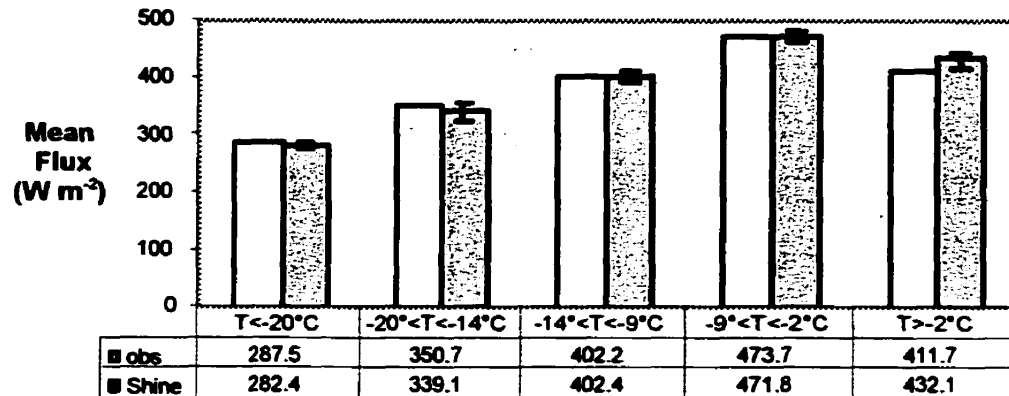
Figure 4.7: The short-wave observed and Shine scheme seasonal clear-sky fluxes ($W\ m^{-2}$). The RMSE error bars are also shown. The coldest temperature category contained 13 data points, 34 in the next warmest, 48 in the next warmest, 20 in the next warmest and 32 in the warmest category.

The overestimation in the late season could be, in part, due to the model's inability to represent the increase in atmospheric optical depth associated with rising temperatures and water vapor loading (see also, Leontyeva and Stamnes, 1993; Blanchet and List, 1983). Integrated total column water vapor using radiosondes launched from the ice breaker increased from 2 kg m^{-2} in mid-April to 5.5 kg m^{-2} by early May then 9 kg m^{-2} in early June and 11 kg m^{-2} by early July. Surface vapor pressures also increased over the

warm season but a de-coupling between the surface and lower troposphere (if it occurred) may affect the results. This is especially important over fast-ice in the cold season under inversion conditions where the near-surface temperature and humidity may not represent total column characteristics. Hanafin and Minnett (2001) built upon results here to further improve the Shine scheme over the polynya in the warm season by increasing the coefficient of the water vapor term. Aerosol effects are unknown since no measurements were available, however, these effects would lead to the most serious errors in the parameterizations (Shine, 1984); the radiative effects of the aerosols being strongly dependent on the atmospheric humidity (e.g. Hänel, 1976) and once again total column variations (Bergin et al., 2000) that are largely unknown in the arctic. Radiative transfer models perform well in mid-latitudes (Jing and Cess, 1998) but have not been tested to the same degree in arctic environments.

The Shine K↓ all-sky scheme (Figure 4.8) excessively depletes radiation in the early and middle part of the season and not enough in the late season (within a 99% confidence interval). This is likely because of optically thinner clouds during the colder part of the season than in the warmer season. Recall that the Shine model has an inherent clear-sky bias that affects the all-sky calculation. If we decrease the cloud optical depth (from its assumed constant value of 7.0) to 1.0 for $T_a \leq -20°C$, the all-sky Shine/Shine mean error drops to the Shine clear-sky mean error for the same temperature category. Using the same procedure for $-20°C < T_a \leq -14°C$, the cloud optical depth becomes 5.5 and stays near 7.0 for warmer temperatures. This suggests an increasing cloud optical

depth would improve the K↓ all-sky estimates as the warm season approaches. The results are consistent with Curry and Ebert (1992) and Leontyeva and Stamnes (1993) who suggest a cloud optical depth near 7.0 for the warm season. I assume the presence of mid and upper cloud has no seasonal trend when obscured by low cloud during ground observations. Other radiative transfer issues such as solar zenith angle, atmospheric gas variations, 3-D cloud variations, and averaging procedures also affect the results (see for example, Li et al., 1993; Evans, 1998; Arking et al., 1992; Bergin et al.; 2000; Barker and Davies, 1992) but can not be realistically accounted for here. These issues also apply to the ice breaker results (section 4.3.1.2).

	T<-20°C	-20°<T<-14°C	-14°<T<-9°C	-9°<T<-2°C	T>-2°C
obs	311.4	273.6	300.2	344.3	379.1
Shine/Shine	286.2	257.4	288.5	351.2	397.9
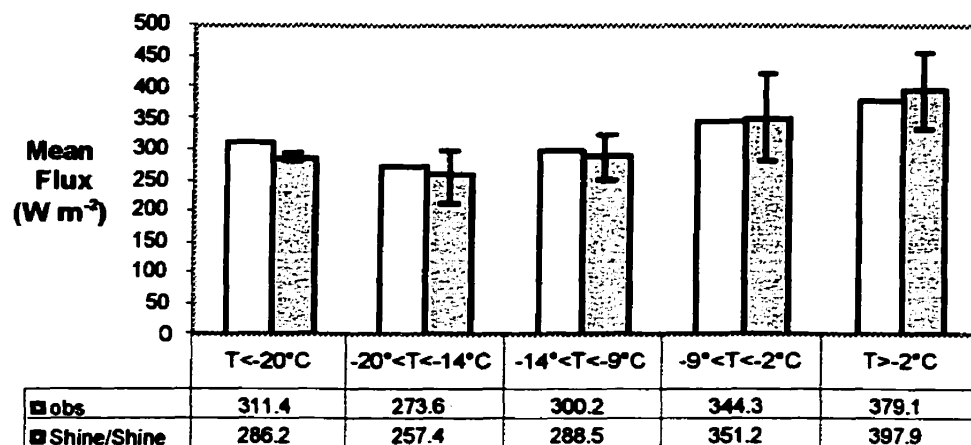
Figure 4.8: The short-wave observed and Shine/Shine scheme seasonal all-sky fluxes (W m⁻²). The RMSE error bars are also shown. The coldest temperature category contained 11 data points, 61 in the next warmest, 156 in the next warmest, 235 in the next warmest and 25 in the warmest category.

The L↓$_{clr}$ seasonal trends of MC (modified) and Efimova (modified) are depicted in Figure 4.9. The MC parameterization does not contain a seasonal bias (with 99% confidence). The scheme of Efimova contains a slight negative bias (with 99% confidence) early in the season and positive bias late in the season. The Efimova emissivity was

adjusted as in MC, but the vapor pressure dependence in Efimova may introduce other complications.

The L↓ all-sky seasonal trends of MC/MC (modified) and Efimova/MC (modified) are depicted in Figure 4.10. The MC/MC combination does not contain a seasonal bias (99% confidence). The Efimova/MC combination also did not have a seasonal bias (99% confidence) but contains a consistent negative error similar to what was shown earlier in Table 4.7. It should be emphasized that this analysis is intended to illustrate seasonal biases only and not compare each parameterization since their fluxes are very similar in magnitude (i.e. one scheme may not necessarily be more accurate than the other).

	T<-20°C	-20°<T<-14°C	-14°<T<-9°C	-9°<T<-2°C	T>-2°C
▢ obs	166.1	180.3	193.4	216.8	252.2
▨ MC	166.9	179.4	194	216.8	252.5
▤ Efimova	165.3	178.5	194.1	219	255.4
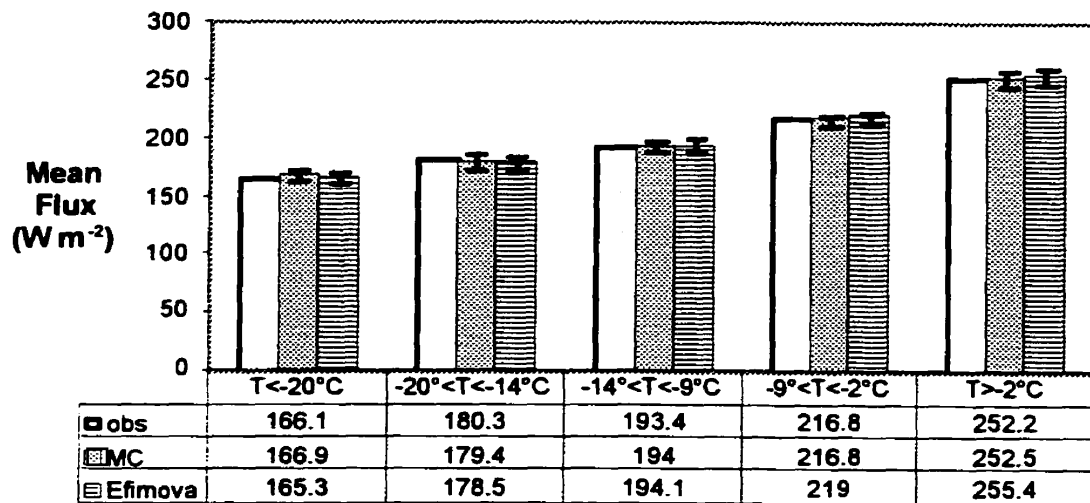
Figure 4.9: The long-wave observed (clear bar), MC (middle bar) and Efimova schemes seasonal clear-sky fluxes (W m⁻²). The RMSE error bars are also shown. The coldest temperature category contained 29 data points, 61 in the next warmest, 73 in the next warmest, 21 in the next warmest and 34 in the warmest category.

	T<-20°C	-20°<T<-14°C	-14°<T<-9°C	-9°<T<-2°C	T>-2°C
obs	169.9	202.4	228.5	253.9	274.3
MC/MC	170.1	205.4	227.3	254.4	272.8
Efimova/MC	164.3	199	221.6	251	269.6
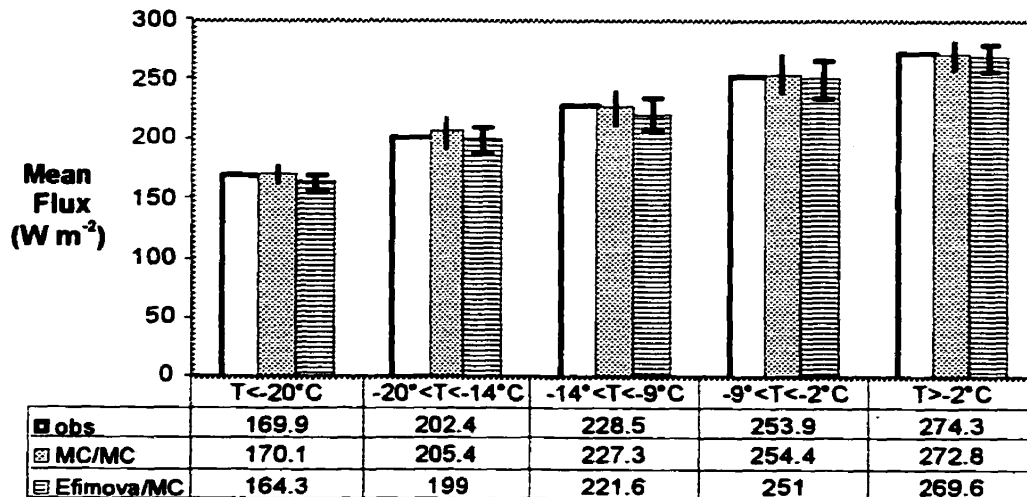
Figure 4.10: The long-wave observed (clear bar), MC/MC (middle bar) and Efimova/MC schemes seasonal all-sky fluxes (W m⁻²). The RMSE error bars are also shown. The coldest temperature category contained 34 data points, 139 in the next warmest, 239 in the next warmest, 257 in the next warmest and 28 in the warmest category.

4.3.1.2 Ice Breaker Platform

A similar analysis to the last section was conducted on the ice breaker $K\downarrow$ and $L\downarrow$. All of the different parameterizations were used for the analysis, including the original and modified long-wave schemes. The same seasonal bias analysis was used except polynya air temperatures were marine-like (greater than $-8°C$).

4.3.1.2.1 Incident Short-wave Fluxes

The $K\downarrow_{clr}$ results show the Shine and Bennett schemes perform worst within the polynya relative to the fast-ice and terrestrial sites (Table 4.1). Note that all ice-breaker data in the Tables appear in brackets. The schemes overestimate fluxes with RMSE 2-3 times larger than the fast-ice results. Both the Shine and Bennett schemes contained a more pronounced positive seasonal bias (with 99% confidence) (Figure 4.11). The general overestimation of clear-sky fluxes is likely due to greater total column water vapor than the schemes were originally intended for, especially for the marine environment. Hanafin and Minnett (2001) have corrected for this in the Shine scheme.

	-14°<T<-9°C	-9°<T<-2°C	T>-2°C
◪ obs	378.9	387.3	434.7
▢ Shine	388.9	406.3	461.6
▤ Bennett	375.9	391.6	444
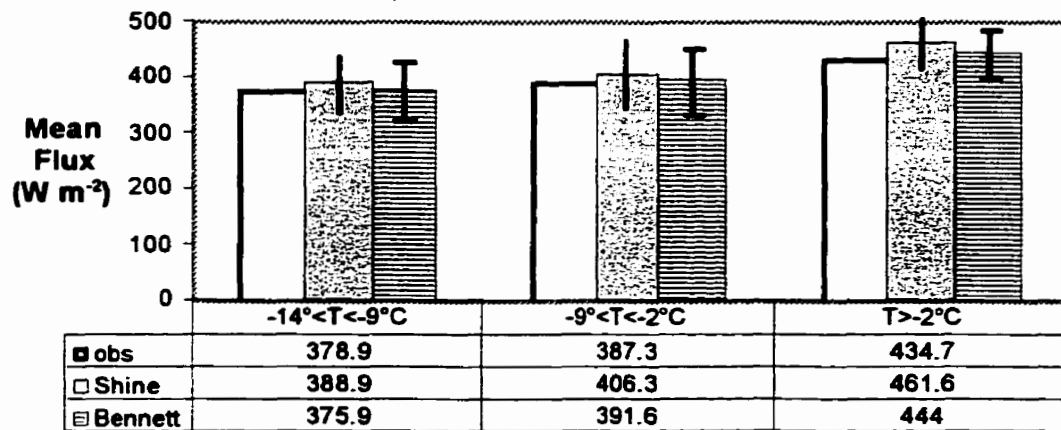
Figure 4.11: Same as Figure 4.7 except for the ice-breaker. The coldest temperature category contained 7 data points, 26 in the next warmest, and 71 in the warmest category.

The ice-breaker results for $K\downarrow$ all-sky show larger RMSE relative to the clear-sky case (Table 4.2). The mean errors and RMSE in the ice breaker results are also much

greater than the fast-ice. The cause is likely the result of marine clouds being optically thicker than the fast-ice environment. There is a positive seasonal bias in the ice breaker-derived fluxes where fluxes are overestimated more so as the ambient temperatures increase (with 99% confidence) (Figure 4.12). If cloud optical depth is increased from 7.0 to 9.0 for $-14°C < T_a ≤ -9°C$, the all-sky Shine/Shine mean error dropped to the Shine clear-sky mean error for the same temperature category. Similarly, for $-9°C < T_a ≤ -2°C$, the cloud optical depth increases to 14 and further increases to 20 for $T_a > -2°C$. These optical depths are consistent with typical arctic stratus clouds (Herman and Curry, 1984; Leontyeva and Stamnes, 1993). This is also different than the fast-ice site where an optical depth of 7.0 works well for warmer temperatures. Once again I assume there is no seasonal bias in the presence of mid and upper level cloud when they are obscured by low cloud during ground observations.

Mean Flux (W m²)	-14°<T<-9°C	-9°<T<-2°C	T>-2°C
☐ obs	310.4	245.6	251.1
☐ Shine/Shine	326.9	302.1	342.8
☐ Bennett/Jacobs	334.4	314.2	363.9
☐ Bennett/Shine	313.5	294.8	332.1
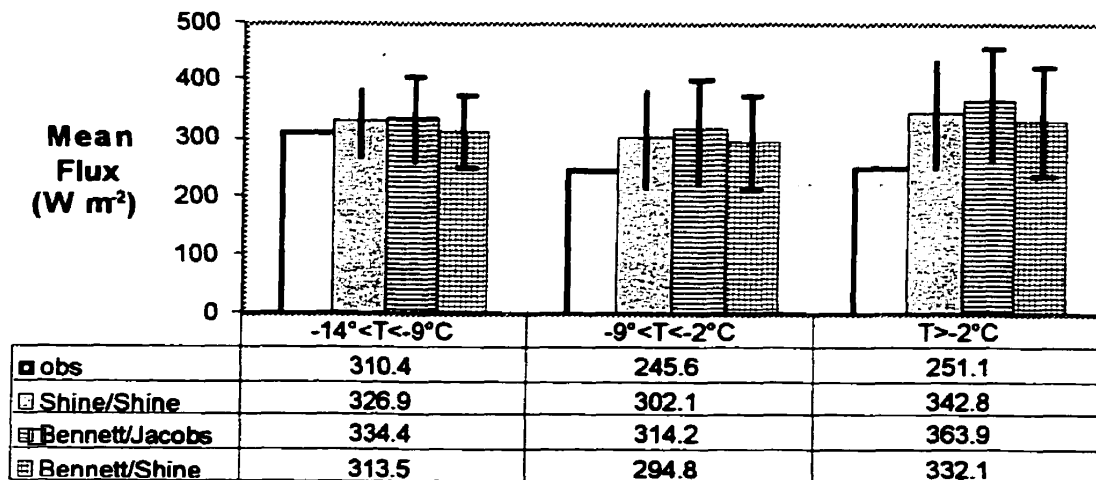
Figure 4.12: Same as Figure 4.8 except for the ice-breaker. The coldest temperature category contained 9 data points, 139 in the next warmest, and 407 in the warmest category.

4.3.1.2.2 Incident Long-wave Fluxes

The MC and Efimova $L\downarrow_{clr}$ overestimate smaller fluxes (i.e., $L\downarrow$<240 $W\cdot m^{-2}$), consistent with results from Table 4.3. The error terms are improved when applying the fast-ice adjustment to the MC and Efimova schemes. Both the MC and Efimova schemes do not contain the seasonal bias (with 99% confidence) over the polynya (Figure 4.13). Recall that a slight positive bias was found in the Efimova scheme for the fast-ice.

	-14°<T<-9°C	-9°<T<-2°C	T>-2°C
obs	186.5	217.5	252.2
MC	197.1	213.7	256.2
Efimova	197.7	215.5	263.2
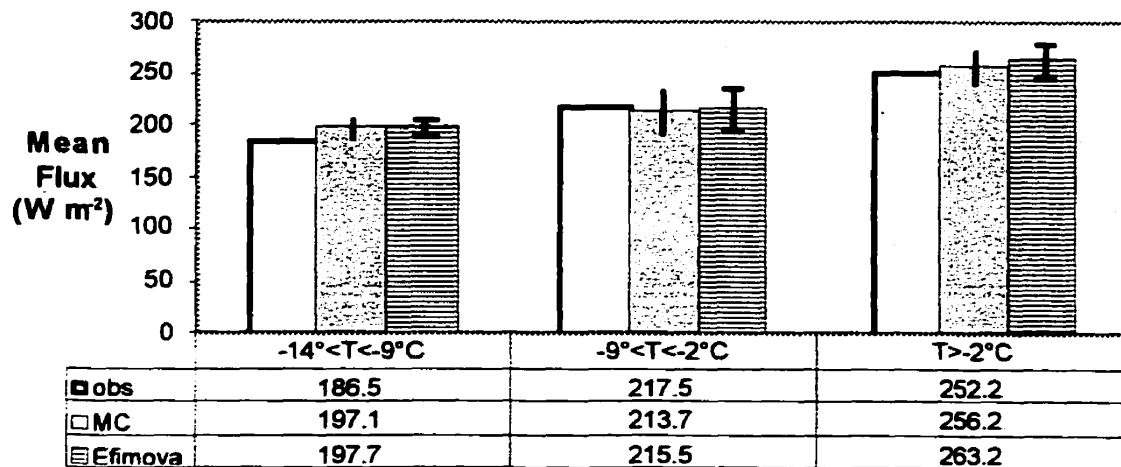
Figure 4.13: Same as Figure 4.9 except for the ice-breaker. The coldest temperature category contained 15 data points, 35 in the next warmest, and 81 in the warmest category.

The ice breaker $L\downarrow$ all-sky errors improve when using the modified schemes from section 4.3.1.1 (comparing Tables 4.5 and 4.7; see also Figure 4.14). However, there is more variation in the mean errors than the fast-ice results with slightly larger RMSE and smaller R^2 (Table 4.7). Note the MBE is more negative than the fast-ice site (Table 4.7).

This may be due to 1) warmer mean ambient temperatures (and later data collection dates) accompanying the ice breaker data, 2) the cloud emissivity may need to be increased in a full marine environment (with optically thicker clouds) compared to the fast-ice regime, and 3) cloud base heights being lower in the marine environment. The first reason can be ruled out since the ice-breaker mean error is consistently more negative than the fast-ice mean errors for similar temperatures and data collection dates. This suggests the cloud emissivity needs to be increased for the marine schemes and/or the cloud base heights were lower in the marine environment. The $K\downarrow$ all-sky results suggest a greater cloud optical depth in the polynya implying higher within-cloud precipitable water and in turn higher cloud emissivity. A higher cloud emissivity is required to match the parameterization schemes with measured flux density within the polynya. Cloud base heights would also contribute to the differences.

	-14°<T<-9°C	-9°<T<-2°C	T>-2°C
obs	214.5	258.1	289.9
MC/MC	207.7	241.8	278.4
Efimova/Jacobs	216.3	250	291.4
MC/Jacobs	221.2	253.8	292.8
Efimova/MC	203.1	238.3	277.1
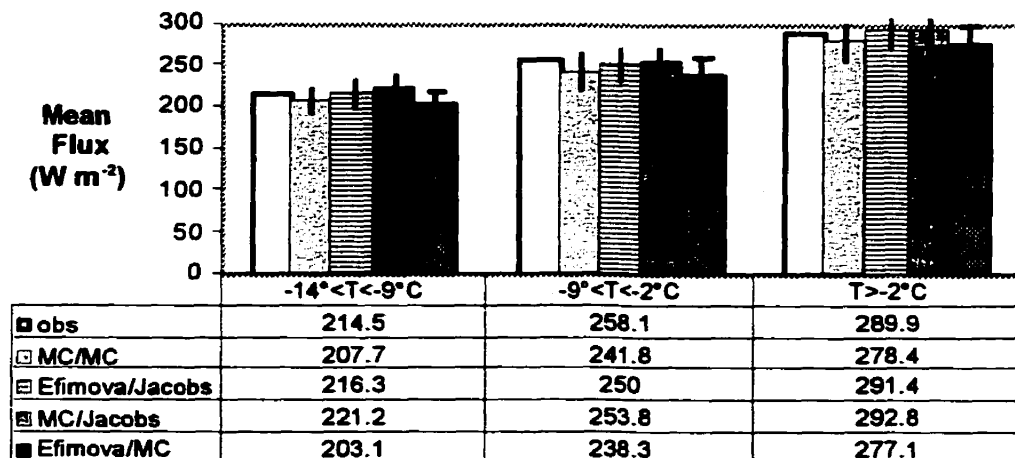
Figure 4.14: Same as Figure 4.10 except for the ice-breaker. The coldest temperature category contained 29 data points, 256 in the next warmest, and 572 in the warmest category.

Combinations using the Jacobs cloudy-sky scheme are more consistent over the seasons and have the smallest mean errors. The Jacobs scheme was developed from data during the warm season to early winter (June-December) that may contribute to its better performance in a marine setting. The modified MC/MC and Efimova/MC scheme combinations were best in the fast-ice and terrestrial sites but would need to be further adjusted for the marine data. Hanafin and Minnett (2001) have built upon these results to improve the MC/MC L↓ all-sky scheme in the polynya setting.

Given that the open water of the polynya is the major source of atmospheric water vapor in the area, it is to be expected that the water vapor burden and distribution will show differences between open water and land. The dominant wind direction in the area is from the NNW (Barber et al., 2001) and so the terrestrial and fast-ice data are predominantly under the influence of winds blowing over the land surface of Ellesmere Island; the ice-breaker measurements include a wide range of conditions, in terms of sea-ice cover and open water, that are unparameterized in the formulations used here. In particular the water vapor distribution is a strong function of fetch over open water for situations of off-ice winds. This has the potential for not only increasing the variability of the parameterization uncertainties, but also introducing bias errors.

While there are convincing physical reasons to explain the observed increases in uncertainty in the parameterized fluxes when compared to ship-based measurements, as opposed to measurements from fixed platforms, there is always the possibility that these are a result not of shortcomings in the parameterizations, but of flawed measurements. Of obvious concern is ship motion. In an attempt to reduce ice breaker tilting of the

141

radiometers, they were mounted on gimbals. This means that, on average, they are level; but at any moment may be tilted as a result of ship motion. Observations showed that in most cases the amplitude of the oscillation was only a few degrees, with some infrequent large amplitudes when the ship was breaking thick ice. The consequence of tilt is severe in the $K\downarrow$ measurements, as this has the effect of changing the apparent Z. However, while mean tilts can lead to significant errors, especially in clear skies, small-amplitude oscillating tilts do not significantly degrade the data (MacWhorter and Weller, 1991). The $L\downarrow$ measurement is inherently less sensitive to tilts of the pyrgeometer, but there is an error source caused by the temperature contrast between the sky and land, sea or ice. As the pyrgeometer tilts, it receives radiation from a warmer source, below the horizon, than the sky. Oscillating tilts do not cancel out but combine to produce a positive bias error. The effect on this would be to make a parameterization of $L\downarrow$ appear to predict fluxes low compared to the measurements, and this is indeed observed in some cases. Such an effect would be indistinguishable from the environmental factors discussed above. Clearly the issue of making accurate $K\downarrow$ and $L\downarrow$ measurements from ships requires further attention, but it is certainly not clear that these instrumental effects are of sufficient magnitude to dominate the error characteristics of the results discussed here.

4.4 Conclusions

Incident radiation fluxes are critical parameters within the SEB, and accurate representation of these fluxes is necessary in all types of model simulations of sea ice. Many of the current simple incident radiation schemes in sea ice models have not been validated in the environments investigated in this chapter and yet they are central areas for many biological species. The purpose of this chapter was to assess the performance of simple incident short-wave and long-wave radiation parameterizations used in several thermodynamic ice models and to investigate any inherent temporal and or spatial biases in these parameterizations (question 1). The second question was related to offering improved versions of these parameterizations where possible.

4.4.1 Question 1

The fast-ice and terrestrial regimes showed very similar characteristics (within ± 2%) due to their close geographic proximity and snow covered surfaces. Differences arose when comparing the terrestrial/fast-ice results to the marine environment sampled by the ice-breaker.

The fast-ice preferred $K\!\downarrow_{clr}$ scheme was Shine (1984) that contained no solar zenith angle (Z) bias, unlike the scheme of Bennett (1982). However, the Shine scheme contained a positive seasonal bias where it underestimated fluxes in the cold season and

overestimated fluxes in the warm season. The positive bias was more dramatic in the marine data. Hanafin and Minnett (2001) built on these results to improve the Shine clear-sky scheme over the polynya. Likely causes and errors for the differences were offered.

The preferred fast-ice $K\downarrow$ all-sky combination scheme was the Shine (1984) clear-sky and Shine (1984) cloudy-sky. The Jacobs (1978) cloudy-sky scheme depleted too much radiation. The Shine cloudy-sky scheme depletes too much radiation in the colder season and not enough in the warm season, especially in the marine warm season. An improved implementation of the Shine scheme was made by varying the cloud optical depth. If cloud optical depth is allowed to vary seasonally from 1 to 7 in the fast-ice environment (late March to early June) and 9 to 20 in the marine setting (early May to mid July), the Shine cloudy-sky fluxes become closer to observed values. These optical depths are within the limits of arctic clouds (Herman and Curry, 1984; Shine et al. 1983; Shine, 1984). Sea ice models should allow for seasonal cloud optical depth variations with respect to incident short-wave radiation, even if they are used in a climatological sense.

The preferred fast-ice $L\downarrow_{clr}$ parameterization is Maykut and Church (1973) after adjusting (decreasing) the clear-sky emissivity to account for a less emissive atmosphere at colder temperatures in NOW. This correction was sufficient for the marine conditions. The Maykut and Church scheme did not contain a seasonal bias once this correction was made.

The preferred fast-ice $L\downarrow$ all-sky combination was Maykut and Church clear-sky and Maykut and Church cloudy-sky. I increased the cloudy-sky emissivity to account for under-estimations when clouds were present which also alleviated a slight seasonal bias.

The Maykut and Church exponential dependence of cloud fraction (equation (4.9)) was also found to be important.

Different $L\downarrow$ all-sky results were found for the marine environment. Overall, the ice-breaker consistently had more negative mean errors compared to the fast-ice site. This was not due to warmer ambient marine temperatures. The all-sky short-wave flux results suggested the marine environment had greater cloud optical depths compared to the fast-ice and terrestrial sites and is consistent with the long-wave results where a higher cloud emissivity may be required; although cloud base height differences could also be a factor. The Jacobs cloudy-sky scheme is more consistent over a seasonal basis and has the smallest mean errors. The Maykut-Church cloudy-sky scheme was further improved by Hanafin and Minnett (2001) for the marine setting.

4.4.2 Question 2

I recommend using 1) the modified Maykut-Church $L\downarrow$ clear and cloudy sky schemes for a polynya fast-ice and terrestrial environment, 2) the modified Efimova/Jacobs or Maykut-Church/Jacobs schemes for the Arctic marine environment and 3) the modified Efimova/Jacobs scheme for application to all three environments simultaneously since it was the most consistent for this purpose. The modified Maykut-Church and Efimova $L\downarrow_{clr}$ formulations are, respectively:

$$L\downarrow_{clr} = 0.729 \ \sigma \ T_a^4 \qquad (4.10)$$

145

$$L\downarrow_{clr} = \sigma \, (0.7 + 0.0066 \; ea) \; T_a^4 \qquad\qquad (4.11)$$

The modified Maykut-Church and Jacobs $L\downarrow$ all-sky formulations are, respectively:

$$L\downarrow_{all} = L\downarrow_{clr} \, (1 + 0.32 \; c^{2.75}) \qquad\qquad (4.12)$$

$$L\downarrow_{all} = L\downarrow_{clr} \, (1 + 0.275 \; c) \qquad\qquad (4.13)$$

4.5 Summary

In summary, the incident short-wave and long-wave parameterizations investigated here estimate these fluxes reasonably well in some cases and not so well in others for a polynya environment. Seasonal biases were found to be the major problem as well as environmental conditions (i.e. near-shore fast-ice conditions were much different than the full marine environment). An attempt was made to correct these biases and different forms for various parameterizations were presented. An important consideration for the incident short-wave fluxes under cloudy skies is the surface albedo due to multiple reflections between the surface and clouds. Chapter 5 explores the spatial variations in surface albedo during the spring melt season over FYI given the dearth of albedo information during this time of year. This will provide insight into the important surface cover types and their associated albedo for better representation in sea ice model albedo parameterization schemes.

CHAPTER 5: Local and Regional Albedo Observations of Arctic First Year Sea Ice During Melt Ponding

5.1 Introduction

In this chapter, I expand on the examination of surface short-wave albedo during the melt season that was initially looked at in Chapter 3. The surface albedo is also linked to Chapter 4 through the incident short-wave radiation. The surface albedo is a critical climatological parameter controlling short-wave responses in the surface energy balance, and has been a major focus in several modeling and observational studies (see for example, Shine and Henderson-Sellers, 1985; Ebert and Curry, 1993; Robinson et al., 1986; Ross and Walsh, 1987; De Abreu et al., 1994; Grenfell and Maykut, 1977; Grenfell and Perovich, 1984). Albedo representation in sea ice models is also critical to modeled sea ice evolution (Shine and Henderson-Sellers, 1985) and still require improvement, especially during melt pond formation to break-up due to multiple surface types that affect albedo during this period. This chapter is designed to investigate the spatial aspects of FYI albedo and provide more insight to albedo characteristics from chapter 3. I also examine the sensitivity of sea ice ablation to percent pond fraction and the associated spatial variability in surface albedo using the 1-D thermodynamic sea ice model discussed in chapter 3.

The research questions are designed to examine the spatial aspects of fractional surface cover types with surface albedo and to determine the role melt ponds play in

these processes over land-fast FYI in the Canadian Arctic Archipelago. Because of the paucity of observational data on melt pond surface albedo, particularly in the Archipelago, the following research questions are addressed:

1) What are the local spatial variations (sub-km scale) of both broadband and spectral albedo using *in situ* observations?

2) How do the surface albedo measurements in (1) scale up to semi-regional (10's km) and regional (100's km) albedos over FYI as related to issues of larger scale albedo estimation during spring melt conditions?

3) How sensitive is sea ice ablation to percent pond fraction and the associated spatial variability in surface albedo?

The primary purpose of deriving larger scale albedo is to provide climate model-scale first-year sea ice albedo during the melt season to see which surface features become important at these scales. The core material in this chapter has previously been published in Hanesiak et al. (2001c).

5.2 Methods

5.2.1 Site Description

Data consist of surface albedo measurements made on snow covered smooth first-year sea ice (FYI), aircraft video and satellite observations. Data were collected during the second intensive observation period of C-ICE97 (Collaborative - Interdisciplinary

Cryospheric Experiment) conducted between Year Day 175 (YD175; June 24) and YD193 (July 12), 1997 in Wellington Channel and Lancaster Sound, Nunavut. Standard meteorological observations from Resolute, Nunavut along with data from the first intensive observation period of C-ICE97 are used to initialize and force the sea ice model simulations between YD119 (April 29) to YD212 (July 31). The intensive field program was based on the east coast of Cornwallis Island near Read Bay (75° 3.073' N; 93° 33.193' W) about 65 km NE of Resolute, Nunavut (Figure 5.1). A secondary camp (ice camp) installation was located approximately 4 km ESE of the land camp on a triangular-shaped patch of a thin snow covered (10 cm) smooth FYI (Figure 5.1). The ice camp was the primary albedo sampling site with supplemental locations visited by helicopter.
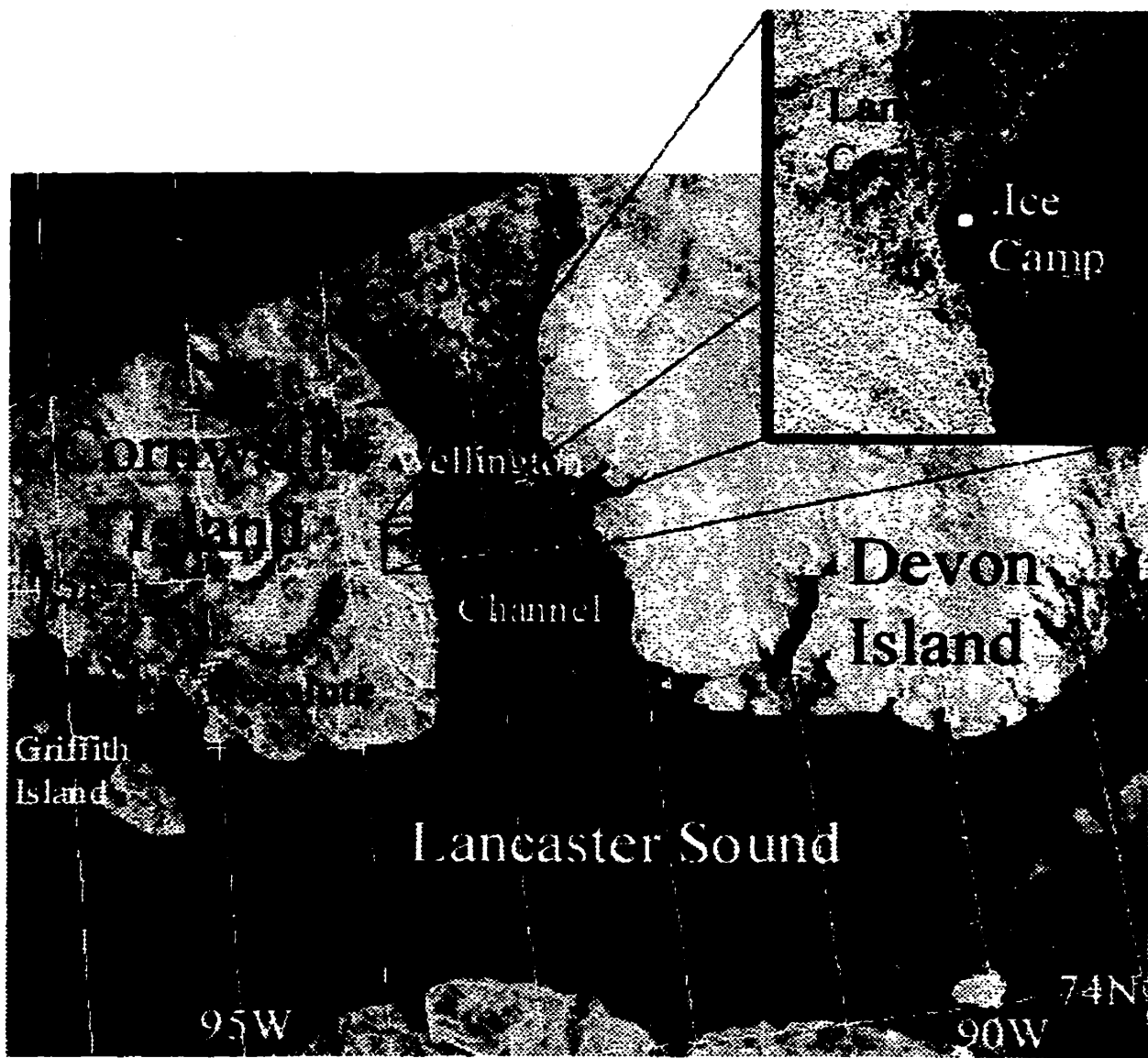
Figure 5.1: Geographic locations of the land camp (black dot), ice camp (white dot) and ice conditions within Wellington Channel and Lancaster Sound depicted by ERS2 Synthetic Aperture Radar (SAR) on April 3, 1997. Note the arc of rafted and rubbled first-year ice (FYI) with multi-year ice (MYI) embedded north of the ice camp in Wellington Channel (north of 75N). Also note the slightly rafted and rubble FYI ice southwest of Devon Island at the southern end of Wellington Channel and marginally rougher FYI as one proceeds from Griffith Island toward the ice edge in Lancaster Sound. The ice edge is aligned SW-NE beginning at 74N, 90W with open water to the east.

Upon our field site arrival (YD175; June 24), snow conditions were in the mid-

stages of melt with snow depths ranging from 5 – 20 cm and ice thickness near 1.9 m on

the smooth FYI site; no melt ponds were present. By the end of the experiment (YD193; July 12), poor ice conditions and little terrestrial snow made access to the FYI site difficult with full melt pond advancement of about 75% coverage and initial stages of pond drainage. The top layer of the ice surface became crusty, thin and very porous adjacent to the melt ponds from advanced snowmelt stages.

Ice conditions within Wellington Channel and Lancaster Sound were generally FYI between 1.7 – 2.0 m thick. This ice was not as smooth as the FYI ice sampling site according to visual observations and active microwave satellite images (see Figure 5.1). Various pressure ridges and multi-year ice inclusions existed near the coast of Cornwallis and Devon Islands (see Figure 5.1). Highly variable snow depths ranged from 10 – 60 cm, with deeper drifted snow near rougher ice (ie: near pressure ridges). Melt ponds were not present at these locations upon arrival, but developed into similar pond conditions as the FYI site over the 2.5 week period of the experiment.

5.2.2 Surface Measurements of Albedo

Prior to melt pond formation, spectral and broadband albedo measurements were made over various surfaces (see section 5.3) at a consistent location and other locations on the smooth FYI site. Snow physical property measurements (density, wetness, salinity, layer descriptions, and depth) were made but were discontinued beyond YD180 (June 29) due to either the disappearance of snow or development of layers impenetrable to the sampling equipment. Snow density and salinity were collected in 2 cm vertical layers with

a density sampler 2 x 3 cm and salinities measured by a refractometer once the samples melted, accurate to within 0.5 ppt. When conditions permitted, snow wetness between 1% – 10% water by volume (Wv) was measured in 2 cm layers with a capacitance plate precise to within 0.5%. Snow grain measurements were obtained episodically due to melting conditions. Once melt ponds formed, location-consistent and feature-driven albedo sampling was conducted. Broadband surface-based albedo measurements were made along a 1 km long linear transect aligned E-W at the FYI ice camp. These measurements were collected to assess the spatial variability in albedo over local scales. Surface-based albedo was also measured along the aircraft transects for surface validation (section 5.3.1) over a portion (150 m to 300 m) of the full transect distance.

Broadband albedo were measured using a portable Middleton EP16 pyrano-albedometer spanning 300-3000 nm. Measurement accuracy is factory calibrated to within 1.6%. The instrument was mounted on a metallic conduit 0.75 m in length and placed on a tripod approximately 1 m above the surface and leveled.

Spectral albedo was measured with an Analytical Spectral Device (ASD) VIR Spectrometer. High-resolution (1.4 nm bandwidth) spectral measurements were made between 330 - 1064 nm, however, precision of the unit permitted reliable data between 380 – 950 nm. Detector noise was removed (via dark current correction) from each measurement. The unit allows for real-time graphical display and manipulation of spectral albedo data. The foreoptics used included 26° field of view (FOV) and calibrated remote cosine receptor (RCR) with 180° FOV mounted on a tripod 1 m above the surface and leveled. Foreoptics are independent FOV instrumentation that are connected to the ASD

unit. The 26° foreoptic provides directional hemispheric reflectance to focus the sensor over a particular smaller surface as opposed to the RCR which covers a much broader area of measurement over all hemispheric angles. Down-welling irradiance was measured directly with the RCR, which was then inverted to measure up-welling irradiance to measure spectral albedo. A standard white reference barium-sulphate panel was used to convert the 26° foreoptic radiance measurements to albedo. The 26° foreoptic was directed at each surface type in order to sample the most homogeneous parts to ensure no other surface types were part of the measurements. All reflectance measurements are accurate to 1-2% and made under overcast sky conditions. Clear sky sampling led to specular reflection errors, especially using the 26° foreoptic, that could not be corrected since the angular distribution of up-welling radiance was not measured. The unit and white reflector were properly calibrated by the manufacturer (ASD) before the field season.

5.2.3 Airborne-Derived Albedo

Direct broadband albedo measurements were made using a helicopter (Bell Jetranger 206B) on YD185 by mounting the EP-16 albedometer to the pontoon (Figure 5.2) and manually logging the data. Two horizontal flights were made at 152 m and 244 m (500 ft and 800 ft above ground level (AGL)) within 10 minutes of each other under complete overcast conditions (300 m ceiling) near the ice camp. The albedometer was very stable during the flights and the down-welling short-wave component was derived

from surface measurements since this component may have been biased by the helicopter. The albedometer was mounted low enough so the helicopter frame was not hindering the up-welling short-wave radiance. Errors associated with these measurements are unknown, however, instrument stability, variability in measurements ($\pm5\%$) and a stable solar illumination suggest that measurements were made under the best possible conditions.

Indirect albedo measurements were made using aircraft aerial survey (Figure 5.3) video that were digitized and classified into albedo categories according to surface measurements. A Hi-8 video camera was mounted in the belly of a Twin Otter aircraft looking 'near-to-vertical' flying 610 m (2000 ft) AGL at a speed of 100 knots. The aerial surveys (linear transects) began at 74° 15' N, 95° 20' W (start of transect #1) and proceeded eastward to 74° 15' N, 95° 0' W (end of Transect #1) near the ice edge in Lancaster Sound (bottom right corner in Figure 5.3). Positional information was annotated directly from an onboard Global Positioning System (GPS) where GPS (±100 m) readings were taken at the beginning and end points and notable features along each line. Transects were flown at 5' latitude increments north through Wellington Channel with the last line over dense rubble and multi-year ice regions (transect #17) along 75° 35' N. The first 5 transects had the same length (from 95° 20' W to the ice edge) and the remainder began on Cornwallis Island, ending on Devon Island (Figure 5.3). The first 6 lines were flown on YD181 and the following 11 lines on YD184. Poor weather prevented further surveys.
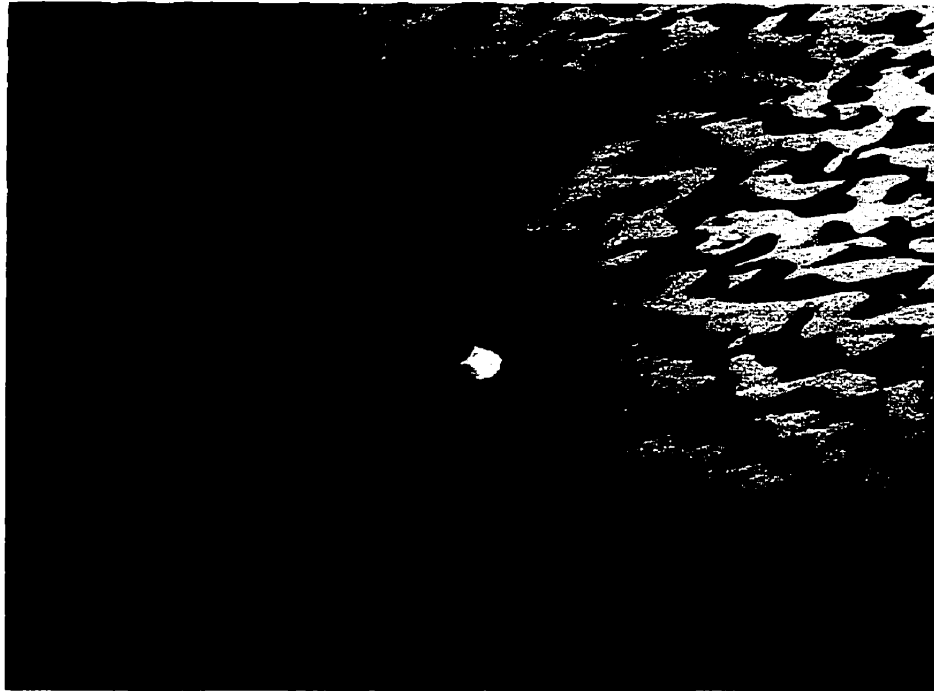
Figure 5.2: In-cabin helicopter photo of the albedometer mounted to the pontoon. The height above ground was approximately 330 m and total pond fractions were near 35%.
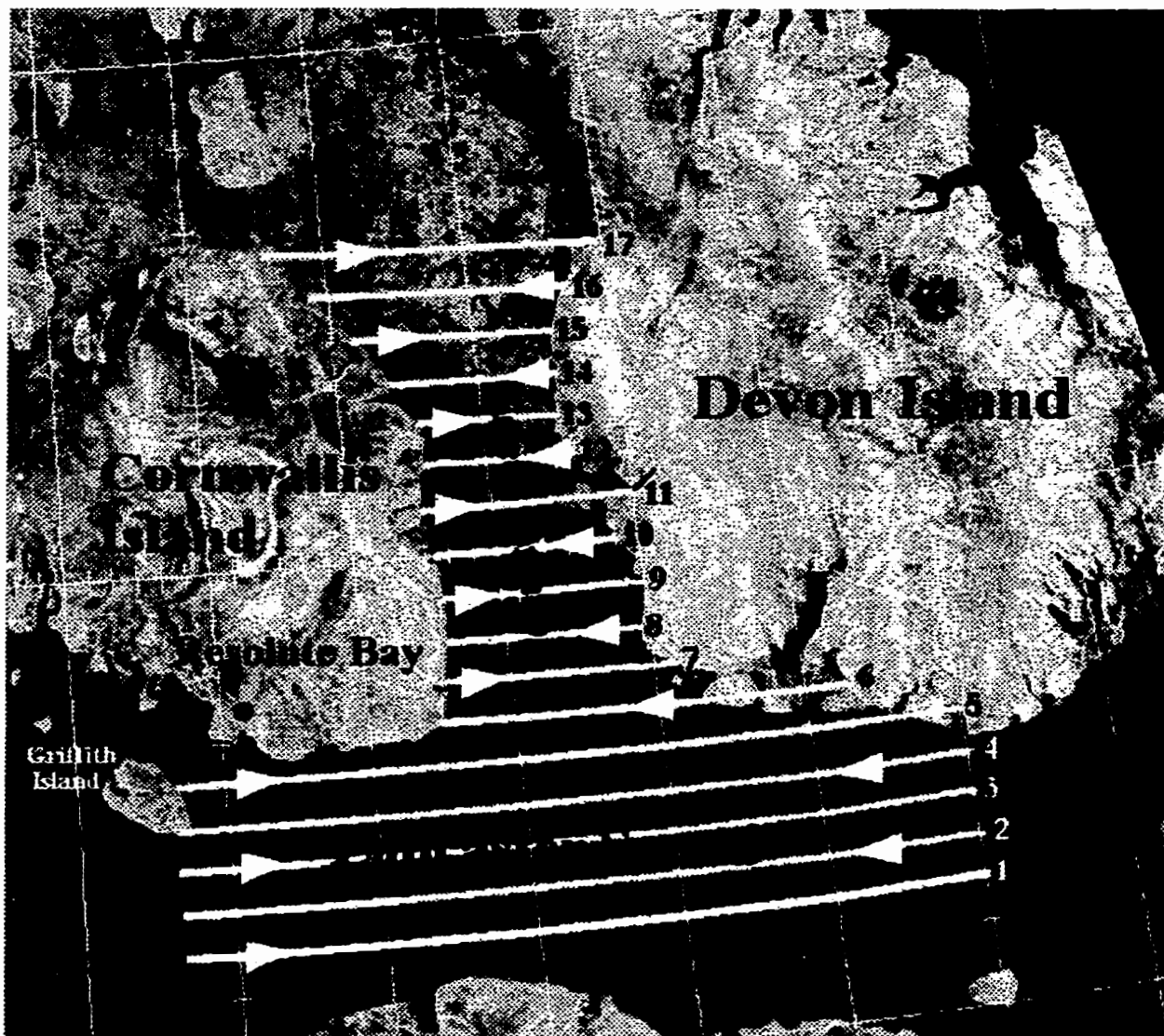
Figure 5.3: Geographic locations of the aircraft video surveys (linear transects) within Lancaster Sound and Wellington Channel (SAR image date is April 5, 1997). The arrows indicate the direction flown by the aircraft for each transect line. The first 6 lines were flown on YD181 (June 30) and the following 11 lines on YD184 (July 3). Only the first 10 transect lines were used to derive surface albedo from the video.

Video data were digitized using an automated routine that separated the continuous analog flight record into adjacent frames of 8-bit grey-scale images. Frame spacing was dependent on aircraft speed. Each frame represented an area average of 1.06 km wide x 1.2 km long with a spatial resolution of 16.56 m^2 on the ground and was standardized by the overall mean from the entire aerial survey. An unsupervised cluster analysis was performed on a full cross-section of cover types. This type of analysis is common for aerial video and a detailed description of the image analysis scheme can be found in Barber and Yackel (1999). Cluster analysis results consistently identified four classes, corresponding to the four cover types identified in the field; 1) wet snow, 2) a blend of water/snow mixture or highly granulated, wet surface and high/low density bubbled ice surface beneath a very shallow pond perimeter, 3) light colored ponds, and 4) dark ponds. All images were then reclassified into one of four cover types using standard digital image classification techniques.

The fractional cover type mean and standard deviation of percent cover was calculated for each transect for spatial comparisons. Each cover type was assigned an albedo according to surface observations (see section 5.3.2) to assess the spatial variation of surface albedo and make inter comparisons along each transect. Albedos were only derived from transects 1-10 since there were no surface albedo measurements made over rougher ice and multi-year floes. Image data most likely contained shadow contamination due to low arctic sun angles, however, the surveys were conducted during peak daylight hours with an SZA near 52° and removing any shadow effects is difficult. The majority of the data were collected over smoother first-year sea ice where minimal shadow effects

157

took place. The most significant errors include: 1) misidentification of surfaces under marginal transition conditions, 2) unstable aircraft flight (roll, altitude and latitudinal drift) and GPS error resulting in area and linearity fluctuations of the transects, and 3) assignment of cover type albedo (using ground measurements) with a single albedo value, especially the mixed cover type. Quantifying these errors is difficult, however, albedo magnitudes are expected to be accurate within ±5% based on helicopter validation. Aircraft video-derived albedos were then compared to the Advanced Very High Resolution Radiometer (AVHRR) albedo to corroborate aircraft results and to further upscale albedo measurements to regional estimates (see section 5.3.2).

5.2.4 AVHRR-Derived Albedo

Surface albedos were estimated using the Advanced Very High Resolution Radiometer (AVHRR) onboard the National Oceanic and Atmospheric Administration (NOAA) 11 and 12 satellites. AVHRR narrow band VIS and NIR radiances [channel 1 (0.58-0.68 μm) & channel 2 (0.73-1.1 μm)] are typically used to estimate top of the atmosphere (TOA) albedos. After cloud-screening the AVHRR data, only one NOAA 14 AVHRR scene, on YD180 (June 29 at 04:09:00 CDT), was considered clear enough to accommodate comparison with airborne albedo measurements. The AVHRR albedo are therefore valid under clear-sky conditions. To compare surface broadband albedo measurements with AVHRR values, the up-welling signal recorded by the satellite at the

158

TOA must be adjusted to account for: 1) sun-sensor view geometry, 2) calibration drift, 3) atmospheric attenuation, 4) anisotropic reflectance, and 5) the limited spectral response of the narrow band sensor. A multistep procedure was developed and is discussed in detail in De Abreu (1996). A brief description of the procedure is given here pertaining to the YD180 NOAA 14 scene.

The pre-launch calibration must be adjusted due to sensor degradation (Holben et al., 1990). Updated calibration coefficients for the YD180 data, provided by NOAA/NESDIS, were used to convert the raw data to up-welling TOA radiances (Kidwell (1991). NOAA 12 data were not considered here due to the lack of appropriate calibration update information. TOA radiances (L_{sat}) were then converted to surface narrowband AVHRR albedos (α_s) by the following:

$$\alpha_s^i = \frac{L_{sat}^i \pi - a^i fE_{toa}^i \cos\theta_z}{b^i fE_{toa}^i \cos\theta_z} \tag{5.1}$$

where L_{sat} is the satellite measured up-welling radiance, f is the anisotropic reflectance factor (ARF) of Taylor and Stowe (1984) taken from the ARF sea ice dataset developed by Lindsay and Rothrock (1994), E_{TOA} is the inband irradiance at the top of the atmosphere, θ_z is the solar zenith angle and i denotes AVHRR channel 1 or 2. The coefficients a, b describe the atmospheric attenuation of the radiances and are provided for AVHRR 1 and 2 in Koepke (1987). For AVHRR 1, these coefficients are dependent on the solar zenith angle, the atmospheric aerosol optical depth and columnar ozone amount. Coefficients for AVHRR 2 are dependent on the solar zenith angle, aerosol

159

optical depth and atmospheric water vapour amount expressed as a precipitable water amount. In the absence of appropriate *in situ* data, I used the following climatological estimates of these variables to select the appropriate coefficients: aerosol optical depth 0.05 (@ 0.55 µm), precipitable water content 2 cm, ozone amount 0.36 NTP (Normal Temperature and Pressure). The surface narrowband albedos were converted to broadband albedo (0.15-4.0 µm) via the following model taken from Li and Leighton (1992):

$$\alpha_A = 0.0453 + 0.389\alpha_s^1 + 0.452\alpha_s^2 \tag{5.2}$$

This method was found to estimate broadband surface albedo in this geographic region with an accuracy of ± 5%. I suspect the accuracy to be degraded somewhat due to: 1) the lack of *in situ* measurements, especially for aerosol optical depth, and 2) the large average solar zenith angle of 78° of the study scene including specular reflection that can amount to errors within ±0.1 albedo units.

5.2.5 Sea Ice Model Simulations

The one-dimensional thermodynamic sea ice model (Flato and Brown, 1996; Hanesiak et al., 1999), described in chapter 3, was used to show how changes in pond fractions and their associated albedo can alter sea ice thermodynamics and thereby its mechanical strength. The melting ice albedo parameterization in the model is based on Arctic lake ice observations of Heron and Woo (1994) that uses ice thickness as a proxy

for time which attempts to capture melt pond evolution. The model's albedo parameterization may produce a quicker temporal decline in surface albedo than observations indicate (shown in chapter 3). Differences in forcing data between the C-ICE97 location and Resolute can cause ice evolution differences, however, surface albedo is of primary importance during late spring ice decay according to field observations.

The ice model was forced with hourly air temperature (T_a), relative humidity (RH), wind speed (u), cloud fraction (c), and snowfall (sfall) from standard meteorological observations at Resolute, Nunavut between the first intensive observation period of C-ICE97 (YD119; April 29) to complete modeled ice melt (YD200; July 19). Unfortunately, no continuous set of forcing data were available from the C-ICE97 experiment so Resolute forcing was required. The model was initialized with snow and ice data from C-ICE97 on YD119 were the snow depth = 14 cm, ice thickness = 1.75 m, T_a = -18°C, RH = 77%, u = 4.7 m s^{-1}, c = 0.9, and sfall = 0 mm/h. The objective of this modeling exercise is to illustrate the model's effectiveness in recreating observed C-ICE97 snow and ice thickness evolution as well as the seasonal changes in albedo for this particular field year.

The next set of modeling experiments intends to assess how the thermodynamic state and mechanical strength of sea ice is affected by variations in fractional pond cover since thermodynamics determine the ice's susceptibility to break-up (Barber et al., 1998). The sea ice volume reaches a thermodynamic state to a point where the brine volumes in the ice are sufficiently large that sea ice breakup can occur with either oceanic or atmospheric forcing (Wakatsuchi and Kawamura, 1987; Cox and Weeks, 1988). This

point is referenced as 'breakup potential' as it relates to the susceptibility of the sea ice to break-up. To show how discreet changes in pond fraction (PF) affects ice thermodynamics, a set of experiments were conducted using the FB sea ice model and consistent changes in PF. A week-long model simulation beginning on YD164 (start of continuous snow melt) and ending YD170 was performed using a constant PF (and albedo) over the week beginning with a 10% PF and ending with an 80% PF in steps of 10%. A week-long simulation was used instead of a longer time period since it is more realistic to have similar pond fractions over a one week period but still run the model long enough to produce noticeable changes in the ice volume. PF's of 10, 20, 30, 40, 50, 60, 70, and 80% corresponded to albedos of 0.66, 0.62, 0.58, 0.54, 0.50, 0.46, 0.42, and 0.38 respectively. The albedos were estimated using the formula,

$$\alpha_{total} = f_{snow}*\alpha_{snow} + PF*\alpha_{pond} \tag{5.3}$$

where α_{total} is the resulting albedo, f_{snow} is the snow fraction (wet snow and mixed cover type), α_{snow} is the snow albedo (combination of wet snow and mixed cover type) = 0.7, PF is the pond fraction (light and dark ponds), and α_{pond} is the pond albedo (combination of light and dark ponds) = 0.3. The snow (pond) albedo was computed as an average of the wet snow and mixed cover type (light and dark ponds) weighted more toward the wet snow (light pond) since these cover types are dominant over their counterparts in early ablation stages.

The effects of pond fraction on ice thermodynamics is gauged upon how much the vertical ice temperature gradient changes (ITGC) (warmed) between the bottom of the ice

and the 25 cm depth (from the snow/ice interface) from the initial condition to the end of the week-long simulation. This interval of depth was used since it is felt to represent the average ice temperature profile between the ice surface and ice bottom and also to exclude any near-ice-surface temperature waves that can diurnally bias the profile. The simulations were forced using the same data as the simulations above between YD164-YD170 and conducted with an initial snow depth = 0 since ponds are assumed to be present.

5.3 Results

5.3.1 Surface Measurements of Albedo

Spectral albedo and snow physical property measurements were made at the ice camp over different surfaces from melt onset to full melt pond advancement described in section 5.2.1. Sampled surfaces (Table 5.1) ranged from a 22 cm deep snow cover to 20 cm deep melt ponds. The snow pack underwent several freeze-thaw cycles prior to and during the sampling period. Hence, all of the snow albedo sampling was done with some liquid water in the snow pack. Most or all of the brine within the snow pack drained to the bottom layer prior to YD175. All measurements were made under complete overcast skies (unless otherwise stated) to minimize specular reflection and since no bi-directional reflectance data were obtained.

163

Table 5.1: Surface type samples of spectral and broadband albedo conducted during C-ICE97 between YD175 (June 24) and YD193 (July 12), 1997. The "S" and "B" refers to either spectral or broadband measurements taken, respectively. All surfaces that were spectrally measured were done so using the 26° and 180° foreoptics. Most measurements were done under cloudy skies unless otherwise stated in the text.

Surface Type	Depth Range	Spectral/Broadband
Snow	3 – 22 cm	S and B
Dense Snow (after rainfall)	0.5 – 2 cm	S and B
Saturated Snow	0.5 – 2 cm	S and B
Snow/Water Mix	0 – 0.5 cm	S and B
High Density Bubble Pond Perimeter	1 – 3 cm	S
Low Density Bubble Pond Perimeter	4 – 6 cm	S
Light Melt Pond	2 – 8 cm	S and B
Dark Melt Pond	10 – 22 cm	S and B
Shallow Pond w/ Ice Skin	4 – 7 cm (Pond); 0.5 mm (Ice Skin)	S
Shallow Pond w/ No Ice Skin	4 – 7 cm	S

Rapid snow albedo changes were observed over 3 days (Figure 5.4) during extended warm periods (daily average T_a near 2°C between YD177 and YD179) using the RCR foreoptic. The spectral albedo decreases not only in the NIR due to grain size changes and increased liquid water (by increasing the effective grain size and absorption) (Wiscombe and Warren, 1981) but also in the VIS. VIS changes were caused by the snow surface becoming visibly porous with greater air inclusions as the snow melted along with increased snow grain sizes and likely greater airborne dust contamination from strong winds off nearby land, although this was not directly measured. At the top of the snow layer (top 4 cm), snow densities increased from 380 kg m^{-3} to 405 kg m^{-3} and wetness values increased from 5%Wv to over 10%Wv over the 3 day period. Spectral curves in Figure 5.4 are similar to measurements made by Grenfell and Maykut (1977), Grenfell and Perovich (1984), De Abreu et al. (1995) and Radionov et al. (1997).

Figure 5.5 shows the variability in directional hemispheric spectral albedo using the 26° foreoptic typical of melting FYI surfaces (Table 5.1) in the spring. The spectral curves represent a typical progression if one walked from snow patches to the deeper part of a melt pond. The 26° foreoptic data are shown to highlight spectral albedo differences between various pond depths. The albedo difference between a deeper (22 cm) moist snow and shallow (3 cm) moist snow is roughly 0.1 across the optical spectrum (Figure 5.5). Differences are due to increased liquid water (5% Wv to >10%Wv at the surface), grain sizes (0.75-1 mm to 1-2.5 mm at the surface) and the underlying ice surface in the shallow snow case. Once the snow becomes very shallow and saturated, the ice surface that is blue in color becomes more visible (relative albedo maximum at blue wavelenghts 450-480 nm) and liquid water plays a greater role in the NIR, making an albedo difference of 0.25 across the spectrum compared to shallow moist snow (Figure 5.5). The albedo of melt ponds are dictated by scattering of the underlying ice below 500 nm, a sharp decrease between 500-725 nm caused by increasing liquid water absorption with increasing wavelength and very strong absorption by liquid water beyond 725 nm (Figure 5.5). Similar FYI full-hemispheric (180°) spectral measurements are found in De Abreu et al. (1995) and a few measurements made in other Arctic regions (Grenfell and Maykut, 1977; Grenfell and Perovich, 1984).

In early to mid melt pond stages, pond perimeters have high and low density bubbled ice surfaces. The higher density bubble regions had shallower water depths (0 – 4 cm) and lower density bubbles were beneath 4 – 7 cm of pond water. Inspection of many ponds (>35) revealed that the bubbled regions were non-existent where pond depths were

165

>7 cm. This is likely due to radiative processes and mechanical erosion of wave action on the pond "shore" releasing the bubbles. Typical spectral albedo differences are 0.1-0.13 albedo units over the optical spectrum between the high bubble density and low bubble density pond surfaces and have 0.05-0.2 higher albedo magnitudes compared to deeper parts of the ponds. The extent or fractional cover of the bubbled regions with respect to the overall pond area varied between 25% - 75% for young ponds 1-4 days old and 5% - 20% for more developed ponds 5-6 days old. By the late stages of ponding (≥ 1 week), the "shoreline" of the ponds no longer contained bubbled regions where radiative processes and waves made the pond perimeter slope fairly steep with a >7 cm drop from the snow-pond edge to the first few cm in the pond.
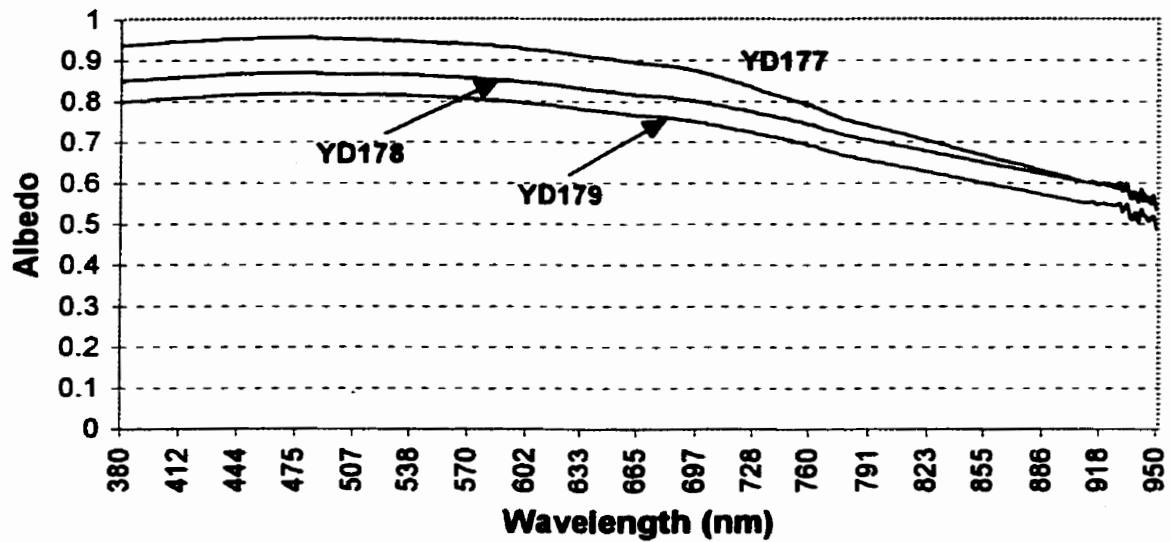
Figure 5.4: Temporal spectral albedo (using the RCR foreoptic) evolution of a 22 cm moist snow pack undergoing rapid melt between YD177 (top curve), YD179 (middle line), and YD180 (bottom line). Measurements were made under overcast skies near solar noon.
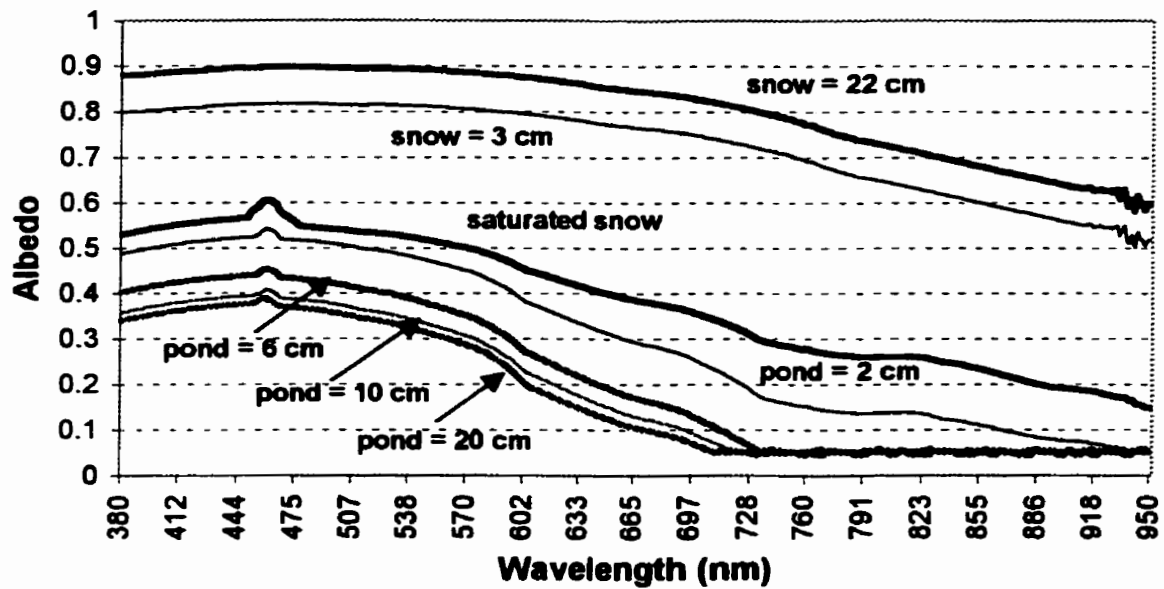
Figure 5.5: Directional hemispheric spectral albedo of various surfaces over FYI (26° foreoptic) on YD185 under overcast skies at a solar zenith angle near 54°. Surfaces include: melting snow (22 and 3 cm deep), saturated snow (0.5 cm deep), high density bubble pond perimeter (2 cm water depth), low density bubble pond perimeter (6 cm water depth), shallow light pond (10 cm water depth), deeper dark pond (20 cm water depth).

167

Overnight cooling can create a thin ice layer on the pond. The RCR spectral albedo of melt ponds 4 and 7 cm deep with a thin ice layer 0.5 mm thick can be very different from ponds with no ice layer (Figure 5.6). The increase in the VIS (0.06-0.07 albedo units for 4 cm pond depth; 0.03-0.04 albedo units for 7 cm pond depth) when ice is present is mainly due to backscatter from tiny air bubbles trapped within the ice layer. A greater density of bubbles in the shallower pond ice layer creates the greater change in the VIS compared to the deeper pond. There is less of a change in the NIR wavelengths (0.02-0.03 albedo units) when a thin layer of ice is present. These results are similar to partially refrozen ponds of Grenfell and Maykut (1977), however, they do not show relative changes in spectral albedo over precisely the same ponds. The ponds sampled here also contained a bubbled underlying ice surface which may account for the higher spectral albedos for ponds with no ice layer compared to that of Grenfell and Maykut (1977) and De Abreu et al. (1995).

Broadband albedo (300 – 3000 nm) sampled surfaces during clear skies with an SZA near 53° (Figure 5.7) range from deeper moist snow (22 cm depth) to dark melt ponds (23 cm water depth). Figure 5.7 shows the mean albedo for each surface from ten to fifteen samples of each with only slight deviations of ± 0.02 albedo units. A steady decrease in albedo occurs as a function of surface type between deeper moist snow (near 0.75) to dark ponds (0.21-0.25) between the range of surfaces that were sampled. The albedo of dark ponds 5 to 23 cm in water depth range slightly between 0.25 to 0.21, similar to other observations (Grenfell and Perovich, 1984). Deeper moist snow here (albedo = 0.73) is similar to the melting snow surface (0.75) of Perovich (1996). The

shallow and saturated snow surfaces (albedos 0.52 − 0.65) in Figure 5.7 are similar to the melting white ice surface (0.56 − 0.68) of Perovich (1996). The melting (blue) ice albedo (0.33) and FYI ponds (0.21) of Perovich (1996) are similar to the Figure 5.7 light pond albedo (0.35) and dark pond albedos (0.21 − 0.25), respectively.
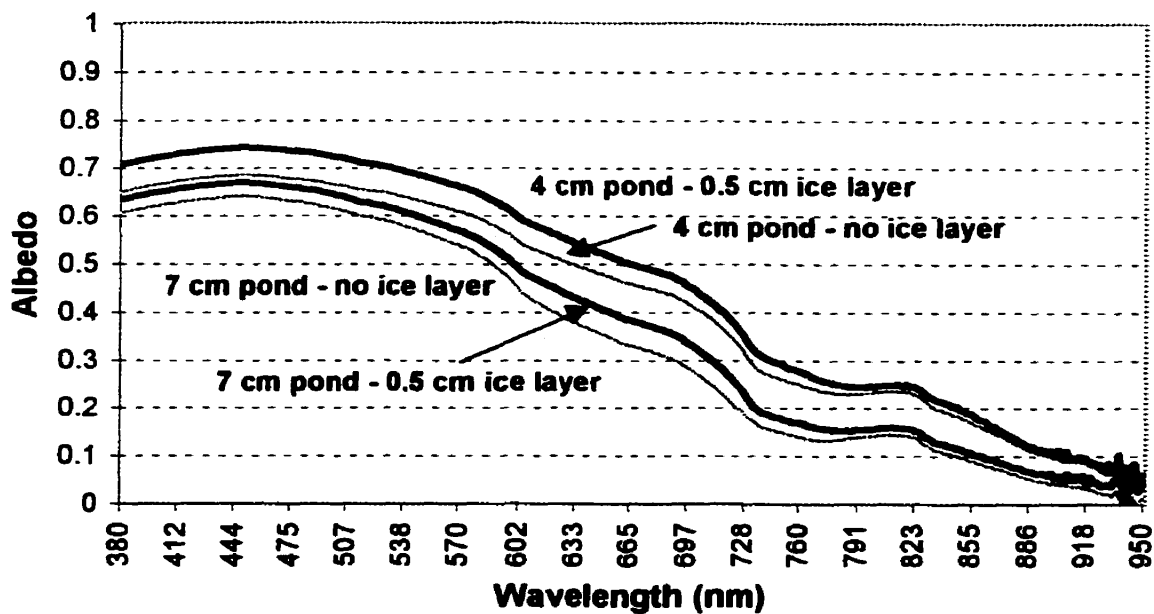
Figure 5.6: Spectral albedo of a 4 cm deep early season pond and 7 cm deep early season pond with and without a thin (0.5 cm) ice layer. Measurements were made under overcast skies using the RCR foreoptic near 1030 CDT.
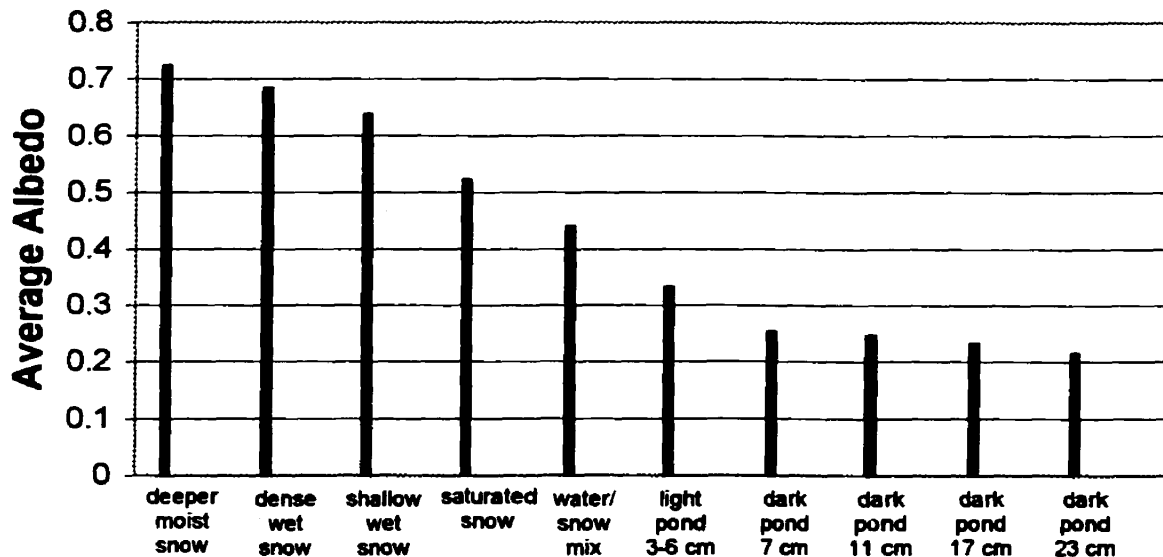
Figure 5.7: Broadband albedo of various surfaces over FYI. Surfaces include: 1) deeper moist snow (4-6 cm), 2) dense snow (refrozen after a rainfall; 1-2 cm), 3) shallow wet snow (2-3 cm), 4) saturated snow (0.5 – 2 cm), 5) water/snow mixture (0.5 – 1 cm), 6) light colored pond (3-6 cm water depth), and 7) dark ponds (8, 11, 17, 23 cm water depth).

170

The spatial variation in surface broadband albedo from ground linear transect measurements shows the changing nature in the distributions of snow patches and melt ponds (Figure 5.8) with albedos ranging between 0.28 over young ponds and 0.75 over moist snow patches with an overall mean of 0.53. Figure 5.8 depicts measurements taken along the 1 km transect at the ice camp on YD183.

Ground linear transect measurements of broadband albedo along aircraft transects 9 - 7 made on YD184 showed slightly different ice conditions compared to the ice camp region (not shown). Melt ponds over the aircraft transects were not as advanced as the ice camp. Albedos ranged between 0.7 for snow and 0.43 for very young bubbled ice surface ponds, with a mean of 0.55 over transect 9, 0.75 to 0.35 with a mean of 0.55 over transect 8, and 0.75 to 0.35 with a mean of 0.6 over transect 7. Melt pond advancement south of the ice camp was delayed by at least 2 days compared to the ice camp. The 2-day lag inference was based on a visual inspection of greater fractional pond cover over the ice camp compared to the other aircraft transect sites and is manifested in the aircraft video analysis (see next section). The greater pond cover at the ice camp was due to less snow accumulation where the very smooth ice (less surface roughness) inhibited snow accumulation.
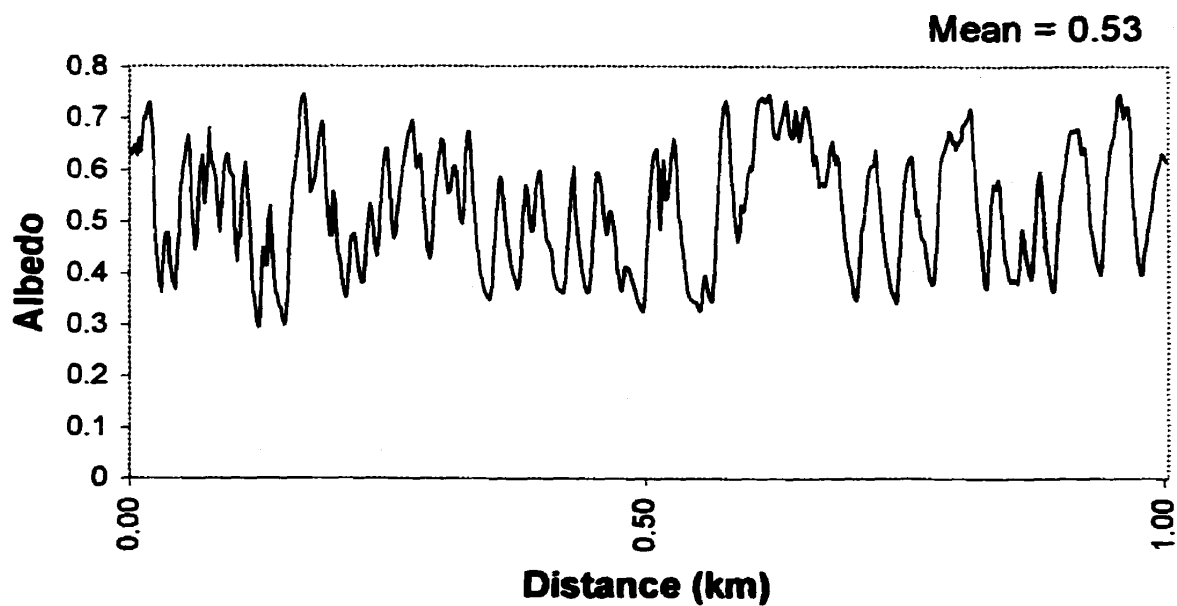
Figure 5.8: Ground-based broadband albedo along the 1 km transect at the ice camp on YD183.
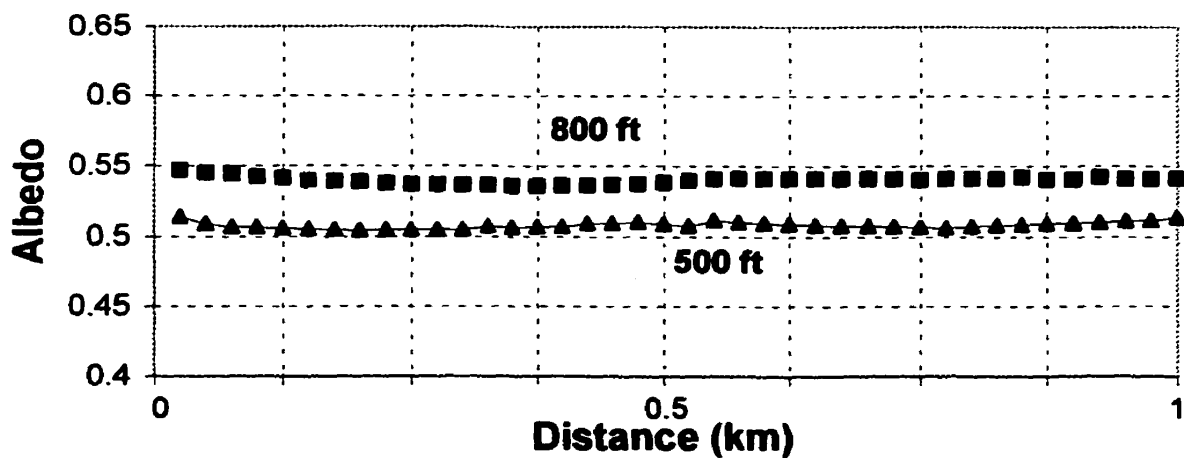
Figure 5.9: Helicopter horizontal flight albedo at 152 m (bottom line) and 244 m (top line) AGL along the 1 km transect at ice camp on YD185.

172

5.3.2 Upscaling Surface Albedo to Sub-Regional and Regional Scales

Helicopter measurements of broadband albedo were made during a horizontal flight described in section 5.2.2 and were conducted to compare to and scale-up from surface-based observations (section 5.3.1). All measurements were made on YD185 under overcast conditions (ceiling near 300 m AGL). Broadband albedo along the 1 km ice camp transect showed fairly consistent magnitudes at 152 m AGL and 244 m AGL (Figure 5.9). The average albedo at 152 m was 0.51 ± 0.015, and 0.54 ± 0.016 at 244 m. The higher albedo at 244 m is the result of more distant, whiter surfaces being measured within the albedometer FOV, including more of the cloudy sky. For example, the albedo at and below 152 m were similar but increased by 0.01 points per 30.8 m between 152 m and 300 m. The helicopter albedos were similar to the ground-based average albedo that was measured two days earlier (0.53). The albedo did not change much over these days due to extended cloud cover and sub-zero air temperatures in contrast to previous days (YD177-179). The albedometer field of view (FOV) was much greater in the helicopter measurements compared to ground measurements averaging out all small scale surface variations, making Figure 5.9 much smoother than Figure 5.8.

Next, aircraft video-derived broadband albedo were estimated over the transects discussed in section 5.2.2. Given the four cover types that were identified in section 5.2.2 (wet snow, a blend of water/snow mixture and high/low density bubbled ice surface beneath a very shallow pond perimeter, light ponds, and dark ponds), each cover type was assigned an albedo based on surface measurements. For convenience, the blend of a

water/snow mixture and high/low density bubbled ice surface beneath a very shallow pond perimeter cover type will be referred to as mixed cover type. Wet snow cover types were assigned an albedo of 0.7, 0.4 for the mixed cover type (average of water/snow mix (0.45) and light ponds (0.35) from ground measurements), 0.35 for light colored ponds and 0.23 for dark ponds (average dark pond albedo from ground measurements).

The percent cover mean and standard deviation for each cover type and transect line are shown in Figure 5.10 with the mean and standard deviation of albedos along each aircraft transect line (Table 5.2 and Figure 5.11). Over FYI, snow patch fractions stayed relatively constant between transects (53-57% ± 5%) with light and dark pond fractional covers increasing from transect 7 - 10 at the expense of the mixed cover type surface (Figure 5.10). This increase in pond cover may be the result of transects 7 - 10 being flown 3 days later than transects 1 - 6 with further melt progressing over that time. The mixed cover type fractional cover varied between 30-38% ± 10% between transects 1 - 6 and decreased to near 20% ± 5% by transect 10. Light pond fractional cover stayed near 10% ± 6% between transects 1 - 6 and increased to near 20% ± 5% by transect 10. Dark pond fractional cover also remained fairly constant near 1% ± 2% between transects 1 - 6, increasing to about 5.5% ± 3% by transect 10.
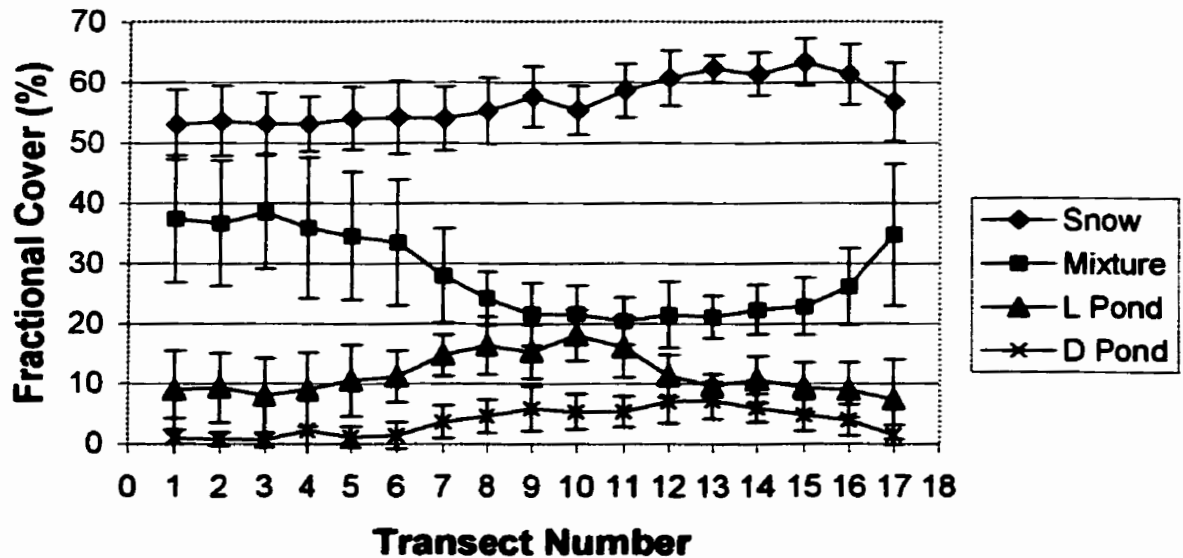
Figure 5.10: The mean and standard deviation (error bars) fractional coverage of each cover type over each aircraft transect line. All land contamination has been omitted from the data.
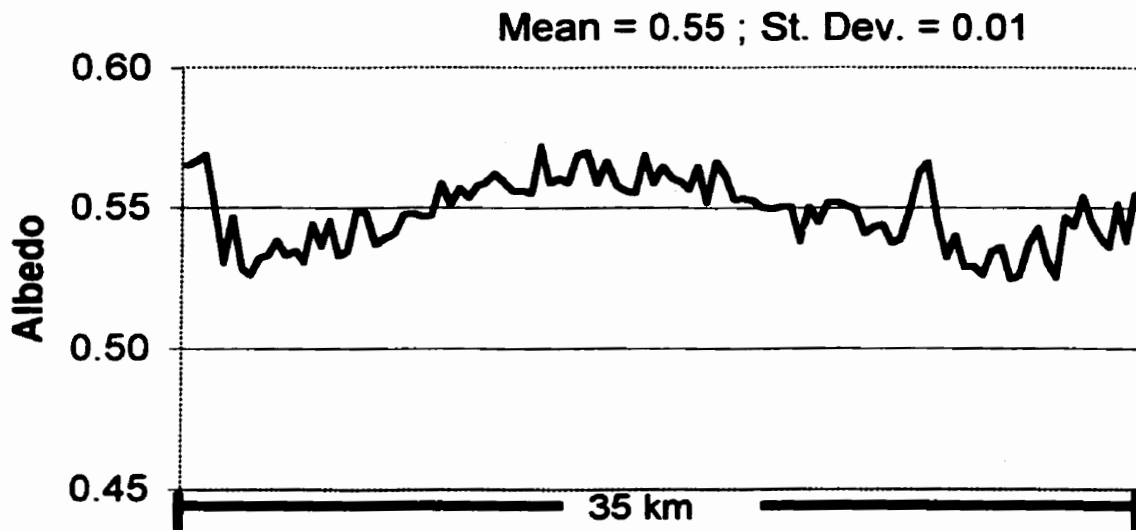
Figure 5.11: Example of aircraft video-derived broadband albedo along transects #10. Note that the data is displayed in the direction of the flight (that is, data at the left side of the figure represents the beginning of the transect).

175

	Aircraft		AVHRR	
Transect #	Mean Albedo	St. Dev.	Mean Albedo	St. Dev.
1	0.553	0.018	0.50	0.05
2	0.555	0.016	0.53	0.07
3	0.555	0.015	0.54	0.09
4	0.551	0.014	0.56	0.10
5	0.555	0.013	0.56	0.09
6	0.555	0.012	0.60	0.08
7	0.548	0.014	0.61	0.05
8	0.549	0.017	0.62	0.05
9	0.555	0.014	0.61	0.08
10	0.548	0.012	0.60	0.07
MEAN	**0.552**	**0.015**	**0.573**	**0.074**

Over rougher and multi-year ice (transects 11-17), as expected, the snow fractional cover is higher than over FYI about 62% compared to 52-53%. Melt pond fractions decrease from nearly 10% to 5% with an increase of multi-year and rougher ice as one proceeds north. The increase in fractional cover of the mixed cover type with increasing multi-year and rough ice concentration is most likely due to the brighter color of very shallow ponds and a greater occurrence of shallow water/snow mixtures in these ice regions according to visual observations.

The resulting albedos along each transect line indicate an overall mean value near 0.55, ranging between 0.548 and 0.555 with standard deviations between 0.012 and 0.018 (Table 5.2; Figure 5.11). This appears that the albedo did not change appreciably across individual transects. However, the maximum and minimum range of albedo derived from

video were 0.60 to 0.47 depending on the transect. As expected, relatively higher albedos correspond to rougher ice conditions since melt pond cover was less prominent there. The video-derived albedo within the ice camp region (between 0.52-0.55; 1st quarter of figure 5.11) is equivalent to the helicopter albedo (0.51-0.54) and the ground-based transect mean (0.53 on YD183). Once again, video-derived albedo shows greater spatial variability than helicopter measurements since the helicopter measurements are highly auto-correlated. Video-derived albedos were purposely less auto-correlated by not overlapping sequential images in the processing (see Section 5.2.2).

Video-derived mean albedo along transects 7 – 9 (Table 5.2) are also very similar to the *in situ* ground-based measurements along the same transects (recall they were 0.60 for #7; 0.55 for #8 and #9). Ground-based albedo averages along transect 8 and 9 are nearly identical to the video-derived mean albedo (0.55). The ground-based mean albedo (0.6) measured at transect 7 is slightly higher than the video-derived albedo mean (near 0.55), however, the ground measurements were taken near the vicinity of higher local video-derived albedos (not shown).
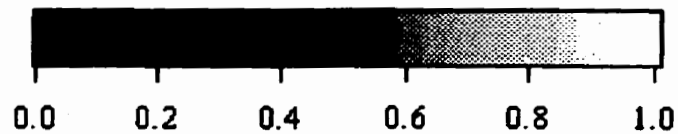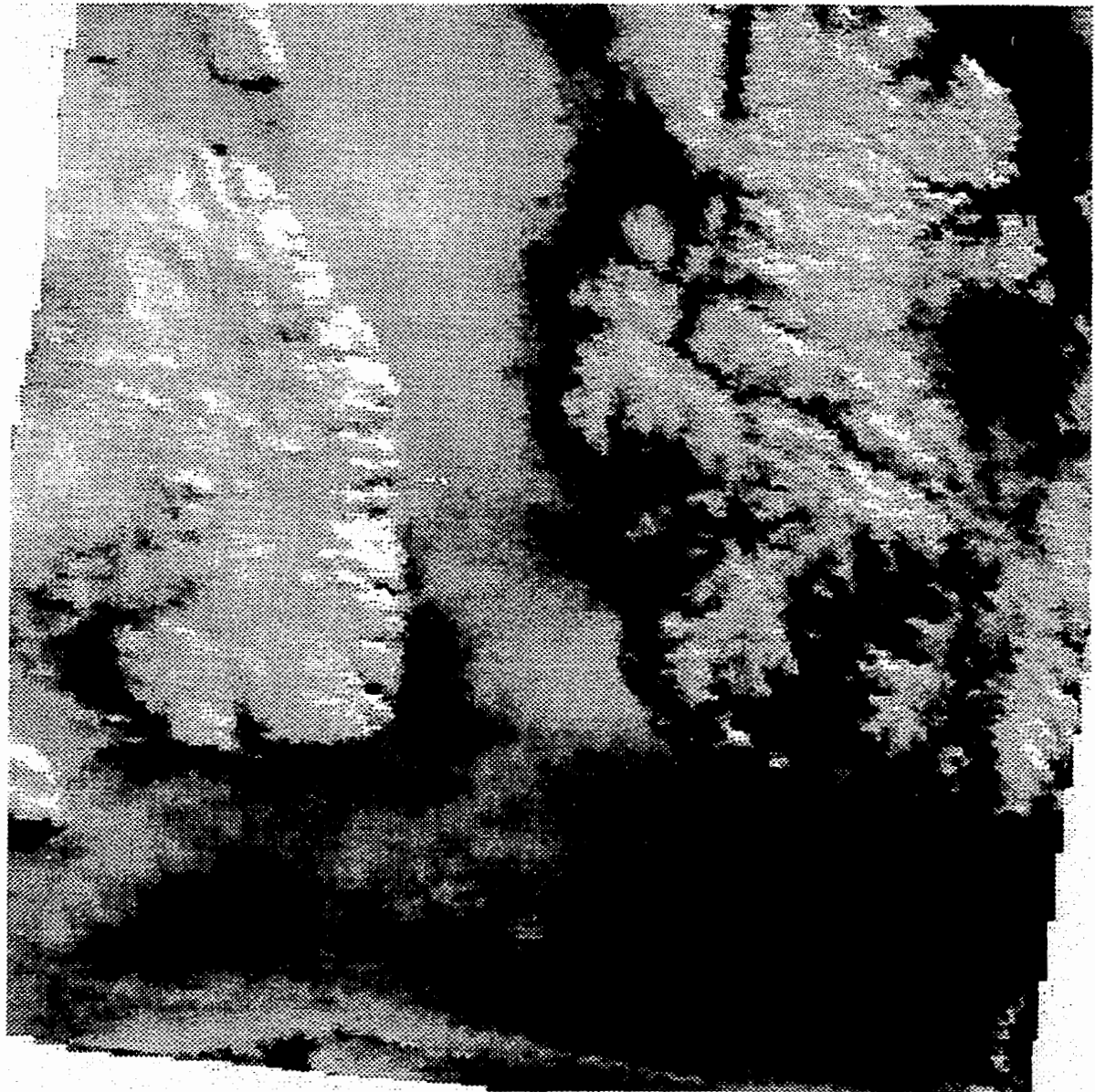
Broadband Albedo

Figure 5.12: NOAA-14 AVHRR-derived albedo on YD180 (June 29) at 0909 UTC (0409 CDT) in Lancaster Sound and Wellington Channel, one day prior to the first 6 aircraft video survey transects. Cloud contamination was present southwest of Griffith Island but did not contaminate the study region at this time. Note the ice edge in the bottom right corner of the figure. The legend indicates grey-shading corresponding to broadband surface albedo.

Regional albedo derived from AVHRR imagery shows similar overall ice conditions as Figure 5.1 with generally higher albedo in rafted and rubble ice regions (Figure 5.12). In fact, the defined rubble zone (arc of rougher ice) in Wellington channel, north of transect #10, is typified by an arc of higher AVHRR-derived albedos within and north of the same region as the SAR imagery (Figure 5.1). The rougher FYI zone depicted by SAR imagery south-west of Devon Island at the southern end of Wellington Channel is also apparent with higher AVHRR-derived albedo (Figure 5.12). Slightly higher AVHRR-derived albedo occurs in Lancaster Sound as one proceeds from the ice edge toward Griffith Island, similar to video-derived albedo along transects #1-4 (not shown). Two features may contribute to this spatial albedo pattern; 1) slightly rougher FYI in east Lancaster Sound contained greater amounts of snow compared to the smoother FYI in west Lancaster Sound, leading to more extensive ponding and deeper ponds in east Lancaster Sound, 2) warm air advection from the open water near the ice edge would promote greater surface melt near the ice edge.

Surface albedos were extracted from the AVHRR image nearly geographically coincident to the first 10 aircraft video transects. The geographic location of the transects were subjectively derived after geo-correcting the AVHRR image to correspond as close as possible to the aircraft transect GPS data. The error associated with displacements between actual aircraft transects and AVHRR transects are estimated to be approximately 1-3 km. However, this is expected to be a minor problem due to the relatively homogeneous ice surface over most of the region. Biases may arise under rougher ice

conditions such as the south-west corner of Devon Island where it is difficult to estimate these errors.

The mean values of the AVHRR-derived albedo transects are similar to the aircraft transects in the southern half of the region (transects 1-5) but are slightly greater than the aircraft data by 5% in the northern part (transects 6-10) (Table 5.2). The variability in the AVHRR data is also greater than the video albedo by roughly 0.06 (Table 5.2) making the AVHRR albedo slightly higher in Wellington Channel compared to Lancaster Sound. The variations in cloud cover between albedo measurement platforms would cause some differences between 0.03 to 0.06 albedo units based on our measurements. However, it is possible that Wellington Channel's melt progression was slower than Lancaster Sound primarily due to open water warm air advection in Lancaster Sound. I suspect that if the aerial surveys were conducted all in one day (YD181; June 30), the video data may have shown the spatial albedo differences between Lancaster Sound and Wellington Channel similar to the AVHRR data. The most significant errors in the AVHRR albedos arise from a high SZA and lack of *in situ* aerosol and ozone data at the time of the image. The high SZA induces specular reflection and artificially increases albedos in higher pond fraction regions and increased shadows (lower albedo) on the west coast of the islands, particularly Devon Island. Localized low level undetected morning fog may have also increased albedos, especially in extreme southern Lancaster Sound. Incorrect aerosol and ozone amounts would also affect albedo estimates depending on whether there were more or less of each constituent compared to what was assumed.

5.3.3. Effect of Pond Fractions on Ice Thermodynamics

In this section I examine how the thermodynamic state (and mechanical strength) of the sea ice is affected by variations in fractional pond cover (my third question in this chapter). In effect I am asking the question: "How important is it that the magnitude and spatial pattern of surface albedo (as examined via *in situ* and aerial survey approaches) is correctly parameterized within the annual cycle of sea ice ablation?" First, if we assume the evolution of surface albedo is unknown, the modeled albedo would have to be used to simulate it. A model simulation (standard run) was produced using the model's existing albedo parameterization with the exception of changing its dry snow albedo from 0.75 to 0.83 and the melting snow albedo from 0.65 to 0.73 based on measurements cited here and previous studies. In this case, the standard run produced complete ice melt by YD200 (July 19), 16 days earlier than the observed break-up date (YD217; August 5, indicated by the Canadian Ice Service charts) where *ice still existed* but was mechanically weak enough to break-up.

I define "mechanically weak ice" to be a near-isothermal vertical ice temperature profile near $-1.8°C$ based on previous work (Barber et al., 1998). This also corresponds to a bulk brine volume of about 5% where the brine drainage channels interconnect (Wakatsuchi and Kawamura, 1987) thereby severely reducing the mechanical strength of the sea ice (Cox and Weeks, 1988). In addition, the model produced albdeos near 0.28 on the same dates (YD181-185) where field measurements showed values between 0.53-0.55

(Figure 5.13) (also see section 5.3.2). This suggests the model over estimates the temporal decline in albedo and ice thickness over the melt period in this case.

The time between initial continuous snow melt to the final stages of ice ablation and mechanically weak ice ranges between 3-12 weeks in the Wellington Channel/Lancaster Sound fast-ice region based on 9 years of fieldwork and recorded break-up dates. On average then, it takes about 7 weeks from continuous snowmelt to mechanically weak ice that easily breaks up. The 1997 field season was a "typical" sea ice year based on ice and atmospheric climatology. An albedo progression over this 7 week period is shown in Figure 5.13 ("typical" curve) based on typical fractional cover type changes over this period (Table 5.3) and assuming the last week (in Figure 5.13) includes a thinner ice albedo progression to open.

Table 5.3: The "typical" or climatological fractional cover types and resulting total albedo over a 7 week period (used in Figure 5.13) produced from several years of field experiments over first-year sea ice.

Week	Wet Snow	Mixed	L. Pond	D. Pond	Total Pond	Total Albedo
1	85	15	0	0	0	0.68
2	70	20	10	0	10	0.63
3	55	30	13	2	15	0.56
4	35	25	30	10	40	0.47
5	0	20	70	10	80	0.35
6	0	50	48	2	50	0.37
7	Decay to	Open	Water	(0.15)	Or constant	at 0.37
α =	0.73	0.4	0.35	0.23		
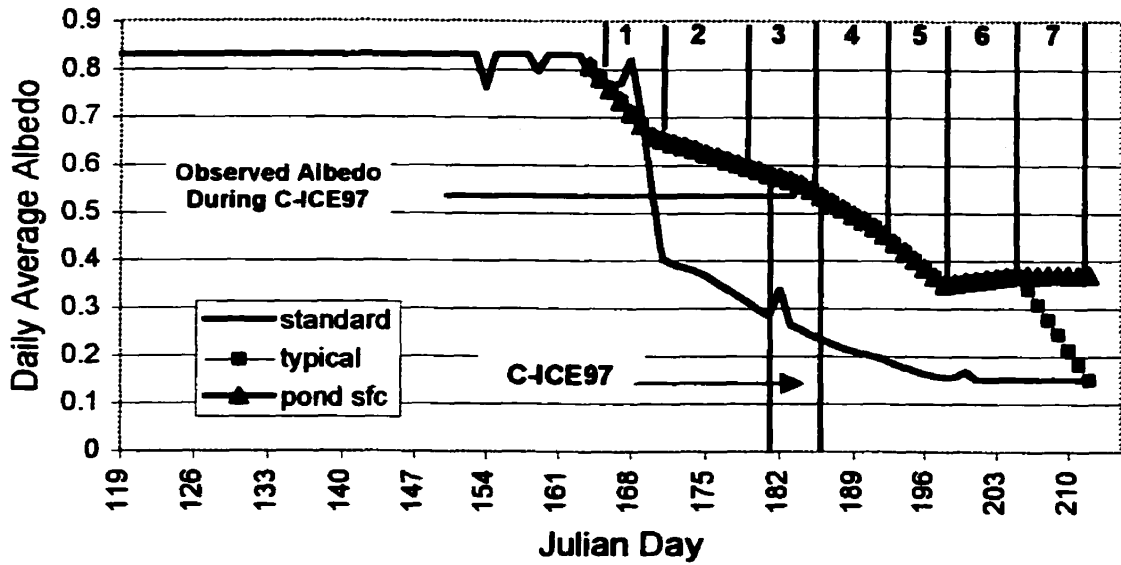
Figure 5.13: Daily average albedo between YD119 and YD212, 1997 using the model albedo parameterization (standard), a "typical" albedo progression over a 7 week period, and a "pond surface" (pond sfc) albedo progression (same as "typical" curve except using a constant albedo (0.37) for the 7th week) - See text. The "typical" and pond sfc albedo curves were derived by linearly interpolating between values in Table 5.3 over 7 weeks (labeled 1-7). The observed albedo between YD181-185 during C-ICE'97 is also indicated.
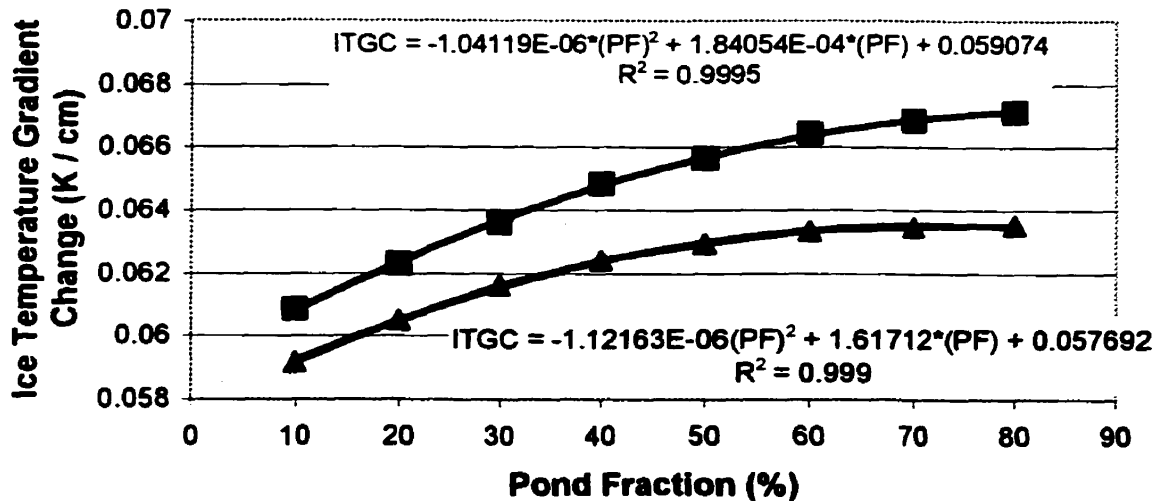
Figure 5.14: Ice temperature gradient change (ITGC) versus pond fraction (PF) after 4 days (bottom curve) and 7 days (top curve) of model simulation beginning on YD164. The quadratic equations and their R^2 describing the ITGC and pond fraction relationship for each curve are also shown.

183

Week 6 (in Figure 5.13) showed a slight increase in albedo to simulate typical pond drainage effects. If we use this "typical" albedo curve in the standard model simulation instead of using the model's albedo parameterization, the ice does not completely disappear by the end of the seventh week (YD212) but reaches a thickness near 0.7 m with a near-isothermal vertical ice temperature profile at −1.8°C. Since the ice is still thick by YD212, it is better to assume a stable albedo over week 7 instead of declining the albedo curve to open water values (0.15) (pond surface curve in Figure 5.13). Using this curve further increases the final ice thickness to 0.8 m with an ice vertical temperature profile close to becoming near-isothermal by YD212. These ice conditions are closer to the actual break-up date conditions compared to the standard simulation since ice still existed during actual break-up. Although this experiment is somewhat arbitrary (since we decouple the surface albedo from snow and ice surface changes), the point is to diagnostically illustrate how the knowledge of changes in pond fraction can affect the thermodynamic state of sea ice during its ablation stage.

The next set of modeling experiments assesses how the thermodynamic state and mechanical strength of sea ice is affected by variations in fractional pond cover (outlined in section 5.2.4) since thermodynamics determine the ice's susceptibility to break-up (Barber et al., 1998). The results of the sensitivity tests show that the ITGC (warming) can be predicted using a quadratic equation with respect to pond fraction (Figure 5.14). The quadratic relationship appears due to the physical quadratic dependence of sea ice heat capacity on temperature. The difference between the two curves in Figure 5.14 shows how the quadratic relationship changes (and the ITGC increases) between the

184

middle (4 days) and end (7 days) of the week-long simulation. As PF increases, the ITGC increases, moving the ice toward an isothermal vertical profile quicker (Figure 5.14).

The greatest acceleration in the ITGC toward an isothermal profile (greatest change in ITGC) is when ponds first form ($10\% \leq PF \leq 40\%$) and is explained by the following. As the ice approaches an isothermal profile, there is less opportunity for a temperature increase to occur in the ice (limited to near-melting temperatures), causing the ITGC to flatten out as PF increases. The quadratic relationship will change according to external forcing such as available short-wave energy (time of year and cloud cover), time the surface energy balance has to act on the ice, and to a lesser degree other atmospheric forcing variables. Pond fraction can have significant effects on the timing of near-isothermal ice profiles (Figure 5.15; using data from Figure 5.14). In this case, over a 4-day model simulation, an 80% PF can produce a near-isothermal ice profile whereas any $PF \leq 70\%$ will not. Over a 1 week simulation, PF's $\geq 50\%$ produced near-isothermal ice profiles and PF's $\leq 40\%$ did not (Figure 5.15). At these rates of warming, the difference in timing to reach an isothermal ice profile (and mechanically weak ice) is >3 weeks between a surface with 10% PF compared to 80% PF. This shows the sensitivity of sea ice temperatures and its susceptibility to break-up according to variations in pond fraction.

These model experiments strongly suggest that it is preferable to either better parameterize or remotely measure (by satellite) pond fractions and their associated albedo for use in annual operational or diagnostic model simulations. Due to the dynamics of how the seasonal evolution combines with snow distribution and sea ice topographic

snow catchment, I consider the remote estimation of pond fractions a preferred approach

for model input under operational or diagnostic settings.
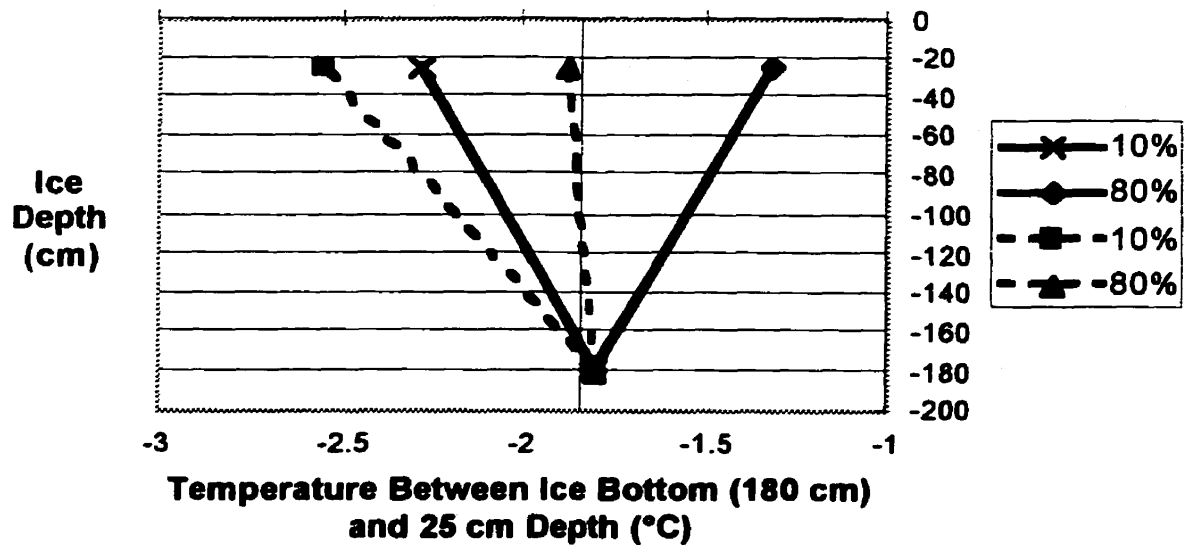
Figure 5.15: Ice depth (cm) versus temperature (°C) between the ice-ocean interface and 25 cm from the top ice surface. Dashed (solid) lines are the final ice temperature profiles after 4 days (7 days) of model simulation using 10% and 80% pond fractions.

5.4 Conclusions

The main theme of this chapter has been to examine the spatial aspects of

fractional surface cover types and surface albedo and to determine the role melt ponds

play in thermodynamic evolution of land-fast FYI in the Canadian Arctic Archipelago. I

outlined three basic questions toward this theme: 1) what are the surface albedos over FYI

and how do they vary over local scales?, 2) how do the surface measurements scale up to

regional scales for larger scale albedo mapping?, and 3) how sensitive is sea ice ablation to percent pond fraction and the associated spatial variability in surface albedo?

5.4.1 Question 1

Results show large variations in broadband and spectral albedos associated with various surface features that one would encounter during the FYI melt season. Albedo varied between 0.75 and 0.21 for a deeper moist snow cover to dark older ponds, respectively. Intermediate surfaces include dense wet snow (0.67), shallow wet and saturated snow (0.52-0.65). Light colored melt ponds with 3-6 cm water depths had albedos which range between 0.32-0.36. Our observations were similar to Grenfell and Perovich (1984) and Perovich (1996), over comparable surfaces.

5.4.2 Question 2

The second set of results used the surface albedo measurements, applying them to aircraft video-derived surface cover type identification over a large region to obtain regional scale (100's km) albedo to compare them to satellite-derived AVHRR albedo. Four basic cover types and their statistics (% cover) were identified. Snow patch fractions ranged between 53-58%, mixed cover type fractions 20-38%, light pond fractions 6-18%, and dark pond fractions 1-5%. Over rougher and multi-year sea ice

(MYI), snow fractions were higher than over the smooth FYI (62-65% compared to 53-58%) and MYI melt pond fractions were half those over FYI. These fractional cover types were then converted to overall albedo revealing similar regional albedos over smoother FYI ranging between 0.54 – 0.56 with standard deviations of 0.01 – 0.02. These were similar to helicopter-measured albedos (0.52-0.55), ground-based measurements and the overall AVHRR-derived mean albedo (0.57) over the same region. Relatively higher albedos corresponded to rafted/rubbled ice conditions since melt pond cover was less prominent there.

5.4.3 Question 3

For the final question, I used a one-dimensional thermodynamic sea ice model to show how the various fractional cover types can affect the thermodynamic state and hence the ice's susceptibility to break-up. Mechanically weak ice can be defined by a near-isothermal vertical temperature profile near −1.8°C (Barber et al., 1998). This experiment also revealed the importance of being able to monitor melt pond fractions and surface albedo through the course of the melt season to indicate when the ice is most likely to break up. This is of particular importance to climate change research for improved understanding of sea ice processes, Arctic shipping, and indigenous people's safety who use the ice for traveling and hunting. First, if we do not know the albedo or pond fraction throughout the model simulation, the use of an albedo parameterization is required. Using the model's albedo parameterization resulted in a 16-day earlier break-up

than observed with complete ice ablation taking place. Complete ablation did not take place in actuality since the ice broke up before this could happen. The model produced a more rapid decrease in albedo and ice thickness over time than was observed. I then assumed a climatological temporal albedo progression produced by several years of fieldwork in the region under study. This resulted in more realistic ice conditions (physically and thermodynamically) when break-up actually occurred. The experiment is somewhat arbitrary since we decoupled the albedo from modeled snow and ice changes, however, the point was to diagnostically show how the albedo affects these kinds of simulations.

The simulations above set the stage for another set of experiments designed to explicitly show how changes in melt pond fraction can alter the ice's thermodynamic state and thus susceptibility to break-up. It was found that the vertical ice temperature gradient change (ITGC) increased as a quadratic with respect to linear increases in pond fraction (PF) in this case. Using the ITGC, an ice surface with 80% pond fraction can produce a near-isothermal ice profile more than 3 weeks earlier than an ice surface with 10% pond fraction. Factors that alter the ITGC relationship with PF are external forcing such as available short-wave energy (time of year and cloud cover), time the surface energy balance has to act on the ice, and to a lesser degree other atmospheric forcing variables. The modeling exercise shows the sensitivity of sea ice temperatures and its susceptibility to break-up according to variations in pond fractions. The model experiments also show that we require either better parameterizations or remotely measured (by satellite) pond fractions and their associated albedo for use in model simulations.

5.5 Summary

In summary, I have added to the number of albedo measurements made over FYI during the critical melt pond period and scaled up these surface measurements to regional scales. This was done by understanding which surface cover types become the most important features for modeling large scale albedo in FYI sea ice models. The results will ensure the SEB short-wave responses are appropriately handled in FYI models during the melt pond period (thereby addressing the second issue of my dissertation). I have also linked the changes in short-wave response by means of pond fraction to the thermodynamic state of FYI. That is, if the pond fraction is known, one may determine how long it will take for FYI to become mechanically weak given certain atmospheric forcing, assuming the atmospheric conditions and pond fraction do not change appreciably. This information is useful for climate change research for improved understanding of sea ice processes, arctic shipping (operational ice forecasting), and indigenous people's safety who use the ice for traveling and hunting.

This chapter (Chapter 5) primarily focused on the melt pond period when snow has virtually entirely melted. The following chapter looks at the period of time prior to melt pond formation by outlining the importance of the snow layer in annual FYI cycles from a modeling perspective. However, several albedo measurements of melting snow from Chapter 5 can be applied to results in Chapter 6 in the future. Chapter 6 focuses on improving the handling of the snow layer within thermodynamic models of sea ice. If the models do not realistically recreate the snow layer evolution, the simulated melt pond

period may occur too soon or too late in the year, ultimately leading to unrealistic FYI evolution. The next chapter compares snow and ice simulations from a FYI model that treats the snow layer as a single bulk homogeneous slab (as in Chapter 3) and a coupled snow sea-ice model that treats the snow layer in a much more rigorous and realistic fashion. Results will suggest whether using a more sophisticated model is warranted for annual cycles of FYI. The coupled model is also a necessary step for linking thermodynamic modeling to microwave remote sensing in Chapter 7.

CHAPTER 6: Coupled 1-D Thermodynamic Snow Sea-Ice Model: Climate Processes

6.1 Introduction

This chapter is devoted to illustrating the importance of the snow layer and its processes on FYI over annual cycles using numerical modeling techniques. This is done by advancing the modified 1-D sea ice model of Flato and Brown (1996) used in Chapter 3 by coupling it to a 1-D mass and energy balance snow model called SNTHERM (see Jordan, 1991; Jordan et al., 1999). The purpose is to illustrate snow and ice evolutionary differences between the simpler 1-D sea ice model (in Chapter 3) and the more sophisticated coupled snow sea-ice model and compare them to *in situ* observations. This will suggest whether there is an advantage of using a more sophisticated model for annual snow-covered FYI. The other purpose for developing and testing a coupled snow sea-ice model is for microwave remote sensing applications (Chapter 7).

SNTHERM was adapted to simulate snow thermal and mass balance processes over sea ice by Jordan et al. (1999) but lacks other physical processes (such as an ocean mixed layer) to be used exclusively over FYI that ablates every summer and reforms in the fall. The coupling of SNTHERM to the Flato and Brown ice model allows the coupled model to simulate full FYI annual cycles with more sophisticated layered snow processes instead of a single bulk homogeneous snow slab.

The snow layer portion of the coupled model (SNTHERM) is designed to numerically simulate within-snow temperatures, bulk density, snow grain diameter, liquid water content, and other mass and energy exchanges for each snow layer (or node) over time. It does this by accounting for many of the physical processes outlined in Chapter 2

including the surface energy balance (SEB), snow metamorphism, compaction, melt effects, settling from age and overburden, liquid water filtration, blowing surface snow and wind packing, and newly fallen snow evolution to name a few. All of these processes are important for determining the optical, thermal and mass balance properties in the snow. Some of the model limitations have been described in section 2.3.3.

Salinity in snow is also an important feature that is typical of snow over FYI. Salinity plays a large role in snow thermodynamics (Papakyriakou, 1999) and microwave dielectric properties (see for example Barber et al., 1994; Barber and Nghiem, 1999). Thermal conductivity and specific heat parameterizations have been implemented in the coupled model to account for salinity affects on snow thermal properties (see section 6.2) since SNTHERM did not account for salinity in this manner. Note however the physical presence of salt in snow is not parameterized with regards to its affects on partial fractions of ice, air and liquid (brine) which can further affect the thermal snow state. The result of this simplification will be seen throughout Chapters 6 and 7. A description of how salinity was parameterized, the model coupling process, and model forcing is given in the following section.

In summary, the main objective of this chapter is to demonstrate the basic differences between a coupled 1-D snow sea-ice model and a similar model that uses only a single bulk property snow layer. In situ observations from SIMMS'92-93 (LeDrew and Barber, 1994) are used to quantify model performance. I also explore coupled model sensitivity to salinity in the snow layer through its effects on thermal conductivity and specific heat using parameterizations outlined in Papakyriakou (1999). Crocker (1984) demonstrated that salinity in snow and its effect on thermal conductivity improved a

193

simple fast-ice growth model, although his study did not include a full annual cycle for comparisons. Other studies suggest the importance of snow thermal conductivity on sea ice in a global climate context (see for example, Fichefet et al., 2000) but do not account for salinity effects directly. The specific research questions include:

1) Are there model differences in seasonal snow and ice thickness evolution and how do they compare to observations?

2) What are the model thermodynamic differences and how do they compare to observations?

6.2 Observational Data and Numerical Models

6.2.1 Observational Data

The field observations used here are the same as those in Chapter 3 that were collected in the spring/summer periods during the SIMMS (Seasonal Ice Monitoring and Modeling Site) experiments between 1992-1993 near Resolute, Nunavut. The 1992-93 sea ice cycle was selected to perform the numerical model simulations since the non-coupled model simulations during this period were previously conducted in Chapter 3 appearing in Hanesiak et al. (1999). These two spring periods also offered distinctly different sea ice and meteorological conditions (see Chapter 3).

The field observations included incident and reflected short-wave radiation ($K\downarrow$, $K\uparrow$), net short-wave ($K^* = K\downarrow - K\uparrow$) downwelling and upwelling long-wave radiation ($L\downarrow$, $L\uparrow$), net long-wave ($L^* = L\downarrow - L\uparrow$) and net radiation ($Q^* = K^* + L^*$). The observations also include vertical temperature profiles within the snow/ice volumes and

snow and ice thickness. Instantaneous on-the-hour data were used since this corresponds to the temporal forcing used in the model simulations. Errors in snow and ice temperature measurements are roughly 0.2 - 0.5°C but may be higher in snow during the melt period. Snow and ice thickness were measured periodically throughout each field season with typical errors near 1 cm and 8 cm for snow and ice, respectively.

Other surface observations include hourly standard meteorological observations taken at Resolute, Nunavut between YD107, 1992 to YD170, 1993 by the Meteorological Service of Canada (MSC). The pertinent data include air temperature (T_a), relative humidity (RH), wind speed (u), precipitation (sfall), and 3 cloud layer fractions (c).

The snow layer salinity profiles used in the model simulations were derived from measurements in Barber et al. (1995b). A third-order polynomial was fit along the data to produce an average (AVG) profile and conservative upper limit (UPR) profile (Figure 6.1) given by

$$S\,(AVG) = 17.3882 - 172.212\,z + 571.259\,z^2 - 634.732\,z^3 \qquad (6.1)$$

$$S\,(UPR) = 25.5346 - 249.507\,z + 821.958\,z^2 - 913.287\,z^3 \qquad (6.2)$$

where z is the increasing snow depth above the ice surface (in meters) and S is salinity (ppt). Note that snow depths >30 cm will produce unrealistic negative salinities. A provision in the model was inserted to ensure negative salinities did not occur. The use of more accurate (but more computationally expensive) cubic spline fits did not offer advantages over the third-order polynomials and were not used. The salinity profiles were held constant in time for simplicity and is considered a valid assumption until significant liquid water filtration occurs within the snow (i.e. brine flushing; see Barber et al. 1994).
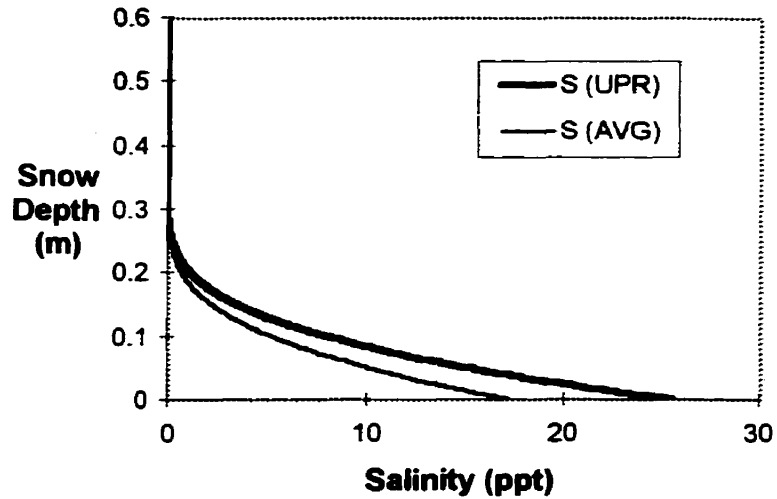
Figure 6.1: The snow salinity (ppt) versus depth above the ice surface (m) third-order polynomials fit along average (AVG) and upper limit (UPR) observations made by Barber et al. (1995b) for a 60 cm snow depth.

6.2.2 Numerical Models

The modified FYI model of Flato and Brown (1996) (in Chapter 3 and Hanesiak et al., 1999) is coupled to SNTHERM (Jordan et al., 1999); a type of coupled model that has previously been unavailable. The non-coupled model is the modified FYI model of Flato and Brown (1996) in Chapter 3. The ice and snow models are coupled at the top ice layer with similar thermal properties (temperature, density, thermal conductivity and heat capacity). This was done to preserve the snow model handling of mass balance at the snow-ice interface, i.e. excess liquid water that is not re-frozen at the base of the snow pack is artificially drained to simplify mass exchanges (Jordan et al., 1999). Heat fluxes from the snow model are passed into the ice model that computes the new ice temperatures that are in turn passed back into the snow model at each time step. The time step is variable to a minimum of 5 s during water flow within the snow. The SEB is

controlled by the snow portion of the model when snow is present and by the ice model if snow is absent. This was done since the turbulent exchange parameterization in the snow component of the model is more sophisticated than the ice model. When snow is not present during the melt pond season, the surface properties such as albedo are better (although very simply) handled in the sea ice model.

The coupled and non-coupled models are forced with basic hourly meteorological data; air temperature, relative humidity, wind speed, incident short-wave and long-wave radiation along with measured surface albedo. If incident radiation and albedo are not measured, they can be parameterized with additional cloud cover input data. The coupled model is initialized with snow and ice physical profiles (densities, grain sizes, layer thickness) and temperature profiles. The non-coupled model is similarly initialized but without the internal snow physical properties. Fifty ice layers are used here in both models that remain constant in number over time. A variable number of snow layers exist in the coupled model depending on snow layer characteristics (see Jordan et al. 1999). Specific information about the snow and ice components of both models can be found elsewhere (Flato and Brown, 1996; Jordan et al., 1999; Hanesiak et al., 1999).

The snow thermal conductivity (k_s) and specific heat (C_s) parameterizations are discussed next since they are used for the inclusion of salinity within the snow. Note that the physical presence of salt in snow is not parameterized with regards to its affects on partial fractions of ice, air and liquid (brine) which can further affect the thermal snow state. The result of this simplification will be discussed later. Salinity inclusions significantly reduces the snow thermal conductivity and increases the snow specific heat (when excluding salinity from the mass balance) depending on salt content and

197

temperature (Papakyriakou, 1999). The snow effective thermal conductivity (k_s) without inclusion of salinity is estimated from density (ρ_s) by Jordan et al. (1999) as

$$k_s = k_a + (7.75 \times 10^{-5} \rho_s + 1.105 \times 10^{-6} \rho_s^2) (k_i - k_a) \qquad (6.3)$$

where k_a and k_i are the thermal conductivities of air (0.023 W m^{-1} K^{-1}) and ice where k_i varies with temperature as

$$k_i = (780 / T) - 0.615 \qquad (6.4)$$

where k_i is in W m^{-1} K^{-1}, ρ_s in kg m^{-3} and T is in Kelvin.

The effective thermal conductivity for saline snow (k_{ss}) is estimated from the modified Pitman and Zuckerman (1967) model by Crocker (1984) and further by Papakyriakou (1999). Conservative limits of this model are between snow salinities (S) of 0 to 40 ppt, ρ_s between 100 to 450 kg m^{-3}, and liquid water contents up to about 8% Wv (water by volume). The k_{ss} scheme was used in place of the original k_s parameterization even for non-saline snow layers. A lower limit to k_{ss} was arbitrarily set to 0.001 W m^{-1} K^{-1} in snow to prevent unrealistically low values at or near melting temperatures and preserve model stability during these events.

The apparent specific heat (C_s) (sensible and latent heating) for non-saline snow is parameterized as in Jordan et al. (1999) by

$$C_s = C_t + L_{li} (\gamma_w / \rho_t) (\partial f_i / \partial t) \qquad (6.5)$$

where C_t is the combined specific heat in terms of mass fractions (ice and water) = $(1/\rho_t)($ $\gamma_i C_i + \gamma_l C_l)$, ρ_t is the combined density, γ_i is the bulk ice density, γ_l is the bulk liquid density, γ_w is the combined bulk density, C_i is the specific heat of ice (= -13.3 + 7.8 T),

C_l is the specific heat of water (4217.7 J kg^{-1} K^{-1}), L_{li} is the latent heat of fusion for ice

(3.335 x 10^5 J kg^{-1}), and (∂f_l / ∂t) is the time rate of change for mass liquid-water fraction

($f_l = \gamma_l$ / γ_w). Mass-liquid water fraction (f_l) takes an empirical form from Guryanov

(1985) and is outlined in detail in Jordan (1991). All units are in standard SI.

The apparent specific heat for saline snow (C_{ss}) was empirically derived from

experimental measurement via Ono (1966) given by

$$C_{ss} = 2.114 + 0.0075 \; T + 18052.0 \; S \; / \; T^2 - 3.35 \; S + 0.84 \; S \; T \qquad (6.6)$$

where C_{ss} is in units of kJ kg^{-1} °C^{-1}, T is in °C and S in kg kg^{-1} (ppt/1000). The C_{ss}

scheme replaced the original C_s parameterization, similar to the thermal conductivity. An

upper limit to C_{ss} was arbitrarily set to 5x10^4 J kg^{-1} C^{-1} in snow to prevent extreme high

values at or near melting temperatures and preserve model stability. A comparison

between k_s, k_{ss}, C_s, and C_{ss} for the non-saline and saline cases is discussed in chapter 7

where a more detailed investigation of the coupled model is performed.

6.3 Methods

To examine the first question, the non-coupled (NC), coupled model without

salinity (C), and coupled model with salinity (UPR; using the UPR salinity curve in

equation 6.2) were forced with Resolute meteorological data between YD107, 1992 to

YD170 1993. The models were initialized and forced with exactly the same snow/ice,

radiative and meteorological data. Further to question 1, sensitivity runs were conducted

to examine detailed differences in snow and ice evolution and ice growth between the

models in a fall freeze-up scenario. This involved similar model runs as above except they were initialized with an ice thickness equal to 1 cm and 8 cm snow layer on YD195. Because of significant snow thickness differences between the coupled and non-coupled models (see section 6.4), the NC was forced to use precisely the same snow thickness evolution as C for the freeze-up case. This allowed a very detailed look at snow and ice evolution differences between C, NC, and UPR.

To examine the second question, NC, C and UPR were forced with SIMMS'92 *in situ* radiative and meteorological data between YD107 to YD177, 1992. The models were initialized with YD107 SIMMS'92 snow and ice data. Snow and ice thickness evolution variations were examined as above. In addition, the coefficient of determination (R^2), mean bias error (MBE), and root-mean-squared error (RMSE)) were computed for thermodynamic variables including the snow surface temperature (T_{sfc}), ice surface temperature (T_{isfc}), and net surface heat flux (Q_{net}). Q_{net} is defined here to include the net radiation and turbulent heat fluxes and was included since it directly impacts the thermodynamics. This allowed a detailed look at model differences given similar forcing and high temporal resolution *in situ* data to gauge model performance.

6.4. Results

6.4.1 Seasonal Snow and Ice Evolution

The C snow and ice thickness evolution is closer to observations compared to NC for both years that were simulated (Figure 6.2). This is partially due to the blowing snow parameterization in C; NC does not parameterize blowing snow. The fractional stress

gradient in the blowing snow scheme of C was altered to provide a more realistic snow evolution according to the wind conditions at the SIMMS site (see Chapter 2 and Jordan et al., 1999). If C produced a deeper snow cover, its simulated snow decay would be closer to observations (see section 6.4.2). In general, differences between actual and parameterized incident radiation as well as meteorological conditions between Resolute and the SIMMS site can create discrepancies between modeled and observed snow/ice evolution; this can be seen in section 6.4.2 and has been noted previously (Hanesiak et al., 1999). It is interesting to note the 1992 break-up (BU) and freeze-up (FU) dates of C (BU = YD198; FU = YD293) lie between the hourly simulation and the daily simulation from Chapter 3, within the BU and FU periods indicated by the Canadian Ice Service (CIS) charts (see Figure 3.2). Also note the NC simulation is not the same as the hourly simulation from Chapter 3 due to differences in forcing (i.e. NC was forced with incident radiation derived from C).

The differences between C and UPR were fairly small so only UPR is shown in the figures. For instance, salinity delayed complete snow ablation by 1 day and only 2 days for the ice cover in 1992. This resulted in a 1 day sooner freeze-up date for UPR compared to C, and the final ice thickness for UPR was only 4 cm thicker than C by the end of SIMMS'93. However, if snow would have fallen during the final 2 days of ice melt in UPR, this would have, 1) prolonged the ice cover existence, 2) induced earlier freeze-up and, 3) increased the final ice thickness by the end of SIMMS'93. It should be noted the results may have been slightly different if salinity were treated in the UPR mass balance since liquid water (brine) would be generated sooner in the spring period. Future work will investigate this.
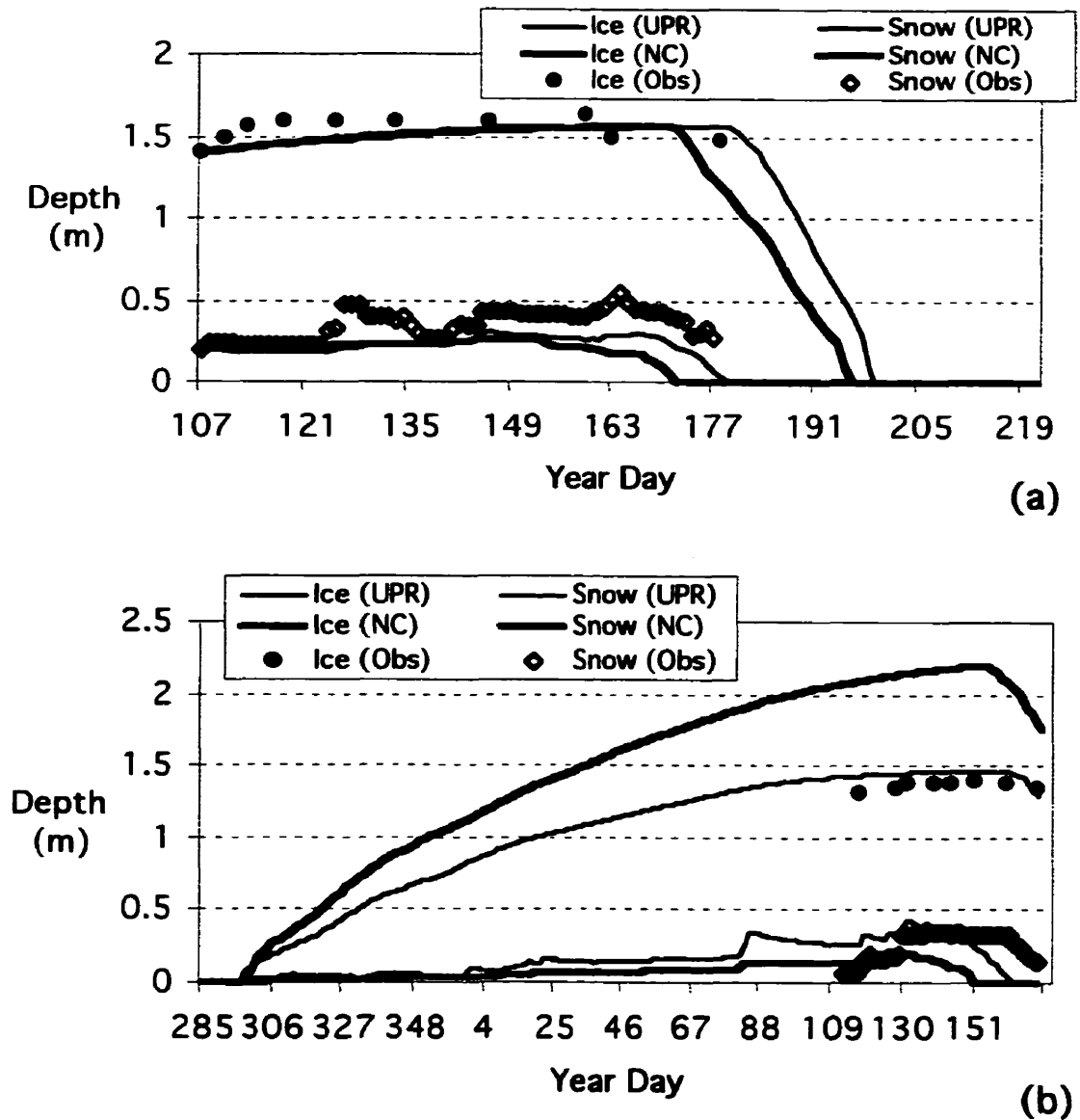
*Figure 6.2a, b: Observed (obs), UPR and NC snow and ice thickness evolution from a)
the beginning of SIMMS'92 to break-up, and b) freeze-up to the end of SIMMS'93 using
Resolute meteorological forcing from YD107, 1992 to YD170, 1993. Note that C and
UPR were very similar, hence only UPR is shown.*

To illustrate a more detailed look at model differences on ice growth and seasonal

snow and ice evolution, a freeze-up sensitivity scenario was conducted (discussed in

section 6.3). In this case, maximum ice thicknesses were 1.4 m and 2.05 m for C and NC,

respectively; a difference of 65 cm (Figure 6.3). Once again, snow thickness evolution

202

between C and NC was also significant due to blowing snow (Figure 6.3). If NC is forced to have the same snow thickness evolution as C, the maximum ice thickness of NC is reduced to 1.95 m (FS curve in Figure 6.3), making the difference between C and FS 55 cm. Adding salinity to the snow did not alter the freeze-up simulations appreciably, hence only the UPR curve is shown (Figure 6.3). Ice growth with salinity was slightly reduced (by a few cm) in the cold period but ice ablation in the spring period was also reduced effectively nullifying k_s and C_s salinity effects on the ice seasonal evolution differences. The maximum ice thickness difference between C and UPR was only 3 cm.
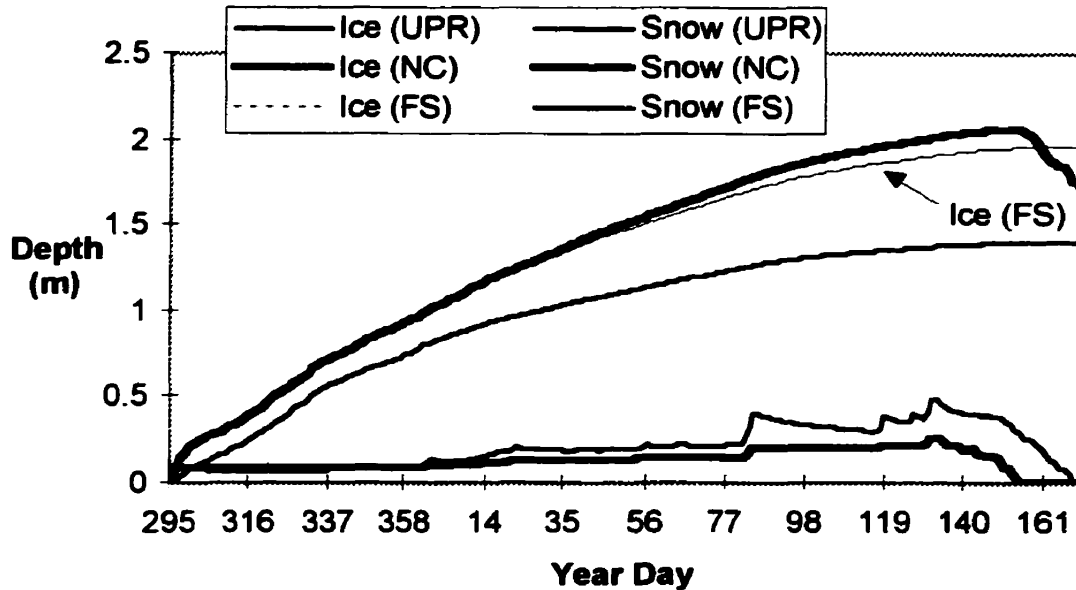
Figure 6.3: UPR and NC snow and ice thickness evolution for the freeze-up sensitivity study between YD195, 1992 to the end of SIMMS'93. The "ice (FS)" curve is the ice thickness evolution for NC when it is forced to have the "snow (UPR)" curve. The "snow (FS)" and "snow (UPR)" are overlapping in the figure. Note that C and UPR are virtually the same for snow and ice.

The above results clearly show the coupled snow sea-ice model produces thinner ice and more realistic snow and ice conditions using this data set. As expected, salinity

effects on k_s and C_s act to slightly reduce both ice growth rates in the cold season and ablation rates in the spring melt period. Once again, the results may have been slightly different if salinity were accounted for in the UPR mass balance. Predicting these effects over an entire annual ice cycle is difficult due to the liquid water (brine) influence on snow density and thermal properties. Further work is required in this regard.

6.4.2 Thermodynamic Evolution

To examine the second question, NC, C and UPR were forced with *in situ* data over the SIMMS'92 duration (discussed in section 6.3). The snow thickness evolution of C (and UPR) follows the observed progression fairly well (Figure 6.4) for reasons discussed in section 6.4.1. The result of using *in situ* radiative and meteorological forcing instead of parameterized radiation and Resolute data is revealed when comparing Figures 6.2a and 6.4 and the ice conditions; i.e. snow and ice ablation are delayed and slower than those in section 6.4.1. Ice thickness changed from 1.4 m (initial value) to 1.53 m for C and 1.4 m to 1.58 m for NC over the 70 day simulation; observed values at the end of the experiment were 1.5 ± 0.08 m. There was no difference between C and UPR so only UPR is shown (Figure 6.4).
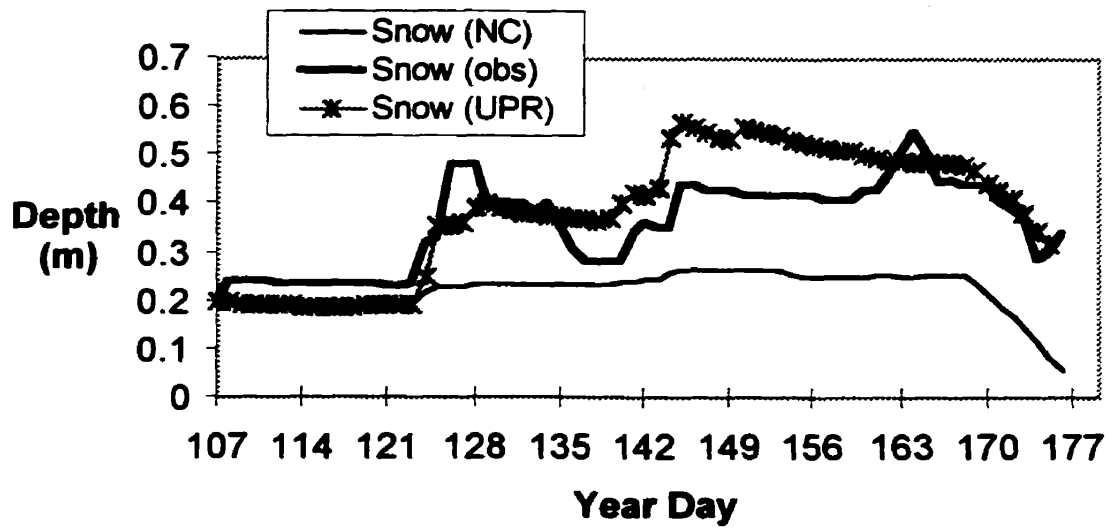
Figure 6.4: The observed (obs), NC and UPR snow thickness evolution between YD107 and YD177, 1992 using SIMMS'92 in situ data as model forcing. The UPR snow evolution is different than "snow UPR" in Figure 6.2a due to greater wind speeds on the ice compared to Resolute.

Table 6.1 Non-coupled (NC) model, coupled model without salinity (C), and coupled model with salinity (UPR) R^2, mean bias error (MBE) and root-mean-squared error (RMSE) compared to observations of Q_{net} (W m-2), T_{sfc} (°C), and T_{isfc} (°C). NC model data are adapted from Hanesiak et al. (1999). Note there was no difference between C and UPR for Q_{net} and T_{sfc}. Observed mean values are shown for reference.

	$Q_{net}(NC)$	$Q_{net}(C)$	$T_{sfc}(NC)$	$T_{sfc}(C)$	$T_{isfc}(NC)$	$T_{isfc}(C)$	$T_{isfc}(UPR)$
R^2	0.56	0.74	0.98	0.99	0.98	0.99	0.99
MBE	-2.00	+3.00	-0.10	-0.06	-0.58	+0.95	+0.98
RMSE	25.0	21.0	1.7	1.3	0.7	0.5	0.5
Mean Obs	-1.4	-1.4	-9.8	-9.8	-7.2	-7.2	-7.2

In addition, the statistical comparison between T_{sfc} and Q_{net} for C and NC indicates that C reproduces Q_{net} more accurately but little difference is apparent in T_{sfc} (Table 6.1). It can be expected that differences in T_{sfc} would be small between C and NC

due to thermal balancing between the snow surface and atmosphere. However, since C (and UPR) use very different turbulent exchange parameterizations than NC, one may expect to see larger differences in their respective Q_{net}. The C T_{sfc} is very close to the observed T_{sfc} evolution, even during the critical melt period (Figure 6.5). There was no difference in T_{sfc} evolution between C and UPR.
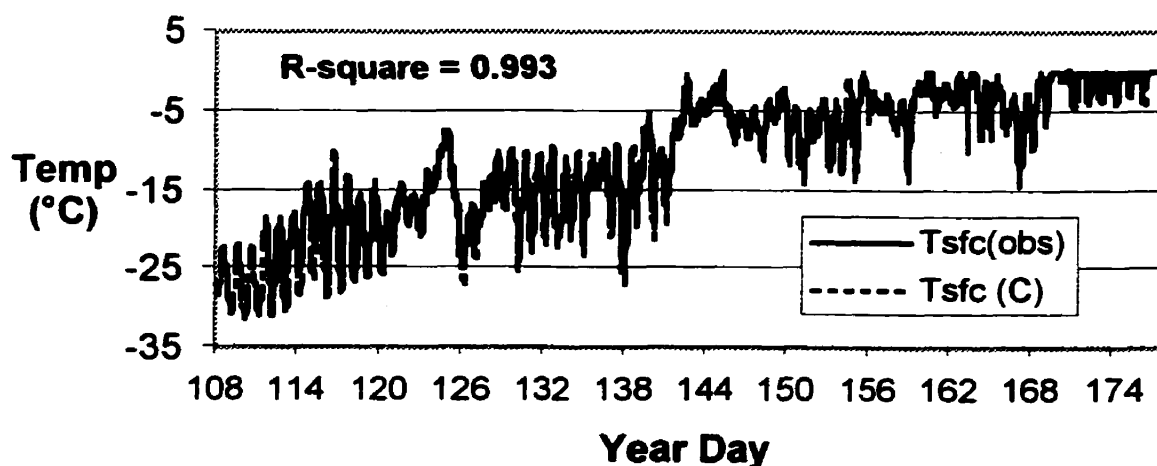
Figure 6.5: The C snow surface temperature (T_{sfc}) versus observations (obs) between YD107 and YD177, 1992 using SIMMS'92 in situ data as model forcing. The R^2 is also shown. Note there was no difference between C and UPR.

The simulated ice surface temperatures (T_{isfc}) in C are slightly too warm and NC are slightly too cold for the middle period of SIMMS'92 (Figure 6.6a and Table 6.1). The addition of salinity to k_s and C_s acts to increase T_{isfc} in the colder season and decrease T_{isfc} in the melt season, with more dramatic effects in the melt season (i.e. the decrease in snow thermal conductivity and increase the snow specific heat are more pronounced during melt). The warming effect of salinity in the colder season may or may not be counteracted if salt were parameterized in the UPR mass balance since the complicated

effects of liquid water (brine) and latent heat due to phase changes would be generated sooner in the spring period. The NC T_{isfc} is closer to observations in the cold season compared to C. It will be shown (Chapter 7) that snow density during the cold season may be under estimated in C and UPR at several layers. This would artificially decrease snow thermal conductivity and effectively cause C and UPR T_{isfc} to be too warm as shown here. Effects of salinity in the mass balance would also complicate the process, as explained above.

An interesting observation is the diurnal cycling (waves) of temperatures within UPR are better reproduced compared to C and NC (Figure 6.6b). Cross-correlation analysis suggests NC T_{isfc} diurnal waves are about 5-6 hours out of phase with observations, whereas C was 2-3 hours out of phase during the colder season; the inclusion of salinity in the snow k_s and C_s further decreased this phase difference between 0-1 hour. This suggests NC does not damp out air temperature changes sufficiently; this is evident beyond YD124 where air temperatures significantly declined along with NC T_{isfc}, whereas the observations, C and UPR do not (see Figure 6.6b). The complex problem of snow thermal conductivity, specific heat, thermal diffusivity and salinity effects on mass balance are still largely under debate and very detailed. I will only state that more work is required in these areas.
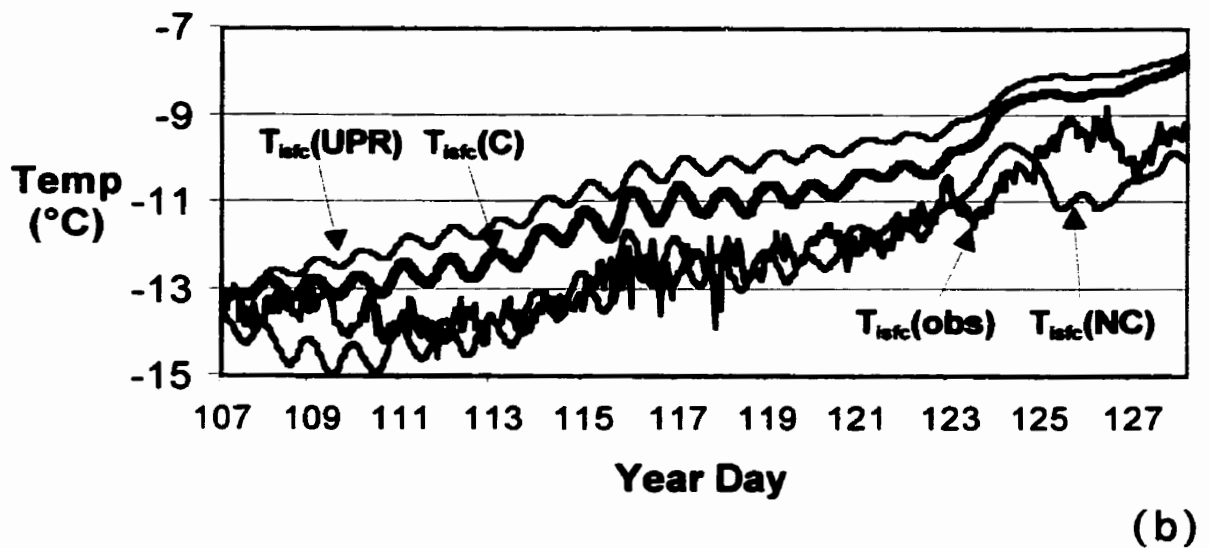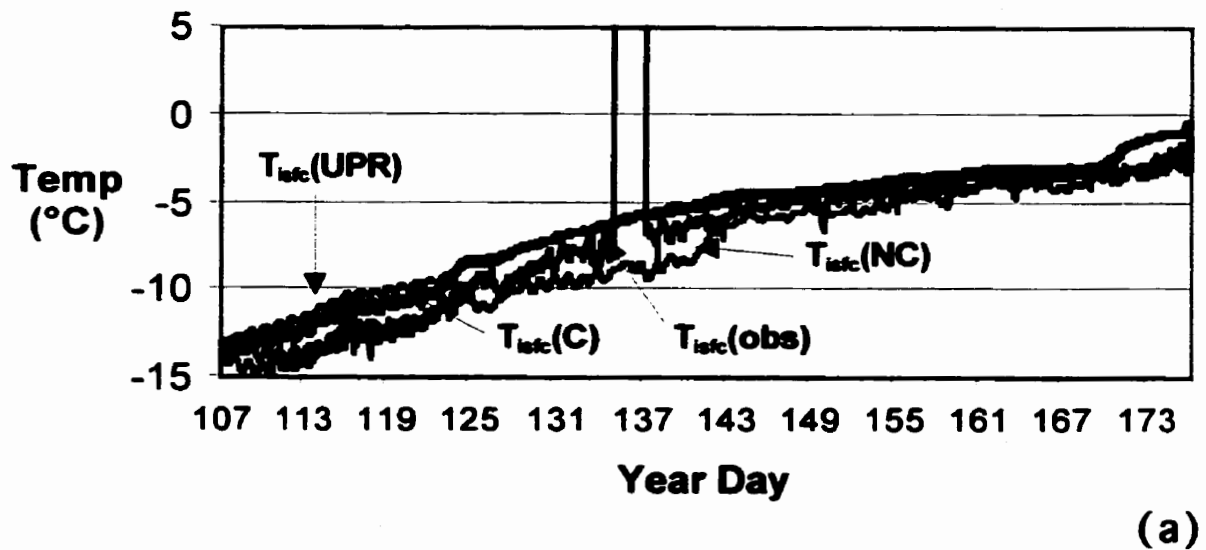
Figure 6.6a,b: The NC, C, and UPR simulated ice surface temperature (T_{isfc}) versus observations (obs) between, a) YD107 to YD177 and b) YD107 to YD128. Observed data between YD135 - YD138 are missing.

6.5. Conclusions

The goal of this chapter is to examine whether there are advantages of using a more sophisticated treatment of the snow layer for modeling the annual cycles of snow-covered FYI. This was accomplished by comparing model simulations of a 1-D coupled snow sea-ice model (C) and another 1-D sea ice model that uses a single bulk property snow layer (NC). The C model was developed in light of previous chapters outlining the importance of the snow layer and the surface energy balance on FYI annual cycles. The coupled model not only treats the snow layer in a much more rigorous fashion in terms of mass and thermal balance, but also includes a better handling of blowing snow processes, turbulent exchanges, and albedo when snow is present. I also illustrated the effects of salinity on the snow and ice physical and thermal evolution by including snow thermal conductivity (k_s) and specific heat (C_s) parameterizations that account for salinity in snow (given in Papakyriakou, 1999). Saline snow, which is common over FYI, can influence snow and sea ice thermal evolution and microwave remote sensing properties (seen in Chapter 7). Two specific research questions were designed to address the goal of this chapter.

6.5.1 Question 1

In the first question, I investigated differences between NC and C in terms of the seasonal evolution of snow and ice thickness. The C snow and ice thickness evolution is better simulated compared to observations partially due to the coupled model's blowing

snow parameterization. Maximum ice thickness differences between C and NC can be between 55 - 65 cm from freeze-up to the early summer melt period, which is significant for annual FYI simulations. It is unknown whether these differences can be accounted for in NC since C and NC are very different in terms of snow layer treatment, blowing snow, turbulent exchange, albedo and incident radiation. It can be concluded that using the coupled model is advantageous for seasonal snow-covered sea ice, however, it is more computationally expensive and has a longer run time than NC. For example, it takes nearly one minute for NC to produce a simulation between YD107, 1992 and YD170, 1993, whereas C takes an order of magnitude longer (~10 minutes). It takes between 13-16 minutes for UPR. The addition of salinity in the snow k_s and C_s reduces ice growth rates in the cold season and ablation rates in the spring melt season. These thermal variations do not appear to be significant in terms of overall annual snow cover and FYI evolution. Results may be different if salinity were included in the snow mass balance.

6.5.1 Question 2

In the second question, the thermodynamic comparisons between NC and C showed there is very little difference in simulated surface temperatures, however, C reproduces the net surface flux better due to its more sophisticated turbulent exchange parameterization. It will been shown the coupled model also does a reasonable job simulating other snow layer temperatures (see Chapter 7). Differences also arise at the ice surface where C temperatures are consistently slightly too warm and NC slightly too cold in the transitional season compared to observations presented here. This may be due to

several factors, some of which include errors in snow density, snow thermal properties and the neglect of salinity in the mass balance. The addition of salinity in the snow k_s and C_s for C further makes the ice surface temperatures too warm in the cold season but improves them during the melt season. This is due to the overall salinity effect that slightly warms the ice in winter and cools it during the melt period; the cooling effect is more significant during melt due to larger departures between snow thermal conductivity and specific heat when comparing snow with and without salinity. The net warming effect of salt in snow k_s and C_s may or may not be counteracted if salts were accounted for in the modeled mass balance.

6.6 Summary

In summary, the snow layer is very important for FYI evolution and thus modeling its processes effectively are also critical. The coupled model developed in this chapter simulates many of the critical aspects of a seasonally evolving snow-covered FYI volume. This type of model with its sophistication and application to FYI has previously been unavailable and one that will provide a better means to address future arctic sea ice climate process studies. In addition, the sophistication of the coupled model is required for application to microwave remote sensing in Chapter 7. The focus of Chapter 7 is to use the coupled snow sea-ice model to predict the snow and ice physical and thermal characteristics that give rise to their respective microwave dielectric properties.

CHAPTER 7: Electro-Thermophysical Model of the Snow Sea-Ice System (ETSSIS) for Microwave Remote Sensing

7.1 Introduction

One-dimensional (1-D) thermodynamic models of snow and sea ice are valuable tools for examining polar climate processes over a variety of ice types and temporal scales (see for example, Ebert and Curry, 1993; Flato and Brown, 1996; Hanesiak et al., 1999; Jordan et al., 1999). In addition, satellite microwave remote sensing is also useful for inferring snow and sea ice physical and thermal properties (besides ice type and concentration) over a wide range of seasonal spatial and temporal scales (see for example, Livingstone and Drinkwater, 1991; Shuchman et al., 1996; Jefferies et al., 1997; Barber and Nghiem, 1999; Barber and Yackel, 1999). Microwave forward and inverse scattering models have also advanced to a state as supplementary tools for understanding the remote observations (see reviews by Golden et al., 1998a,b).

In this chapter I argue for the integration of a thermodynamic model and time series microwave remote sensing data in the development of an 'electro-thermophysical' relationship of snow covered sea ice. In this framework the intent is to develop a model which couples knowledge of the scattering physics of the surface with a 1-D thermodynamic model of the sea ice/snow system. The advantage of this approach is that the geophysical and electrical properties of the surface give rise to scattering and emission in the microwave portion of the spectrum; changes in the geophysical and or electrical state of the volume are driven by the thermodynamics across the interface. A model of these relationships would allow researchers to measure both the geophysical

state of sea ice at any particular time (t_1) and also evaluate the temporal evolution of this scattering over a period coinciding with the seasonal evolution of the surface (t_n). Since the surface energy balance (SEB) also evolves directly from the thermodynamic and physical state of the system, it is expected to be able to determine proxy measures of certain SEB state variables such as surface temperature, albedo, long-wave flux, etc. This information can also be useful in determining the timing of accretion and ablation and producing estimates of the mechanical strength of sea ice and/or timing of fast ice break-up.

Chapter 1 and 2 outlined issues that need to be addressed before fully exploiting thermodynamic modeling toward microwave scattering. First, typical 1-D sea ice models treat the snow layer as a bulk homogeneous slab with very few internal processes which limits their usefulness for microwave remote sensing applications. This is because the variables that contribute to microwave scattering are not simulated in the models such as ice surface roughness, snow liquid water content, basal snow grain sizes, and brine volumes in the bottom snow and top ice layers (Barber and Nghiem, 1999; Nghiem et al., 1998; Barber et al., 1995b)). Second, most detailed snow models do not consider salinity in snow which is a common occurrence in snow over FYI (Barber et al. 1995a). This limits their applicability to microwave remote sensing since salinity plays a large role in snow thermodynamics (Papakyriakou, 1999) and dielectric properties (see for example Barber et al., 1995b; Barber and Nghiem, 1999). The coupled snow sea-ice model in Chapter 6 was specifically developed for application to microwave remote sensing, although it has its use for arctic sea ice climate processes shown in Chapter 6.

The intent of this chapter is to begin the initial steps of linking thermodynamic modeling with microwave remote sensing in a forward sense, that is, determine microwave dielectrics and scattering given modeled estimates of the thermophysical variables that control dielectrics through the electro-thermophysical relationship. I develop and test a working numerical model that enables one to interpret satellite microwave remote sensing (active or passive) in a more physical sense. This will lead to better ways of monitoring the thermophysical properties of the snow/sea ice system within the context of climate variability and sea ice related processes.

Output from the coupled snow sea-ice model in Chapter 6 provides the necessary input to a microwave dielectric model of the Debye form (Barber et al., 1995b); the amalgamation of the models represents an Electro-Thermophysical model of the Snow Sea-Ice System that I will refer to as ETSSIS. The research questions to be addressed in this chapter are designed to utilize *in situ* observations to validate the model's ability to simulate the critical variables that control microwave scattering and emission.

1) Is ETSSIS capable of reproducing snow and ice thermodynamic characteristics of a seasonally variable FYI snow/sea ice system (both with and without salinity in the snow)?

2) Is ETSSIS capable of reproducing the physical characteristics of a seasonally variable FY snow/sea ice system?

3) Can ETSSIS be used toward the interpretation of the microwave time series scattering over a FYI snow/sea ice system?

It is not the intent to fully validate the snow sea-ice model since this has been done by others in the non-coupled forms (see Jordan et al., 1999; Flato and Brown, 1996; Hanesiak et al., 1999). However, it is necessary to illustrate the model's ability to simulate the primary variables that control microwave scattering and emission using *in situ* data utilized here.

7.2 Field Data and Numerical Model

7.2.1 Observational Data

Field observations illustrated in previous chapters from SIMMS'92 are utilized here as well. SIMMS'92 had a variable snow depth up to a maximum near 50 cm and operated between Year Day (YD) 107 (April 18) to YD177 (June 27).

Measurements include SEB parameters for incident and reflected short-wave radiation ($K\downarrow$, $K\uparrow$), incident and emitted long-wave radiation ($L\downarrow$, $L\uparrow$), and net surface heat flux (Q_{net}), vertical temperature profiles within the snow/ice volumes, snow and ice thickness, and physical sampling of the snow and ice (snow density, salinity, wetness, grain diameter). Q_{net} is defined here to include the net radiation and turbulent fluxes at the surface. Instantaneous hourly data were used for model forcing and snow physical sampling were measured periodically.

Some noteworthy errors associated with the measurements include the following. First, snow density measurement accuracy is between 30-60 kg m^{-3} (Barber et al., 1995b). Second, snow wetness (i.e. water volume fractions) may not represent real conditions due to instrument limitations when snow salinity is roughly >3 ppt (parts per thousand);

measurement accuracy is roughly 0.1% water by volume. Third, snow salinity is considered to be both precise and accurate to within ±0.5 ppt (Barber et al., 1995b).

7.2.2 Coupled 1-D Snow Sea-Ice Model

ETSSIS was forced with SIMMS'92 air temperature, relative humidity, wind speed, incident short-wave and long-wave radiation along with measured surface albedo between YD107 (April 18) to YD177 (June 27). Initialization was done using measured snow and ice physical profiles (densities, grain sizes, layer thickness) and temperature profiles. Model runs were conducted using the non-saline version of ETSSIS (C), the average salinity profile (AVG) from chapter 6, and the upper salinity profile (UPR) in chapter 6.

7.2.3 Snow and Sea Ice Dielectric Modeling

Methods of modeling the microwave dielectric constants and penetration depths of snow and sea ice have been discussed in various studies (see for example, Barber, 1993; Drinkwater, 1989; Drinkwater and Crocker, 1988; Barber et al., 1995b), hence only a brief discussion is given here.

To model the dielectric constant of the snow and or sea ice one must separate the material into its host and inclusion components. In the lower portion of the snow pack there is a considerable amount of salinity in the form of brine. This brine is treated as an 'inclusion dielectric' within a dry snow 'host dielectric', following the approach of

Matzler et al. 1984b and Drinkwater and Crocker, 1988. The mixture model is expressed as (7.1).

$$\Delta\varepsilon_{mix}^{\bullet} = \chi V_b \left\{ \frac{\varepsilon_b^{\bullet} - \varepsilon_{ds}^{\bullet}}{1 + [\frac{\varepsilon_b^{\bullet}}{\varepsilon_{ds}^{\bullet}} - 1]A_0} \right\} \tag{7.1}$$

Where $\varepsilon_{ds}^{\bullet}$ and $\varepsilon_b^{\bullet}$ are expressed in complex terms and represent the dielectric constants of dry snow and brine, χ, A_0, and V_b are: a coupling factor representing the fraction of brine accounted for by A_0; the dominant depolarization factor; and the volume of brine contained within the saline snow layer; χ is set at 0.66667, a value appropriate for modeling the brine inclusions as isotropically oriented oblate spheroids (Drinkwater and Crocker, 1988). The depolarization factor is set at 0.053, following Denoth, 1980, and the brine volume is computed as in Barber (1993).

In (7.1) the host dielectric is considered as a dry snow matrix, consisting of ice grains and air. The parameter $\varepsilon_{ds}^{\bullet}$ is computed using an empirical model attributable to Hallikainen et al. (1986). The permittivity of dry snow was computed as (7.2) and the loss as (7.3).

$$\varepsilon_{ds}' = 1.0 + 1.9\rho_{ds} \tag{7.2}$$

$$\varepsilon_{ds}'' = \frac{0.34 V_i \varepsilon_i''}{(1 - 0.417 V_i)^2} \tag{7.3}$$

Where ρ_{ds}, ε_i'', and V_i, are the density of dry snow, the dielectric loss, and the volume fraction of freshwater ice in the snow matrix.

In (7.1) the inclusion dielectric is considered to consist of brine pockets held within the interstices of the snow grains. The parameter ε_b^* is defined as the complex dielectric constant of brine computed from (7.4 and 7.5) based on models of the Debye form, following Ulaby et al. (1986).

$$\varepsilon_b' = \varepsilon_{w\infty} + \left[\frac{\varepsilon_{b0} - \varepsilon_{w\infty}}{1 + (2\pi f \tau_b)^2}\right] \qquad (7.4)$$

$$\varepsilon_b'' = (2\pi f \tau_b) \cdot \left[\frac{(\varepsilon_{b0} - \varepsilon_{w\infty})}{1 + (2\pi f \tau_b)^2}\right] + \left[\frac{\sigma_b}{2\pi f \varepsilon_0}\right] \qquad (7.5)$$

Where $\varepsilon_{w\infty}$; ε_{b0}; f; τ_b; σ_b; ε_0 are: the high frequency limit of the dielectric constant of pure water; the static dielectric constant of pure water; the frequency of electromagnetic energy (Hz); the relaxation time of the brine; the ionic conductivity of the brine solution ($S \cdot m^{-1}$); and the permittivity of free space ($F \cdot m^{-1}$). These parameters are estimated using a series of polynomial models which will not be reproduced here (see Stogryn, 1971; Ulaby et al. 1986; and Hallikainen and Winebrenner, 1992).

When free water becomes available within the snow pack the dielectric properties change considerably. The relationships between ε' and ε'' for wet and dry snow have been determined empirically. Models for computation of ε' and ε'' of wet snow relative to the values for dry snow, have been developed by Tiuri et al., (1984) and are presented in (7.6 to 7.8).

218

$$\Delta \varepsilon'_{ws} = \varepsilon'_{ws} - \varepsilon'_{dry} \tag{7.6}$$

$$\Delta \varepsilon'_{ws} = \varepsilon'_{w}(0.1W_v + 0.8W_v^2) \tag{7.7}$$

$$\varepsilon''_{ws} = \varepsilon''_{w}(0.1W_v + 0.8W_v^2) \tag{7.8}$$

Where: ε'_{dry} is the permittivity of dry snow from (7.2); Wv is the volumetric liquid water content measured *in situ*; and ε'_{ws} and ε''_{ws} are the permittivity and loss of wet snow. The complex dielectric constant of water (ε'_{w} and ε''_{w}) are computed using the Debye model for liquid water (7.9) and (7.10).

$$\varepsilon'_{w} = \varepsilon_{w\infty} + \left[\frac{\varepsilon_{w0} - \varepsilon_{w\infty}}{1 + (2\pi f \tau_w)^2} \right] \tag{7.9}$$

$$\varepsilon''_{w} = (2\pi f \tau_w) \cdot \left[\frac{(\varepsilon_{w0} - \varepsilon_{w\infty})}{1 + (2\pi f \tau_w)^2} \right] \tag{7.10}$$

Where the parameters are the same as in (7.4) and (7.5) but for liquid water rather than brine.

Through use of these dielectric mixture models it is possible to compute the penetration depth (δp) of various frequencies of electromagnetic energy into a seasonally dynamic snow covered sea ice volume (7.11), following Drinkwater (1989).

$$\delta_p = \frac{\lambda}{4\pi} \left\{ \left[\left(1 + \left(\frac{\varepsilon''}{\varepsilon'} \right)^2 \right)^{\frac{1}{2}} - 1 \right] \frac{\varepsilon'}{2} \right\}^{-\frac{1}{2}}$$

(7.11)

Where λ is the SAR wavelength in meters, ε' and ε'' are the dielectric permittivity and loss given a particular water volume within the snow pack. I have computed the maximum penetration depths for selected snow and ice layers for a 5.3 GHz frequency (typical of active microwave sensors) for illustrative purposes. A similar analysis can be performed for other microwave frequencies such as passive sensors (for example 19 GHz).

7.3 Analysis Methods

To quantify ETSSIS's ability to simulate the thermodynamic, physical and electrical properties of the snow and ice volumes, the coefficient of determination (R^2), mean bias error (MBE), and root-mean-squared error (RMSE)) were computed from modeled and observed values. The statistics were calculated for the non-saline model case (C), average saline case (AVG) and upper limit saline case (UPR). Thermodynamic variables included temperatures at various levels in the snow and ice surface, including the snow surface (T_{sfc}) and ice surface (T_{isfc}), net surface heat flux (Q_{net}), and snow and ice thickness. Q_{net} and snow and ice thickness are included since they impact, or are the direct result of the thermodynamics. Physical variables included snow density (ρ_s), grain diameter (d), liquid water fraction (Wv), salinity (S), and brine volume (Vb). Although salinity is held constant in the model, it is useful to illustrate differences between

modeled and observed values for error analysis. The microwave dielectric variables included permitivity (ε'), loss (ε'') and penetration depth (δp) at various levels in the snow and ice. The ε' and ε'' were estimated by the dielectric mixture model in section 7.2.3 using snow and ice T, ρ, Wv, and S as input. "Observed" ε' and ε'' are defined as values computed by the dielectric model using observed thermodynamic and physical variables as input. Microwave maximum penetration depths were computed from ε' and ε'' at 5.3 GHz to define which snow layers become important for microwave remote sensing interpretation over the various seasonal stages of snow-covered FYI. In particular, we are interested in the dry snow (cold season) scenario, when water in liquid phase appears in snow (the pendular regime with Wv between 1-7% water by volume), and full snow melt (funicular regime with Wv between 8-15% water by volume). These seasons were defined according to *observed* snow Wv measurements (see section 7.5).

The R^2 was only computed for model and observed data in continuous hourly time increments since they were more consistent in time (i.e. Q_{net}, T_{sfc}, and T_{isfc}). The MBE and RMSE were computed for other variables with periodic daily samples. The thermodynamic and physical variables used in the analysis were selected based on their importance to microwave dielectrics.

7.4 Results

7.4.1 Thermodynamic Evolution

This section gives an overview of how well ETSSIS models the important thermodynamic variables for microwave remote sensing (question 1). A more detailed look at which model errors may or may not be important will be discussed in section 7.5.

The modeled temporal evolution of the snow thermal conductivity and specific heat over SIMMS'92 for various snow layers shows a progressive spread between the non-saline model run (C) and saline model runs (AVG and UPR) (Figure 7.1). This is mainly due to the increase in snow temperature over time in conjunction with salinity effects. The maximum difference in thermal conductivity is between $0.1 - 0.15$ W m^{-1} K^{-1} (15-25%) and an order of magnitude (> 1.2 x 10^4 J kg^{-1} C^{-1}) for specific heat before the onset of significant snow melt (prior to YD170). Beyond YD170, significant separation between saline and non-saline values occurs because of the extreme nature of k_{ss} and C_{ss} during melt.

The model's snow and ice thickness evolution are fairly well simulated compared to observations (see Figure 6.4); the snow thickness evolution is mainly due to ETSSIS's blowing snow parameterization. The improved snow thickness distribution should allow for more realistic snow and ice thermodynamic evolution. Ice thickness changed from 1.4 m (initial value) to 1.53 m for the C simulation and 1.4 m to 1.51 m for the UPR simulation over the 70 day period; observed values at the end of the experiment were 1.5 ± 0.07 m. Qualitatively, the model simulates the snow and top ice layer temperatures

fairly well (Figure 7.2). Statistically, the comparisons between observed and modeled T_{sfc}

and Q_{net} indicates the model reproduces these parameters very well (Table 7.1).
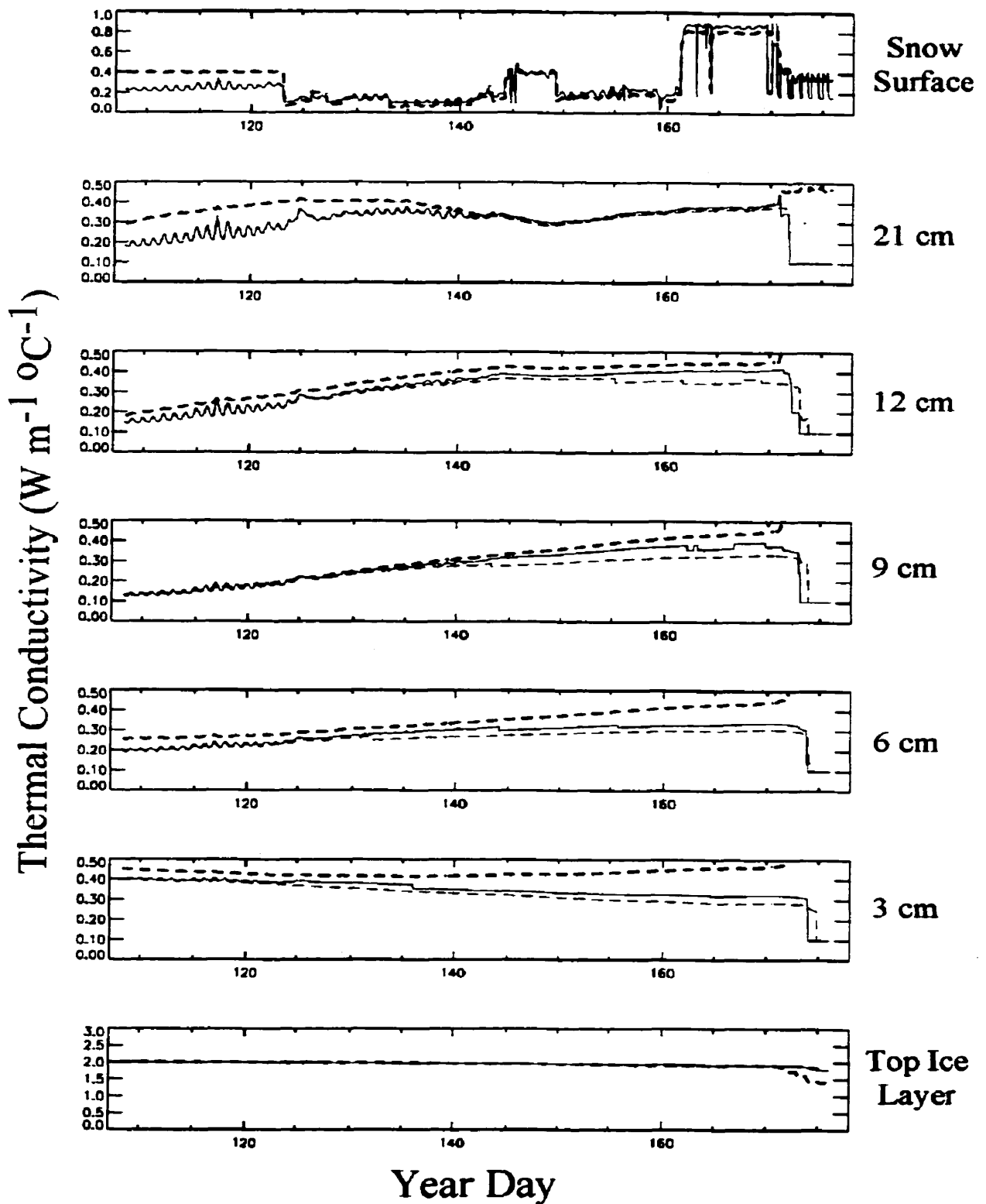
Figure 7.1a: Non-saline (C – heavy dashed line) and saline (AVG – solid; UPR – dashed line) ETSSIS thermal conductivity (W m⁻¹ K⁻¹) for various snow and top ice layers.
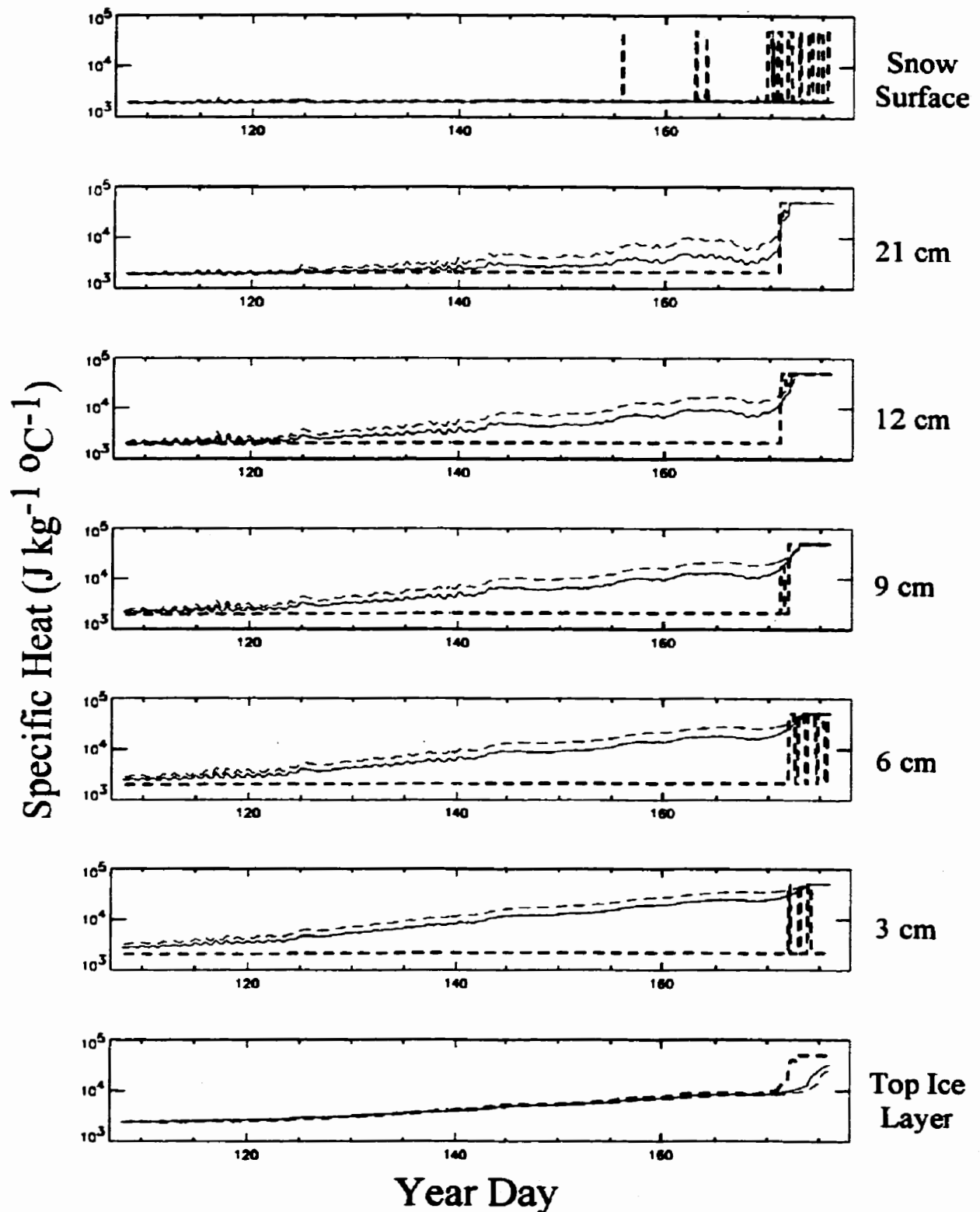
Figure 7.1b: Non-saline (C – heavy dashed line) and saline (AVG – solid; UPR – dashed line) ETSSIS specific heat (J kg^{-1} C^{-1}) for various snow and top ice layers.

Figure 7.2: Modeled and observed temperature (°C) evolution between YD107 and YD177 of various snow layers for C (heavy dashed line), AVG (solid line), UPR (not noticeable beneath solid line), and observed data (triangles). Observed values represent instantaneous morning temperatures corresponding to days where snow sampling took place.

A detailed look at the modeled T_{sfc} shows a close resemblance to the observed T_{sfc} evolution, even during the critical melt period (see Figure 6.5). The melt period is important to simulate well not only for microwave dielectrics and penetration depths but for climate process studies. There was no change in the T_{sfc} and Q_{net} results when comparing the C, AVG and UPR simulations due to very little or no salinity in the top of the snow pack.

Table 7.1: ETSSIS without salinity (C), average salinity (AVG) and upper limit salinity (UPR) R^2, mean bias error (MBE) and root-mean-squared error (RMSE) compared to observations of Q_{net} (W m^{-2}), T_{sfc} (°C) and T_{isfc} (°C). Positive MBE implies the model overestimates observations. Observed mean values are also included for refence.

	Q_{net} (C)	T_{sfc} (C)	T_{isfc} (C)	T_{isfc} (AVG)	T_{isfc} (UPR)
R^2	0.74	0.99	0.99	0.99	0.99
MBE	+3.00	-0.06	+0.96	+0.98	+1.04
RMSE	21.0	1.3	0.49	0.74	0.79
Mean Obs	-1.4	-9.8	-7.2	-7.2	-7.2

The simulated top ice layer temperatures (T_{isfc}) are slightly too warm (by a maximum of 2°C) in all model runs but improve during the warm season when salinity is included (see Figure 6.6a). The over prediction in the cold and mid-spring seasons may be the result of middle snow layer densities being under estimated and/or the neglect of brine drainage (see section 7.4.2). That is, higher snow densities and liquid water increase the thermal conductivity to promote cooling. Overall thermal effects of including salinity in snow k_s and C_s are to raise temperatures in the colder season (up to YD130) and reduce them during the warmer season (beyond YD130) (Figure 7.3). This effect would be complicated if the physical presence of salt was parameterized with regard to snow

mass balance since liquid water (brine) would be generated much sooner in the spring season (see section 7.4.2).
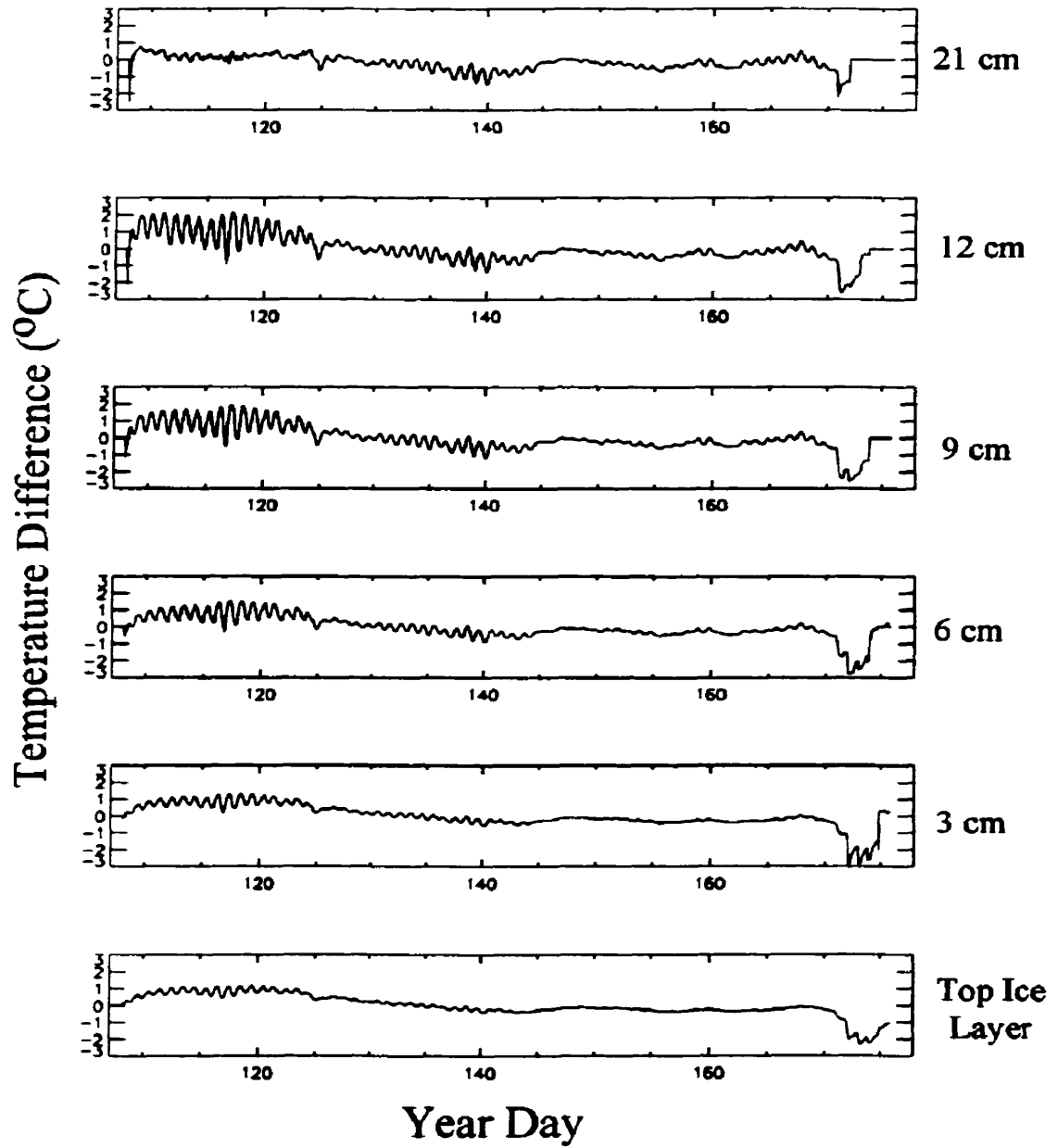
Figure 7.3: Temperature difference (°C) between non-saline (C) and saline (UPR) ETSSIS simulations for various snow layers and top ice layer between YD107 to YD177. Positive values indicate warmer UPR simulated temperatures.

An interesting thermal feature is that diurnal cycling (waves) of T_{isfc} within the model are better reproduced when the effect of salt is considered in the snow k_s and C_s (see Figure 6.6b). Diurnal temperature cycling can be important for cold season microwave dielectrics that affect the appearance of time-series diurnal SAR image pairs and their physical interpretation (Barber and Nghiem, 1999; Nghiem et al. 1998). Cross-correlation analysis suggests the C simulation T_{isfc} diurnal waves are at least 3 hours out of phase with observed values during the colder season but are reduced to as little as 0 hours in UPR. This suggests the C simulation snow thermal diffusivity may be too large by not damping out air temperature changes sufficiently or other factors related to k_s and C_s. The complex problem of snow k_s, C_s, and thermal diffusivity are still largely under debate and too detailed to be included here, hence I will only state that more work is required in this regard.

Given these results and various small thermodynamic errors in the model and observations, results in section 7.5 will show whether these errors significantly impact microwave dielectrics.

7.4.2 Physical Evolution

This section gives an overview of how well ETSSIS models the important physical variables for microwave remote sensing (question 2). A more detailed look at which model errors may or may not be important is presented in section 7.5.

230

The difference between C, AVG and UPR are very small (<5%) in terms of bulk density and grain sizes until water in liquid phase appears (Figures 7.4 to 7.6). The differences in density and grain sizes amongst the model simulations becomes 30-75% due to the different timing of the first appearance of water in liquid phase. The initial appearance of water in liquid phase is delayed with higher snow salinities which cools overall snow temperatures in the warm season; C snow liquid water appears 3 days earlier than AVG (YD170 compared to YD173) and 4 days earlier than UPR (YD170 compared to YD174). These differences would be greater if salt were explicitly parameterized in the mass balance.

Time series modeled versus observed ρ_s, d and Wv indicates that ρ_s is simulated fairly well but slightly under estimated at 21 cm and the snow surface where larger discrepancies arise from fresh snow falls (see Figure 7.4 and Table 7.2). Modeled ρ_s prior to YD120 at 9 and 12 cm is also under estimated. This may contribute to the warmer ice surface temperatures in the cold season by artificially reducing the snow thermal conductivity. Also note that field sampling of ρ_s may introduce errors between modeled and observed values. Grain sizes are generally simulated reasonably well over most of the period except near the bottom part of the snow pack during the melt season where observed liquid water contents increase (see Figures 7.5 and 7.6 and Table 7.2). Grain growth can accelerate rapidly with available liquid water. The non-existence of simulated liquid water prior to YD170 inhibits modeled grain growth and increases discrepancies between modeled and observed values. Note that snow grains do not affect microwave dielectrics but become physically important for the total volume scattering contributions.

Grain sizes are particularly important in development of algorithms for estimating snow

water equivalent (SWE) on sea ice (Markus and Cavalieri, 1998).

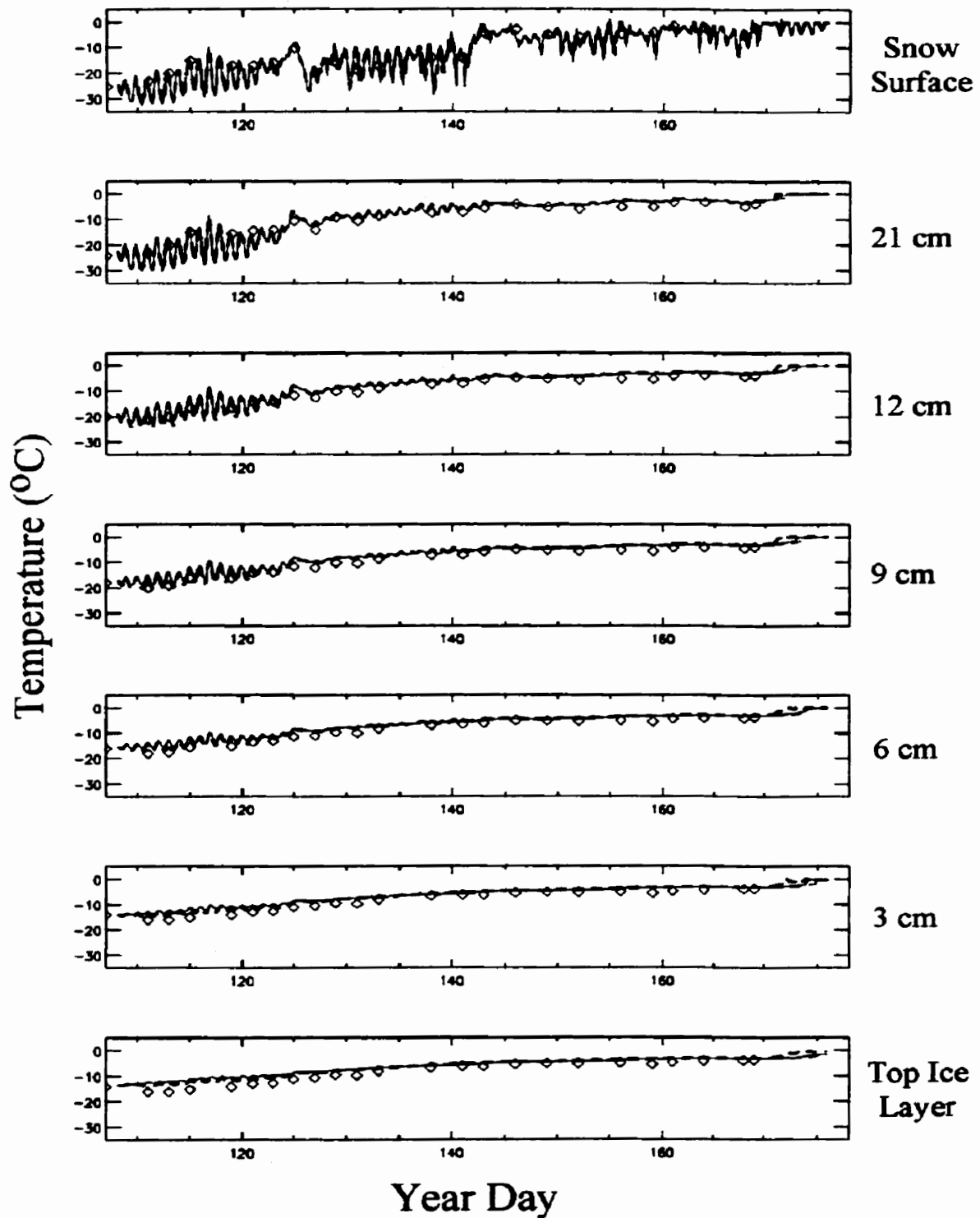*Figure 7.4: Modeled and observed density (kg m⁻³) evolution between YD107 and YD177 of various snow layers for C (heavy dashed line), AVG (solid line), UPR (dashed line), and observed data (triangles). Observed values represent averages as in Barber et al. (1995b) corresponding to days where snow sampling took place.*
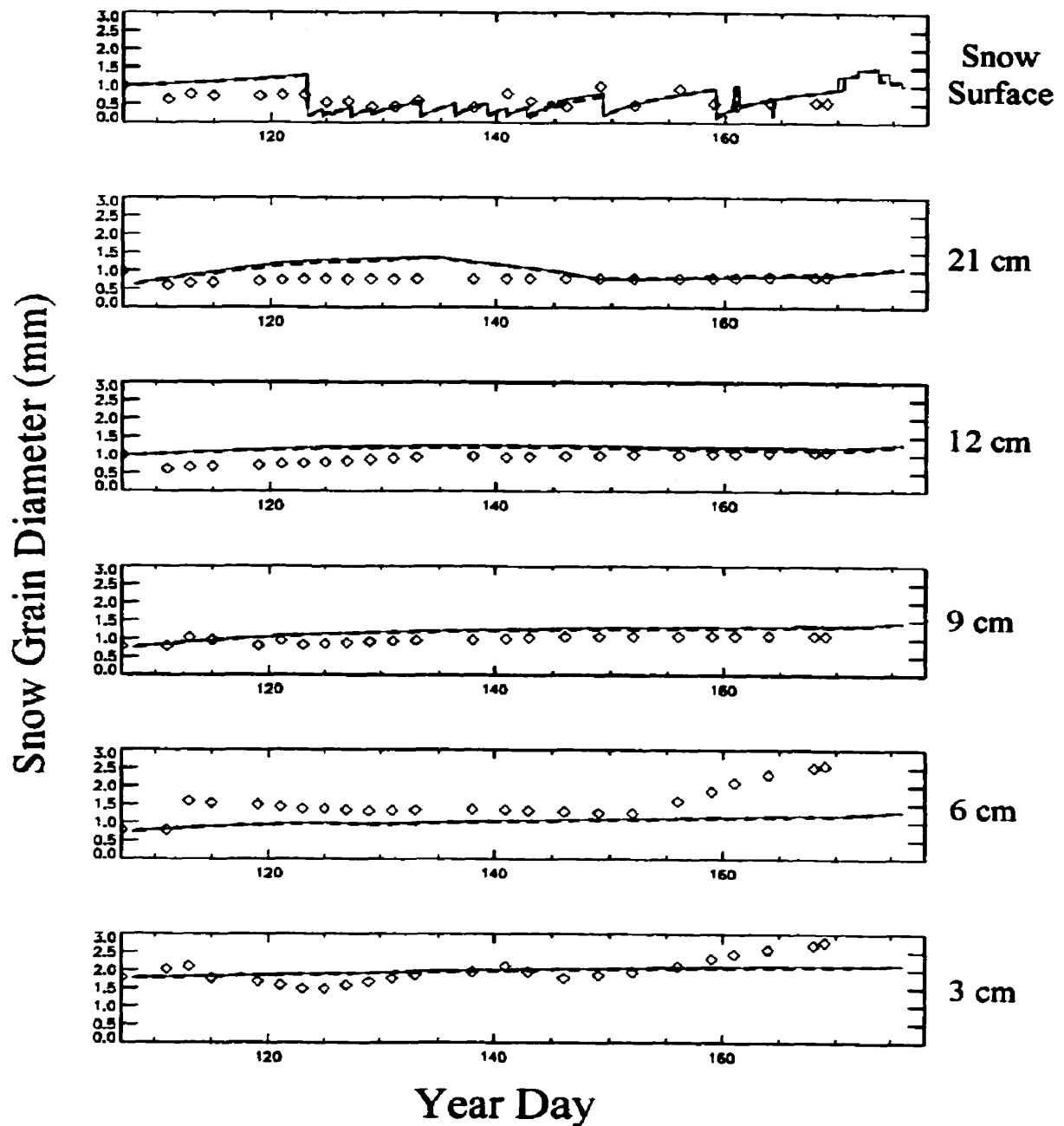
Figure 7.5: Modeled and observed grain size (mm in diameter) evolution between YD107 and YD177 of various snow layers for C (heavy dashed line), AVG (solid line), UPR (not noticeable beneath solid line), and observed data (triangles). Observed values represent averages as in Barber et al. (1995b) corresponding to days where snow sampling took place.
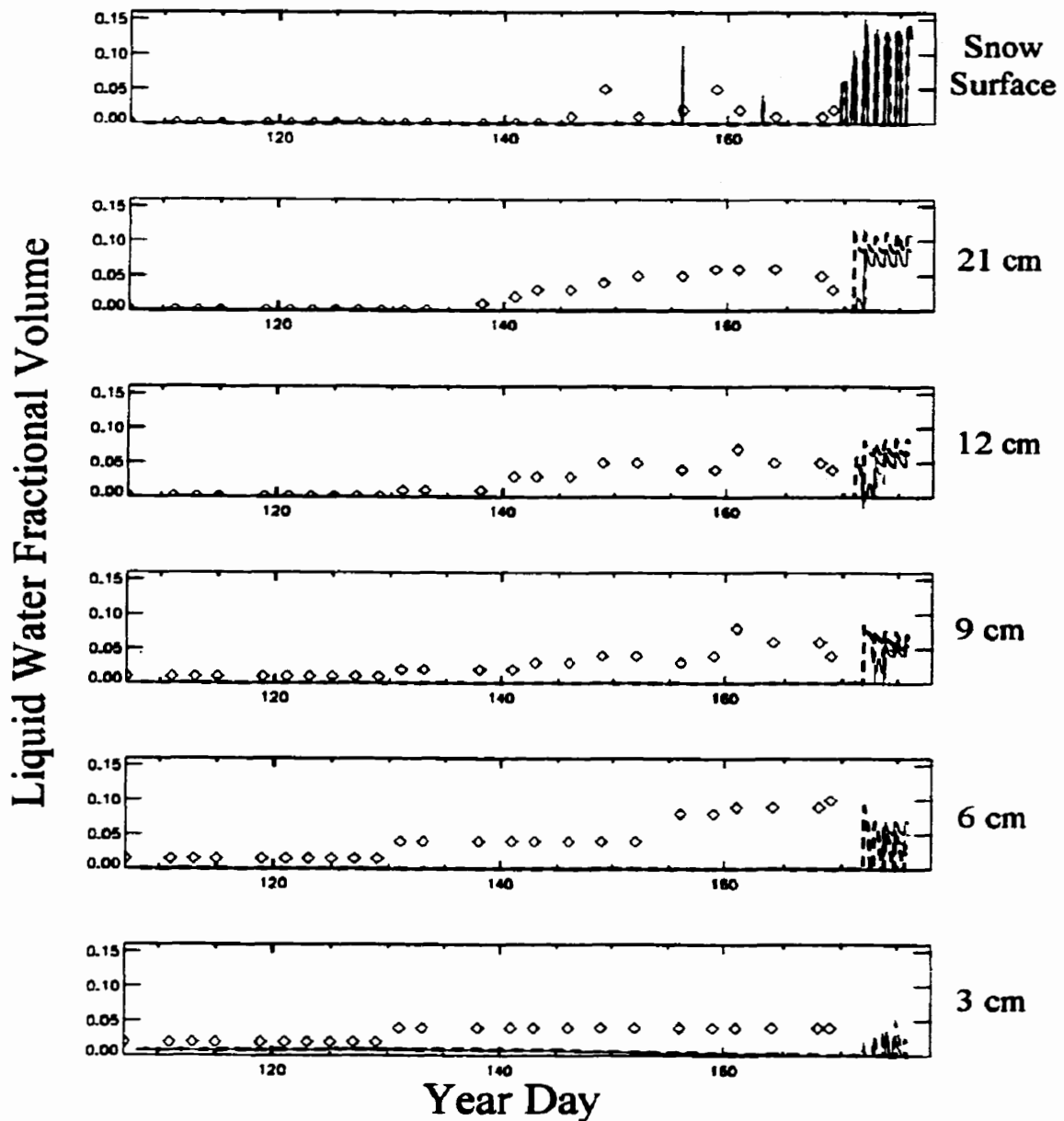
Figure 7.6: Modeled and observed fractional water volume evolution between YD107 and YD177 of various snow layers for C (heavy dashed line), AVG (solid line), UPR (dashed line), and observed data (triangles). Observed values represent averages as in Barber et al. (1995b) corresponding to days where snow sampling took place. Observed water volumes with significant salinity (>3 ppt) may not represent actual conditions due to instrument limitations.

The modeling of Wv clearly needs improvement in most snow layers (Figure 7.6 and Table 7.2) which impacts the dielectric properties (shown later). This is due to not explicitly including the presence of salt in the snow mass balance of the model; future work will address this issue. Salinities are also not simulated very well since the model does not account for snow pack desalination over time as liquid water drains freely toward the ice surface in the late season (Figure 7.7). The model holds salinity constant over time since a physical parameterization for snow desalinization is currently not available. Note here that errors in sampling, especially ρ_s and Wv can have an impact on the analysis presented.

Table 7.2: ETSSIS without salinity (C) mean bias error (MBE) and root-mean-squared error (RMSE) snow density, grain sizes, water volume fraction for various snow depths compared to observations. The first (second) value in the salinity column represents the AVG (UPR) simulation. Positive MBE implies the model overestimates observations. Observed values (in brackets) represent averages as in Barber et al. (1995b) corresponding to days where geophysical snow sampling took place. Instantaneous morning model data were used for comparison to observations. Water volume fraction observations may not represent real conditions when salinities are >3 ppt.

	Density (kg m^{-3})		Grain Size (mm)		Water Vol. Frac.		Salinity (ppt)	
	MBE	RMSE	MBE	RMSE	MBE	RMSE	MBE	RMSE
Surface	-14	107	+0.1	0.3	+0.01	0.02	-0.02/-0.01	0.02/0.01
	(310)		(0.65)		(0.02)		(0.1)	
21 cm	-97	41	-0.3	0.2	+0.03	0.04	+0.5/+0.8	1.0/1.2
	(395)		(0.73)		(0.035)		(1.1)	
12 cm	-15	38	+0.2	0.3	+0.02	0.04	+1.2/+3.1	2.5/4.9
	(340)		(0.75)		(0.037)		(1.9)	
9 cm	-25	45	+0.2	0.3	+0.03	0.04	+1.1/+4.2	4.2/6.5
	(355)		(0.8)		(0.042)		(4.7)	
6 cm	-8	17	-1.1	1.8	+0.05	0.07	+1.5/+5.2	4.4/5.8
	(300)		(1.6)		(0.051)		(8.1)	
3 cm	+13	20	-0.1	1.2	+0.03	0.04	-7.8/+0.6	8.9/3.5
	(280)		(1.9)		(0.038)		(17.1)	

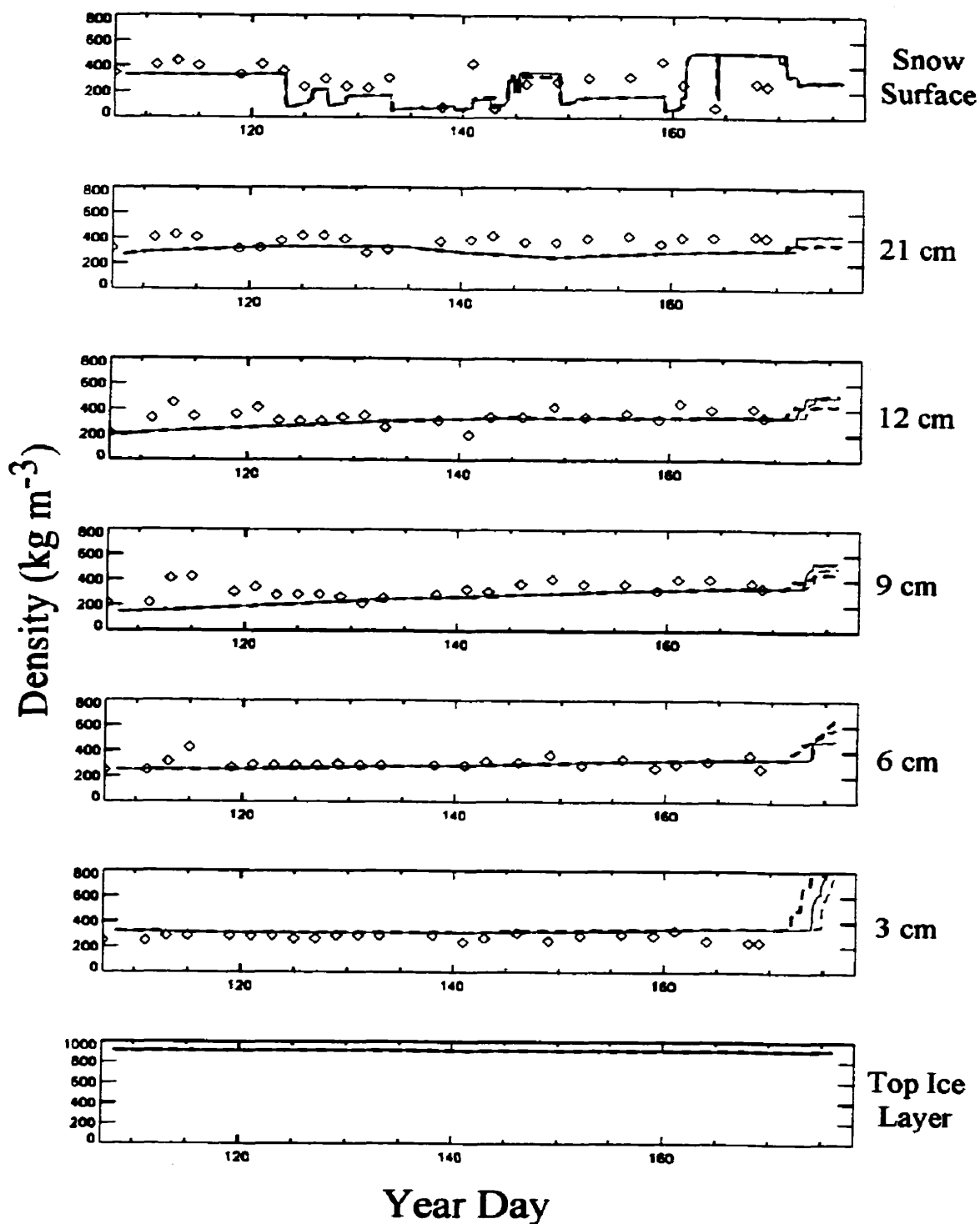*Figure 7.7: Modeled and observed salinity (ppt) evolution between YD107 and YD177 of various snow layers for C (always zero), AVG (solid line), UPR (dashed line), and observed data (triangles). Observed values represent averages as in Barber et al. (1995b) corresponding to days where snow sampling took place.*

Brine volumes were estimated as in Barber et al. (1995b) using observed and modeled time series snow temperatures, densities, salinity and wetness. The overall modeled brine volume evolution for C, AVG and UPR (Figure 7.8) for various snow layers is somewhat different than those estimated using the observed input data. Desalination in the mid and lower snow layers over time is the main cause of the larger discrepancies between modeled and observed estimates of Vb, especially in the warmer season. The major sources of error include inadequately modeled liquid water evolution and related feedbacks along with measurement error in snow temperature (up to $\pm 1°C$ in the warmest part of the season), ρ_s, S and Wv. A sensitivity analysis of snow Vb given the relative errors in input parameters discussed in section 7.2 suggests that Vb is virtually insensitive to a 1% error in Wv measurement and 0.5°C error in temperature. Vb changes by only 1% for a 60 kg m^{-3} error in density and 0.5 ppt error in salinity. With all of these errors combined, Vb changes by about 2% - 4% with the largest effects seen near the base of the snow pack.

Given these results and various errors in the model and observations, section 7.5 will show whether these errors significantly impact microwave dielectrics.
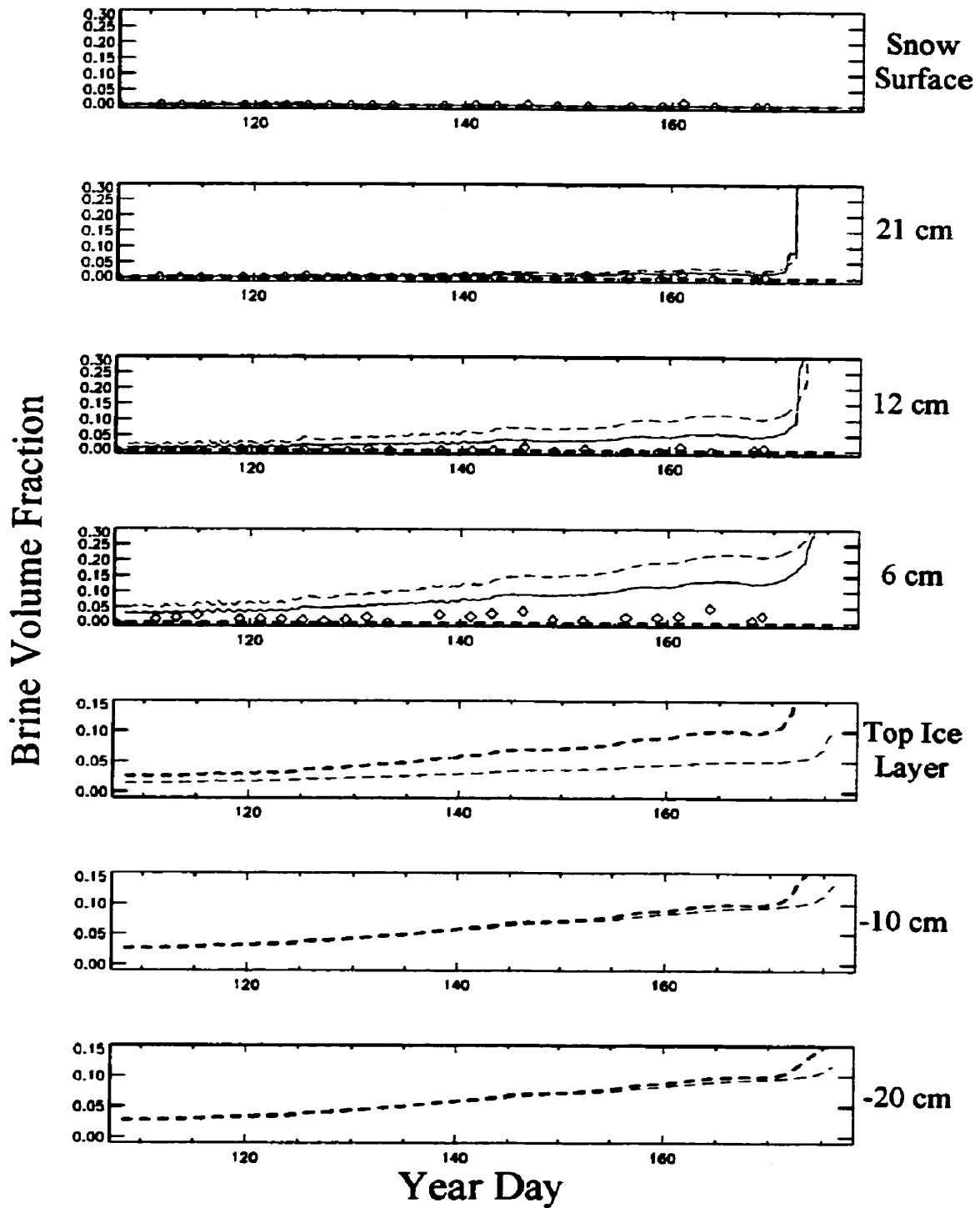
Figure 7.8: Brine volume evolution for various layers of snow (positive depths) and ice (negative depths) between YD107 to YD177 for C (heavy dashed line), AVG (solid line), UPR (dashed line) and "observed" estimates (triangles). Only snow layers showing significant differences between them are depicted and C and UPR are shown for ice. Observed values represent estimates derived from input variable averages as in Barber et al. (1995b) corresponding to days where snow sampling took place.

7.5 Microwave Dielectrics

In this final section I investigate differences in the snow and ice layers microwave dielectric properties and penetration depth given ETSSIS simulations without salinity (C) and with salinity (AVG and UPR) compared to estimations from available observations. The purpose is to show ETSSIS's direct application to microwave remote sensing (question 3). Due to the lack of physical observational data in the ice layers, only modeled results are presented. I present results according to the various observed snow evolutionary seasons (i.e. cold dry snow; pendular regime; funicular regime). A sensitivity analysis of snow dielectrics to observational measurement errors is also conducted to illustrate their effects on results.

7.5.1 Cold Dry Snow

The temporal evolution of dielectric permitivity (ε') and loss (ε'') estimated from C, AVG, UPR and those from observations for various snow depths reveal that both are estimated well by ETSSIS at all snow depths in the colder, dry snow season (YD107 to about YD135). This is due to ETSSIS's ability to simulate snow temperature and density (which are most important for ε') during the cold season. Inclusion of salinity in snow improves ε' and ε'' (as well as δp) at the snow pack base (Figures 7.9 to 7.11 and Table 7.3). The results suggest ETSSIS is capable of reproducing low snow dielectric properties in the cold season which in turn makes the ice volume the dominant microwave scatterer and emitter according to penetration depths (Figure 7.11). The snow volume is virtually

transparent (at 5.3 GHz) in this season since the penetration depths at each snow layer are much larger than the thickness of the snow at each layer (Figure 7.11). Penetration depths within the ice are roughly 15 to 20 cm which means active microwave sensors would primarily "see" ice characteristics originating at these depths within the ice; this is why ice data down to 20 cm is presented in Figures 7.9 - 7.11. Modeled penetration depth errors would be caused by inaccurate ice temperatures, salinities and density. ETSSIS ice temperatures below 4 cm were within ± 1°C at all levels (not shown), whereas salinity and density in the model are typical of FYI (see Figures 7.4 and 7.7; top ice layer). Therefore, errors in ice penetration depths are expected to be minimal.

.
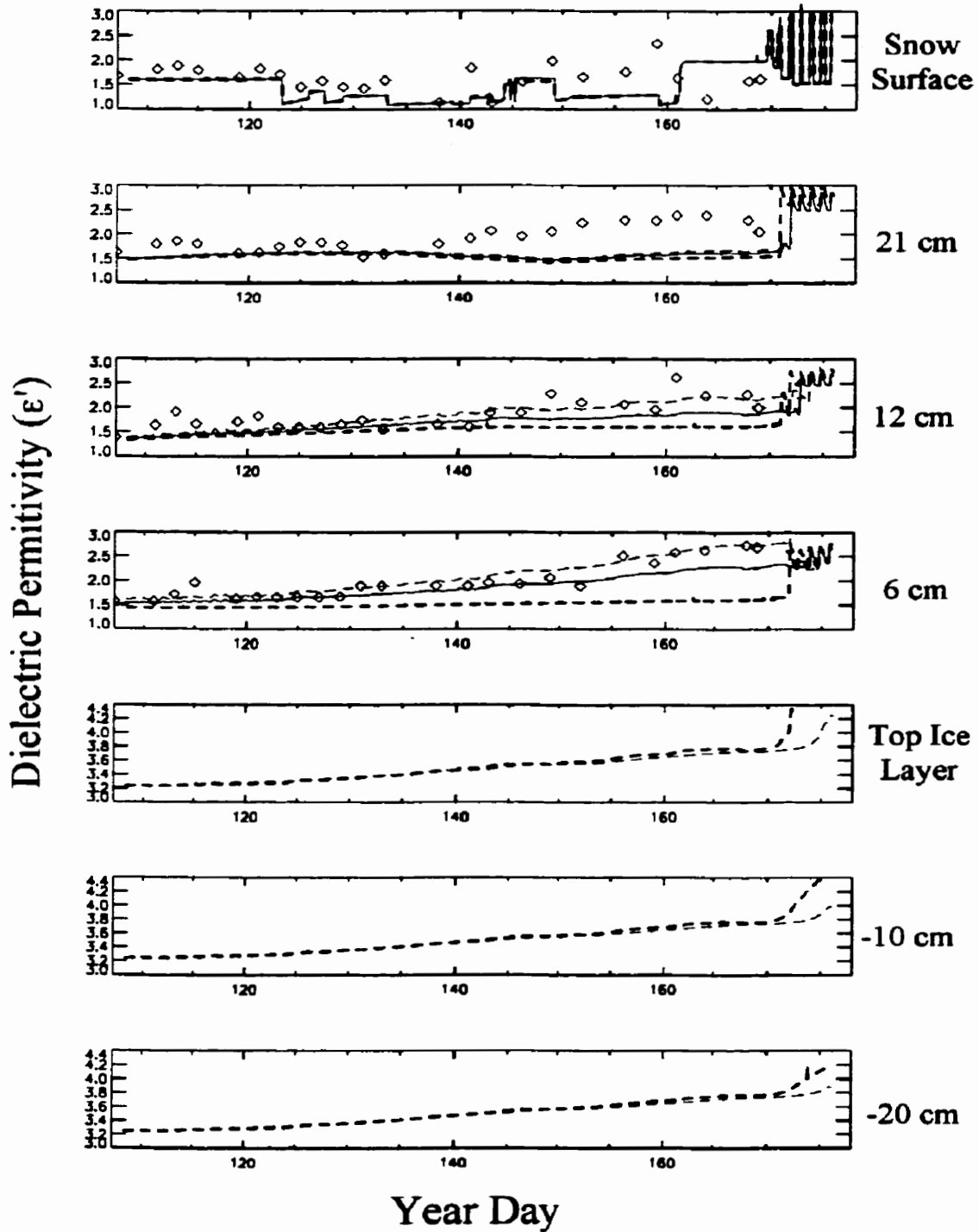
Figure 7.9: Dielectric permitivity (ε') evolution for various layers of snow (positive depths) and ice (negative depths) between YD107 to YD177 for C (heavy dashed line), AVG (solid line), UPR (dashed line) and "observed" estimates (triangles). Only snow layers showing significant differences between them are depicted and C and UPR are shown for ice. Observed values represent estimates derived from input variable averages as in Barber et al. (1995b) corresponding to days where snow sampling took place.
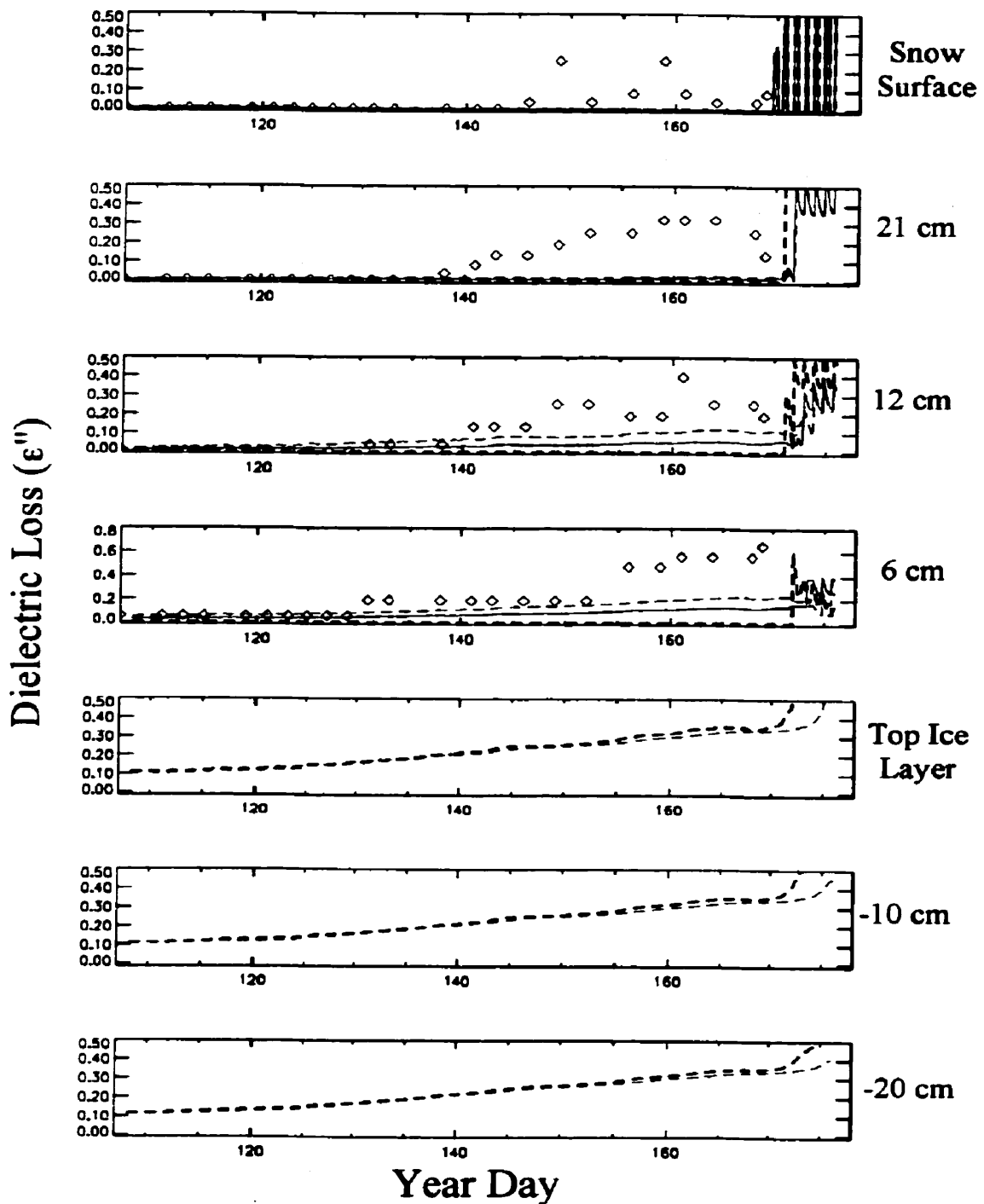
Figure 7.10: Dielectric loss (ε") evolution for various layers of snow (positive depths) and ice (negative depths) between YD107 to YD177 for C (heavy dashed line), AVG (solid line), UPR (dashed line) and "observed" estimates (triangles). Only snow layers showing significant differences between them are depicted and C and UPR are shown for ice. Observed values represent estimates derived from input variable averages as in Barber et al. (1995b) corresponding to days where snow sampling took place.
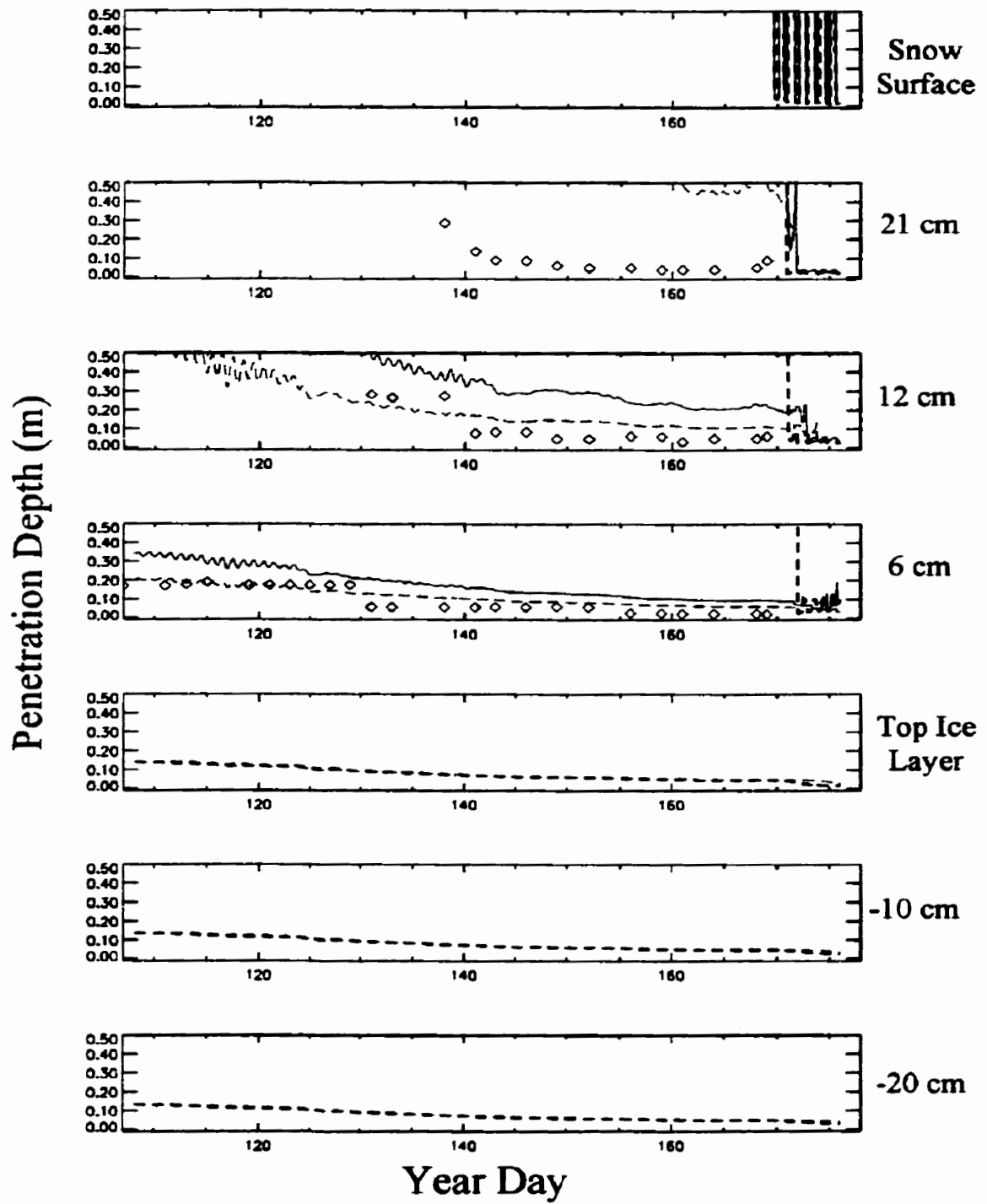
Figure 7.11: Penetration depth (δp – in meters) evolution for various layers of snow and ice between YD107 to YD177 for C (heavy dashed line), AVG (solid line), UPR (dashed line) and "observed" estimates (triangles). Only snow layers showing significant differences between them are depicted and C and UPR are shown for ice. Observed values represent estimates derived from input variable averages as in Barber et al. (1995b) corresponding to days where geophysical snow sampling took place.

Table 5.3a-c: ETSSIS C, AVG and UPR mean bias error (MBE) and root-mean-squared error (RMSE) permitivity (ε'), loss (ε") and penetration depth (δp) compared to observational estimates for various snow depths. Positive MBE implies the model overestimates observations. Observed values (Mean Obs) represent estimates derived from input variable averages as in Barber et al. (1995b) corresponding to days where geophysical snow sampling took place.

Permitivity (ε')

	Mean Obs	MBE (C)	MBE (AVG)	MBE (UPR)	RMSE (C)	RMSE (AVG)	RMSE (UPR)
Surface	1.5	-0.2	-0.2	-0.2	0.6	0.6	0.6
21 cm	2.0	-0.8	-0.8	-0.7	0.5	0.5	0.4
12 cm	1.9	-0.8	-0.4	-0.1	0.6	0.4	0.3
6 cm	2.0	-0.9	-0.3	+0.1	0.6	0.3	0.2

(a)

Loss (ε")

	Mean Obs	MBE (C)	MBE (AVG)	MBE (UPR)	RMSE (C)	RMSE (AVG)	RMSE (UPR)
Surface	0.08	-0.12	-0.12	-0.12	0.07	0.07	0.07
21 cm	0.17	-0.20	-0.19	-0.18	0.13	0.12	0.12
12 cm	0.15	-0.25	-0.20	-0.11	0.16	0.11	0.09
6 cm	0.5	-0.38	-0.27	-0.20	0.52	0.41	0.34

(b)

Penetration Depth (m)

	Mean Obs	MBE (C)	MBE (AVG)	MBE (UPR)	RMSE (C)	RMSE (AVG)	RMSE (UPR)
Surface	2.9	+0.15	+0.12	+0.10	0.18	0.15	0.13
21 cm	0.35	+0.90	+0.60	+0.45	0.42	0.35	0.30
12 cm	0.2	+0.95	+0.27	+0.11	0.24	0.13	0.09
6 cm	0.09	+0.97	+0.10	+0.04	0.30	0.10	0.05

(c)

245

7.5.2 Pendular Snow Regime

The temporal evolution of dielectric permitivity (ϵ') estimated from C, AVG, UPR and those from observations for various snow depths reveal that ϵ' is estimated well by ETSSIS at most snow depths in the pendular regime (YD135 to YD155). This is mainly due to ETSSIS's ability to simulate snow temperature and density (which are most important for ϵ') during this season. Inclusion of salinity in snow dramatically improves ϵ' and δp at the snow pack base (Figures 7.9 and 7.11 and Table 7.3). Because ETSSIS has difficulty reproducing liquid water in the observed pendular regime, it does not reproduce ϵ" very well (Figure 7.9) and will continue to make the ice volume the dominant microwave scatterer and emitter since penetration depths within the snow remain higher than observed values (Figure 7.11). Observations suggest the snow cover would contribute between 75-90% of the total microwave scattering and emission during the pendular regime in which case snow grain size would become an important variable to simulate for volume scattering considerations (for active sensors).

7.5.3 Funicular Snow Regime

The temporal evolution of dielectric permitivity (ϵ') estimated from C, AVG, UPR and those from observations for various snow depths reveal that ϵ' is estimated well by ETSSIS at most snow depths in the funicular regime (YD155 to YD177). Once again this is due to ETSSIS's ability to simulate snow temperature and density during this season. Inclusion of salinity in snow improves ϵ' and δp at the base and middle portions

of the snowpack (Figures 7.9 and 7.11 and Table 7.3). Once ETSSIS generates water in liquid phase (near YD170), the simulated ε" becomes close to expected values (Figure 7.9) and will begin to make the snow volume more of a dominant microwave scatterer (active) or emitter (passive), illustrated by the penetration depths at 5.3 GHz (Figure 7.11). Observations up to YD169 suggest the top 5 - 10 cm of the snow cover will contribute 100% of the total microwave scattering during the funicular regime and ETSSIS suggests similar magnitudes once it generates liquid water beyond YD170.

7.5.4 Dielectric Sensitivity to Measurement Errors

Finally, errors in input parameters made from observations that control ε' and ε" (similar to Vb) were investigated to examine their effects on the results. The measurement errors for snow temperature, density, liquid water content, and salinity are applied to the observed time series data shown in Figures 7.2, 7.4, 7.6 and 7.7. It should be noted that conducting an error analysis using the differentials of the various parameters may lead to larger errors than those cited here.

There is virtually no change in ε' with a 0.5°C error in temperature or a 0.5 ppt error in salinity; ε' changes by 0.1 units for a 1% Wv error and 60 kg m^{-3} error in density. With all errors included simultaneously, ε' changes by roughly 0.25 units. There is virtually no change in ε" with similar errors above in temperature, salinity and density, however, ε" changes by 0.05 units with a 1% error in Wv. With all errors induced simultaneously, ε" of course also changes by 0.05 units. Thus, the microwave model sensitivity analyses of ε' and ε" suggests the *in situ* measurement errors in ρ_s and Wv can

contribute to small errors in the dielectric snow properties and the discrepancies between modeled and "observed" ε' and ε''. The combined errors in ε' and ε'' result in snow layer penetration depth uncertainties up to 30 cm in the cold season and only a few cm in the pendular and funicular regimes. With very high snow penetration depths in the cold season, the 30 cm error does not significantly affect the results nor does a few cm in the pendular and funicular regimes. Thus, errors in ε' and ε'' resulting from observational sampling errors in Wv, ρ_s, salinity and temperature do not significantly affect microwave penetration depth estimates here.

7.6 Conclusions

The intent of this chapter is to begin the initial steps of linking thermodynamic modeling with microwave remote sensing in a forward sense, that is, determine microwave scattering given the variables that control scattering through an electro-thermophysical relationship. The overall goal was to develop a working numerical model (ETSSIS) that enables us to interpret satellite microwave remote sensing signatures (active or passive) in a more physically meaningful way leading to better ways of monitoring the arctic climate and interpreting arctic climate change via microwave satellite remote sensing. Three specific questions were designed to utilize *in situ* field observations from SIMMS'92 to validate ETSSIS's ability to simulate the critical variables that control microwave scattering.

7.6.1 Question 1

The first question was to examine ETSSIS's ability to simulate the snow sea-ice thermodynamic characteristics that are related to microwave remote sensing. Results suggest the snow and upper ice layer thermal evolution are simulated fairly well (but slightly too warm in winter) even with the new salinity parameterization in k_{ss} and C_{ss}. Bottom snow and top ice layer temperatures are dramatically improved, relative to observations, during the melt season when salinity is included in k_{ss} and C_{ss}. The overall effect of the addition of salinity in the snow is to increase temperatures in the cold season and decrease temperatures in the warm season by its relative effects on snow k_{ss} and C_{ss}. If salt were explicitly treated in the snow mass balance of ETSSIS, salinity effects on the thermal evolution would be further complicated due to liquid water (brine) and latent heat release due to phase changes in this period. This would result in different thermodynamic effects within the snow pack in terms of vertical temperature structure.

7.6.2 Question 2

The second question was to examine the model's ability to simulate the snow's physical characteristics which are important for the interpretation of both active and passive microwave remote sensing. ETSSIS handles the relevant physical characteristics fairly well in most cases. However, since salinity effects on ETSSIS's mass balance are not parameterized, ETSSIS does not generate free liquid water (brine) within the snow soon enough in the spring season. This in turn affects modeled snow brine drainage

(brine volumes) and grain growth in the late season. Despite this, the modeled snow density (ρ_s) is simulated fairly well at all levels but may under estimate density in the colder season at mid levels. Snow grain size (d) trends are also realistic, however, d is underestimated near the base of the snow pack in the late season since liquid water is not generated soon enough.

7.6.3 Question 3

The final question was designed to illustrate the use of ETSSIS for direct application to microwave remote sensing through the first two questions and the electro-thermophysical relationship over the course of various snow stages (cold dry snow; pendular regime; funicular regime). This was done by examining "observed" and modeled microwave dielectric permitivity (ε'), loss (ε") and microwave penetration depth (δp) for various snow and ice layers. In the cold, dry snow season, ETSSIS reproduces the low snow ε' and ε" well, making the ice volume the dominant microwave scatterer and emitter with large penetration depths into the ice (i.e. the snow is virtually transparent in this season). This makes ETSSIS a valuable tool for interpreting microwave satellite signatures during the cold season that have potential for deriving snow depth estimations over thick smooth FYI (e.g., Barber and Nghiem, 1999; Markus and Cavalieri, 1998).

During the pendular snow regime, ε' is again simulated well by ETSSIS, however, since ETSSIS does not generate free liquid water (brine) soon enough in this regime, it continues to maintain a low snow ε" during this period and too high δp. Liquid water in snow makes the snow a more lossy material to microwaves and hence a larger ε"

and smaller δp would occur during the pendular regime. This implies ETSSIS would not produce enough of a snow layer contribution toward the total microwave scattering and emission. Once ETSSIS's mass balance considers the physical presence of salt in snow during the warmer spring season (snow temperatures $\geq$ -7°C), it will improve liquid water (brine) generation in this period and modeled ε" and δp.

Once liquid water is generated within the snow layer in ETSSIS, it produces ε' and ε" magnitudes that would be expected in the funicular snow regime. This also improves δp magnitudes within the snow and would allow a much greater proportion of the total scattering and emission to originate from snow.

7.7 Summary

In summary, this chapter has developed a 1-D electro-thermophysical model of the snow sea-ice system (ETSSIS) that attempts to predict snow-covered sea ice dielectric properties from late winter to advanced snow melt in late spring. This is a valuable tool for interpretation of microwave remote sensing signatures over this type of surface. It will allow researchers to better understand the climate processes occurring within the surface that cause the signatures viewed in microwave satellite remote sensing imagery given a certain environmental forcing. In a perfect scenario, the need for *in situ* observation (besides environmental forcing for the model) is alleviated and many aspects of arctic sea ice climate monitoring can be conducted through microwave satellite remote sensing alone. ETSSIS is a step toward this goal. ETSSIS reproduces many of the critical physical and thermodynamic variables that alter the dielectric properties of the snow and

sea ice volumes. However, like every model, it has limitations and needs further improvements, particularly in part of the spring season. Previous chapters have not only provided insight into some of the processes necessary for ETSSIS to be used for microwave remote sensing, but have also eluded to processes that require further attention. The following chapter summarizes the goals and results of my dissertation and outlines future work geared toward improving some of the processes within ETSSIS.

CHAPTER 8: Conclusions and Future Research

8.1 Conclusions

The Canadian Arctic is experiencing changes in its atmosphere and cryosphere which can ultimately lead to widespread biosphere changes. Evidence of arctic climate change has not only been scientifically indicated, but has also been voiced by the Inuit who rely on their environment as a way of life. Arctic climate change is expected to be significantly enhanced over the next hundred years due to various feedbacks in its climate system. World leaders have become aware of these climate change issues that affect the polar regions and the entire global climate system. However, in light of the most drastic changes projected in the polar regions, world authorities are now beginning to focus more attention on the polar regions.

Polar researchers have commonly used satellite remote sensing, numerical modeling and *in situ* observation to better understand polar climate processes and monitor any changes occurring in the polar climate. Recent research has shown there is an electro-thermophysical relationship between the electrical properties of snow-covered FYI that control microwave remote sensing signatures and the thermophysical evolution of snow-covered sea ice. The dielectric (or electrical) properties of the snow and sea ice are dictated by their thermophysical evolution which is driven by the surface energy balance (SEB). Numerical models of snow-covered sea ice can simulate the SEB and the associated

thermophysical evolution of the snow and ice. Dielectric models can simulate snow and sea ice electrical properties that in turn suggest the scattering signals we see in microwave satellite data. A model that couples the thermophysical evolution of snow-covered FYI with its electrical properties can simultaneously predict all of these characteristics over the various seasons.

The overall goal of my dissertation is to begin the process of linking thermodynamic snow sea-ice modeling to microwave remote sensing in a forward sense. This entails the development of a coupled one-dimensional thermodynamic snow sea-ice model where its output provides the necessary input to a snow and sea ice microwave dielectric model; the amalgamation of the models produces a new approach to modeling which I call the Electro-Thermophysical model of the Snow Sea Ice System (ETSSIS). The utility of this model allows one to predict the microwave scattering and emission within snow-covered first-year sea ice. The scientific application of such a model is to essentially by-pass *in situ* observation by utilizing ETSSIS over various FYI locations throughout the arctic to predict the thermophysical evolution and mechanical state of the ice. This in conjunction with actual microwave satellite data at similar locations will guide validation of the accuracy of the model within real conditions. If not, sensitivity analyses of various model runs may suggest other thermophysical reasons for the scattering that is taking place. In addition, with the advent of new microwave satellites (passive and active) with ever increasing spatial resolutions, ETSSIS can be a valuable tool for interpretation of these data sets over FYI.

The practical application of ETSSIS is to use its thermophysical information to predict locations where the ice is thermally and mechanically weak (or high break-up potential). This is not only useful for marine navigation but for the Inuit people and others who use the ice for travel, hunting and scientific investigations.

In a global climate context, the applications above spanning several years can lead to a better understanding of the FYI thermophysical changes that may take place in a global climate warming scenario. That is, relationships between arctic climate change, the surface energy balance and thermophysical changes within FYI can be made over several years of investigation. Furthermore, the detailed thermophysical processes of ETSSIS (i.e. climatic processes) can be used to conduct sensitivity studies that can suggest ways of scaling up the important processes to GCMs. This would improve current GCMs by ensuring they properly handle the critical climate processes that pertain to the polar regions.

As the development of this model progressed, several issues needed to be addressed and along with them, newer findings and improved understanding of snow-covered sea ice climate processes followed. These issues included: 1) ensuring the existing one-dimensional sea ice models treat the SEB and snow/ice thermodynamics in the appropriate time scales we see occurring in field experiments, 2) ensuring the snow and ice thermodynamics are not compromised by differences in environmental and spatial representation within components of the SEB, 3) ensuring that the snow layer is properly handled in the modeling environment, and 4) how satellite microwave remote sensing data can be used within the model environment.

In chapter 3, the first two issues were addressed by three research questions concerning, 1) the differences between diurnal time scales as opposed to daily averages in modeling seasonal snow covered fast-ice, 2) the representation of shorter time scale processes in the model's parameterizations, and 3) the differences between using actual "on ice" meteorological data as forcing as opposed to using "land-based" data as forcing within the model. I showed there were significant variations in snow and ice evolution using diurnal time scales when compared to daily averages, a fact that previously has never been addressed. Reasons for the differences are due to non-linear responses of the SEB within the snow cover with 1) the diurnal distribution of short-wave energy exchange within the snow cover accounting for 33% of the difference, 2) turbulent flux exchanges between the snow surface and atmosphere accounting for 17% of the difference, and 3) the positive albedo feedback mechanism of enhanced short-wave absorption during melt events accounting for 50% of the difference. This result highlighted the importance of accounting for diurnal processes within sea ice models which have also been cited as being predominant in time-series microwave satellite signatures (see for example, Barber and Nghiem, 1999; Barber et al., 1999).

The simple incident radiation parameterizations are capable of representing these energy fluxes over diurnal time scales in most cases. The radiation parameterizations require somewhat accurate knowledge of cloud cover and cloud optical depth with tropospheric aerosols and solar zenith angle dependencies being secondary factors. The current albedo parameterization of the FB sea ice model requires further attention, especially during the late snow melt and melt pond periods. The albedo scheme decreases

magnitudes too quickly during these periods causing the snow and fast-ice to decay too rapidly. I found that the biases between meteorological conditions on land and sea ice are significant enough to cause differences in fast-ice model simulations (i.e. spatial variations become important). Typically, land-based meteorological measurements are used to drive model simulations, however, I found that this can cause an abnormally quick decay of seasonal snow-covered sea ice. This is primarily due to variations in incident radiation, larger wind speeds over the ice surface (increased turbulent exchange), and differences between modeled and observed surface albedo. The results suggest that improvements in surface albedo parameterizations during the melt season and that atmospheric information over the sea ice surface are required to improve sea ice model simulations. This would also provide better feedback for deciphering microwave satellite signals that are dictated by SEB and surface changes.

In chapter 4, I expanded on addressing the first two issues and Chapter 3 results by addressing two research questions that further concentrated on incident radiation parameterizations, in light of their critical importance to the SEB. In particular, I critically assessed selected $K\downarrow$ and $L\downarrow$ parameterizations against *in situ* field measurements to identify any seasonal or environmental/spatial biases and offered improved representations of these parameterizations. Many of the parameterizations were developed from arctic coastal stations in the northwest arctic and Canadian Archipelago and were never validated over other important arctic locations such as polynyas or near large open water regions. Unique data collected within and around an arctic polynya suggests the $K\downarrow$ clear-sky schemes produce a positive seasonal bias where they

underestimated fluxes in the cold season and overestimated fluxes in the warm season. The positive bias is more dramatic in the full marine environment. The K↓ cloudy-sky schemes deplete too much radiation in the colder season and not enough in the warm season, especially in the marine warm season. An improved implementation of the schemes was made by varying the cloud optical depth. The L↓ clear-sky fluxes were improved after adjusting (decreasing) the clear-sky emissivity to account for a less emissive atmosphere at colder temperatures. This correction was sufficient for the marine conditions and corrected any seasonal bias. The L↓ cloudy-sky emissivity also needed to be increased for the near-shore fast-ice regime to account for under-estimations when clouds were present. This also alleviated a slight seasonal bias. An exponential dependence of cloud fraction was found to be important for the L↓ all-sky fluxes. Different L↓ all-sky results were found for the marine environment. Overall, the marine region consistently had more negative mean errors compared to the fast-ice site. This was not due to warmer ambient marine temperatures. The all-sky short-wave flux results suggested the marine environment had greater cloud optical depths compared to the fast-ice and terrestrial sites and is consistent with the long-wave results where a higher cloud emissivity may be required; although cloud base height differences could also be a factor. I concluded by offering newer forms of the L↓ clear-sky and all-sky parameterizations.

In Chapter 4 I highlighted the effects of various arctic environments on the simulation of incident short-wave and long-wave radiation. Improvements to the parameterization schemes will help reduce errors in these fluxes and improve sea ice

258

simulations for these environments. This will enhance our ability to better correlate microwave satellite signatures with sea ice model simulations.

In Chapter 5 I continued with a focus on the first two issues and built upon results from Chapters 3 and 4 by examining another important SEB variable; the surface albedo. The albedo is linked to Chapter 4 since it implicitly affects incident short-wave fluxes when clouds are present. Very few albedo observations and its spatial characteristics exist over FYI, especially during the melt season. Three research questions were designed to examine the spatial aspects of fractional surface cover types and surface albedo and to determine the role melt ponds play in these aspects over land-fast FYI. The results offered unique information on surface albedo during the melt pond season over FYI. In response to the first question, I included surface-based broadband and spectral albedo measurements over various cover types (deeper snow to deep melt ponds) during the melt pond season. The second question considered scaling up the surface measurements to regional scales by applying them to aircraft video data. These regional albedo estimates were corroborated by independent helicopter measurements. The last question involved a modeling experiment using the one-dimensional sea ice model (non-coupled) that showed that its albedo parameterization during the pond season progressed too quickly according to observations made in the first two questions. If a climatological albedo progression over a seven week period is used, simulated ice evolution improved. Further model experiments explicitly showed how changes in melt pond fraction can alter the ice thermodynamic state and thus its susceptibility to break-up. It was found that the vertical ice temperature gradient change (ITGC) increased as a quadratic with respect to

linear increases in pond fraction. Using the ITGC, an ice surface with 80% pond fraction can produce a near-isothermal ice profile more than 3 weeks earlier than an ice surface with 10% pond fraction.

Results from Chapter 5 contribute to the growing knowledge of albedo measurements over FYI for implementation into process models and GCMs. The four primary cover types identified during the melt season highlight their importance when attempting to model albedo over FYI and should be included in process models and GCMs. All of the modeling exercises showed the importance of improved melt pond representation in model albedo parameterizations and included a more realistic albedo progression over FYI in a climatological sense. These results will ultimately improve our ability to simulate the polar climate and interpreting microwave satellite observations.

Chapter 6 specifically focussed on the third issue of improving the sea ice model's representation of the snow layer. This chapter is implicitly linked to Chapters 3 to 5 by ensuring the snow layer is appropriately treated in FYI models. That is, errors in modeled snow layer characteristics will lead to errors in SEB parameters (e.g. albedo and hence incident short-wave radiation), ice growth and ablation. The model improvement involved coupling a detailed one-dimensional energy and mass balance model of snow to a one-dimensional thermodynamic first-year sea ice model. This type of coupled model has previously not been available. In addition, salinity effects in snow were parameterized with respect to snow thermal conductivity and heat capacity but were not parameterized within the snow mass balance. Salinity in snow is a common and important feature over

FYI due to its thermodynamic and microwave remote sensing implications. Until now, snow salinity has been ignored in sea ice models.

Two research questions investigated differences in modeled snow/ice evolution (question 1) and thermodynamic behavior (question 2) between the coupled model with and without salinity (coupled model without salinity - C; coupled model with salinity - UPR) and the non-coupled model with a single bulk property snow layer (non-coupled model - NC). Results suggest there can be significant differences in snow and ice evolution between C and NC. This is due to C treating the snow in a more rigorous and realistic fashion and its more sophisticated turbulent exchange, incident radiation, and snow albedo parameterizations. It was concluded that C was superior in modeling the snow and ice evolution and is advantageous to use over simpler models. The drawback of C is, of course, computational expense (run time).

Accounting for salinity in snow thermal conductivity and specific heat acts to reduce ice growth rates in the cold season and ablation rates in the spring melt season but does not appear to be a significant factor for annual sea ice cycles in most cases. However, results may be slightly different if salt were treated in the modeled mass balance since liquid water (brine) would be generated sooner in the spring period. Thermodynamically, there is no difference in simulated snow surface temperatures between NC and C but ice surface temperatures are slightly too warm in C; salinity amplifies this error in the cold season but significantly reduces the error during the melt season. However, it was not apparent that these inaccuracies affected FYI annual cycle simulations. It is unknown what effect the addition of salinity in the snow mass balance

261

would have on the thermodynamic results over the course of annual simulations due to complex feedbacks that would take place.

In Chapter 6 I highlight the importance of the snow layer when simulating FYI evolution and offer a new type of model for conducting polar climate processes. This will ultimately lead to future improvements in accounting for critical processes within GCMs as well as directly linking microwave remote sensing to the snow and ice models.

In the final chapter I examined the last issue by investigating the coupled snow sea-ice model and its use for passive and active microwave remote sensing applications. The coupled model was developed because current sea ice models do not provide enough physical information within the snow layer to be useful in the interpretation of microwave scattering. The coupled model provides the necessary output to be used as input to a microwave dielectric model of the Debye form; the amalgamation of the models produces an Electro-Thermophysical model of the Snow Sea Ice System (ETSSIS). This type of sophisticated forward modeling approach has previously never been conducted for microwave remote sensing of sea ice. The first two research questions looked at how well ETSSIS simulated the critical thermodynamic (question 1) and physical (question 2) variables required for input to the dielectric model by comparing the simulated variables to time-series observations. The last question illustrates how well ETSSIS predicts microwave dielectric properties and penetration depths.

Results suggest ETSSIS simulates the thermodynamic and physical properties reasonably well in most cases (with exception to salinity) but does not generate free liquid water within the snow pack early enough in the spring period. This is due to salinity not

being parameterized in the snow mass balance of the model. Salt embedded within and around the snow crystals causes internal melt at temperatures well below zero (near - 8°C). Liquid water fractions during this melt typically range between 1 - 7% water by volume (i.e. pendular snow regime). The lack of modeled liquid water in this regime causes ETSSIS to under predict dielectric loss and over predict penetration depths (at 5.3 GHz), the result being that the snow layer would not contribute enough of the total microwave scattering and emission. Despite this drawback, ETSSIS is still very useful for applications in deciphering microwave remote sensing imagery of snow-covered sea ice in the winter and full melt seasons. In winter dry snow, ETSSIS produces snow and ice dielectric properties and penetration depths at expected magnitudes, making the ice volume the dominant microwave scatterer and emitter; snow is virtually transparent in this regime. In the full snow melt (funicular) regime, ETSSIS produces enough free liquid water in the snow pack (7 - 11% water by volume) to increase (decrease) the dielectric loss (penetration depths) to expected values making the snow pack the dominant scatterer and emitter.

Results from Chapter 7 provides an exciting new tool for linking the thermophysical characteristics and microwave remote sensing of snow covered FYI. The model can be applied to various locations throughout the polar regions to infer thermophysical changes from microwave satellite observations given certain environmental forcing. This will ultimately lead to better understanding the relationships between polar climate change and the associated electro-thermophysical changes that will accompany those changes.

8.2 Summary

Typically, microwave remote sensing and thermodynamic modeling of snow-covered FYI are used independently for studying and monitoring the arctic sea ice climate. The overall theme of my dissertation is to link thermodynamic modeling and microwave sensing of snow-covered FYI. Issues that needed to be addressed before this was possible have been discussed in various chapters. Results from these issues have added to the knowledge base of current sea ice climate processes as well as providing a new modeling tool for understanding these processes and interpretation of microwave remote sensing. Continuation of model improvements and exploiting other remote sensing/modeling techniques to further understand and monitor the arctic climate should be conducted in the future. This is based on the fact that many processes and feedbacks in the arctic climate system are still largely unexplored and unknown (e.g. cloud-precipitation-albedo feedbacks, and interdisciplinary feedbacks such as physical sea ice regimes and biological coupling). With the advancement of new microwave remote sensing satellites and improved modeling, further implementations of linking the two will provide us with better tools to understand these processes and feedbacks. In light of this, the last section provides some insight for further improving thermodynamic modeling efforts toward microwave remote sensing and sea ice climate processes.

8.3 Future Research

In light of the results contained in my dissertation, several areas for model improvement arise. Future arctic field work will address some of these modeling and remote sensing issues.

1) Incorporate newer incident radiation parameterization schemes (i.e. radiative transfer models) that can be more accurate for shorter time scales.

Total column atmospheric radiative transfer (RT) models have become computationally efficient enough to use within various scales of sea ice models for estimating incident short-wave and long-wave radiation. Implementation of these radiation schemes in the coupled snow sea-ice model would be relatively simple provided the appropriate input is available. Current RT schemes can reproduce incident radiative fluxes to within 3-9% for short-wave and 1-5% for long-wave (see for example, Li and Leighton, 1993; Allan, 2000) which are better than the simpler schemes in Chapter 4. Vertical profiles of pressure and humidity, ozone and aerosol optical depth, cloud amounts and optical depth, cloud top heights, and broadband surface albedo are typically required as input to RT schemes. The main problem is obtaining these data in arctic locations, unless one is fortunate enough to have upper air observations available. If the input parameters are not accurate, the RT estimates will also be inaccurate and potentially can be worse than those of the simpler schemes. The use of numerical weather prediction models or

satellite-derived parameters may provide most of the input required for arctic applications of RT models if upper air soundings are not available.

2) Improve the temporal representation of melt ponds in current albedo parameterizations or ingest microwave satellite-derived albedo into the model for operational ice forecasting.

A current limitation of all sea ice models is the temporal representation of the melt season (including melt ponds) in their albedo parameterizations. The fractional area of the critical cover types, and hence total surface albedo, (in Chapter 5) change dramatically in time and space over the course of the melt season. Currently, there are no physical models to temporally represent these surface cover and albedo changes. Future field work will be tailored toward temporal measurements of fractional cover type changes and the associated parameters that control these changes (the SEB and snow/ice melt input, precipitation, melt pond drainage mechanisms, mechanical wave forcing (by wind), and warm/cold air advection) in an attempt to develop new melt pond albedo parameterizations over FYI. Another approach is to use satellite microwave remote sensing-derived melt pond fraction that can be ingested by the sea ice model. Yackel and Barber (1999) have shown that melt pond fraction (and albedo) may be inverted from active microwave satellite imagery in windy conditions. This information can be input directly into the model without the use of (or supplement) albedo parameterizations.

3) Include a more physically-based snow grain growth parameterization that includes wet snow growth processes (vapor growth and liquid water scavenging).

Snow grain growth processes in many snow models include a combination of physical and empirical relationships. A major deficiency particularly exists during the pendular regime (liquid water fractions between 1-8%) when grain growth can rapidly accelerate by liquid water "scavenging" (illustrated in Chapter 7). Free liquid water in sub-freezing temperatures along with a vertical temperature gradient causes existing large grains to increase in size. Although this growth is very complex and difficult to measure, future field work and/or further theoretical studies will attempt to improve our physical understanding of these processes for implementation into the model.

4) Include salinity in the mass balance of the model to account for salts (brine), ice and air volume fractions to improve the snow layer's thermal behavior between 0°C and -8°C. A physical parameterization of how salinity becomes introduced into the various snow layers over time is also required.

A limitation of ETSSIS is its simplification of saline snow where salts (brine) can physically occupy space within the snow layer besides air, ice and liquid (if melting). In terms of mass balance, salt (brine) inclusions affect the overall snow mass, density, and physical make up of snow structure (grains and bonding). This ultimately affects the snow's thermal characteristics. The local freezing temperature of the snow pack is reduced depending on salt (brine) content and fractional volumes of air, ice and liquid. These factors are accounted for in the thermal conductivity and specific heat of the

267

current version of ETSSIS and the routine that does this can be applied to the mass balance of the model. That is, a routine to include salt (brine) in the mass balance of ETSSIS already exists, however, the parameters within the routine must replace existing mass balance parameters; this procedure is fairly involved and one that could not be implemented before the completion of this work. Future work will address this.

Currently, little is known about how salt gets introduced into the various snow layers. Initially, when young ice grows, salts are forced upward toward the atmosphere (Ono and Kasai, 1985) and can "contaminate" the snow layer near its surface. The physical mechanism of how salinity appears in the middle snow layers is uncertain. Future field work will explore this phenomena in an attempt to develop a physical relationship for implementation into ETSSIS. This would alleviate the need for specifying a snow salinity profile as is done in the current version of ETSSIS.

5) Include the desalination process. That is, liquid water filtrates toward the ice surface during melt and flushes salt (brine) to the base of the snow pack where dilution also takes place.

Once liquid water is generated in the snow pack, gravitational forces cause liquid water to drain to the bottom of the snow pack; the rate of drainage is dependent on the various amounts of liquid available from each snow layer. This process is accounted for within ETSSIS. If the snow is saline, brine is also flushed out of the middle snow layers and gets diluted by liquid water in lower layers. In effect, the middle snow layers entirely desalinate and the lower layers become less concentrated with salt (brine) over time until

the entire snow pack becomes desalinated. This is not accounted for in ETSSIS and is shown in Chapter 7. This is not only important for the snow's thermal evolution but for microwave dielectrics (see Chapter 7). Desalination processes could be tied to current liquid water filtration processes within ETSSIS. Future field work will attempt to monitor snow desalination processes by directly measuring snow salinity over short time scales (minutes to hours). These measurements would act as a proxy for monitoring liquid water filtration since direct measurement of liquid water movement is difficult, especially when snow is saline (due to instrument limitations). However, consistent *in situ* measurement of salinity both spatially and temporally is also difficult. Hopefully, new techniques for measuring snow salinity or liquid water will become available (either directly or remotely).

6) Include a physical mechanism for brine/liquid water filtration across the snow-ice interface (this is also pointed out by Jordan et al., 1999).

Once liquid water (or brine) reaches the ice surface from snow melt, it either refreezes or filtrates into the ice surface where it can refreeze within the ice or filtrate through the ice itself. ETSSIS refreezes and/or drains this liquid water once it reaches the ice surface. This simplification results in neglected latent and sensible heating associated with phase changes (and brine effects) at the ice surface and within the ice (if liquid (brine) flows through the ice volume). The process of liquid water allowing to pass through the snow-ice interface will be implemented in future versions of SNTHERM (R. Jordan, pers. Com., 2000) as well as ETSSIS. Attempting to validate and measure this

process in the field is difficult due to instrumentation limitations and knowing whether the liquid water at the ice surface is due to snow melt or ice surface melt.

7) *Include a physical representation of blowing snow to account for accumulation/erosion due to wind.*

If snow models were capable of recreating the physical characteristics of surface snow accurately (i.e. roughness characteristics and impact of airborne snow), natural accumulation or erosion according to wind speed would take place. The need for "tuning" the fractional stress gradient in ETSSIS would no longer be required to reproduce snow depths. All of the required snow characteristics are difficult to recreate in a 1-D model, such as downstream roughness and topography. Researchers involved in blowing snow processes are actively engaging in improving these types of processes in 2-D and 1-D modeling of snow (J. Pomeroy, pers. Com., 2000). Future field work is necessary toward this goal.

8) Focus on incorporating remote sensing into snow sea-ice models such as ingesting real satellite data to guide model parameterizations. Another approach would be to expand the snow sea-ice model coupling to a forward or inverse full microwave scattering/emission model.

Inversion of microwave satellite remote sensing can provide several snow and sea ice parameters that can be potentially ingested by ETSSIS (such as albedo). This data can either supplement or replace model parameterizations to ensure the model appropriately

represents these processes or parameters. This would ultimately allow for more accurate simulations of snow-covered sea ice. One difficulty arises with this approach since the remote sensing parameter that is ingested by the model is inherently decoupled from the model's physics (e.g. the satellite-derived albedo may represent a different surface than the model is creating). Another option is to couple a numerical microwave inverse or forward scattering model to ETSSIS. This approach is more physically attractive since we can explicitly model total microwave scattering and emission given the snow-sea ice thermodynamic and physical evolution and compare this to actual remote observations. This would elude to a) why we are seeing certain signatures in satellite imagery over a full annual sea ice cycle, and b) possibly suggest areas for future model improvement if we can not explain what we are seeing in the satellite imagery. Regardless of the approach, using microwave remote sensing and modeling of snow-covered sea ice in tandem can lead to feedbacks between the two. That is, limitations in one approach can be counteracted or built upon by the strengths of the other.

References

Aagaard, K., L.K. Coachman and E. Carmack, 1981: On the Halocline of the Arctic Ocean. *Deep-Sea Res.*, 28A, 529-545.

Alford, D., 1974: Snow. In: *Arctic and Alpine Environments*, Ed: J. Ives and R. Barry, 85-110.

Allan, R.P., 2000: Evaluation of simulated clear-sky longwave radiation using ground-based observations. *J. Climate*, 13, 1951-1964.

Anderson, E.A., 1976: A point energy and mass balance model of a snow cover. *NOAA Tech. Report NWS 19*, pp. 150.

Arking, A., O.M. Izakova and Y.E.M. Feygel'son, 1992: Use of satellite, ground, and aerological data for calculating IR fluxes. *Atmos. Oceanic Phys.*, 28, 283-287.

Bader, H. P. and P. Weilenmann, 1992: Modeling temperature distribution, energy and mass flow in a (phase-changing) snowpack. I, Model and case studies. *Cold Reg. Sci. Technol.,*, 20, 157-181.

Barber, D.G., D.D. Johnson and E.F. LeDrew, 1991: Measuring climatic state variables from SAR images of sea ice: The SIMS SAR validation site in Lancaster Sound. *Arctic*, 44, 108-121.

Barber, D.G., 1993: Assessment of the interaction of solar radiation with a seasonally dynamic snow covered sea ice volume, from microwave scattering. Ph.D. Thesis. University of Waterloo, Waterloo, Ontario, pp. 266.

Barber, D.G., T.N. Papakyriakou and E.F. LeDrew, 1994: On the relationship between energy fluxes, dielectric properties and microwave scattering over snow covered first year sea ice during the spring transition period. *J. Geophys. Res.*, 99(C11), 22,401-22,411.

Barber, D.G. and E.F. LeDrew, 1994: On the links between microwave and solar wavelength interactions with snow-covered first-year ice. *Arctic*, 47, 298-309.

Barber, D.G., T.N. Papakyriakou, E.F. LeDrew and M.E. Shokr, 1995a: An examination of the relation between the spring period evolution of the scattering coefficient and radiative fluxes over landfast sea ice. *Intl. J. Remote Sensing*, 16(17), 3343-3363.

Barber, D.G, S.P. Reddan, and E.F. LeDrew. 1995b. Statistical Characterization of the Geophysical and Electrical Properties of Snow on Landfast First-Year Sea Ice. *J. Geophys. Res. (Oceans)*. 100(C2): 2673-2686.

Barber, D.G., 1997: Sea Ice Decay for Marine Navigation – Phase 1 Report: prepared for the Arctic Ice Regime Shipping System (AIRSS), Marine Safety Division, Transport Canada, pp. 112.

Barber, D.G., J.J. Yackel, R. Wolfe and W. Lumsden, 1998: Estimating the thermodynamic state of snow covered sea ice using time series synthetic aperture radar (SAR) data. *Proc. 8th Intl. Offshore and Polar Eng. Conf.*, Montreal, Canada, May 1998. Intl. Soc. of Offshore and Polar Engineering. Vol. III, 50-54.

Barber, D.G. and A. Thomas, 1998: The influence of cloud cover on the radiation budget, physical properties and microwave scattering coefficient of first-year and multi-year sea ice, *IEEE Trans. Geosci. Rem. Sens.*, 36(1), 38-50.

Barber, D.G., A. Thomas, and T.N. Papakyriakou, 1998: Role of SAR in surface energy flux measurements over sea ice. In: Analysis of SAR Data over the Polar Oceans. Ed: C. Tsatsoulis and R. Kwok. Published by Springer-Verlag Berlin Heidelberg, pp. 35-67.

Barber, D.G. and J. Yackel, 1999: The physical, radiative and microwave scattering characteristics of melt ponds on Arctic landfast sea ice. *Intl. J. Remote Sensing*, 20, 2069-2090.

Barber, D.G. and S.V. Nghiem, 1999: The role of snow on the thermal dependence of microwave backscatter over sea ice. *J. Geophys. Res.*, 104(C11), 25789-25803.

Barber, D.G., J.J. Yackel and J.M. Hanesiak, 1999: Perspectives on sea ice, Radarsat-1 and Arctic climate change. *Can. J. Remote Sensing*, in press.

Barber, D.G., J.M. Hanesiak, W. Chan and J. Piwowar, 2001: Sea ice and meteorological conditions within Baffin Bay and the North Water Polynya between 1979 and 1996, *Atmos.-Ocean* (in review).

Barber, D.G. et al., 2001: The North Water Polynya Project: Physical Processes, *Atmos.-Ocean* (in review).

Barry, R.G., A. Henderson-Sellers, and K.P. Shine, 1984: Climate sensitivity and the marginal cryosphere. In: Climate Processes and Climate Sensitivity, Ed: J.E. Hansen, T. Takahashi. Geophysical Monograph 29, Maurice Ewing Vol. 5, Am. Geophysical Union, pp. 221-237.

Barry et al., 1989: Characteristics of arctic sea ice from remote sensing data and their relationship to atmospheric processes. *Ann. Glaciol.*, 12, 9-15.

Barry, R.G. and J. Maslanik, 1989: Arctic sea ice characteristics and associated atmosphere-ice interactions in summer inferred from SMMR data and drifting buoys: 1979-1984. *Geo. Journal*, 18, 35-44.

Barry, R.G., 1996: The parameterization of surface albed ˙ for sea ice and its snow cover. *Progress in Phys. Geog.*, 20(1), 63-79.

Bennett, T.J., 1982: A coupled atmosphere-sea ice model study of the role of sea ice in climatic predictability. *J. Atmos. Sci., 39, 1456-1465.*

Bennington, K.O., 1963: Some crystal growth features of sea ice. *J. Glaciol.*, 4(36), 669-688.

Bradley, C.C., R.L. Brown and T.R. Williams, 1977: Gradient metamorphism, zonal weakening of the snow-pack and avalanche initiation. *J. Glaciol.*, 19, 335-342.

Bergin, M.H., et al., 2000: Comparison of aerosol optical depth inferred from surface measurements with that determined by sun photometry for cloud-free conditions at a continental U.S. site. *J. Geophys. Res.*, 105(D5), 6807-6816.

Blanchet, J-P and R. List, 1983: Estimation of optical properties of Arctic haze using a numerical model. *Atmos.-Ocean*, 21, 444-465.

Boer, G.J., G.M. Flato and D. Ramsden, 2000: A transient climate change simulation with greenhouse gas and aerosol forcing: projected climate to the twenty-first century. *Climate Dynamics*, 16, 427-450.

Brown, R.J., 1995: Global change in agriculture. Canadian Remote Sensing Contribution to Understanding Global Change, Dept. of Geography Publication Series, No. 38, University of Waterloo, 125-150.

Brown, R.D. and P. Cote, 1992: Interannual variability of landfast ice thickness in the Canadian high Arctic, 1950-1989. *Arctic*, 45, 273-284.

Brown, R.D. and B.E. Goodison, 1994: The sensitivity of the Arctic climate system to snowfall: evidence from the Canadian high Arctic. *Proc. 51st Annual Meeting of the Eastern Snow Conf.*, Dearborn, Mich., June 15-16.

Brown, R.D., 2000: Northern hemisphere snow cover variability and change, 1915-97. *J. Climate*, 13, 2339-2355

Brun, E., E. Martin, V. Simon, C. Gendre and C. Colleou, 1989: An energy and mass model of snow cover suitable for operational avalanche forecasting. *J. Glaciol.*, 35, 333-342.

Brun, E., P. David, M. Sudul and G. Brunot, 1992: A numerical model to simulate snow-cover stratigraphy for operational avalanche forecasting. *J. Glaciol.*, 38, 13–22.

Budyko, M.I., 1966: Polar ice and climate. In: Proceedings of the symposium on the Arctic Heat Budget and Atmospheric Circulation. Ed: J.O. Fletcher, The Rand Corporation, Santa Monica, CA, RM-5233-NSF, pp. 3-22.

Burns, B.A., 1990: SAR image statistics related to atmospheric drag over sea ice. *IEEE Trans. Geosci. Rem. Sens.*, 28(2), 158-165.

Camiso, J.C., 1986: Characteristics of Arctic winter sea ice from satellite multispectral microwave observations. *J. Geophys. Res.*, 91(C1), 975-994.

Carmack, E.C., R.W. Macdonald, R.G. Perkin, F.A. LcLaughlin, and R.J. Pearson. 1995. Evidence of warming of Atlantic water in the Southern Canadian Basin of the Arctic Ocean. *Geophys. Res. Letters.* 22. 1061-1064.

Carsey F. Microwave Remote Sensing of Sea Ice. American Geophysical Union. 1993. Geophysical Monograph #68. 462 pp.

Cavalieri, D.J., 1994: A microwave technique for mapping thin sea ice. *J. Geophys. Res.*, 99, 12,561-12,572.

Colbeck, S.C., 1973: Theory of metamorphism of wet snow. *CRREL Res. Rep. 313.*

Colbeck, S.C., 1980: Thermodynamics of snow metamorphism due to variations in curvature. *J. Glaciol.*, 26, 291-301.

Colbeck, S.C., 1982: An overview of seasonal snow metamorphism. *Rev. Geophys. Space Phys.*, 20, 45-61.

Colbeck, S.C., 1983: Theory of metamorphism of dry snow. *J. Geophys. Res.*, 88(C9), 5475-5482.

Colbeck, S.C., 1986: Statistics of coursening in water-saturated snow. *Acta Metalurgica*, 34, 347-352.

Colbeck, S.C., 1987: Snow metamorphism and classification. In: *Seasonal Snowcovers: Physics, Chemistry, Hydrology.* New York: D. Reidel, 1-35.

Colbeck, S.C., 1989: Air movement in snow due to wind pumping. *J. Glaciol.*, 35, 209-213.

Colbeck, et al., 1990: The International Classification for Seasonal Snow on the Ground. Prepared by: The Intl. Commission on Snow and Ice of the Intl. Association of Scientific Hydrology and the Intl. Glaciology Society. pp. 24.

Colbeck, S.C., 1991: The layered character of snow covers. *Rev. Geophys.*, 21(1), 81-96.

Cox, G.F. and W.F. Weeks, 1988: Numerical simulations of the profile properties of undeformed first-year sea ice during the growth season. *J. Geophys. Res.*, 93(C10), 12449-12460.

Crocker, G.B, 1984: A physical model for predicting the thermal conductivity of brine-wetted snow. *Cold Reg. Sci. Technol.*, 10, 69-74.

Curry, J.A. and E.E. Ebert, 1992: Annual cycle of radiation fluxes over the Arctic Ocean: sensitivity to cloud optical properties. *J. Climate.*, 5, 1267-1280.

Curry, J.A., J. L. Schramm and E.E. Ebert, 1995: Sea ice-albedo climate feedback mechanism. *J. Climate.*, 8, 240-247.

DeAbreu, R.A., J. Key, J. Maslanik, M.C. Serreze and E.F. LeDrew, 1994: Comparison of in-situ and AVRHH-derived broadband albedo over Arctic sea ice. *Arctic*, 47(3), 287-297.

De Abreu, R.A., D.G. Barber, K. Misurak and E.F. LeDrew, 1995: Spectral albedo of snow covered first-year and multi-year sea ice during spring melt. *Annals of Glaciol.*, 21, 337-342.

DeAbreu, R.A. and E.F. LeDrew, 1996: Multispectral analysis of fast sea ice albedo using AVHRR data. *Proc. IGARSS'96*, 651-653.

De Abreu, R.A., 1996: In Situ and Satellite Observations of the Visible and Infrared Albedo of Sea Ice During Spring Melt. Ph.D. Thesis, Department of Geography, University of Waterloo, Waterloo, Ontario, 326 p.

Drinkwater, M.R. and G.B. Crocker, 1988: Modeling changes in the dielectric and scattering properties of young snow-covered sea ice and GHz frequencies. *J. Glaciol.*, 34(118), 274-282.

Drinkwater, M.R., 1989: LIMEX'87 Ice surface characteristics: implications for C-Band SAR backscatter signatures. *IEEE Trans. Geosci. Rem. Sens.*, 27(5), 501-513.

Ebert, E.E. and J.A. Curry, 1993: An intermediate one-dimensional thermodynamic sea ice model for investigating ice-atmosphere interactions. *J. Geophys. Res.*, 98, 10,085-10,109.

Efimova, N.A., 1961: On methods of calculating monthly values of net long-wave radiation. *Meteorol. Gidrol., 10, 28-33.*

Evans, K.F., 1998: The spherical harmonics discrete ordinate method for three-dimensional atmospheric radiative transfer. *J. Atmos. Sci.*, 55, 429-446.

Fichefet, T., B. Tartinville and H. Goosse, 2000: Sensitivity of the antarctic sea ice to the thermal conductivity of snow. *Geophys. Res. Letters*, 27, 401-404.

Fily, M. and D.A. Rothrock, 1986: Extracting sea ice data from satellite SAR imagery. *IEEE Trans. Geosci. Rem. Sens.*, GE-24, 849-854.

Flato, G.M. and W.D. Hibler, 1992: On modeling pack ice as a cavitating fluid. *J. Phys. Oceanogr.*, 22, 626-651.

Flato, G.M. and R.D. Brown, 1996: Variability and climate sensitivity of landfast Arctic sea ice. *J. Geophys. Res.*, 101(C10), 25767-25777.

Fowler, C., J.A. Maslanik and W. Emery, 1994: Observed and simulated ice motion for an annual cycie in the Beaufort Sea. *Proc. IGARSS'94.*

Fukami, H., K. Kojima and K. Aburakawa, 1985: The extinction and absorption of solar radiation within a snow cover. *Ann. Glaciol.*, 6, 118-122.

Fukusako, S., 1990: Thermophysical properties of ice, snow and sea ice. *Int. J. Thermophys.*, 11, 353-372.

Gabison, R., 1987: A thermodynamic model of the formation, growth, and decay of first-year sea ice. *J. Glaciol.*, 33, 105-119.

Golden, K.M. et al., 1998a: Forward electromagnetic scattering models for sea ice. *IEEE Trans. Geosci. Rem. Sens.*, 36, 1655-1674.

Golden, K.M., et al., 1998b: Inverse electromagnetic scattering models for sea ice. *IEEE Trans. Geosci. Rem. Sens.*, 36, 1675-1703.

Gower, J.F.R, 1995: Global change: Impact on oceans and fisheries, contributions of remote sensing to future studies. Canadian Remote Sensing Contribution to Understanding Global Change, Dept. of Geography Publication Series, No. 38, University of Waterloo, 111-124.

Grenfell, T.A. and G.A. Maykut, 1977: The optical properties of ice and snow in the Arctic basin. *J. Glaciol.*, 18(30), 445-463.

Grenfell, T.C. and D.K. Perovich, 1984: Spectral albedos of sea ice and incident solar irradiance in the Beaufort Sea. *J. Geophys. Res.*, 89, 3573-3580.

Grenfell, T.A., 1996: Microwave and thermal infrared emission from young sea ice and pancake ice. *Proc. IGARSS'96*, 959-961.

Gruelll, J.W. and T. Konzelmann, 1994: Numerical modeling of the energy balance and the englacial temperature of the Greenland ice sheet: Calculations for the ETH-Camp location. *Global Planet. Change*, 9, 91-114.

Guryanov, I.E., 1985: Thermal-physical characteristics of frozen, thawing and unfrozen grounds, *4th Intl. Symp. Ground Freezing*, Sapporo, Japan, 225-230.

Hanafin J. A. and P. J. Minnett, 2001. Cloud forcing of surface radiation in the North Water Polynya. *Atmos.-Ocean*, (in press).

Hänel, G, 1976: The properties of atmospheric aerosol particles as functions of the relative humidity at thermodynamic equilibrium with the surrounding moist air. *Advances in Geophysics*, 19, 73-188.

Hanesiak, J.M., 1998: Historical Perspective. In: *NOW'98 Sea Ice/Climate Dynamics Subgroup Field Summary*, Ed. Papakyriakou, T.N., C.J. Mundy, and D.G. Barber, Centre for Earth Observations Science, Department of Geography, University of Manitoba, CEOS tech 98-8-2, pp. 15-20

Hanesiak, J.M., D.G. Barber and G.M. Flato, 1999: The role of diurnal processes in the seasonal evolution of sea ice and its snow cover. *J. Geophys. Res.*, 104(C6), 13593-13604.

Hanesiak, J.M., D.G. Barber, T.N. Papakyriakou and P.J. Minnett, 2001a: Parameterization schemes of incident radiation in the North Water. *Atmos.-Ocean*, (in press).

Hanesiak, J.M., D.G. Barber, T.N. Papakyriakou and R.E. Jordan, 2001b: Utility of a coupled 1-D thermodynamic snow-sea ice model toward microwave remote sensing. *J. Geophys. Res.*, (in review).

Hanesiak, J.M., D.G. Barber, R.A. De Abreu and J.J. Yackel, 2001c: Local and regional observations of arctic first-year sea ice melt pond albedo. *J. Geophys. Res.*, 106(C1), 1005-1016.

Herman, G. F., 1986: Arctic stratus clouds. In, *The geophysics of sea ice*. Ed. Untersteiner, N. (Plenum press, New York) p. 9-164.

Herman, G.F. and J.A. Curry, 1984: Observational and theoretical studies of solar radiation in Arctic stratus clouds. *J. Climate and Appl. Meteorol.*, 23, 5-24.

Heron, R. and M.K. Woo, 1994: Decay of high Arctic lake-ice cover: Observations and modeling. *J. Glaciol.*, 40, 283-292.

Holben, B.N., Y.J. Kaufman, and J.D. Kendall,1990: NOAA-11 AVHRR visible and near-IR inflight calibration. *Intnl. J. Remote Sensing*, 11(8), 1511-1519.

Holland, D.M., L.A. Mysak and D.K. Manak, 1993: Sensitivity study of a dynamic thermodynamic sea ice model. *J. Geophys. Res.*, **98**(C2), 2561-2586.

IPCC (Intergovernmental Panel on Climate Change), 1996. Climate Change: The IPCC Assessment. J.T. Houghton, G.J. Jenkens, and J.J. Ephraums (eds.) Cambridge University Press, Cambridge, U.K.

Jacobs, J.D., 1978: Radiation climate of Broughton Island, energy budget studies in relation to fast-ice breakup processes in Davis Strait, edited by R.G. Barry and J.D. Jacobs, *Occas. Pap.* 26 pp. 105-120, Inst. Of Arctic and Alp. Res., Univ. of Colorado, Boulder.

Jeffries, M.O., K. Schwartz and S. Li, 1997: Arctic summer sea-ice SAR signatures, melt-season characteristics, and melt-pond fractions. *Polar Record*, 33, 101-112.

Jezek, K.C., D. Perovich, K.M. Golden, C. Luther, D.G. Barber, P. Gogineni, T. Grenfell, A. Jordan, C. Mobley, S. Nghiem, and R. Onstott. 1998 A broad Spectral, Interdisciplinary Investigation of the Electromagnetic Properties of Sea Ice. *IEEE Trans. Geosci. Rem. Sens.*. ONR ARI special issue. 36(5):1633-1641.

Jing, X. and R.D. Cess, 1998: Comparison of atmospheric clear-sky shortwave radiation models to collocated satellite and surface measurements in Canada. *J. Geophys. Res.*, 103(D22), 28817-28824.

Johannessen, O.M., M.W. Miles and E Bjorgo, 1996: Global sea ice monitoring from microwave satellites. *Proc. IGARSS '96*, 932-934.

Jordan, R.E., 1991: A one-dimensional temperature model for a snow cover: Technical documentation for SNTHERM.89, *Rep. 91-16*, 49 pp., Cold Reg. Res. and Eng. Lab, Hanover, NH.

Jordan, R.E., E.L. Andreas and A.P. Makshtas, 1999: Heat budget of snow-covered sea ice at North Pole 4. *J. Geophys. Res.*, 104(C4), 7785-7806.

Kattenburg, A. et al., 1996: Climate Models – Projections of Future Climate. In: *Climate Change 1995: The Science of Climate Change*. Cambridge University Press, pp. 285-357.

Key, J. R., R.A. Silcox and R.S. Stone, 1996: Evaluation of surface radiative flux parameterizations for use in sea ice models. *J.Geophys. Res.*, 101(C2), 3839-3849.

Kidwell, K.B., 1991: NOAA Polar Orbiter Data Users Guide. US Dept. of Commerce, NOAA NESDIS, Washington, D.C., pp. 250.

Koepke, P., 1989: Removal of atmospheric effects from AVHRR albedos. *J. Appl. Meteorol.* 28(12), 1341-1348.

Lake, R.A. and E.L. Lewis, 1970: Salt rejection by sea ice during growth. *J. Geophys. Res.*, 75(30), 583-597.

Langleben, M.P., 1971: Albedo of melting sea ice in the southern Beaufort Sea. *J. Glaciol.*, 10, 101-104.

LeDrew, E.F. and D.G. Barber, 1994: The SIMMS Program: a study of change and variability within the marine cryosphere. *Arctic*, 47, 256-264.

Leontyeva, E. and K. Stamnes, 1993: Estimations of cloud optical thickness from ground-based measurements of incoming solar radiation in the Arctic. *J. Climate*, 7, 566-578.

Li, Z. and H.G. Leighton, 1992: Narrow to broadband conversion of spatially autocorrelated reflectance measurements. *J. Appl. Meteorol.*, 31, 421-432.

Li, Z., H.G. Leighton, K. Masuda and T. Takashima, 1993: Estimation of SW flux absorbed at the surface from TOA reflected flux. *J. Climate*, 6, 317-330.

Lindsay, R.W. and D.A. Rothrock, 1993: The calculation of surface temperature and albedo of Arctic sea ice from AVHRR. *Annals of Glaciol.*, 17, 391-397.

Lindsay, R.W. and D.A. Rothrock, 1994: Arctic sea ice albedo from AVHRR. *J. Climate*, 7(11), 1737-1749.

Livingstone, C.E., R.G. Onstott, L.D. Arsenault, A.L. Gray and K.P. Singh, 1987: Microwave sea-ice signatures near the onset of melt. *IEEE Trans. Geosci. Rem. Sens.*, GE-25(2), 174-187.

Livingstone, C.E. and M.R. Drinkwater, 1991: Springtime C-band SAR backscatter signatures of Labrador Sea marginal ice: measurements versus modeling predictions. *IEEE Trans. Geosci. Rem. Sens.*, 29, 29-41.

Lock, G.S.H., 1990: The Growth and Decay of Ice. Cambridge University Press, New York, pp. 444.

Lofgren, G. and W.F. Weeks, 1969: Effect of growth parameters on the substructure spacing in NaCl ice crystals. *J. Glaciol.*, 8(52), 153-164.

Loth, B., H.F. Graf and J.M. Oberhuber, 1993: Snow cover model for global climate simulations. *J. Geophys Res.*, 98, 10451-10464.

Lynch-Steiglitz, M., 1994: The development and validation of a simple snow model for the GISS GCM. *J. Climate*, 7, 1842-1855.

Makshtas, A., 1991: The heat budget of arctic ice in the winter. Intl. Glaciological Society, Cambridge, UK, pp. 77.

Malinas, N.P. and R.A Shuchman, 1994: SAR derived sea ice thickness during ICEX'92. *IEEE trans. Geosci. Rem. Sens.*, 1756-1758.

Markus, T. and B.A. Burns, 1995: A method to estimate subpixel-scale coastal polynyas with satellite passive microwave data. *J. Geophys Res.*, 100, 4473-4487.

Markus, T. and D.J. Cavalieri, 1996: Comparison of open water and thin ice areas derived from satellite passive microwave data with aircraft measurements and satellite infrared data in the Bering Sea. *Proc. IGARSS'96*, 1523-1525.

Markus, T. and Cavalieri, D.J., 1998. Snow depth distribution over sea ice in the southern ocean from satellite passive microwave data. *Antarctic Sea Ice Physical Processes, Interactions and Variability*, Antarct. Res. Ser. 74, AGU, Washington, D.C., pp.19-39.

Maslanik, J.A. and H. Maybee, 1994: Assimilating remotely-sensed data into a dynamic-thermodynamic sea ice model. *IGARSS'94*, 1306-1308.

Maykut, G.A. and N. Untersteiner, 1971: Some results from a time dependent thermodynamic model of sea ice. *J. Geophys. Res.*, 76, 1550-1575.

Maykut, G.A. and P.E. Church, 1973: Radiation climate of Barrow, Alaska, 1962-66, *J. Appl. Met.*, 12, 620-628.

Maykut, G.A. and T.C. Grenfell, 1975: The spectral distribution of light beneath first-year sea ice in the Arctic Ocean. *Limnol. And Oceanog.*, 20(4), 554-563.

Maykut, G.A., 1978: Energy exchange over young sea ice in the central arctic. *J Geophys. Res.*, 83(C7), 3646-3658.

Maykut, G. A., 1982: Large scale heat exchange and ice production in the central Arctic. *J. Geophys. Res.*, 87, 7971-7984.

Maykut, G.A., 1985: *The Ice Environment*. Sea Ice Biota, Ed: R.A. Horner, CRC Press, Boca Raton, FL, pp. 21-82.

Maykut, G.A., 1986: The surface Heat and Mass Balance. In: *The Geophysics of Sea Ice*. Ed: N. Untersteiner, Plenium Press, New York, 395-464.

Minnett, P.J., 1999: The influence of solar zenith angle and cloud type on cloud radiative forcing at the surface in the Arctic. *J. Climate*, 12, 147-158.

Moritz, R. E., and D. K. Perovich, Ed, SHEBA, A Research Program on the Surface Heat Budget of the Arctic Ocean, Science Plan, Rep. No. 5, U. of Washington, 64 pp., 1996.

Nghiem, S.V. et al., 1998: Diurnal thermal cycling effects on backscatter of thin sea ice, *IEEE Trans. Geosci. Rem. Sens.*, 36(1), 111-124.

Ohmura, A., 1981: Climate and energy balance of the Arctic tundra. *Zurcher Geogr. Schr* 3, 448 pp. Geogr. Inst., Zurich, Switzerland.

Ono, N., 1966: Thermal properties of sea ice: III; On the specific heat of sea ice, *Low Temp. Sci.*, A24, 249-258.

Ono, N. and T. Kasai, 1985: Surface layer salinity of young ice. *Ann. Glaciol.*, 6, 298-299.

Ono, N. and M.S. Krass, 1993: Theoretical approach describing the thermal regime of snow-covered sea ice. *Ann. Glaciol.*, 18, 79-84.

Onstott, R.G., 1992: SAR and scatterometer Signature of Sea Ice. Chapter 5. In; Carsey F. (Editor) Microwave Remote Sensing of Sea Ice. (American Geophysical Union. 1992. Geophysical Monograph 68)

Owens, W.B. and P. Lemke, 1990: Sensitivity studies with a sea ice-mixed layer-pycnocline model in the Weddell Sea. *J. Geophys. Res.*, 95, 9527-9538.

Papakyriakou, T.N., 1999: An examination of relationships among the energy balance, surface properties and climate over snow covered sea ice during the spring season. Ph.D. Thesis, University of Waterloo, Waterloo, Ontario, pp. 364.

Parkinson, C.L. and W.M. Kellogg, 1979: Arctic sea ice decay simulated for a CO_2-induced temperature rise. *Clim. Change*, 2, 149-162.

Parkinson, C.L., D. Cavalieri, P. Gloersen, H.Zwally and J. Comiso, 1999. Arctic sea ice extents, areas and trends, 1978-1996. *J. Geophys. Res.* 104(C9), 20837-20856.

Perovich, D.K., 1996: The Optical Properties of Sea Ice. USA Cold Regions Research and Engineering Laboratory, Hanover, NH, Monograph 96-1, 25 pp.

Petzold, D. E., 1977: An estimation technique for snow surface albedo. *Climat. Bull.*, 21, 1-11.

Pitman, D. and B. Zuckerman, 1967: Effective thermal conductivity of snow at -88, -27, and -5°C. *J. Appl. Phys.*, 38, 2698-2699.

Pomeroy, J.W., P. Marsh and D.M. Cray, 1997: Application of a distributed blowing snow model to the arctic. *Hydrol. Processes.*, 11, 1451-1464.

Preller, R.H., J.E. Walsh and J.A. Maslanik, 1992: The use of satellite observations in ice cover simulations. Microwave Remote Sensing of Sea Ice, American Geophysical Union, 385-404.

Radionov, V.F., N.N. Bryazgin and E.I. Alexandrov, 1997: The snow cover of the Arctic Basin. *Tech. Report APL-UW TR 9701*, Applied Physics Laboratory, University of Washington, Seattle, Washington, pp. 63.

Robinson, D.A., G. Scharfen, M.C. Serreze, G. Kulka and R.G. Barry, 1986: Snow melt surface albedo in the Arctic basin. *Geophys. Res. Letters*, 13, 945-948.

Robinson, D.A., G. Scharfen, M.C. Serreze, R.G. Barry and G. Kukla, 1992: Large-scale patterns and variability of snow melt and parameterized surface albedo in the Arctic basin. *J. Climate*, 5(10), 1109-1119.

Ross, B., and J.E. Walsh, 1987: A comparison of simulated and observed fluctuations in summertime Arctic surface albedo. *J. Geophys. Res.*, 92, 13,115-13,125.

Rothrock, D.A., Y. Yu, and G.A. Maykut, 1999: Thinning of the Arctic sea-ice cover. *Geophys. Res. Letters.*, 26, 1-5.

Semtner, A.J. Jr., 1976: A model for the thermodynamic growth of sea ice in numerical investigations of climate. *J. Phys. Oceanogr.*, 6, 379-389.

Semtner, A.J. Jr., 1987: A numerical study of sea ice and ocean circulation in the Arctic. *J. Phys. Oceanogr.*, 17, 1077-1099.

Serreze, M.C. et al. 2000: Observational evidence of recent change in the northern high-latitude environment. *Climate Change*, 46, 159-207

Shine, K.P, A. Henderson-Sellers and R.G. Barry, 1983: Albedo-climate feedback: The importance of cloud cryosphere variability, In: *New Perspectives in Climate Modeling.* Eds: A. Berger and C. Nicolis, published by Elsevier.

Shine, K.P., 1984: Parameterization of shortwave flux over high albedo surfaces as a function of cloud thickness and surface albedo. *Q. J. R. Meteorol. Soc.*, 110, 747-764.

Shine, K.P and A. Henderson-Sellers, 1985: The sensitivity of a thermodynamic sea ice model to changes in surface albedo parameterization. *J. Geophys. Res.*, 90(D1), 2243-2250.

Shirasawa, K. and R.G. Ingram, 1997: Currents and turbulent fluxes under the first-year sea ice in Resolute Passage, Northwest Territories, Canada. *J. Marine Systems.*, 11, 21-32.

Shuchman, R.A., R.G. Onstott, R.W. Flett and C.C. Wackerman, 1996: Satellite remote sensing of the Beaufort Sea during LEADEX'92. *IEEE trans. Geosci. Rem. Sens.*, 1015-1017.

St. Germain, K.M and D.J. Cavalieri, 1996: A microwave technique for mapping ice temperatures in the Arctic seasonal ice zone. *Proc. IGARSS'96*, 1208-1210.

Steffen, K. and T. DeMaria, 1996: Surface energy fluxes of Arctic winter ice in Barrow Strait. *J. Appl. Meteorol.*, 35, 2067-2079.

Sturm, M., 1991: The role of thermal convection in heat and mass transport in the subarctic snow cover. U.S. Army Core of Engineers Cold Regions Research and Engineering Lab, Hanover, New Hampshire, CRREL Report 91-19, pp. 52.

Sturm, M., J. Holmgren, M. Konig, and K. Morris, 1997: The thermal conductivity of seasonal snow. *J. Glaciol.*, 43, 26-41.

Svendsen, E., et al., 1983: Norwegian Remote Sensing Experiment: Evaluation of the Nimbus 7 Scanning Multichannel Microwave Radiometer for sea ice research. *J. Geophys. Res.*, 88, 2781-2791.

Taylor, V.R.and L.L. Stowe, 1984: Atlas of reflectance patterns for uniform Earth and cloud surfaces (NIMBUS-7 ERB -- 61 days). NOAA Technical Report NESDIS 10, 66 pp.

Tiuri, M.E. et al., 1984: The complex dielectric constant of snow at microwave frequencies. *IEEE J. Oceanic Engineering OE-9*, 5, 377-382.

Tucker, W.B., A.J. Gow and W.F. Weeks, 1987: Physical properties of summer sea ice in Fram Strait. *J. Geophys Res.*, 92(C7), 6787-6803.

Ulaby, F.T., R.K. Moore and A.K. Fung, 1986: Microwave Remote Sensing: Active and Passive. Vol 3, Norwood, MA: Addison-Wesley Publishing Company.

Vant, M.R., R.O. Ramseier and V. Makios, 1974: Dielectric properties of fresh snow and sea ice at 10 and 36 GHz. *J. Appl. Physics.*, 45, 4712-4717.

Vant, M.R., R.O. Ramseier and V. Makios, 1978: The complex dielectric constant of sea ice at frequencies in the range 0.1 to 40 GHz. *J. Appl. Phys.*, 49(3), 1264-1280.

Wakatsuchi, M. and T. Kawamura, 1987: Formation processes of brine drainage channels in sea ice. *J. Geophys. Res.*, 92(C7), 7195-7197.

Walsh, J.E., W.L. Chapman, and T. Shy, 1996. Recent decrease of sea level pressure in the central Arctic. *J. Clmate*. 9. 480-486.

Warren, S.G. and W.J. Wiscombe, 1981: A model for the spectral albedo of snow. I: Snow containing atmospheric aerosols. *J. Atmos. Sci.*, 37, 2735-2745.

Weaver, R.L., C. Morris, R.G. Barry, 1987: Passive microwave data for snow and ice research: planned products from the DMSP SSM/I system. *EOS (Trans. Amer. Geophys. Union)*, 68, 769, 776-777.

Weaver, R.L. and V.J. Troisi, 1996: Remote sensing data availability from the Earth Observation System (EOS) via the Distributed Active Archive Center (DAAC) at NSIDC. *Proc. IGARSS'96*, 73-77.

Weeks, W.F. and A.J. Gow, 1980: Crystal alignments in the fast-ice of arctic Alaska. *J. Geophys. Res.*, 84(C10), 1137-1146.

Wenshanan, M.R., T.C. Grenfell, D.P. Winebrenner and G.A. Maykut, 1993a: Observations and theoretical studies of microwave emission from thin saline ice. *J. Geophys. Res.*, 98(C5), 8531-8545.

Wenshanan, M.R., G.A. Maykut, T.C. Grenfell, D.P. Winebrenner, 1993b: Passive microwave remote sensing of thin sea ice using principle component analysis. *J. Geophys. Res.*, 98(C7), 12,453-12,468.

Wilson, K. et al, 2001: Validation of the TRACKER algorithm for sea ice motion. *Atmos.-Ocean* (in press).

Winebrenner, D.P., E.D. Nelson, R. Colony and R.D. West, 1994: Observations of melt onset on multi-year Arctic sea ice using the ERS-1 SAR. *J. Geophys. Res.*, 99, 22,425-22,442.

Winebrenner, D.P, 1996: Polarmetric backscatter at 23 cm wavelength from Antarctic lead ice and estimation of ice thickness. *Proc. IGARSS'96*, 941-943.

Wiscombe, W.J. and S.G. Warren, 1981: A model for the spectral albedo of snow. I: Pure snow. *J. Atmos. Sci.*, 37, 2712-2733.

Yackel, J.J., D.G. Barber and J.M. Hanesiak, 2000: Melt ponds on sea ice in the Canadian Archipelago: 1, variability in morphological and radiative properties, *J. Geophys. Res.*, 105(C9), 22049-22060.

Yackel, J.J. and D.G. Barber, 2000: Melt ponds on sea ice in the Canadian Archipelago: 2, on the use of RADARSAT-1 synthetic aperture radar for geophysical inversion. *J. Geophys. Res.*, 105(C9), 22061-22070.

Zhang, T., K. Stamnes and S.A. Bowling, 1996: Impact of clouds on surface radiative fluxes and snowmelt in the Arctic and Subarctic. *J. Climate*, 9, 2110-2123.